Neutralisation of myoelectric interference from recorded nerve signals using models of the electrode impedance

Ioannis Pachnis

A thesis submitted in partial fulfilment of the requirements for the degree of Doctor of Philosophy

Principal supervisor: Dr. Andreas Demosthenous

Subsidiary supervisor: Prof. Nick Donaldson

September 2010

Department of Electronic and Electrical Engineering

University College London

Official declaration

I, Ioannis Pachnis, confirm that the work presented in this thesis is my own. Where information has been derived from other sources, I confirm that this has been appropriately indicated in the thesis.

Abstract

Any form of paralysis due to spinal cord injury or other medical condition, can have a significant impact on the quality and life expectancy of an individual. Advances in medicine and surgery have offered solutions that can improve the condition of a patient, however, most of the times an individual's life does not dramatically improve. Implanted neuroprosthetic devices can partially restore the lost functionalities by means of functional electrical stimulation techniques. This involves applying patterns of electrical current pulses to innervate the neural pathways between the brain and the affected muscles/organs, while recording of neural information from peripheral nerves can be used as feedback to improve performance.

Recording naturally occurring nerve signals via implanted electrodes attached to tripolar amplifier configurations is an approach that has been successfully used for obtaining desired information in non-acute preparations since the mid-70s. The neural signal (i.e. ENG), which can be exploited as feedback to another system (e.g. a stimulator), or simply extracted for further processing, is then intrinsically more reliable in comparison to signals obtained by artificial sensors. Sadly, neural recording of this type can be greatly compromised by myoelectric (i.e. EMG) interference, which is present at the neural interface and registered by the recording amplifier. Although current amplifier configurations reduce myoelectric interference this is suboptimal and therefore there is room for improvement. The main difficulty exists in the frequency-dependence of the electrode-tissue interface impedance which is complex.

The simplistic Quasi-Tripole amplifier configuration does not allow for the complete removal of interference but it is the most power efficient because it uses only one instrumentation amplifier. Conversely, the True-Tripole and its developed automatic counterpart the Adaptive-Tripole, although minimise interference and provide means of compensating for the electrode asymmetries and changes that occur to the neural interface (e.g. due to tissue growth), they do not remove interference completely as the insignificant electrode impedance is still important. Additionally, removing interference apart from being dependent on the frequency of the interfering source, it is also subject to its proximity and orientation with respect to the recording electrodes, as this affects the field. Hence neutralisation with those two configurations, in reality, is not achieved in the entire bandwidth of the neural signal in the interfering spectrum. As both are less power efficient than the Quasi-Tripole an alternative configuration offering better performance in terms of interference neutralisation (i.e. frequency-independent, insensitive to the external interference fields) and, if possible, consume less power, is considered highly attractive.

The motivation of this work is based on the following fact: as there are models that can mimic the frequency response of metal electrodes it should be possible, by constructing a network of an equivalent arrangement to the impedance of electrodes, to fit the characteristic neutralisation impedance – the impedance needed to balance a

recording tripole – and ideally require no adjustment for removing interference. The validity of this postulation is proven in a series of in-vitro preparations using a modified version of the Quasi-Tripole made out of discrete circuit components where an impedance is placed at either side of the outer electrodes for balancing the recording arrangement. Various models were used in place of that impedance. In particular, representing the neutralisation impedance as a parallel RC reduced interference by a factor of 10 at all frequencies in the bandwidth of the neural signal while removed it completely at a spot frequency. Conversely, modelling the effect of the constant phase angle impedance of highly polarisable electrodes using a 20 stages non-uniform RC ladder network resulted in the minimisation of interference without the initial requirement of continuous adjustment. It is demonstrated that with a model that does not perfectly fit the impedance profile of a monopolar electrochemical cell an average reduction in interference of about 100 times is achieved, with the cell arranged as a Wheatstone bridge that can be balanced in the ENG band.

Acknowledgements

First and foremost, I would like to express my sincere gratitude to both my academic supervisors, Dr. Andreas Demosthenous and Prof. Nick Donaldson, for their valuable help whenever I needed it.

Dr. Demosthenous for his help and support (both emotional and financial) throughout those 5 years of hard work in getting this PhD done. For his guidance, particularly on how to appropriately test the discrete circuit set-up that was part of the concluding in-vitro experiments of Chapter 5, for his valuable insight in designing and developing integrated circuits many of which were not included in this PhD work (e.g. stimulator o/p stage, beta-multiplier voltage-current reference), and finally for his very important feedback comments on the first drafts of the thesis. His instructive criticism only made me better.

Prof. Donaldson for teaching me how scientific research needs to be done and the many more interesting discussions he had with me regarding this PhD work. I particularly would like to thank him for his help in generating the material of Chapter 3, making the sphere electrode monopole used in Chapter 5 towards the verification of the proposed neutralisation technique in-vitro, the derivation of the input impedance of the floating negative impedance converter circuit included in Appendix C, and finally for carefully reading the PhD manuscript and for his many interesting and important suggestions. There is no doubt I learnt a lot from him.

I thank you both!

My colleagues and dear friends at the Analogue and Biomedical Electronics group of the Electronic & Electrical Engineering department for the interesting discussions we had and for being there for me both at good and bad times. In particular, Dr. Panagiotis Kassanos for the many interesting (scientific or not) discussions and for being a truthful source of feedback and a good friend, Dr. Hongwei Hong, Dr. Xiao Liu, Dr. Mohamad Rahal, Dr. Dai Jiang, Virgilio Valente, Dominik Cirmirakis, and Tamin Faiq for the discussions we had, the ideas we shared and the good laughs, and last but not least, Dr. Iasonas Triantis for his very insightful suggestions on my thesis work. It is most certain that all of you will have a bright career and future.

The people at the Implanted Devices group of the Medical Physics & Bioengineering department for the productive discussions and suggestions, and for providing the necessary laboratory equipment and space for carrying out some of the experimental work there.

EPSRC and Royal Academy of Engineering for the funding.

I thank you all!

My parents for their unconditional care and love, and for being a long-time source of inspiration and unanimous support on all counts through my whole life so far.

I cannot thank you enough!

This acknowledgement concludes with what is probably the only paragraph in this thesis that is addressed to the reader in first person: my main intention while writing this piece of work was to offer you, in simple terms, good understanding of the topics covered in it. Each chapter was written as if you – the curious reader (or postgraduate student) – know little (or sometimes nothing) about the subject. Although this thesis deals with several different topics that (I want to believe) belong to the field of biomedical engineering and in particular that of functional electrical stimulation neuroprosthesis, it is focused more on medical instrumentation for neural signal recording and less on the pathophysiology of spinal cord injury. The innovation of this thesis in comparison to past theses on the same subject, at the Analogue and Biomedical Electronics group of UCL, is that greater emphasis has now been given on understanding and modelling of biomedical implanted electrodes and less (but no less than necessary!) with regards to neural signal recording and its underlying theory. Besides, a substantial and most importantly comprehensive literature on the latter can be found in many biomedical books and selected journals; the same cannot be claimed for the former – electrodes are highly nonlinear "devices", the terminology is vast and confusing, and the learning curve is rather steep. Regardless of the struggling that a work of such magnitude like putting a PhD thesis together involves, I enjoyed writing this thesis and you might as well find the material in it helpful once you finish reading it. I sincerely hope so!

Yannis Pachnis

London, September 2010

Contents

CHAPTER 4

Impedance Modelling of Metallic Electrodes   **70**

CHAPTER 6

General Conclusion and Future Work   **173**

APPENDIX A

Ideal Tripolar Cuff Model   **178**

List of Figures

List of Tables

Abbreviations

A/D	Analogue-to-Digital
AT	Automatic- or Adaptive-Tripole
aTT	Adjustable True-Tripole
CAP	Compound Action Potential
CM	Common-mode
CMRR	Common-mode Rejection Ratio
CNS	Central Nervous System
CPE	Constant Phase Element
CSF	Cerebrospinal fluid
ECG	Electrocardiogram
EMF	Electromagnetic field
EMG	Electromyogram
ENG	Electroneurogram
FES	Functional Electrical Stimulation
FPFD	Fractional Power Frequency Dependence
GBW	Gain-Bandwidth Product
IC	Integrated Circuit
IHP	Inner Helmholtz Plane
INIC	Current-inversion NIC
LPF	Low Pass Filter
MICS	Medical Implant Communication Service
mQT	Modified Quasi-Tripole
NIC	Negative Impedance Converter
OHP	Outer Helmholtz Plane
PCB	Printed Circuit Board
PNS	Peripheral Nervous System
Pt	Platinum
Pt-Ir	Platinum-Iridium
QT	Quasi-Tripole
RMS	Root Mean Square
SFAP	Single-Fibre Action Potential
SPI	Spinal Cord Injury
ST	Screened-Tripole
TT	True-Tripole
VNIC	Voltage-inversion NIC

Preface

The purpose of this piece of work is to advance the state of the art of recording amplifiers used towards the acquisition of neural information from peripheral nerves via implanted tripolar cuff electrodes. A novel amplifier configuration is here presented where improvement in the way of neutralising myoelectric interference is demonstrated through a series of in-vitro experiments. The main focus during the development of this novel neutralisation approach was given on simplicity and power efficiency to the degree this was possible.

The thesis covers a broad range of topics in the field of neural signal recording and it is aimed primarily at an audience with an engineering background, like electrical or biomedical, while to the author's personal belief, prior knowledge of the field is not a prerequisite for understanding its contents. This work has grown out of the author's personal frustration of having used a lot of the time during his PhD trying to attain a good understanding of the topics included and having utilised multiple amount of (re)sources, like the very few specialised on the field textbooks and the numerous selected publications, often simply to comprehend a sole aspect of the work. Therefore, every chapter has been written with a great deal of consideration, so the reader can attain a good level of understanding at a reasonable timeframe. Finally, the material in this thesis are provided in a sequential manner and often are fully developed in more than one chapter, while in many cases the use of cross-referencing of information from a particular chapter to others, e.g. for text and figures, is done to ease understanding and maintain a meaningful constant flow of information.

In this thesis, references are indicated by square brackets with the name and year of publication. In case there is more than one reference with the exact same name and year, then an alphabetic letter is added next to the year of publication to signify the difference. Moreover, references are common to the whole thesis and therefore are given in a full alphabetical order at the very end of the thesis, and not provided separately at the end of each chapter. Another important originality of this thesis is the extensive use of footnotes at the bottom of a page whenever that was felt necessary. In particular, footnotes, indicated by a small superscript number, have offered the freedom to deviate from the main text and explain various points in more depth, or even provide additional amount of information when the situation demanded it. Finally, each important equation in a chapter is followed by a number in round brackets in the form of x.y where x is the chapter number and y the dedicated equation number; the same numbering convention applies to the figures and tables of this thesis. Finally, the numbering of footnotes, equations, figures and tables is independent for every chapter and is done using the Arabic numerical notation. In this way, referring to a specific figure or equation can be done without also having to mention separately the chapter number.

CHAPTER
ONE

Introduction

It is estimated that the annual incidence of spinal cord injury (SCI), not including those who die at the scene of the accident, is approximately 40 cases per million population in the U. S. alone (or approximately 12,000 new cases each year). SCI usually affects young adults as a lot of the injuries occur between the ages of 16 and 30. According to the national SCI statistical center [NSCISC, last accessed: September 2010], since 2005, the average age at injury has increased to 40.2 years while 80.8% of SCI reported to the database have occurred among males. Moreover, motor vehicle crashes currently account for 41.3% of reported SCI cases with the next most common cause of SCI being falls, followed by acts of violence and recreational sporting activities. Despite the steady increase in the average age at injury, nowadays, most people with SCI survive and live near-normal life spans. Finally, atraumatic medical conditions such as stroke, ischemia, multiple sclerosis, or even tumour can be another cause of indirect SCI.

The motivation behind this piece of work is the subject of SCI and the realisation of how, and to what extent, it affects the lives of people. This involves the effort needed by a person with SCI to accomplish even simple everyday tasks, the social implications, the dependence on others for assistance, the cost of treatment/support equipment, and finally the reduced life expectancy of an individual in comparison to those with no SCI, are only few of the issues coming along such a devastating occurrence. This is because damage to the spinal cord due to an injury most of the times is irreparable and currently there is no cure. Nevertheless, on-going research has proven that spinal cord repair and regeneration might be possible (e.g. stem cell transplants), and perhaps it could be used in future to reinstate a patient's life to normal. Additionally, new breakthroughs and discoveries in medicine and nanotechnology allow alternative forms of rehabilitation to be currently feasible. In particular, the progress in the field of microelectronics has allowed the development of more advanced implanted neuroprosthetic devices which can help people to better manage quality of life issues associated with SCI such as chronic pain, bladder and bowel control, sexual dysfunction, as well as addressing respiratory problems.

According to [Apparelyzed: SCI peer support, last accessed: September 2010] a SCI is defined as any kind of physical damage or trauma that crushes or compresses the spinal cord which in turn results in a loss or impaired function such as reduced mobility or feeling at the level of injury and to everything below. The damage to the spinal cord (fig. 1.1) is known as a lesion, and the paralysis is known as *quadraplegia* (or tetraplegia) if the injury is in the neck region, which usually results in loss of independent breathing and loss of function to the arms and legs, or as *paraplegia* if the injury is anywhere below that

level, involving some loss of function in the legs and difficulty with bowel/bladder voiding and sexual control. Loss of function and sensation in quadraplegia is very similar to paraplegia with the only difference being that paraplegics have full use of their arms and hands. Also, loss of bladder and bowel control most often occurs with severe injury anywhere along the spinal column.
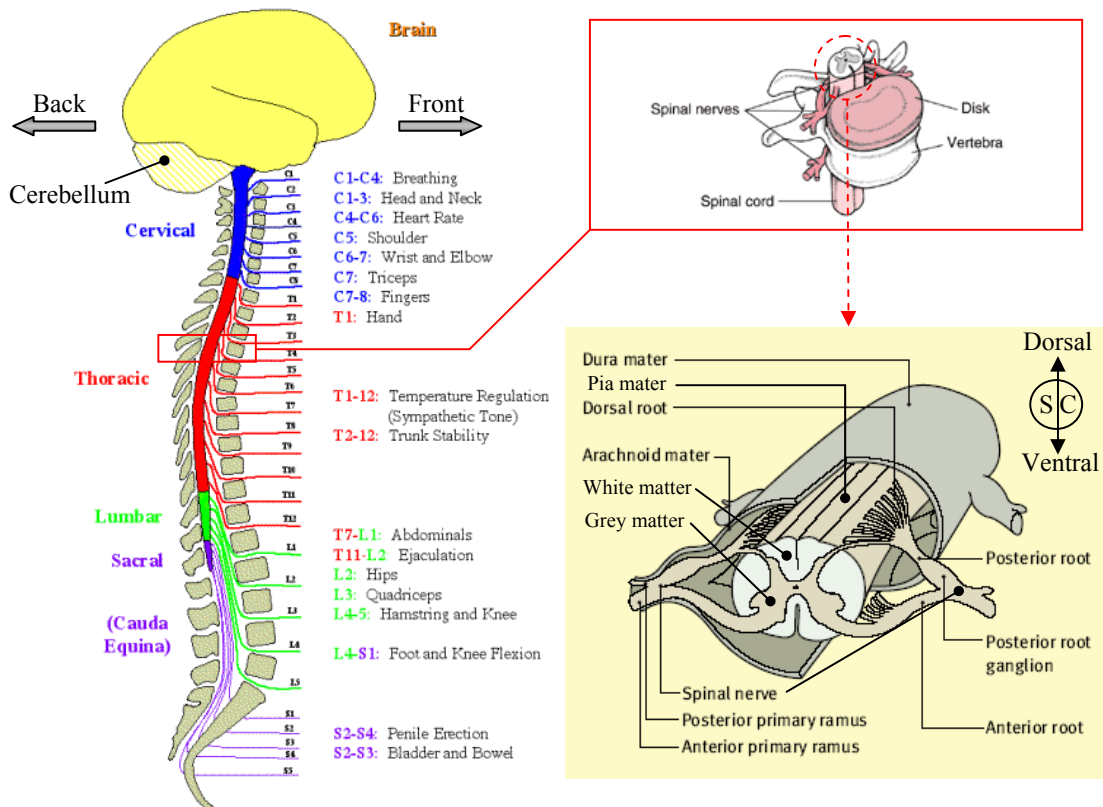
Figure 1.1: (left) Schematic structure of the human spinal cord showing the vertebrae bones (i.e. constituting the vertebral or spinal column) and the 31 spinal nerves emerging through spaces (called intervertebral foramina) between the vertebrae. The single coccygeal spinal nerve located at the very bottom segment of the spinal column is not shown. Figure taken from [Reeve-Irvine research center, last accessed: September 2010]. (right) Thoracic spinal cord cross-section showing 1 out of the 31 left-right pairs of spinal nerves formed by nerve rootlets that exit the spinal cord.

It is important to note that the spinal cord does not have to be completely severed for there to be a loss of function. In fact, the spinal cord remains intact in most cases of SCI. Instead, an injury is more likely to cause fractures and compression of the vertebrae, which then crush and destroy the axons: extensions of nerve cells that carry signals up and down the spinal cord between the brain and the rest of the body. An injury to the spinal cord tissue can damage a few, many, or almost all of these axons. Some injuries will allow almost complete recovery. Others will result in complete paralysis. Persons with tetraplegia have sustained injuries to one of the eight cervical segments of the spinal cord, while those with paraplegia have lesions in the thoracic, lumbar, or sacral regions of the spinal cord. Additionally, there are two types of lesions associated with a SCI; these

are known as *complete* and *incomplete* injuries. A complete injury means the person is completely paralysed below their lesion with absence of motor *and* sensory function, whereas an incomplete injury means only part of the spinal cord is damaged and an individual may have retained some sensation and/or movement below the level of their lesion. Subsequently, a person with an incomplete SCI has been shown to have a better chance of recovery than that of a complete injury with the degree of recovery ranging from significant motor function, to return of sensation. Nevertheless, although some amount of recovery often occurs after SCI, it is uncommon for someone to recover function and sensation to that of their pre-injury ability. Since 2005, the most frequent neurologic category at first stage rehabilitation discharge of persons reported to the database [NSCISC, last accessed: September 2010] is incomplete tetraplegia (38.3%), followed by complete paraplegia (22.9%), incomplete paraplegia (21.5%), and complete tetraplegia (16.9%).

1.1 The human spinal cord

The spinal cord, a cross-section of which is depicted in the insert of fig. 1.1, is a long cylinder of nervous tissue and support cells that extends from the brain (but not through the entire length of the vertebral column), primarily acting as the pathway for transmitting information between the brain and the rest of the body. Different levels of the spinal cord control different parts of the body. The soft, jelly-like spinal cord is situated into the vertebral (or spinal) canal and protected by the vertebral column; it is encased by a series of hard bones, the vertebrae[1], which allow for flexibility of the back and protect the very delicate spinal tissue. Moreover, the spinal cord is enveloped by three membrane layers (i.e. the spinal *meninges*) which provide additional protection and nourishment: the tough outermost *dura mater*, the middle *arachnoid mater*, and the innermost *pia mater*[2] which adheres to the surface of the spinal cord. The vertebral column is made up of 33 vertebrae bones stacked one on top of the other with the spinal cord running through, which in turn can be anatomically divided into 31 spinal segments, also numbered from top to bottom, based on the origins of the spinal nerves[3]. The segment of the spinal cord and what part of the cord at that segment is injured, in

---

[1] The vertebrae are organised into sections, and are named and numbered from top (i.e. base of the cranium) to bottom (i.e. sacrum) according to their location on the vertebral column. These are called: Cervical (7), Thoracic (12), Lumbar (5), Sacral (5), and finally the Coccygeal (4) vertebrae which are located in the tailbone (i.e. also known as the coccyx).

[2] The space between the arachnoid and the underlying pia mater is called the subarachnoid space which contains cerebrospinal fluid (CSF) that mainly acts as a cushion to protect the spinal nervous tissue against damage from forced contact with the inside of the vertebrae. The CSF is also present in the brain.

[3] There are 31 pairs of spinal nerves in the human body: 8 Cervical, 12 Thoracic, 5 Lumbar, 5 Sacral, and 1 Coccygeal [Mathers, 1985, p. 48]. The cauda equina (i.e. Latin for "horse's tail") is the bundle of nerve roots including lower lumbar, all of the sacral, and the single coccygeal nerve found at the end of the spinal cord (i.e. about first to second lumbar vertebral level), in the spinal canal, and enwrapped up to the second sacral vertebrae by the dura mater, which is the point where the dural sac ends [Mathers, 1985, p. 81]. Also, because the vertebral column grows longer than the spinal cord, locations of spinal cord segments do not correspond exactly to vertebral locations, especially in the lower spinal cord. Therefore, the spinal nerves are named from where they come out in the vertebral column and not from the level where they originate in the spinal cord (with respect to the column), e.g., L5 spinal cord segment is level with T11-T12 vertebrae.

accordance to the severity of the injury, will determine which body functions are compromised or lost. Each segment marks where spinal nerves emerge from the cord to connect to specific regions of the body that are responsible for. As an example, cervical level 1-2 (C1-C2), the highest and closest to the skull, controls breathing, C5-C6 (the most common injury site) is at the bump where the neck meets the back and controls fingers and hands. Nerves from the body also enter the spinal cord at each segment (i.e. via the spinal nerve), providing sensory information about specific body parts to the brain. In addition to nerves coming out (or into) the spinal cord at different segments, for the transmission of neural signals between the brain and the rest of the body, the spinal cord also conveys information between the brain and the spinal cord itself. More specifically, the peripheral region of the cord named *white matter* consists of groups of (mostly myelinated) axons passing upward and downward along the long axis of the cord connecting regions of the cord with each other and with the brain, while the central portion of the cord, called *grey matter*, neuronal cell bodies (i.e. the somas; c.f. §2.2.2) as well their branched projections (i.e. the dendrites; c.f. §2.2.2) and (mostly unmyelinated) axons are combined together in a reticular arrangement performing local communication [Mathers, 1985, p. 48]. Furthermore, both white and grey matter also consist of glial cells (c.f. §2.2.1). As an example, large bundles of nerve cells, called *neuronal tracts* or pathways in the white matter, run from the motor centres in the brain down the spinal cord and connect to pools of motor neurons that are responsible for movement. Details of the internal structure of the spinal cord is out of the scope of this section and the reader is referred to [Mathers, 1985, pp. 48-51] or other neuroscience textbooks for the relevant treatment.

It is rather important to devote a small section of this introductory chapter in explaining why damage to the spinal cord is regrettably irreparable. The subsequent summary was compiled with the help of "Anatomy 101" module obtained from [Reeve-Irvine research center, last accessed: September 2010]. It should also be mentioned that any neuroscience-specific terms such as "neuron", "axon", "myelin", etc. will be presented and explained in detail in the next chapter where an introduction to neurophysiology is given.

1.2 Pathophysiology of SCI

Cells of the body, including neurons, can die in 2 ways: *necrosis* or *apoptosis*. Following an injury to the spinal cord, several things happen. First the spinal cord, which contains the neurons and axons that allow the brain and body to communicate is injured, stretching, crushing, or avulsing the axons at the site of the injury. This is followed by a series of events that occur days to weeks after the initial incident. More specifically, the neurons that are injured at the impact site burst resulting in a spreading wave of cell death. This is because what is inside a necrotic (i.e. dead), due to injury, neuron cell is toxic to neighbouring cells and may cause those to burst as well. This spreading wave of cell death, also called *secondary cell death*, can result in much more spinal cord tissue damage than was caused by the original traumatic impact. The end result of this process is a large hole (or cyst) around the injury site which fills with fluid (e.g. CSF) and becomes a barrier for axons trying to re-grow into the injury site. Apart from necrosis due

to factors external to the cell (e.g. infection, toxins, or trauma), there is also apoptotic cell death which in the case of SCI occurs when cells have been compromised in some way (e.g. being linked to the necrotic cells) and actively commit suicide. However, apoptosis does not lead to secondary cell death because the cellular debris left behind is not harmful to other cells as in the case of necrosis.

The spinal cord and brain are fairly isolated from the rest of the body by the blood-brain barrier separating the circulating blood and the CSF. After an injury, this barrier is compromised and cells – like the immune system cells T lymphocyte and macrophage that circulate in blood – from outside the central nervous system arrive at the injury site doing quite a bit of harm. In particular, macrophages clean up cellular debris, but after central nervous system injury, it is believed that they may also damage surviving nerve cells that could potentially recover, leading to an increase in secondary cell dell process. Moreover, as macrophages come into the injury site, they stimulate T lymphocytes, and these also have been shown to dramatically increase the amount of secondary damage following SCI. One function of certain types of astrocytes (i.e. a kind of glial support cell for neurons) is to repair or restore the blood-brain barrier by creating a scar around the injury site. The scar, however, creates several problems for regeneration; it is not only a physical barrier to nerve cells trying to re-grow, but it also gives off chemical stop signs that inhibit axonal regeneration.

Another immune function that is seen after injury, a result of which is swelling of the spinal cord, is inflammation, which can cause nerve and glial cells (e.g. like the oligodendrocyte) to die, while it can contribute to mechanisms like neuronal degeneration and demyelination[4] that essentially disconnect the brain from the spinal cord after injury. While loss of neurons is linked to loss of function, oligodendrocyte and Schwann cell death, the cells responsible for the production of myelin, also contribute to functional loss after a traumatic SCI. This is because, as we shall see in the next chapter, neurons need the insulating substance, myelin, to send messages. Therefore, damaged axons become dysfunctional either because they are stripped of their myelin, or because they are being disconnected from the brain upon SCI. Scientists are currently exploring ways to decrease the amount of damage that follows the initial injury (i.e. secondary cell death), as well as ways to create a bridge through the cyst so that axons can grow through the injury site.

The process of nerve cell damage in the spinal cord after injury is illustrated graphically in fig. 1.2 below. Although axons of neurons outside the spinal cord have – under conditions – the capability to regenerate, this is not the case with axons in the spinal cord. This is because myelin from myelin making cells in the spinal cord releases chemical signals that inhibit axonal regeneration, something which is not the case for myelin of the peripheral nerve cells. For reasons of completeness, the structure of a nerve residing outside the spinal cord (i.e. a peripheral nerve) down to a fascicle[5] (or fasciculus)

---

[4] Axons that are "naked" having lost their insulation and can no longer send messages.

[5] In a peripheral nerve, axons are individually surrounded by a loose connective tissue called the *endoneurium* with group of several axons forming a *fascicle*, which in turn is enclosed and separated in a denser connective tissue: the *perineurium*. A number of fascicles bounded together by another connective

level is also shown in the insert of fig.1.2. In respect to that, it would perhaps be useful to emphasise that the morphological structure[6] of a spinal nerve is not the same to that of a dorsal and ventral root/rootlet. In humans, a number of 6 to 8 dorsal and ventral rootlets emerge on each side of a segment of the spinal cord where they bundle together to become the ventral and the dorsal roots. Those subsequently meet outside the dura mater to form the single spinal nerve, i.e., the dorsal and ventral roots exit the dura mater separately, where they join to form the spinal nerve. Moreover, the spinal nerve does not contain actual intact nerve roots/rootlets but axonal projections of the ventral and dorsal roots, and therefore is not possible to separate. Conversely, the bundle of lumbosacral spinal nerve roots bounded together in the cauda equina, and surrounded only by the pia mater, are possible to separate into rootlets (i.e. by performing laminectomy and through an incision to the dura), making it possible to identify those innervating specific muscles of interest [Vanhoestenberghe, 2007]. Therefore, the cauda equina is an excellent location for electrode placement both in terms of selectiveness of nerves in the lower spinal cord as also in terms of anatomical space for the electrodes.
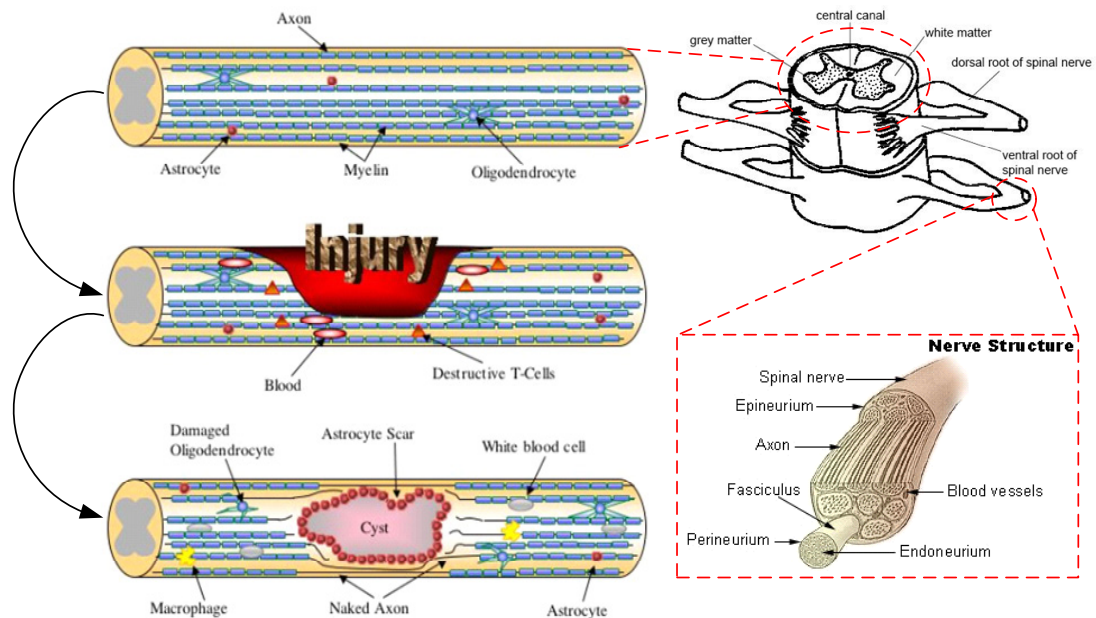
Figure 1.2: (left) Progression of a SCI (adapted from [Reeve-Irvine research center, last accessed: September 2010]). (right) Insert: figure of the inner structure of the spinal nerve root formed by the union of the ventral and dorsal roots of the spinal cord. Each spinal nerve later divides (outside the vertebral column) into a dorsal ramus and a ventral ramus with both containing mixed nerves (i.e. sensory and motor).

---

tissue, the *epineurium*, form a whole (spinal) nerve [Keynes and Aidley, 2001, pp. 8-9]. A peripheral nerve is thus formed by axons organised in fascicles which in turn are grouped together. In this work the word "nerve" or "nerve root" is used to describe the bundles of peripheral axons.

[6] By "structure" here mean the organisation of cells and connective tissue of the nerve and not the cell type composition (e.g. sensory neurons). For example, when nerve rootlets exit the spinal cord, each being surrounded by the thin pia mater, they gather to become a root where the glial cells of the endoneurium give way to Schwann cells in a transition from central to peripheral nervous system [Vanhoestenberghe, 2007].

1.3 Neuroprosthesis and usefulness of FES

Considering the biological complexity of SCI, discovering successful ways to repair injuries and create rehabilitative strategies that significantly reduce disabilities is not an easy task. As a result, following a SCI, therapy and rehabilitation is focused mainly on training and exercise for maintaining the individual fit. Also, at present, conventional medicine does not offer a method of curing the damage and fully restoring function. Neuroprosthesis and more specifically functional electrical stimulation (FES) is a well established method of achieving patient rehabilitation with lower cost (i.e. no need for medication and support equipment) and no major side effects (i.e. apart from mostly implant failures or biological rejection from the body). Neuroprosthesis involves carrying out a neurosurgical procedure to implant a device, often employed to improve or restore the function of an impaired nervous system. The device often makes use of FES; a technique which triggers paralysed muscles/organs via implanted electrodes injecting calibrated pulses of electrical current into the muscle tissue or nerve of interest, in the latter case to activate nerves innervating extremities affected by paralysis resulting from SCI, head injury, or stroke (e.g. stimulate a nerve whose axonal projection terminals connect directly with muscle fibres to make muscle move). This is certainly possible since nerve fibres are excitable by electrical stimuli (i.e. it is possible to trigger the neuromuscular system artificially) and most of the peripheral nerve functions remain unaffected even after injury, while peripheral nerves are self-repairing. Conversely, this means that people with some neurological disorders such as motor neurone disease or infectious disease such as spinal poliomyelitis which target the nervous system will not be able to benefit from FES because the peripheral nerves are in this case affected. FES has been demonstrated through various applications [Agnew and McCreery, 1990] to assist paraplegic individuals to stand, transfer and undertake simple forms of walking [Stein et al., 1992, pp. 233-251; Peckham and Knutson, 2005], quadriplegic to regain respiratory [Peckham and Knutson, 2005] and grasping functions [Stein et al., 1992, pp. 162-187; Peckham and Knutson, 2005], as also allowing bladder and bowel voiding in certain types of incontinence [Peckham and Knutson, 2005], sound perception in the hearing impaired, and managing pain in patients with severe chronic health problems. It should be, however, stressed that FES is not and cannot be considered a cure for SCI.

FES can be combined with recording of electrical activity in an implanted device to increase reliability and achieve better performance via using naturally occurring peripheral nerve signals as control inputs to a stimulator [Popovic et al., 1993; Haugland and Sinkjaer, 1999b]. More specifically, stimulators can be used in open-loop FES systems, and although these systems work satisfactorily, they often have disadvantages. In the case of bladder control implants[7], which throughout the thesis we adapt as a form of case study and a possible application outcome for this work, rhizotomy[8] needs to be performed to the subject to alleviate the problem of detrusor hyperreflexia (i.e. bladder-

---

[7] One of the current methods of treatment for restoring bladder functionality after SCI involves the use of the well-established and highly successful Finetech-Brindley sacral anterior root stimulator [Brindley et al., 1986; Brindley, 1994].

[8] A surgical procedure that cuts or interrupts spinal nerve roots in the spinal cord to treat muscle spasms or to relieve intractable pain of neurologic origin.

emptying reflex) in the likely presence of a neurologic lesion, from occurring, resulting to undesirable incontinence. Moreover, the fact of cutting nerves to allow the bladder stimulator device to work is something that many people with SCI are reluctant to go ahead with, despite of usually living for many years after their injuries, largely due to knowing that the destructive process of rhizotomy might reduce their chances of a cure when that becomes available in future. Conversely, closed-loop FES systems can be used to obtain information from sources around the body, using either artificial sensors attached to it or preferably the body's own natural sensors (e.g. sensory receptor organs) via the appropriately interfaced nerves. Hence, in the case of a bladder control implant, neuromodulation[9] [Craggs and McFarlane, 1999] can be applied (i.e. via electrical stimulus pulses) under certain conditions (i.e. upon onset of bladder spasms with increase in bladder pressure) to suppress the cause and increase bladder capacity without rhizotomy of the posterior (i.e. sensory) sacral roots. The possibility of this technique applied to humans with SCI has been investigated by [Kirkham et al., 2002] which have shown that neuromodulation, via stimulating the pudendal nerve pathway[10] can suppress the undesirable bladder contractions. Researchers are hoping that by combining neuromodulation for reflex incontinence with neurostimulation for bladder emptying, the bladder could be completely controlled without having to cut any of the sacral sensory nerves.

To design an implanted neural recording system several things need to be considered. Here we will outline the most important ones with regards to a general specification and not in terms of system level design. The first is to obtain data that will allow for the design of an appropriate neural interface[11]. This involves measuring the nerve or nerve root diameter to accommodate for the appropriate size of recording electrodes, selecting the material, shape and type of the electrodes used, and most importantly opting for a recording configuration that will be suitable for the particular application (i.e. interference rejection performance, power efficiency, effective noise, etc.). Additionally, someone has to take into account all these neural interface factors that can have an impact on the system's performance, like interference present in form of muscle signals as well as signals generated by other sources outside the cuff in the vicinity of the implanted electrodes, common-mode (CM) interference present, and amount of gain necessary for the neural signal over the bandwidth of interest. It is also often the case for electrodes, despite the significance they present in a system's performance, their design to be left at the end and almost as an afterthought, being preceded by the development of the associated electronic systems first. Also, electrodes with different diameters may exhibit strikingly different impedance characteristics and simply using an electrode with as conductive a metal plate as possible should not be the main reason for selection.

---

[9] A medical procedure used to alter nervous system function in which the influence of activity in one neural pathway modulates the pre-existing activity in another through synaptic interaction, for relief of pain and spasm suppression.

[10] An extension of the sacral spinal nerves (S2 to S4; c.f. fig. 1.1) that innervates the external genitalia of both sexes, as well as sphincters for the bladder and the rectum [Mathers, 1985, p. 90].

[11] Knowledge of the interface impedance between the electrode and tissue is important both for the design of the associated electronic equipment and for the assessment of possible waveshape distortion of the recorded signals.

Metal electrodes are widely used in biological and medical research for stimulating excitable tissue and recording bioelectric events of interest. In this work we are solely concerned with the latter where non-faradaic polarisable electrodes are used in implanted neuroprosthetic devices for successfully acquiring neural or electroneurographic (ENG) signals and using those towards rehabilitation. Nonetheless, the neural signal needs to be free of artifacts which can be in the form of myoelectric or electromyographic (EMG) interference, which we distinguish from electrical noise since it is due to external sources and not an intrinsic artifact of the recording system. As it is most likely that recording implanted electrodes will suffer from such interference, we must be able to compensate against it so the quality of the ENG signal is not degraded.

Various types of implantable electrodes connected to instrumentation amplifiers have been used for recording from peripheral nerves. In this work we are interested in non-invasive electrodes (i.e. electrodes that do not penetrate the nerve) such as cuff electrodes [Hoffer et al., 1974; Stein et al., 1975; Haugland, 1996], book electrodes [Brindley, 1972], helical (i.e. the Huntington helix), and spiral electrodes [Naples et al., 1988; Sahin et al., 1994] to name a few. With cuff electrodes, long-term recording and stimulation is possible as they have been proven to be suitable and safe for the purpose, but most importantly, cuffs reduce interference when made tripolar (c.f. §2.3.2.1) [Popovic et al., 1993; Nikolic et al., 1994; Struijk et al., 1999; Triantis, 2005a]. Reducing interference is of significant importance in the performance of neural recording systems because that essentially manifests the quality of the obtained neural signal, often rendering it unusable if interference is not removed or at least minimised to a certain level. This is because ENG signals are of microvolt level and recording these can be challenging when millivolt EMG interference is present at the neural interface. Additionally, both signals have maximum power at the low end of the audio band and since their spectra overlap, EMG affects the quality of the ENG signal. Fortunately, there exist a number of amplifier configurations that can successfully detect and remove such interference, while at the same time amplify the neural information of interest. Neutralisation of interference, however, is a non-trivial task; cuff electrodes are always affected by factors like manufacturing tolerances and biological changes at the neural interface (e.g. tissue growth). Thus, coming up with amplifier configurations that would appropriately compensate for those factors is challenging. Details on the important properties of cuff electrodes, implant electrode metals, as well as why and how EMG neutralisation is possible by using various recording amplifier configurations, are given in the next chapter.

1.4 Project aims

From discussion in the previous paragraphs the motivation of this research work has been established. It may also have become clear that this work is related to biomedical instrumentation focusing on neuroprosthetic devices that make use of implanted electrodes connected to appropriate amplifier configurations for "reliably" recording neural information from peripheral nerves; either extracting those for further analysis and processing, or using them as feedback to another system (e.g. a stimulator). By "reliably" we mean for the information to be exploitable once obtained, i.e., the signal is clear,

undistorted, and artifact-free. The aim of this work was to come up with a new amplifier configuration that could be used for the task. In the very specific case of a bladder control implant, we wanted to record signals from appropriate neural pathways that would help us determine whether or not the bladder contracts and act accordingly (i.e. neuromodulate). Also, as this approach is meant to be used by a person with permanent disability, it has to be performed for most of the day if the patient makes use of catheters and drainage during the night. [Kurstjens et al., 2005] have shown that small neural signals (i.e. about 0.1 µV) can be detected in human subjects when the bladder contracts, which might be used to trigger neuromodulation; what we call conditional neuromodulation. Those neural signals will be affected by a much higher in magnitude EMG interference in this case, perhaps, generated from the paraspinal muscles. Additionally, a rechargeable battery must be used to provide power to the active implant for the detection part. Therefore, an amplifier configuration that would offer very good interference neutralisation throughout the ENG bandwidth of interest, and low power consumption, is required. Also, since recording electrodes in a tripolar arrangement offer certain advantages, which we will also be discussing later on, we opted for this choice. A tripolar recording configuration combining both the aforementioned requirements is currently unavailable, which is something this work will try to address. This is challenging because since the introduction of the first tripolar amplifier configuration in the mid-70s for the purpose of long-term recording of neural signals from peripheral nerves, although there has been a plethora of research activity in the field of neural signal recording mainly focusing in using nerve signals as control inputs to neural prostheses, not many new tripolar amplifier configurations have emerged. This can be attributed either to the fact that the few existing ones offer sufficiently good performance for the purpose they were used for and therefore there was no need for improvement, or due to saturation of design ideas in this particular area. The latter is a possibility if one thinks the nature of the problem: the recording amplifier is a differential input device with certain properties (e.g. high differential gain, high input impedance, etc.) which can be connected to electrodes in a pretty much standard number of ways, readily exhausted if knowing what needs to be achieved (e.g. each electrode "seeing" a high input impedance). Consequently, coming up with a novel tripolar amplifier configuration is not a straightforward task, with research also focusing on optimising the recording electrodes instead (e.g. size of cuff, number of electrodes used, etc.) in order to improve performance. At the time of writing, a tripolar amplifier configuration employing a novel EMG neutralisation scheme that offers certain advantages over existing configurations has been designed using discrete circuit components and its performance has been successfully evaluated in in-vitro preparations.

As described in [Donaldson et al., 2008], the recording amplifier may become part of an implanted device which has the main function of detecting hyperreflexic bladder contractions by recording naturally occurring signals from motor nerves and suppressing those contractions by stimulating the sensory pathways to prevent incontinence. With conditional neuromodulation, rhizotomy will then become obsolete. The device can also be used to intentionally empty the bladder by stimulating the motor nerve roots. There are two main challenges involved in this kind of device, as far as the recording part is concerned: a) the amplifier has to detect changes in neural signal that are very small (i.e.

sub-microvolt) with interference sharing part of the spectrum and having about 3 orders higher magnitude than the neural signal, and b) it must consume very little power since detection of contractions optimally occurs 24 h per day, which means that for convenience it must be battery-powered. The energy budget is therefore tight. Moreover, the implant will have other electronic parts that will also need power, such as: a microcontroller for managing the handshaking between the different parts, allowing to reconfigure the device (e.g. change the ENG amplitude sampling rate, set the stimulus pulse, etc.), as also performing simple processing tasks and analogue-to-digital (A/D) conversion of the neural signal preparing it for transmission to an external (to the body) controller unit where further processing can be performed. Another part is the medical implant communication service (MICS) allowing bi-directional digital communication between the implant and the external controller unit, while power to the stimulator will be provided externally via an induction link and through a DC-DC convertor that will set the appropriate output voltage level needed for stimulation. Since recording neural activity to detect bladder contractions is performed from the same nerve roots used for bladder emptying, switches can be used to connect the electrodes either to the amplifier or the stimulator depending on the desired functionality. In the latter case, the amplifier will be disconnected from the electrodes during stimulation. Finally, the battery can be recharged by a battery charger circuit connected to a charging coil in the implant while, as described by [Donaldson et al., 2008], an under-mattress charger has been designed for the purpose of charging the battery implant overnight. Fig. 1.3 shows the system design as a concept block diagram. A progress report on the development of the system together with some estimated current consumption figures for various parts of the device can be found in [Donaldson et al., 2008].
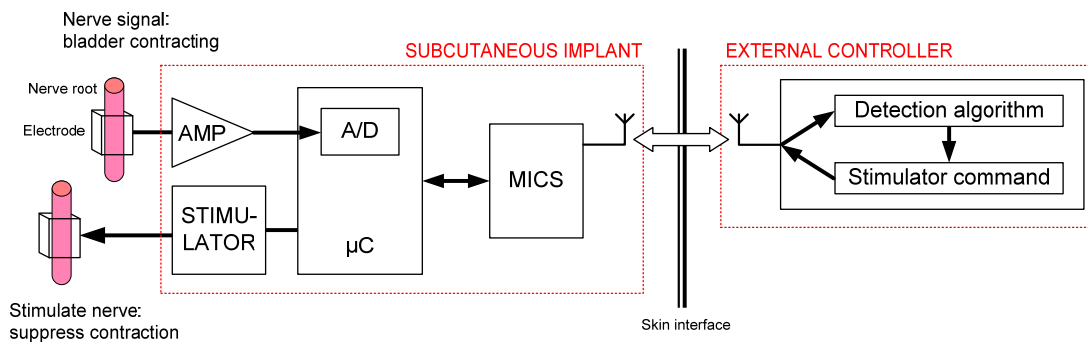
Figure 1.3: Block diagram of the system showing the signal pathway for conditional neuromodulation. The implant comprises the neural signal amplifier, the stimulator, the microcontroller, and the MICS transreceiver with its antenna, while the external controller unit performs all the appropriate signal processing for detecting the onset of bladder contractions and acting accordingly by triggering stimulation to suppress them. Any auxiliary electronic parts such as the battery charger circuit, as well as power supply components (e.g. DC-DC convertor) and arrangements are not shown for clarity. Figure reproduced from [Donaldson et al., 2008].

The subcutaneous implant located in the abdomen area will communicate wirelessly with an external controller unit through a MICS radio link operating at a specific biomedical frequency band between 402 and 405 MHz. The device will record and amplify a neural signal and transmit samples to the external controller where further

processing takes place with an algorithm detecting when bladder has started to contract. A command signal will then be sent to the stimulator to suppress the contractions. In particular, the amplified signal is either sampled (and quantised) by the A/D convertor, or rectified and LP filtered before being sampled. This is done to detect the instantaneous amplitude or slow changes in amplitude (i.e. signal envelope detection) over time for conditional neuromodulation, as with raw ENG this is not possible (i.e. sampling at a low frequency is required in this mode[12]). Conversely, the fast sampled (i.e. above the Nyquist frequency) raw ENG can be used for spectral analysis of the neural signals recorded from the tripole.

1.5 Main contributions

The following is a list of the key points developed in this thesis in the order in which they are introduced in the subsequent chapters.

- Carrying out a series of in-vitro experiments that allowed appreciation of the causes of imbalance in tripolar recording amplifiers, and by utilising a novel passive neutralisation approach, demonstrating that removal of EMG interference is possible. The advantages and limitations of the approach have been successfully identified and possible ways of improvement have been suggested.

- Demonstrating in simulation, using real electrode impedance data obtained in-vitro, that a 3-component circuit model can be used to describe the frequency dispersion of real electrodes sufficiently well, while when the impedance data is from highly polarisable electrodes, a fit can be achieved in the ENG band without the use of a shunt interface resistance. Prior to that, a thorough and very important theoretical treatment on the modelling of metallic electrodes and factors affecting their impedance properties was also presented.

- Proving in-vitro that an RC network of a certain configuration can adapt to the frequency response of the impedance required for balancing an asymmetrical recording tripole and consequently to the impedance profile of the recording electrodes, which can then be used towards improving the neutralisation performance of the proposed technique.

- Performing a critical review of the literature on the causes of frequency dispersion and constant phase element behaviour of metallic electrodes, with the main reasons being identified and clearly explained. Considering this, an in depth comparison of 3 different approaches for the emulation of the constant phase element behaviour of electrodes has been carried out. Consequently, the most suitable emulation approach for the purpose was selected and used in simulation to successfully fit past neutralisation data. A discrete circuit realisation of the model was built where actual measurements were shown to be in very good agreement with simulation results.

---

[12] Due to the very low frequency of the rectified and LP filtered neural signal, the amplitude sampling frequency need not be large (perhaps 10 Hz), as detection of the slow bladder contractions can occur at about every 100 ms.

- Proposing a revised approach where a negative impedance converter circuit was successfully used together with the discrete circuit realisation of the constant phase element in significantly improving the neutralisation performance of the recording configuration. A suitable electrochemical cell was conceived which was used towards assessing the improvement in an in-vitro preparation. Measurement results verified the postulations made on improvement, followed by a discussion on various matters like how the particular neutralisation technique can work in an implanted neuroprosthetic device, IC realisation issues, and noise contribution from this new electrode impedance balancing arrangement.

1.6 Thesis organisation

Following this introductory chapter, which sets the motivation and aims of this work, the rest of the thesis is divided in 6 chapters and 4 Appendices. A brief summary of the contents of each chapter is given below.

Chapter 2 is a purely theoretical chapter and its main purpose is setting the foundations for the subsequent chapters of the thesis. The chapter begins with an essential introduction to neurophysiology in respect to neural signal recording, namely: the human nervous system, the various parts of the nerve cell, how electrical signals propagate along the nerve, and how nerve conduction is possible. The motivation behind recording neural information from peripheral nerves using implanted electrodes is given, the different type of recording electrodes are described with an emphasis to cuff electrodes, and the various tripolar amplifier configurations are presented. Finally, the chapter concludes with a very important section on neural signal detection and in particular how cuff electrodes register the neural signal.

Chapter 3 begins with a discussion on the properties of the cuff with regards to imbalance and how neutralisation of interference is possible with a novel proposed approach where the tripolar configuration is seen as a Wheatstone bridge that can be balanced by adding an impedance to either side of the outer electrodes. Effects of CM interference to the recording electrodes are also analysed, followed by an experimental evaluation of the passive neutralisation technique with results illustrating its working principle and the advantages/disadvantages it has to offer.

Chapter 4 is concerned with the modelling of metallic electrodes for the purpose of accurately mimicking their frequency response and impedance data fitting. The different parts of the electrode-electrolyte interface are analytically explained, and factors affecting the impedance properties of electrodes, such as sources of non-linear behaviour, are also discussed. Subsequently, two well-known models of the electrode-electrolyte interface are presented with one being thoroughly analysed. Finally, the model is put to the test where it is demonstrated in simulation to fit real electrode impedance data sufficiently well.

Chapter 5 is broken down in two parts. In part 1 the theory presented in the previous chapter is used here in terms of modelling the impedance profile of our recording

electrodes so to investigate whether such a network can adapt to the frequency response of electrodes and thus improve the neutralisation performance. At first, it is demonstrated that compensating for imbalance in the recording tripole can be done by using an RC model that resembles the electrode-electrolyte interface impedance. Following that, an in depth literature review of what has been achieved by others in understanding the causes of the observed frequency dispersion and constant phase angle behaviour of electrodes is carried out, where 3 different approaches are used towards modelling that behaviour. The most appropriate is subsequently selected and used in part 2 for neutralising interference in recording tripoles in a hope that it will offer improvement. As such, part 2 is mainly concerned with the experimental verification of the proposed by this thesis novel neutralisation technique where an actual hardware realisation of the constant phase element is used in conjunction with a negative impedance converter circuit. A custom-made electrochemical cell was built and used as part of the in-vitro experiments. Results and some general remarks on the design aspects of a potential recording system employing the proposed neutralisation technique conclude the second part of the chapter.

Chapter 6 contains the general conclusion of the thesis and some recommendations for future work.

1.7 List of publications

The research work described in this thesis has led to a series of publications which are documented below.

Journal publications:

1. Langlois P. J., Demosthenous A., Pachnis I., and Donaldson N., "High-power integrated stimulator output stages with floating discharge over a wide voltage range for nerve stimulation," IEEE Trans. Biomed. Circuits Syst., vol. 4, no. 1, pp. 39-48, December 2009.
2. Donaldson N., Perkins T., Pachnis I., Vanhoest A., and Demosthenous A., "Design of an implant for preventing incontinence after spinal cord injury," Artif. Organs, vol. 32, no. 8, pp. 586-591, August 2008.
3. Pachnis I., Demosthenous A., and Donaldson N., "Passive neutralization of myoelectric interference from neural recording tripoles," IEEE Trans. Biomed. Eng., vol. 54, no. 6, pp. 1067-1074, June 2007.

Conference publications:

1. Pachnis I., Demosthenous A., and Donaldson N., "Towards an adaptive modified quasi-tripole amplifier configuration for EMG neutralization in neural recording tripoles," IEEE Proc. ISCAS, pp. 3144-3147, May 2010.
2. Pachnis I., Demosthenous A., and Donaldson N., "Realization of constant phase element in metallic electrodes for interference reduction in neural recording tripoles," IFMBE Proceedings 25/IX WC, pp. 353-357, September 2009.

3. Pachnis I., Demosthenous A., and Donaldson N., "Interference reduction techniques in neural recording tripoles: an overview," IEEE Proc. PRIME, pp. 332-335, July 2009.

4. Pachnis I., Demosthenous A., and Rahal M., "Adaptive EMG neutralization using the modified QT," IEEE Proc. ISCAS, pp. 2941-2944, May 2008.

5. Demosthenous A., Jiang D., Pachnis I., Liu X., Rahal M., and Donaldson N., "A programmable ENG amplifier with passive EMG neutralization for FES applications," IEEE Proc. ISCAS, pp. 1552-1555, May 2008.

6. Demosthenous A., Pachnis I., Rahal M., Jiang D., and Donaldson N., "An ENG amplifier with passive EMG neutralization," IEEE Proc. ICECS, pp. 66-69, December 2007.

7. Pachnis I., Demosthenous A., and Donaldson N., "Myoelectric and common-mode interference rejection in a quasi-tripole amplifier configuration," IEEE Proc. NER, pp. 118-121, May 2007.

8. Pachnis I., Demosthenous A., and Donaldson N., "Comparison of transconductance reduction techniques for the design of a very large time-constant CMOS integrator," IEEE Proc. ICECS, pp. 37-40, December 2006.

CHAPTER
TWO

Neural Signal Recording Fundamentals

2.1 Introduction

Much of what we know about the workings of the nervous system is based on the possibility of stimulating it electrically and recording its spontaneous electrical activity. The aim of this chapter is to introduce the basic concepts of neural signal recording necessary in understanding subsequent parts and, therefore, it is purely theoretical. We first begin with an introduction on neurophysiology; this includes a short description of the human nervous system and its neural activity, the various elements involved in the electrochemical interfacing and nerve conduction, as also the neurophysiological mechanisms that make this possible. We then move on describing how recording neural information is performed using implanted cuff electrodes, the difficulties involved, as well as present the different tripolar recording amplifier configurations that are being used for the task. We conclude the chapter with a discussion on neural signal characteristics and the theory of neural signal detection using electrodes in tripolar arrangement.

2.2 Basics of neurophysiology

2.2.1 The nervous system

The nervous system is a network of cells – the smallest unit of life that is classified as a living thing – designed for the rapid transfer of information through the body and consists of two main parts (fig. 2.1): the central nervous system (CNS) and the peripheral nervous system (PNS). The CNS is made up of the brain (i.e. including the brainstem and the cerebellum), and the spinal cord with the white and grey matter, while the PNS comprises all the nerves after they have exited the spinal cord[1], being the part responsible for the transmission of information to and from the CNS and the various parts of the body (i.e. limbs and organs) [Bugbee, 2000; Vanhoestenberghe, 2007]. There are several hundred distinct human cell types. The nervous system is primarily made up of two

---

[1] At different levels nerve fibres leave the spinal cord as rootlets, which gather in groups to form the spinal nerve (roots) that in turn exit the vertebral column through the intervertebral foramina. Humans have 31 left-right pairs of spinal nerves (c.f. fig. 1.1 and fig. 1.2) with each being formed by the combination of nerve fibres from the dorsal and ventral roots of the spinal cord. Spinal nerves are then split many times to innervate the whole body. It should be emphasised that nerves are found only in the PNS. In the CNS, the analogous structures are known as (neuronal) tracts [Mathers, 1985, pp. 74, 75].

categories of cells: a) the *neuron* (or nerve cell) which process and transmit information, in and between, the CNS and the PNS by the use of chemical and electrical signals, and b) the *glia* (or glial cell) which performs support functions to neurons [Triantis, 2005a]. Applications of FES-based neuroprosthesis like bladder and bowel emptying [Brindley et al., 1982; Boyer et al., 2000; Sevcencu et al., 2005], foot-drop correction [Haugland and Sinkjaer, 1995], and control of hand-grasp [Haugland et al., 1997] involve interfacing electrodes to nerves that reside outside the CNS. Thus, subsequent discussion about the nervous system will focus more on the PNS part.
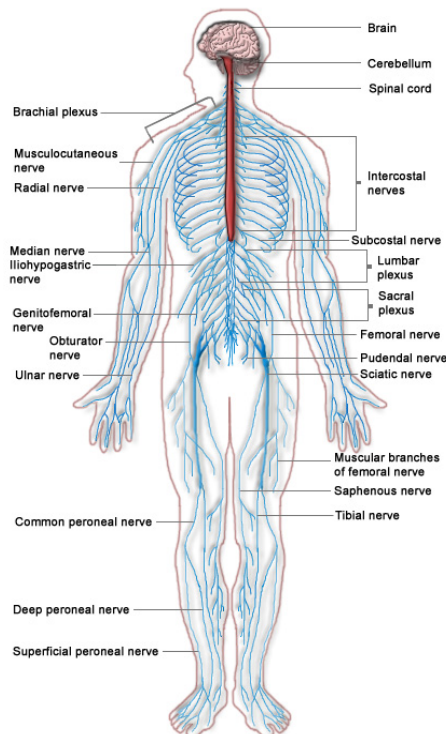
Figure 2.1: The human nervous system. Blue is the PNS while red is the CNS (figure taken from [Wikipedia: the free encyclopedia, last accessed in September 2010]).

2.2.2 The neuron cell

The PNS consists of afferent *sensory* neurons (located *mainly* in the dorsal or posterior nerve roots), gathering information from receptors of the body to the CNS, and efferent *motor* neurons (located *mainly* in the ventral or anterior nerve roots) conveying instructions from the CNS to effectors such as muscles or glands[2] [Keynes and Aidley, 2001, p. 1; Vanhoestenberghe, 2007]. There is also another type of neuron called the *interneuron* (or relay neuron) which provides connections between sensory and motor

---

[2] Neurons are classified according to the propagation direction of nerve impulses, from receptors or to effectors, as being afferent or efferent, respectively. For example, sensory neurons are activated by sensory input (vision, touch, hearing, etc.), and send projections into the CNS that convey sensory information to the brain or spinal cord. Similarly, motor neurons connect the CNS to muscles, allowing the brain to move the body.

neurons and is common in the brain [Triantis, 2005a]. Although a neuron can take many forms with a variety of shapes and sizes (i.e. fractions of a millimetre up to more than a meter), the three main parts of a neuron (fig. 2.2) are: 1) the soma (or cell body), 2) the dendrites, and 3) the axon (or nerve fibre). The branched projections called dendrites receive electrochemical input from other neurons, the soma (with its nucleus) is the main cell body and finally the axon is a long projection of a neuron that carries the outgoing impulses away from the soma [Triantis, 2005a; Vanhoestenberghe, 2007]. The following is a brief description of the various key parts of a neuron as illustrated in fig. 2.2.
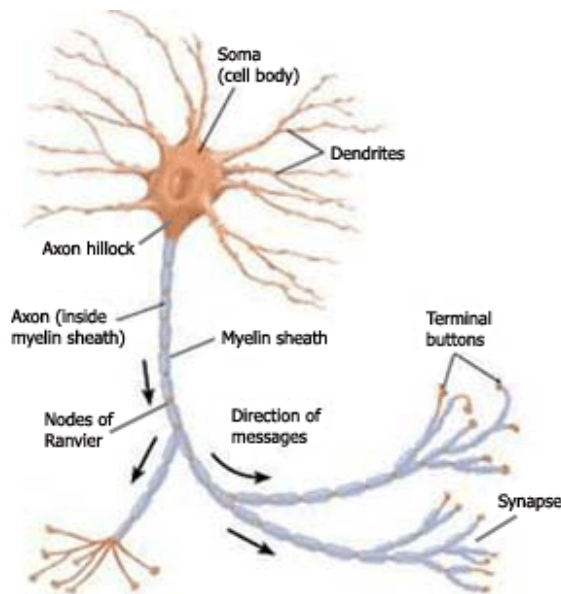
Figure 2.2: Structure of a typical neuron cell (figure taken from [Wikipedia: the free encyclopedia, last accessed in September 2010]).

The neuron is a cell of the nervous system, which conducts nerve impulses, consisting of an axon and several dendrites. The dendrites connect with the ends of other neurons (e.g. interneurons), and provide a vast network in which information can travel down the dendrite of a neuron, from which the dendrites project, to its soma. Within the soma there is the nucleus as well as many other important chemical factors. It is in the soma that a decision for electrical signal (i.e. the action potential[3]) must happen. The soma leads into the axon hillock which is the point at which all the information is accumulated and where the action potential is initiated and transmitted to the axon. From here, the action potential travels down the axon that conducts electrical impulses away from the neuron's soma, carrying all information down a neuron and to its axon (or synaptic) terminals which are distal junctional regions scattered over the terminal branches of an axon, separated from neighbouring neurons by a small gap, the synapse. The axon not only carries information but it also continuously carries resources needed for the cell (like vesicles and mitochondria). The end of the axon sometimes makes contact with other

---

[3] The transport of information within the brain, and between it and the rest of the body, is done via nervous signals of an electro-chemical nature. These impulses, called action potentials, are carried through the body by the nerves [Vanhoestenberghe, 2007].

neurons or muscles using synapses[4], which convert the action potentials to electrical (i.e. electrical synapses) or, in many cases, chemical (i.e. chemical synapses) signals for the dendrites of the next cell[5]. It is at a synapse that interactions between nerve cells take place and where neurotransmitters (i.e. endogenous chemicals) enter specific receptors of a dendrite on the receiving neuron (i.e. the postsynaptic cell). This is the so called electrochemical communication of the neuron cell. Finally, the terminal buttons where neurotransmitters are released are the large bulb part at the end of a neuron (i.e. the presynaptic cell).

2.2.3 Myelinated and unmyelinated nerve fibres

Vertebrates have two main types of nerve fibre. The larger fast-conducting axons (i.e. 1 to 25 μm in diameter), being myelinated and the small slowly conducting ones (under 1 μm), being unmyelinated (or non-myelinated) [Keynes and Aidley, 2001, p. 3]. In the myelinated nerve fibres, the excitable membrane is insulated electrically by the presence of the myelin sheath (about 1 to 2 mm long, depending on the species) formed from successive wrappings of the axon by Schwann cells (i.e. principal glia of the PNS) which encloses the axon of peripheral neurons[6], everywhere except at the regularly exposed patches of axonal membrane called the *nodes of Ranvier* (c.f. fig. 2.2) [Keynes and Aidley, 2001, p. 6]. This wrapping causes the effective membrane resistance and capacitance around the nerve fibre to increase and reduce, respectively, in the internodal intervals[7], and owing to the nodes of Ranvier gaps (about 1 μm in width), the action potential "jumps" from one unmyelinated node of Ranvier to the next down the axon, being regenerated only at these nodes where the external electrical resistance between neighbouring nodes is relatively low. Thus, in those cable-like myelinated axons, action potentials do not propagate as waves but recur at successive nodes and in effect "hop" along the axon. This *saltatory conduction* – a term coined by Lillie in 1925 for this kind of process – greatly increases the propagation speed of nerve impulses[8], as also being less energy consuming (i.e. far fewer ions "leak" across the membrane) than the conduction taking place in unmyelinated nerve fibres of the same diameter [Bugbee, 2000; Keynes and Aidley, 2001, pp. 8, 81]. Conversely, the action potential propagates continuously as a wave along the axon when that is unmyelinated, being generated at each segment of the

---

[4] Most synapses connect axons to dendrites, but there are also other types of connections, including axon to cell body, axon to axon, and dendrite to dendrite. Also, there are no neurons that lack a soma, but there are neurons that lack dendrites, and others that lack an axon. While the cell body of a neuron frequently gives rise to multiple dendrites, it usually does not have more than one axon [Mathers, 1985, p. 18].

[5] More specifically, there is a gap about 20 nm wide between the sending and receiving cells called the synaptic cleft where neurotransmitter molecules diffuse across to the postsynaptic membrane.

[6] In the CNS, it is the glial cells known as oligodendrocytes that lay down the myelin.

[7] The myelin, which adheres to the axon membrane increasing its thickness by a factor of about 100, acts as a dielectric between the extracellular and intracellular – outside and inside the cell – medium (i.e. increasing their distance allows for more charges to be stored, hence the capacitance decreases), preventing ions from entering or leaving the axon along those myelinated segments.

[8] For an axon of a given diameter, myelination improves the conduction rate by a factor of approximately 20 [Webster, 2010, p. 135].

membrane, while the speed of conduction is proportional to its diameter[9] [Triantis, 2005a]. As such, peripheral sensory fibres subserving sensations like pain and temperature where a rapid response is not required are unmyelinated [Keynes and Aidley, 2001 p. 3].

2.2.4 The action potential[10]

2.2.4.1 General description

Every cell is surrounded by a plasma membrane that separates it from the extracellular region. Various types of cells (e.g. neurons, myocytes, etc.) change their electrical membrane potential: at rest, neurons typically maintain a voltage across their cell membrane. The voltage difference between the extracellular fluid and the intracellular space of the neuron is the membrane (or transmembrane[11]) potential, which is called the *resting potential* when the neuron is in a state of readiness to "fire" [Triantis, 2005a]. The resting potential has a typical value of around −70 mV (in human) across the membrane with the internal (i.e. inside of neuron) being more negative. The cell membrane at rest is thus negatively polarised. The summation of synaptic inputs to the dendrites of a neuron may result to the generation of a nerve impulse (fig. 2.3) occurring when the membrane potential reaches the firing threshold (i.e. typically −60 mV)[12]. Thus, if the change in membrane potential exceeds a critical level (i.e. the firing threshold), or in other words if the depolarisation is not small (say, from −70 mV to −60 mV), this produces a rapid depolarisation[13] of the membrane (i.e. rising phase) from −60 to +40 mV within about 1 ms. This rapid depolarisation elicits an electrical "spike" called the *action potential* [Keynes and Aidley, 2001, p. 13]. A peak at the highest level of depolarisation is reached where the membrane potential is at a maximum and has reversed sign (i.e. becoming inside positive), while depolarisation stops. So, at its peak the membrane potential is reversed by about 40 mV before the falling phase (i.e. repolarisation phase or hyperpolarisation[14] of the membrane, occurring from about 2 to 3 ms on the time scale of fig. 2.3) and temporarily going below the initial negative resting potential (i.e. afterhyperpolarisation phase[15]). A refractory period[16] (i.e. from 3 to 4 ms, about 1 ms in

---

[9] A large nerve fibre conducts impulses faster than a small one (and generally gives higher signal amplitudes). Also, smaller fibres need stronger shocks to excite them (i.e. the threshold for excitation is inversely related to the size of the nerve fibre) – also known as the inverse recruitment principle [Keynes and Aidley, 2001, p. 19].

[10] The generation of an action potential involves mainly the exchange of potassium (K+) and sodium (Na+) ions across the cell membrane by their respective voltage-gated ion channels embedded in a cell's plasma membrane. Here, to keep the description of an action potential simple, we avoid discussing the details of such procedures at the biophysical level. These can be found in [Keynes and Aidley, 2001, pp. 25-40].

[11] The electrical potential difference across a cell's plasma membrane.

[12] Before excitation of a nerve fibre begins, the initial depolarisation must reach a threshold of about 10 to 20 mV less negative than the resting potential.

[13] During the rising phase of an action potential the membrane potential changes from negative to less negative, or positive, denoting a depolarisation.

[14] After the peak of the action potential, a hyperpolarisation returns the membrane potential to its resting value, first by making it less positive, until 0 mV is reached, and then by continuing to make it more −ve.

[15] The time when the membrane potential is hyperpolarised relative to the resting potential.

duration) occurs after the initiation of the action potential where no action potential can be generated by depolarising of the membrane until its conductance has returned to the resting potential (since the ion channels have not returned to their usual state). This whole process spreads along the adjoining part of the membrane as an action potential, i.e., generation of an action potential in one region of an axonal membrane causes regenerative action in adjacent regions of the membrane, precipitating a domino-like propagation. Therefore, the refractory period after an action potential means that the action potential will propagate away from its point of origin in only one direction along an axon because previously activated regions cannot be immediately reactivated, limiting the frequency of "firing"[17].
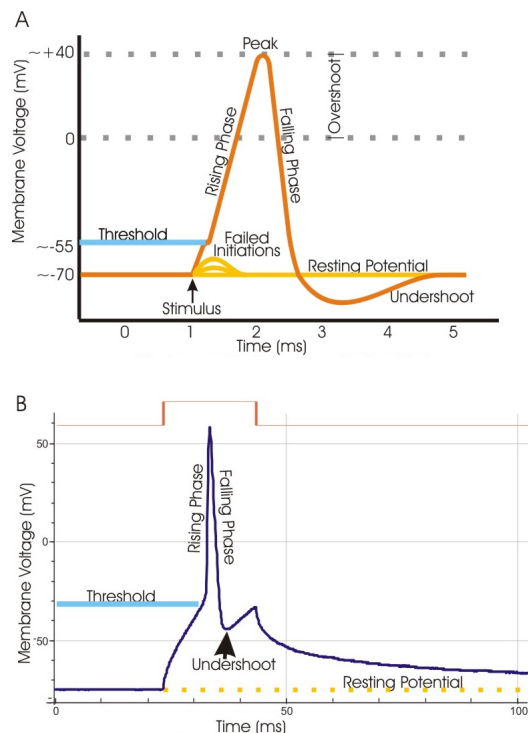
Figure 2.3: A schematic view of an idealised (A) and real (B) action potential illustrating the various phases as the action potential passes a point on a cell membrane. An action potential is self-regenerating and triggers spontaneously only when the stimulus pulse intensity reaches a certain threshold. The axon that produced (A) "fires" with an upper limit of less than 1000 impulses/s because of the refractory period. Overshoot: the period during which the membrane potential is above zero; undershoot: the period during which the membrane potential is below the resting potential. Graphs taken from [Wikipedia: the free encyclopedia, last accessed in September 2010].

---

[16] More specifically the refractory period is defined in two ways: a) the absolute refractory period where a second action potential cannot be initiated during the initial portion of the action potential, and b) the relative refractory period where an action potential can be elicited by an intense superthreshold stimulus [Webster, 2010, p. 133]. To keep things simple the general term "refractory period" here will always denote the absolute refractory period.

[17] However, if a laboratory axon is stimulated in its middle portion, both halves of the axon are unfired and therefore two action potentials will be generated with one travelling towards the axon hillock and the other travelling towards the axon terminals.

It is possible to induce an action potential either naturally (i.e. the stretching of a muscle or the firing of another neuron), or by using electrodes passing a burst of current (i.e. an electrical or stimulus pulse) to lower the external potential below the axon's inner potential (i.e. electric stimulus current flowing outwards across the membrane), reducing the size of the resting potential, causing it to "fire". However, a more intense stimulus does not give rise to a specifically larger or higher action potential – the amplitude of an action potential is independent of the amount of current that produced it, i.e., the "all-or-none" principle – but to a "spike train" whose frequency is related to the stimulus intensity and duration [Vanhoestenberghe, 2007]. Additionally, every nerve fibre has its own activation threshold (i.e. transmembrane voltage necessary to elicit an action potential) and refractory period, while the amplitude, form, and conduction velocity of an action potential remain constant along the length of an axon[18] provided that the axon is uniform in diameter and as long as external conditions, such as temperature (which is proportional to conduction velocity) and composition of the ionic environment that affect the properties of its membrane, are kept constant [Vanhoestenberghe, 2007; Keynes and Aidley, 2001, pp. 15, 74]. Conversely, every kind of excitable tissue, from mammalian motor nerve to muscle and electric organ, gives a similar picture as far as the sizes (i.e. magnitudes) of the resting and action potentials are concerned (however, the shapes and durations of the action potentials show considerable variation; c.f. fig. 2.4 in [Keynes and Aidley, 2001, p. 16]). In fact, the resting potential always lies between −60 and −95 mV, with the potential at the peak of the spike between +20 and +50 mV [Keynes and Aidley, 2001, pp. 14-15].

2.2.4.2 Nerve conduction: the local circuit theory

It was suggested long ago that propagation of an impulse depends essentially on the flow of current in local circuits ahead of the active region which depolarises the resting membrane, causing it in turn to become active [Keynes and Aidley, 2001, p. 20]. For an action potential propagating along a single unmyelinated nerve fibre, the region of the fibre undergoing a transition into the active state (i.e. the active region/node depicted in fig. 2.4) at an instant of time is usually small relative to the length of the fibre [Webster, 2010, p. 133]. Fig. 2.4 shows segments of unmyelinated and myelinated nerve fibres in the vicinity of the active region/node of an axon. For fig. 2.4a, three regions can be distinguished, i.e., an active region where the membrane has been depolarised, the polarised membrane lying ahead (left of) the active region which is still in the resting state, and finally the repolarised membrane lying behind the active region, as in the refractory state. This sequence means that the direction of propagation of the action potential is from right to left. A reversal of polarity is shown within the active region because of depolarisation of the membrane becoming inside positive.

From the indicated charge distribution shown in fig. 2.4a, caused by the polarity differences of the adjacent to the active zone regions, solenoidal (i.e. closed path) local circuit ionic currents are flowing outward through the membrane ahead of the active region, causing a potential drop across the membrane of such a polarity, and starting to

---

[18] An action potential travels uniformly down the axon at a rate of about 10–100 m/s with the speed depending upon the diameter and myelination of the axon.

depolarise the new segment of the membrane. When the membrane is depolarised pass a threshold level above the resting potential, this region also becomes activated. Conversely, the same current pattern is flowing behind the active region but this time is ineffective in re-exciting the membrane since that is in an afterhyperpolarisation phase, having earlier been depolarised by the same action impulse. It is obvious, therefore, that the nature of this process is self-excitatory, with new regions of the membrane being brought to the threshold level by lines of current from the active region, sequentially being activated for a brief period of time and then repolarising completely. In this way, the action potential travels down the length of the axon in an unattenuated fashion and at a constant conduction velocity (i.e. assuming uniform axon diameter) with the signal being built up at each point along the way without the need for an additional excitation being applied.
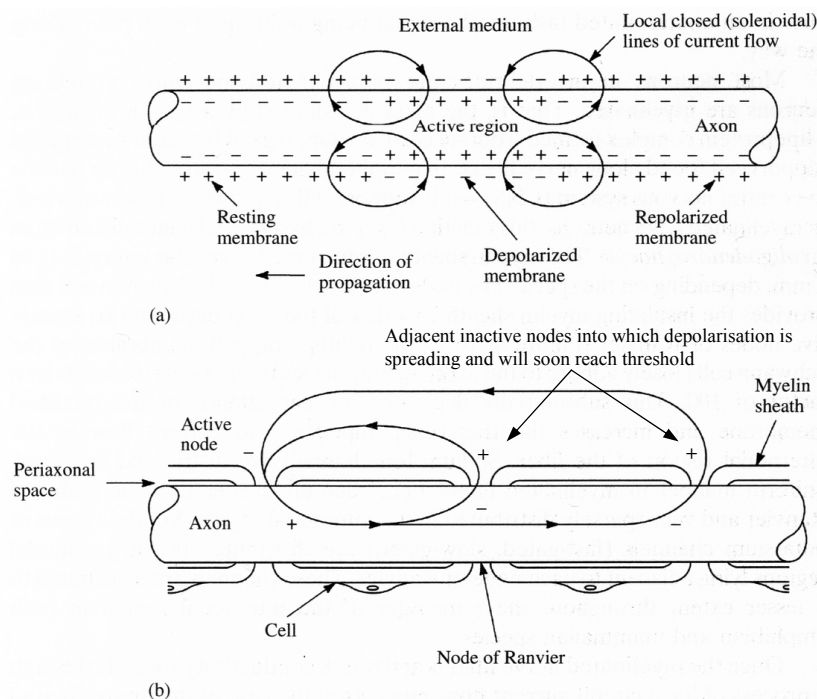
Figure 2.4: Diagrams illustrating the local circuit theory and charge distribution along the membrane of (a) unmyelinated (upper sketch) and (b) myelinated (lower sketch) nerve fibres conducting an impulse. Refer to text for detailed description. Figure taken from [Webster, 2010, p. 133].

Although there are important differences between the solenoidal current pathways in unmyelinated and myelinated nerves fibres, the basic principle is the same [Keynes and Aidley, 2001, p. 21]. For the myelinated nerve fibre of fig. 2.4b, the conduction proceeds through a process of local circuit current flow, much as in the case of the unmyelinated nerve fibre. The difference is that the sources for action current flow are now localised at the nodes of Ranvier and not uniformly distributed along the axonal membrane (i.e. action potentials cannot propagate through the membrane in myelinated internodal segments of the axon due to the insulating property of myelin). Local circuit currents emanating from an active node have an exponentially diminishing magnitude over an

axial distance spanning several internodal lengths, contributing to a drop in nodal potential as current passes outward through a given inactive nodal membrane [Webster, 2010, p. 135]. Hence, local circuit currents provide the underlying mechanism for bringing the nodal membrane voltage to activation threshold, sequentially activating the nodes of Ranvier which generate action potentials to boost the signal to its initial value, and achieving nerve fibre conduction.

Concluding, there exist many models that describe the electrochemical behaviour of both myelinated and unmyelinated nerve fibres and how action potentials in neurons are initiated and propagated. An example of such a model is the pioneering Hodgkin-Huxley mathematical model of differential equations developed in 1952 from their quantitative study of the squid giant axon (i.e. typically around 0.5 mm in diameter despite being unmyelinated). The electrical equivalent circuit of this type model representing the biophysical characteristics of an excitable cell membrane (i.e. for an unmyelinated fibre) can be found in [Webster, 2010, p. 132].

2.3 Neural recording

2.3.1 Motivation

Damage to the CNS because of SCI, injury to neurons in the brain (e.g. stroke), or even due to neurological disorders (e.g. multiple sclerosis) often results in failure of motor function, leading in loss of mobility, many times continence (such as urinary or faecal), and a cause of other secondary complications such as spasms, breathing problems, blood clots, and muscle atrophy. FES can be used in place of conventional rehabilitation techniques such as physical therapy and pharmacological intervention (e.g. drugs for improving sexual dysfunction such as Viagra) to cause motor or sensory reactions and restore limited abilities such as grasping, standing and stepping, bladder and bowel function, phrenic pacing, offer pain management, cardiovascular training, etc. In addition, neural recording can be part of a stimulator system when real-time feedback is required. Depending on the application, this involves the acquisition of muscle (i.e. EMG) or nerve (i.e. ENG) activity of a subject via surface or implanted electrodes. The acquisition of such information is useful in cases like SCI since many functions of the PNS still remain intact and thus FES can be used to restore the link between the CNS and the affected neural pathways.

Implantable stimulators for FES neuroprostheses often utilise open-loop control methods, nevertheless, use of closed-loop techniques for achieving improved performance also seem promising [Popovic et al., 1993; Haugland and Hoffer, 1994; Haugland and Sinkjaer, 1999b; Jezernik et al., 2000; Donaldson et al., 2008]. In particular, sensory signals recorded using implanted electrodes have been used as feedback in closed-loop FES systems for control of foot-drop stimulation in hemiplegics [Haugland and Sinkjaer, 1995; Hansen et al., 2002] and in hand-grasp applications in tetraplegics [Sinkjaer et al., 1994; Haugland et al., 1997; Haugland et al., 1999a]. In that way, external artificial sensors (e.g. force transducers, joint angles, switches, etc.) become obsolete, resulting in less complicated systems, since those are usually difficult

to position and attach to the site of interest and calibrate for every single use [Nikolic et al., 1994]. In addition, artificial sensors are generally undesirable because they introduce other disadvantages like the low quality of information obtained, make system bulky, have information drift with time (i.e. non-reproducible results), are difficult to implant hence more prone to damage, and most likely will increase the system's power consumption [Popovic et al., 1993]. Since the introduction of the quasi-tripole (QT) amplifier configuration in the mid-70s for the purpose of long-term recording of neural signals from peripheral nerves, research efforts are now being focused in using peripheral nerve signals as control inputs to neural prostheses [Stein et al., 1992, pp. 99-125; Haugland and Sinkjaer, 1999b; Donaldson et al., 2008]. Hence, by measuring and processing low-level natural information such as ENG activity from peripheral nerves, it is possible to achieve improved and reproducible FES control based on the fact that the source of feedback information is intrinsically more reliable.

2.3.2 Nerve recording using implanted electrodes

There are numerous designs and types of electrodes to be used within the body to detect biopotentials [Webster, 2010, pp. 215-219; McAdams, 2006, pp. 149-158]. Each FES application imposes its own criteria for the design of a recording implant electrode and the specifications that needs to meet (e.g. selective recording from particular nerve fascicles, anatomical structure it is to be implanted against, etc.). The neural ENG signal is often recorded using electrodes of *cuff* design (fig. 2.5). The cuff encircles the nerve (or nerve root), having a longitudinal opening allowing the nerve to be inserted, with the space between the nerve and the cuff usually filled with conductive fluid. Since nerves are surrounded by salt-containing body fluids it is possible for measurements to take place using electrodes outside the actual nerve fibres, a method which is non-invasive and can therefore be used chronically [Haugland, 1996; Struijk et al., 1999]. A typical cuff type is the tripolar, fitted with three metal ring electrodes equally spaced inside it, covering most of the circumference of the cuff, hence the name. The cylindrical tube is made of biocompatible flexible insulating material such as silicone rubber, though other insulators are possible, and the electrodes of maybe platinum (Pt), or platinum-iridium (Pt-Ir) attached to the inside wall[19]. It is important for the cuff to insulate the whole circumference of the nerve, as this ensures that the flow of ions in the extrafascicular (i.e. outside the bundles of nerve fibres) medium remains within the cuff when action potentials propagate the nerve (i.e. when many nerve fibres are "firing" at the same time). In this way potential differences are created inside the cuff due to the extracellular membrane activation currents, as the action potential propagates across the length of the cuff, which can be measured extraneurally (i.e. outside the nerve) by the ring electrodes placed around it (c.f. §2.3.4.3). In addition, to maximise the amplitude of the neural

---

[19] Platinum has been the most widely used implant electrode metal as it has excellent corrosion resistance and produces relatively low polarisation (i.e. current can flow through the interface relatively unimpeded), rendering it stable both in terms of robustness and in terms of electrical properties. Platinum, however, is mechanically relatively soft and for many applications is alloyed with much harder iridium, producing platinum-iridium. Finally, although stainless steels were used in early pacing electrodes, they do not appear to have the required corrosion resistance for long-term use [McAdams, 2006, pp. 129-130].

signal a nerve cuff should be well matched to the size of the nerve[20] and be approximately as long as the wavelength of the action potential [Popovic et al., 1993].
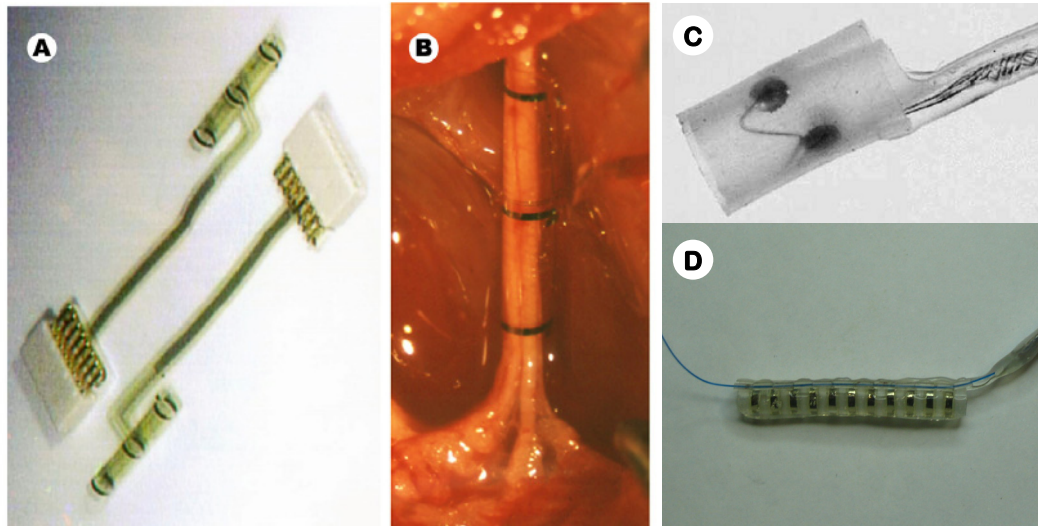
Figure 2.5: (A) Polyimide tripolar cuff electrodes with cable connector. (B) Same cuff electrode being implanted around the sciatic nerve of a rat (both taken from [Raspopovic et al., 2010]). (C) Neural cuff electrode with platinum contacts located on the inside of a cylinder of silicone rubber (taken from [McAdams, 2006, p. 157]). (D) A multipolar cuff electrode (courtesy of Implanted Devices Group, UCL).

2.3.2.1 Why cuff electrodes?

Nerve cuffs can be used in numerous applications which, according to [Struijk et al., 1999], generally fall into 3 categories: a) chronic study of the neuromuscular system pathophysiology, b) monitoring the state of the nerve, and c) using sensory signals as feedback information to control neuroprosthetic devices. If the recorded signal is to be usable for any of the abovementioned purposes, implanted recording electrodes must accurately pick up the desired neural signal while minimising the contributions of extraneous signals. Cuff electrodes are effective and safe for chronic ENG recording, as also being reliable for stimulation of nerves[21] over long periods of time without inflicting damage to the nerve and surrounding tissue [Popovic et al., 1993; Haugland, 1996; Struijk et al., 1999; Triantis, 2005a]. This is advantageous because the same cuff electrode can be used to perform stimulation and recording. Another important reason for using a cuff is due to its intrinsic ability to reduce interference originating from external to the cuff sources, when that is made tripolar.

---

[20] It is generally recommended that the diameter of the cuff be at least 20% larger than the nerve diameter to avoid nerve compression neuropathy and necrosis due to swelling and fibrous tissue ingrowth [Struijk et al., 1999]. Others recommend to be 50% larger [McAdams, 2006, p. 157].

[21] For example, if a tripolar cuff electrode is used, the two outer electrodes can be connected together forming a common-anode (i.e. reference electrode) with the middle electrode being used as a single-cathode (i.e. active electrode). The stimulation current then flows from the anode to the cathode.

The usefulness of the ENG signal recorded with a tripolar cuff depends on the amount of other unwanted biopotentials. Cuffs with 3 symmetrically placed electrodes have been used for recording of ENG activity from peripheral nerves containing many thousands of afferent or efferent (or both) nerve fibres, however with cuffs, nerve signals are very small in amplitude and they are contaminated with other biopotentials like myoelectric interference, since it is often that cuff electrodes are placed in close proximity to muscles, while sometimes are used together with FES [Popovic et al., 1993; Struijk et al., 1999]. In particular, interference in the form of electrical signals from muscles (i.e. EMG) located in the vicinity of the neural interface and stimulus artifacts[22] can cause ionic currents to flow through the tissue inside the cuff (via the generated electric field). Since distortion of the electric field lines causes a voltage drop between the ends of the cuff (due to silicone having much lower conductivity than the tissue and the surrounding fluid), some current flows into the cuff causing potential differences between the electrodes placed inside [Rahal et al., 2000a]. As the medium inside the cuff is mostly resistive[23], there are no significant phase variations to the interfering potentials across the electrodes and the potential varies almost linearly with distance across the length of the cuff. As discussed further in this chapter (c.f. §2.3.3) and actually demonstrated with an experiment in Chapter 3, this property of the cuff to linearise the interference fields from external sources is exploited by tripolar amplifier configurations for removing this type of interference.

2.3.2.2 Cuff electrode types

There are 3 main types of cuff electrodes used for neural recording (fig. 2.6): the monopolar, the bipolar, and the tripolar [Triantis, 2005a]. A fourth one, the screened tripolar cuff, is a simple extension to the standard tripolar cuff utilising two extra electrodes shorted together (c.f. §2.3.3.2). In monopolar cuffs the recording is performed between a ring electrode positioned inside the cuff and a reference electrode[24] placed outside. The inner electrode has to be close to the centre of the cuff to maximize the amplitude of the measured ENG signal (c.f. fig. 2.12). In bipolar cuffs the neural signal measurement is taken differentially between two electrodes inside the cuff with the amplitude being proportional to the separation between the electrodes. However, as the electrodes approach the edges of the cuff the amplitude drops since the low resistivity of the body fluid outside the cuff comes into effect [Rahal et al., 2000a; Triantis, 2005a]. In tripolar cuffs, measurements are taken between the middle and the two end-electrodes. In order to maximise the amplitude of the neural signal, the end-electrodes have to be placed close to the ends of the cuff (i.e. the signals increase as the square of the electrode

---

[22] Interference induced field effect caused by electrical stimulus delivered to the nerve which is instantaneously picked-up by the recording electrodes at the measurement site (i.e. neural interface).

[23] As was shown by [Grill and Mortimer, 1994] the frequency dependence of tissue resistivity is also related to the material enclosing the metal electrodes on which encapsulation tissue is formed (they used Pt and stainless steel electrode contacts moulded within a silicone rubber and epoxy substrates in their experiments with cats).

[24] As implanted devices cannot be grounded in a conventional sense, the neural recording amplifier(s) have to be connected to a reference electrode somewhere inside the body, usually located in the vicinity of the cuff in order to minimise the influence of CM interference (c.f. 3.3.3).

spacing [Popovic et al., 1993]). Nonetheless, the main factor affecting ENG recordings in tripolar cuffs is the spacing between the electrodes and not their actual position or the length of the cuff [Rahal et al., 2000a; Triantis, 2005a]. Bipolar cuffs generally give higher ENG amplitudes than tripolar (i.e. the latter reducing the separation between the signal pickup electrodes). Conversely, tripolar cuffs have the advantage of higher signal-to-interference performance because they can be connected to amplifier configurations and achieve greater interference reduction. Finally, as we shall be discussing later on (c.f. §2.3.4.3), the cuff closing method also has a significant effect on the recording of neural signal.
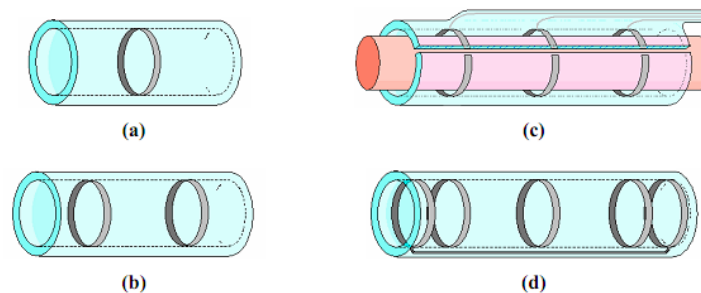
Figure 2.6: Schematic showing 4 different types of cuff electrodes: (a) monopolar (reference electrode not shown), (b) bipolar, (c) tripolar enclosing a nerve with cabling and longitudinal opening, (d) screened tripolar cuff with two additional outer electrodes shorted together (figure taken from [Triantis, 2005a]).

2.3.2.3 Implant electrode metals

Implanted electrodes are essentially made from inert materials such as passive (e.g. titanium, tantalum, zirconium, tungsten, and chromium) or noble (e.g. platinum, iridium, gold, rhodium, and palladium) metals, or even carbon, an inert non-metallic element that has similar electrochemical characteristics to noble metals; all these materials are biocompatible in a sense that they do not react chemically with the surrounding electrolyte or tissue, thus, minimising toxicity problems and moreover being corrosion resistant [McAdams, 2006, pp. 129-130]. Unfortunately, as a consequence, they tend to give rise to large interface impedances and unstable potentials.

Implanted biopotential recording electrodes require a) stable electrode interface potentials, and b) low interface impedances to minimise biosignal distortion and artifact problems[25] [McAdams, 2006, p. 120]. A difficulty, therefore, exists when designing implant electrodes: from a biocompatibility point of view one requires a noble, hence polarisable, electrode system, whereas from an electrical performance point of view one requires a non-polarisable electrode system (i.e. lets current traverse the interface almost unimpeded, wastes little energy at the interface due to the small impedance, and has a

---

[25] If the electrode impedances are very large compared with the input impedance of the amplifier, they can give rise to signal attenuation as a result of the voltage divider effect. This is especially true at low frequencies. The overall signal is not only attenuated, it is also distorted with its low frequency components selectively reduced. Therefore, the measurement system in effect acts as a high pass filter and the signal is differentiated [McAdams, 2006, p. 121].

relatively small overpotential[26]). Real electrodes are neither perfectly polarisable nor perfectly non-polarisable. A compromise is achieved by using a polarisable electrode and either roughening the surface of the electrode or, if the electrode is made of Pt, applying a fine porous coat of platinum black, thus decreasing the large interface impedance [McAdams, 2006, p. 126].

2.3.3 Overview of tripolar amplifier configurations

Natural occurring information obtained from nerves could be recorded more reliably if EMG contamination is reduced. The solution for extracting the ENG signal while removing the EMG interference is via using tripolar amplifier configurations, with the most popular ones being the QT, and the later developed true-tripole (TT). The neural recording amplifiers used in those configurations must be low-power, low-noise, have a high common-mode rejection ratio (CMRR) (c.f. §3.3.3), high differential input impedance, and finally their differential gain must also be high[27]; they need to consume very little power if they are to be integrated into an active implanted device, and low-noise to guarantee that the extracted ENG signal will be well above the amplifier's noise floor. In the following sections an overview on 4 neural recording tripolar amplifier configurations is given, together with their respective properties, and the advantages/disadvantage they have to offer. In addition, the reader is referred to Appendix A where a simplified model of the tripolar cuff is given.

2.3.3.1 The QT configuration

The QT (fig. 2.7) was one of the first amplifier configurations that was utilised by [Stein et al., 1975] for neural signal recording and minimisation of EMG interference. The tripolar cuff is insensitive to EMG owing to both properties of *screening* and *linearisation*. The first is simply the outcome of having the two outer electrodes of the cuff shorted together and this changes the interference field. Less ionic current flows through the tissue inside the cuff, reducing the potential gradient inside it and therefore the EMG interference pick-up by the electrodes. Regrettably, this short-circuiting of the end-electrodes will have a small effect on the EMG voltage appearing between the ends of the cuff, i.e., the non-zero interface impedance of the end-electrodes means that some

---

[26] The degree of electrode polarisation is measured by the additional voltage dropped across the interface upon the passage of faradaic current. If this voltage drop tends to infinity (i.e. because the electrode is highly polarisable) the electrode potential will not be a function of the faradaic current but rely solely on the properties of the interface (i.e. electrode coupling capacitively with the tissue/electrolyte), thus being depended on other factors, drifting randomly, and becoming unstable (i.e. a poorly defined dc potential). Conversely, an ideal non-polarisable electrode would exhibit no resistance to faradaic current. The non-faradaic impedance would effectively be shorted out and the total interface impedance would be zero (i.e. current would pass freely across the interface unimpeded at any frequency while the electrode potential would always remain constant at its equilibrium value). Thus, for perfectly non-polarisable electrodes there are no overpotentials. As such, measured biopotentials would be unattenuated and undistorted [McAdams, 2006, p. 126]. More details that will aid understanding of the reasons why this is the case, are given in Chapter 4.

[27] This is necessary in order to raise the ENG signal from μV level to an appropriate range for the next stage (e.g. A/D conversion).

current will still pass through the cuff such that the effect of screening the tissue inside the cuff is imperfect[28]. Instead, by short-circuiting the end-contacts, a terminal is created that gives the average potential of the two end-electrodes, as long as their respective impedances are equal and the cuff is a perfect insulator [Struijk et al., 1999]. The second property, being the most important of the two, is based on the fact that the cuff, as a very good insulator, linearises the internal field generated by external sources (such as EMG) and thus the interference potential caused by these can be ideally removed with the use of a single differential amplifier [Struijk and Thomsen, 1995]. Nonetheless, this depends on the fact that the cuff is balanced; the 3 identical recording electrodes are placed symmetrically, and tissue growth along the cuff is uniform. If this is not the case, only partial EMG cancellation is possible by exploiting this linearising property of the cuff, and since the QT does not provide a way of adjusting the balance to remove interference, some EMG will inevitably appear at the differential input of the amplifier[29]. Thus, despite its simplicity, this configuration was proved less popular than the TT, which is discussed next.
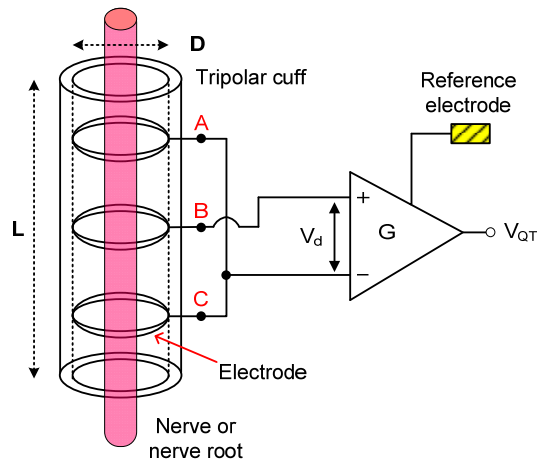
Figure 2.7: The QT amplifier configuration connected to a tripolar cuff. Recording is carried out between the middle and the two interconnected end-electrodes. Cuff dimensions (i.e. length L, diameter D) and end-electrode separation have a significant role on interference pick-up[30].

---

[28] The short-circuiting would have only been effective if the impedance measured between the end-electrodes was less than a few hundred ohms [Struijk et al., 1999].

[29] In Chapter 3 a modified version of the QT amplifier is presented where the idea of placing passive components at the front-end to achieve neutralisation of myoelectric interference is explored.

[30] It has been shown by [Rahal et al., 2000a] that long cuffs are inherently more immune to interference than short cuffs and that interference pick up is very sensitive to electrode separation in the case where the end-electrodes are near the ends of the cuff (i.e. for best results the end-electrodes should not be placed right at the ends of the cuff where the interference field in non-linear (c.f. §3.3.1) and the low resistance of the tissue outside the cuff takes over). Also, according to [Struijk et al., 1999] the optimal cuff length for ENG recording was found to be between 20 and 30 mm, while it was shown that the amplitude of ENG decreases with the square of the cuff diameter for small diameters (i.e. up to 4 mm); in other words the cuff electrodes are most effective for small-diameter nerves.

2.3.3.2 The TT configuration

The TT, introduced by [Pflaum et al., 1995] and shown in fig. 2.8, is another tripolar amplifier configuration used for cancelling out the EMG interference. This configuration differs from the QT in that it uses three amplifiers with electrodes no longer connected together but in pairs to a double-differential amplifier. Albeit still exploiting the linearising property of the cuff, this arrangement offers several advantages compared to the QT. As every electrode is now connected to an input of the differential amplifiers, which presents a high impedance load, the TT is insensitive to the electrode impedance. This reduces phase differences due to the electrode capacitance thus making the TT insensitive to cuff electrode mismatches. Hence balancing the cuff is easier since the reactive term due to the electrode impedances is now less significant. Consequently, it is possible by varying the gain of the two first stage differential amplifiers to compensate for a non-uniform tissue growth along the cuff and cancel out the EMG in the second stage by matching the equal in amplitude but opposite in phase EMG potential gradient at each half of the cuff. Thus, unlike QT, complete nulling of the EMG interference is possible with the TT. Although, as theoretically proven by [Rahal et al., 2000b], the TT has worse EMG rejection comparing to the QT, when cuff is imbalanced (i.e. TT is more sensitive to mismatch in R_{t1} and R_{t2} due to lack of screening), at the same time it offers higher ENG amplitude (i.e. approximately double, while noise is increased by $\sqrt{2}$), and thus by tuning of the gains can potentially improve the ENG to EMG ratio. This has been experimentally demonstrated in-vivo (acute) by [Pflaum et al., 1996] in a comparison made among the two configurations. Finally, another important advantage of this configuration is the possibility of automatically adjusting the gains to compensate for imbalance [Rahal et al., 1999; Triantis et al., 2005b]. Nevertheless, having two low-noise front-end amplifiers is likely to approximately double the current consumption, compared to the QT, and this may be a serious disadvantage in applications like that proposed by [Donaldson et al., 2008] where low power consumption is important.

Figure 2.8: The TT amplifier configuration. By varying the gain of the two first stage differential amplifiers (G_1, G_2) it is possible to cancel the EMG in the second stage, where the neural signal can be further amplified.

Finally, a development from the TT is the screened-tripole (ST). In this arrangement two additional electrodes placed at the ends of the cuff (i.e. outside the two end-electrodes of a tripolar cuff; c.f. fig. 2.6d) are shorted together (i.e. floating short-circuiting), thus creating an interference current bypass path around the cuff which, as in the case of the QT, further decreases the interference field. According to [Rahal et al.,

2000b] this has the same effect on interference as increasing the length of the cuff because it effectively decreases the EMG potential gradient due to less current flowing inside it. More specifically, increasing the length of the cuff significantly reduces interference as the resistance inside the cuff increases, however, this may introduce limitations depending on the location of implantation due to the size increase of the cuff. Nonetheless, this arrangement offers inherently higher signal-to-interference performance comparing to the TT when cuff is imbalanced, while in addition allowing the nulling of the residual EMG signal. A more in depth description of the ST amplifier configuration can be found in [Rahal et al., 2000b], while an in-vivo study using the ST was performed by [Andreasen and Struijk, 2003].

2.3.3.3 The AT configuration

The adaptive or automatic tripole (AT) amplifier configuration (fig. 2.9) proposed by [Rahal et al., 1999] and implemented by [Triantis, 2005a; Demosthenous and Triantis, 2005] is another alternative neural recording configuration which automatically compensates for cuff errors using a closed-loop control approach (i.e. automatic feedback gain adjustment). The system makes use of a frequency independent method, thus reducing the EMG interference and at the same time retaining neural information at the ENG bandwidth of interest[31]. The particular configuration, which is based on the TT, utilises, apart from the three amplifiers, two additional variable gain OTAs and also two rectifiers, a comparator, an integrator, and a feedback OTA for the control stage. An integrated and fully implantable version of this TT amplifier variant has been designed, developed, and tested both through in-vitro and in-vivo preparations, while an in depth description of the system can be found in [Demosthenous et al., 2004; Triantis, 2005a; Demosthenous and Triantis, 2005]. Its reported power consumption was 7.2 mW from a 5 V power supply with a core area of 0.68 mm^2 in 0.8 μm BiCMOS technology [Demosthenous and Triantis, 2005].
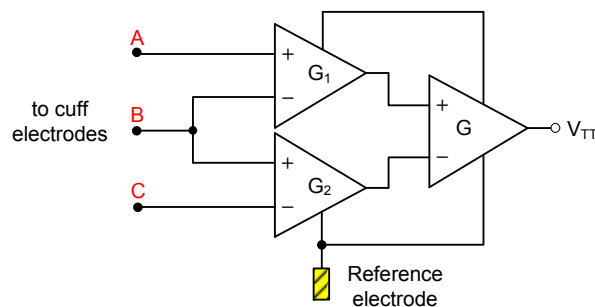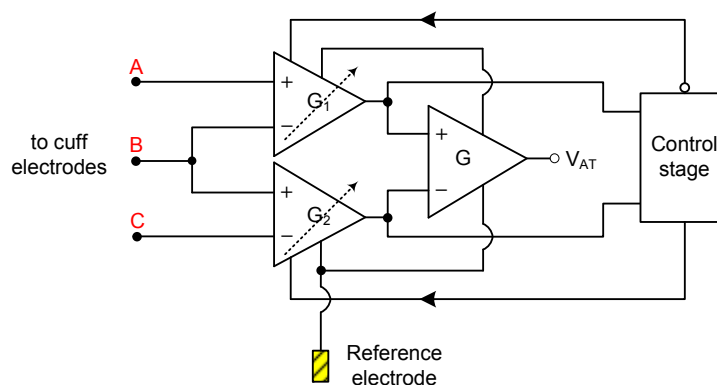

Figure 2.9: The AT amplifier configuration. The gains of the two first stage differential amplifiers (G_1, G_2) are set by differential feedback signals from the control stage. The two low-noise preamplifiers connected to the electrodes are not shown for clarity.

---

[31] In practice, however, there are certain limitations which are further discussed in §3.6.1.

Saline bath experiments with a recording system built using discrete circuit components demonstrated the output ENG to EMG ratio of the AT configuration to be on average 15 and 12 times higher than that of the TT and QT equivalent ratios respectively, for cuff imbalance values of about 10%, while with acute experiments performed on New Zealand white rabbits it was found that the TT is more sensitive to cuff imbalance than both the AT and the QT. Overall, the AT performed the best (i.e. higher ENG to EMG ratio, being less sensitive to cuff imbalance) in 61.9% of the trials, while the QT and the TT performed the best in 23.8% and 14.3% of the trials, respectively [Triantis et al., 2005b]. Nonetheless, as in the case of TT, an important disadvantage of the AT is the increased power requirements due to the number of active circuitry that the configuration is using. Moreover, since the improvement of the AT over the other configurations is achieved in favour of increased system complexity, the neutralisation performance of the AT will be subject to some additional sources of error like [Triantis, 2005a]: phase errors between the two halves of the cuff (e.g. due to source impedance mismatch), input and feedback loop DC offsets (i.e. from the preamplifiers and at the output of the integrator), and spectral harmonic distortion at the AT output due to the settled feedback not being a pure DC value.

2.3.3.4 Alternatives to amplifier configurations

Filtering out the ENG from the EMG signal is also another option, while in many occasions it is used in conjunction with amplifier neutralisation, with analogue or digital filtering being applied to the output signal as means of post-processing to further improve its quality. Although, as discussed next, the frequency spectra of the two signals overlap, the peaks of their power spectral densities differ by about an order of magnitude. Thus, methods of very high-order filtering have been proposed for separating the ENG from the slower EMG [Popovic et al., 1993; Haugland and Hoffer, 1994; Upshaw and Sinkjaer, 1998]. However, since the two signals share part of the spectrum the use of post-filtering results in reduction of the usable ENG bandwidth [Triantis, 2005a]. Specialised algorithms like blind signal separation [Tesfayesus et al., 2003] and artificial neural networks [Rajagopalan et al., 2005] have also been used for separating the two signals, nonetheless, all these solutions result in an increase of system complexity and power efficiency (i.e. when performed at implant level) and therefore are not considered a first choice for neutralising interference.

2.3.4 Neural signal detection

2.3.4.1 Bioelectric signals specification

Although the amplitude of action potentials, as shown in fig. 2.3, is in the mV range the neural signal obtained is significantly attenuated when the recording is not performed using intrafascicular electrodes (i.e. needle electrodes that penetrate the nerve). Nonetheless, this type of electrode is both invasive and inappropriate for long-term recordings as it damages the nerve and is principally used for measurements in acute preparations. The amplitude of naturally occurring ENG signals recorded extrafascicularly using tripolar cuff electrodes lie in the range of a few μV (i.e. typically 3

to 10 µV, depending on factors like whether recording is made from a single nerve or nerve root(s), diameter of cuff and end electrode separation (i.e. cuff length), diameter of the nerve fibre and whether that is myelinated or not, the number of fibres "firing" simultaneously, etc.) with frequency span of about 1 to 10 kHz (peak at around 2 kHz) and most power concentrated between 1 and 5 kHz (maximum power is usually below 3 kHz) [Popovic et al., 1993; Nikolic et al., 1994]. As an example, the mechanically-evoked ENG signal shown in fig. 2.10a is the result of having many nerve fibres "firing" action potentials at the same time (i.e. from about 3 to 5 s of the time scale) producing a relative amplitude difference of 8 µV pk-pk for that duration. Outside this time frame a background noise[32] of probably non-neural origin can be distinguished.
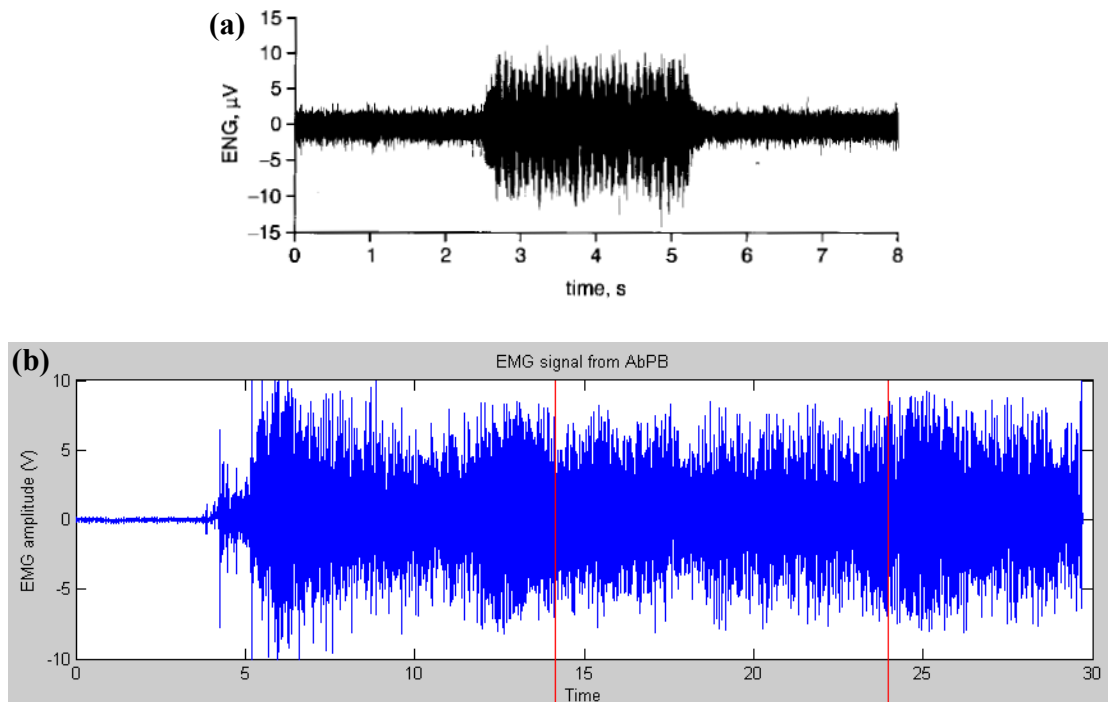
Figure 2.10: (a) Mechanically-evoked neural signals recorded 54 weeks after implantation from a pig's first sacral nerve root (i.e. S1) in the left side using a tripolar cuff electrode (2.2 mm inner diameter and 15 mm length) connected to a QT amplifier. Data were recorded for a period of 8 s during which the skin of the S1 dermatome[33] was rubbed for approximately 3 s to produce cutaneous sensory signal in nerve. Graph taken from [Donaldson et al., 2003]. (b) EMG signal recorded for a period of about 30 s from the abductor pollicis brevis (AbPB) muscle of the right hand of a young female adult. The gain of the recording amplifier was set to 330 (i.e. EMG amplitude is approximately 15 mV pk-pk). Graph courtesy of Implanted Devices Group, UCL.

The ENG signals contain lower frequencies but it is difficult to record them in presence of the much slower electrical activity of surrounding muscles. In particular, peripheral nerves are surrounded by muscles whose electrical activity (i.e. EMG) induce signals in the millivolts range (i.e. typically 10 to 100 mV), with frequency that varies

---

[32] The noise of recording amplifier and thermal electrode noise is comparable in amplitude with the neural signals [Popovic et al., 1993; Nikolic et al., 1994; Struijk et al., 1999].

[33] A dermatome is a cutaneous region innervated by a single spinal nerve of a given spinal cord segment.

from 1 Hz to 3 kHz (peak near 200 Hz), and most power below 1 kHz [Popovic et al., 1993; Haugland and Hoffer, 1994; Nikolic et al., 1994]. An example of a raw EMG signal recorded from a hand muscle using surface electrodes (i.e. ST50D 50 mm round electrodes) is shown in fig. 2.10b. The subject was asked to grip a force sensitive resistor (i.e. used for measuring the grip force) with their thumb and index fingers. Recording of EMG activity began with the muscle rested during which there was barely any EMG activity. Subsequently, the subject started to squeeze the sensor (at about 4 s on the time scale) using maximum force which resulted in a burst of EMG activity. The subject was then asked to maintain a constant force with the EMG activity showing a nearly constant amplitude variation (i.e. holding phase from about 14.5 to 24 s of the time scale). Finally, comparing the two time-domain signals of fig. 2.10, both have a similar appearance whenever the nerve or muscle is firing, with the main difference being in their amplitudes (i.e. in this example the ENG is about 2000 times less than the EMG).

Although fitting the nerve snugly inside the cuff and closing it tightly shut: a) restricts the extracellular space confining the action currents within a long, narrow resistive path therefore producing significantly measurable ENG voltages between the electrodes [Struijk et al., 1999], and b) partially suppresses the EMG signal due to having less ionic current flowing inside the small diameter cuff [Popovic et al., 1993], this on its own may not be sufficient in acquiring a useable (i.e. sufficiently uncontaminated) ENG signal, since the amplitude of the EMG is several orders of magnitude larger (i.e. approximately three orders), and taking into account that the spectra of the two signals overlap, EMG significantly degrades the ENG signal, especially at frequencies which are at the low end of the band. Factors affecting the degree of EMG amplitude pick-up from (implanted) recording electrodes are: cuff length, end electrode separation and recession into the cuff, number of interference sources present, proximity and orientation of the interference source (i.e. actual amplitude of the interference is reduced with distance from the cuff [Triantis and Demosthenous, 2006]), etc.

2.3.4.2 Bandwidth of interest

Recording neural activity from the sacral anterior (i.e. efferent) left and right nerve roots (i.e. S3 and S4; the same roots used for bladder and bowel emptying), via intra-thecal (i.e. inside the dura in the spinal canal) tripolar cuff electrodes in order to detected bladder contraction so that neuromodulation of the sacral posterior (i.e. afferent) nerve roots (i.e. S3) can be applied to suppress bladder contraction, and before urine escapes, is a type of closed-loop FES neuroprosthesis application that we have investigated in terms of required ENG bandwidth. It has been shown[34] that the passbands for nerve fibres of different diameter can be estimated by calculating their energy spectral density as a function of the action potential conduction velocity[35]. Knowing from the literature [Mathers, 1985, p. 70] that the motor nerve fibres innervating the bladder in the SA(3+4) roots have a mean velocity of 60 m/s with diameters 7–14 μm (i.e. being myelinated), the ENG passband in which might be necessary to optimise the signal-to-interference

---

[34] Personal communication with N. Donaldson on March 2006.

[35] The amount of energy per action potential is very strongly dependent on the fibre size and therefore velocity of conduction.

performance of the recording amplifier should be about 2 to 10 kHz. Reducing the low frequency cut-off by taking into account nerve fibres of lower velocity and smaller diameter that might be present, we can be sure about the bandwidth coverage. Conversely, according to [Keynes and Aidley, 2001, p. 19], the amplitude of the voltage change picked up by an extraneural recording electrode also varies with fibre diameter, i.e., when the electrical activity in a sensory nerve is recorded in situ, the picture is dominated by what is happening in the largest diameter fibres, and it is difficult to see anything at all of the action potentials in the small unmyelinated fibres. Therefore, it seems highly unlikely that we will be able to detect anything from small and slow conducting fibres, meaning that opting for a significantly low frequency cut-off will be redundant[36]. For that reason in this work the spectrum of the ENG signals is set to be from 500 Hz to 10 kHz and any attempt to neutralise the EMG interference should be made in that bandwidth.

2.3.4.3 Underlying theory of ENG recording

The shape and amplitude of the ENG signal recorded using a cuff depends on various parameters including cuff closing methods[37] (e.g. longitudinal slit with sutures, interdigitating tubes [Kallesoe et al., 1996], etc.), cuff dimensions (i.e. diameter and length), number of electrodes inside the cuff, and interference present [Andreasen et al., 1997; Andreasen et al., 2000]. The cuff can be placed around a single nerve, or around a nerve root, which later separates into single nerve fibres close to innervating organs. If the source is an active nerve root, the extracellular field potential is formed from the superimposed electric fields of individual active fibres within the nerve root [Webster, 2010, p. 137]. In particular, if one fibre is active the ENG represents a single-fibre action potential (SFAP), whether if *all* (or most) nerves are active *simultaneously* as a result of a stimulus pulse the elicited signal is a compound action potential (CAP). A CAP usually has greater amplitude (i.e. several mV [Struijk et al., 1999]) than a naturally occurring ENG, since many neurons "fire" simultaneously [Triantis, 2005a]. As such, the neural activity depicted earlier in fig. 2.10a, although being the result of many nerve fibres being active at one time (simultaneously or not), it cannot be considered a CAP because it is not the outcome of an electrical stimulus pulse but, instead, of naturally occurring ENG activity. Traditionally, the cuff dimensions are based on SFAP amplitude optimisation, however, in many applications it is rather a CAP than the SFAP that is of interest. In such cases, the information obtained is closer related to the RMS value of the ENG signal (i.e. the CAP) than to the amplitude of the SFAP [Andreasen and Struijk, 2002].

According to [Triantis, 2005a], the principle of cuff electrode ENG measurements in the literature were developed and described in terms of SFAP measurements with modelling of nerve conduction having been successfully applied to both myelinated and

---

[36] The low and high frequency cut-offs of the action potential passband depend on the diameter of the fibre, which for small fibres the conduction velocity reduces, and with that the low and high frequency cut-offs as well as the actual value of the passband.

[37] An imperfect closure of the cuff around the nerve can easily lead to more than 50% loss of the signal amplitude due to the shunting of the high impedance obtained inside the cuff, as was demonstrated in-vitro by [Andreasen et al., 2000] using cuffs with a number of different closures and an artificial nerve fibre.

unmyelinated nerve fibres. The simple example presented in this section illustrates how the neural signal is registered by a tripolar cuff based on recording from a myelinated nerve fibre[38] and is only one of the many models used for the analysis of nerve cuff electrodes. Despite a tripolar cuff electrode is used in this example, the main principle remains the same, meaning that a monopolar cuff is shown to register a similar shape (i.e. triphasic) SFAP with that registered by a tripolar cuff of same dimensions [Andreasen et al., 2000]. Therefore, it is the properties of the cuff as a volume conductor and not the electrodes in it that dictate the shape of the SFAP. Moreover, analysis of SFAP signals from myelinated fibres in the cuff electrode has shown that cuff dimensions have a strong influence on the amplitude and shape of the recorded signal [Andreasen et al., 2000].

When an action potential is propagating along a nerve fibre, each node of Ranvier generates identical action currents i_{AC}, delayed by the time it takes for the action potential to propagate from one node to the next respective node k. In particular, from node to node the delay t_d is given by $t_d = L/v_c$, where L is the internodal distance and v_c is the conduction velocity in m/s [Andreasen et al., 1997; Andreasen et al., 2000]. The amplitude of the action current (i.e. in the order of nanoamperes, typically $i_{AC} \approx |1.5|$ nA) as well as the conduction velocity (i.e. $v_c = 5.58 \times 10^6 \cdot d$) are assumed to be linear with the fibre diameter d[39] (in μm) [Andreasen et al., 1997; Andreasen et al., 2000; Andreasen and Struijk, 2002]. Hence, these "current sources" are activated (i.e. produce an action current) in sequence as the action potential propagates in the fibre, reaching each distinctive node at time t. As a result, the same signal appears at the different electrode contacts inside the cuff at different times.

Since an action potential is spread out over several nodes of Ranvier, many nodes will be active at the same time, and the cuff recorded signal (i.e. the SFAP) will be a superposition of each of the identical but delayed action currents. The contribution of the current from a single node of Ranvier k to the recorded voltage at the electrode is, according to [Andreasen et al., 2000], equal to the convolution of the action current at that node and the transfer function h_k which relates each node's position k to the recording electrode in the cuff. Thus, the SFAP recorded in the middle of the cuff, where the signal peaks can be calculated from [Andreasen et al., 2000]:

$$SFAP(t) = \sum_{k=1}^{number\ of\ nodes} \left[i_{AC}(t - kt_d) \otimes h_k(t) \right]$$

where $i_{AC} \cdot (t - k \cdot t_d)$ is the delayed action current and h_k is the transfer function at axial position x_k of the node and time t. According to [Andreasen et al., 2000] the transfer function h_k in ohms can be represented by the voltage V_k recorded at node k over the current i_k if only that node was active, while it depends on the position of the point

---

[38] When a single myelinated nerve fibre is modelled as a line with point current sources, located at the nodes of Ranvier, this greatly facilitates in theoretically explaining how the SFAP is constructed.

[39] The action current is assumed to increase linearly with fibre diameter because the area of the node of Ranvier changes linearly with fibre diameter. Thus, for a certain number of nodes inside the cuff, the SFAP and the RMS value of the ENG saturate with cuff length (distance between the electrodes) [Andreasen and Struijk, 2002].

current source inside the cuff and on the properties of the cuff electrode itself. From the above equation it is apparent that the measured SFAP occurs by the convolution of the action current with the electrode transfer function, and therefore, by the weighted and delayed action currents of each node summed together. Therefore, the SFAP recorded by a nerve cuff electrode is the result of a superposition of contributions from the currents of all the nodes of Ranvier of the nerve fibre with the contribution of each node being dependent on the nodal current and the properties of the volume conductor around the fibre and the cuff electrode, as also on the electrode properties [Andreasen et al., 2000]. However, assuming that the transfer function is independent of frequency within the bandwidth of the SFAP[40], the convolution becomes a multiplication (i.e. due to the transfer function being constant). The transfer function is close to zero for nodes outside the cuff tripole, so only nodes inside the cuff contribute significantly to the SFAP. An illustration of how the SFAP is constructed is shown in fig. 2.11.

For a simple monophasic action potential (c.f. fig. 2.3) of a single nerve fibre, the associated potential waveform at the outer surface of the membrane, due to the generated extracellular field potential from the activation current, is a) triphasic in nature, b) of greater spatial extent than the action potential, and c) much smaller in pk-pk magnitude. The field potential magnitude at the fibre surface depends on the amount of active cell membrane surface area contributing to the signal, while changes on the properties of the volume conductor (e.g. specific resistivity ρ, size of the volume conductor) can have an effect on the field potential magnitude [Webster, 2010, pp. 135-136]. Therefore the shape of the SFAP of fig. 2.12 is generally like it should be.
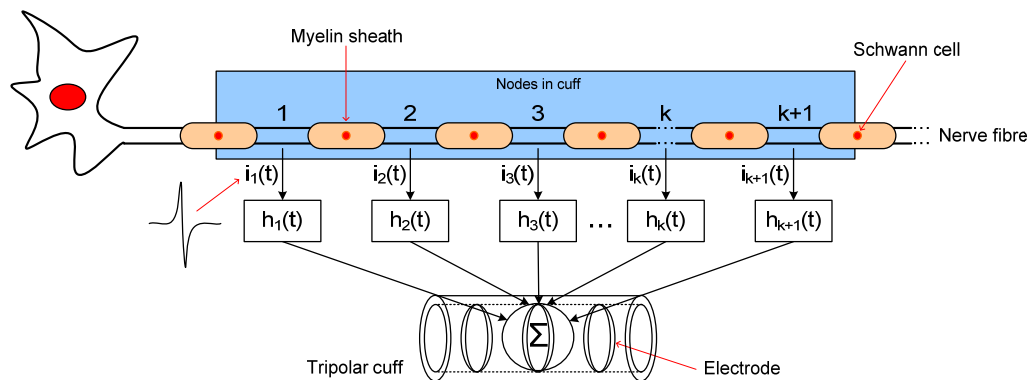
Figure 2.11: Schematic representation of the recorded SFAP being the sum of the contributions of each of the current sources that represent the nodes of Ranvier (figure reproduced from [Andreasen et al., 1997]). The nerve fibre has a structure analogous to that of a shielded cable, with a central conducting core (i.e. axon) surrounded by insulation owing to the presence of Schwann cells (i.e. high resistance myelin nerve membrane).

---

[40] Measurements in [Andreasen et al., 2000] of the transfer functions in the frequency band 200 Hz–2.5 kHz showed a maximum variation of less than 2%.

The transmembrane potentials contribute to the SFAP only where there is a change of the gradient of the transfer function[41]; this happens at the 3 electrode contacts [Andreasen and Struijk, 2002]. An example of a typical transfer function h, as a function of the axial position of node k inside a tripolar cuff is given in fig. 2.12a. The plot clearly shows that the transfer function can be approximated as a triangle. Therefore it is obvious that cuffs linearise the fields of both the nerve signal and the muscle interference[42]. For an idealised cuff (i.e. relatively long and narrow), the peak of the triangle at half the cuff length is given by the value of the potential at the centre electrode caused by a unit current at a node of Ranvier in the centre of the cuff [Andreasen and Struijk, 2002]. Fig. 2.12b illustrates that the contributions of the transmembrane action potential wave to the SFAP happens at the electrode contacts.
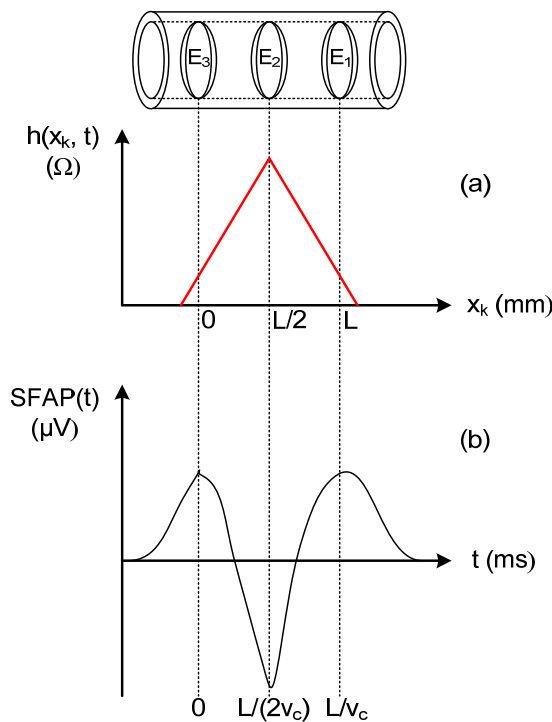
Figure 2.12: Diagram showing the shape of: (a) a typical transfer function as a function of the position of the nodes of Ranvier (i.e. x_k is the axial position of node inside cuff) and how that subsequently affects the SFAP amplitude along the cuff length [Andreasen et al., 2000]; (b) the SFAP obtained by a convolution of the transmembrane action potential and the transfer function, where E_1, E_2, and E_3 are the 3 electrode contacts inside the cuff. The change in polarity of charge across the active membrane can be detected extracellularly by the small current generated in the extracellular fluid. Figure reproduced from [Andreasen and Struijk, 2002].

---

[41] The SFAP is created from 3 transmembrane action potentials by scaling and superpositioning. As the length of the cuff varies, the distance between the electrodes varies and the degree of overlap of the 3 transmembrane action potential waves will vary accordingly [Andreasen and Struijk, 2002].

[42] Due to the transfer function h_k, the shape of the action potential propagating along a single nerve fibre is not important. The cuff would register a SFAP in the same way even if the action current had the form of a sinusoidal current, as has been demonstrated by [Andreasen et al., 1997; Andreasen et al., 2000] through the artificial nerve fibre experiment.

Since a longer cuff gives a relatively higher signal amplitude, the choice of the optimal cuff length is often a compromise of available anatomical space at the cuff implantation site and the amplitude of the signal. Experiments in [Andreasen and Struijk, 2002] indicated that the amplitude of the recorded SFAP reaches a maximum and saturates after the cuff is made longer than the wavelength of the transmembrane action potential (i.e. longer cuffs do not improve the SFAP amplitude significantly). In the same study it was shown that the RMS value of the nerve signal is considerably more sensitive to the cuff length than the SFAP pk-pk amplitude, and that the RMS of the ENG is a linear function of the fibre diameter (in contrast to the pk-pk amplitude of the SFAP, which increases nearly with the square of the diameter). Finally, the number of nodes of Ranvier inside the cuff (i.e. manifested by the cuff length) is a key parameter determining the shape and the pk-pk amplitude of the SFAP (and of the CAP) recorded by a cuff electrode[43], which allows for simple approximations for the choice of optimal cuff length for recording of neural signals from peripheral nerves [Andreasen and Struijk, 2002].

2.3.4.4 Effect of stimulus pulse on neural signal recording

Stimulating electrodes may be used in combination with recording cuff configurations for use of ENG as feedback to FES neuroprosthesis. Often, however, neural signal recording is affected by interference caused from the stimulus current pulses. A stimulation-induced ENG is made up from the stimulus artifact (i.e. the first event in the cuff signal), the CAP, and the M-wave (fig. 2.13). The stimulus artifact, usually several mV in amplitude, is a spike-like signal evoked by the current pulses of the stimulating electrodes (i.e. via the induced electric field), which is picked-up by the recording cuff when stimulation is applied close or even onto the nerve branch that the cuff is attached to [Triantis, 2005a]. The CAP is a result of all nerve fibres being activated simultaneously by that stimulus pulse, while the neuromuscular structures activated by the electrically stimulated nerves results in large electric fields from those structures at the site of recording electrodes. The electrical signal caused by these fields is termed the M-wave (i.e. the EMG interference) and its shape depends on which muscles are active and their proximity and orientation in relation to the recording cuff[44]. As both the stimulus artifact and M-wave interference signals are undesirable in neural signal recording for that reason the recording amplifier must be designed to be usable when stimulation is occurring[45]. Finally, both the stimulus artifact and the M-wave may be cancelled by balancing the cuff [Triantis et al., 2003; Triantis et al., 2005b].

In theory, the QT is insensitive to external electric fields produced by EMG activity or stimulation currents. [Triantis et al., 2005b] performed acute in-vivo recordings on 8

---

[43] The longer the cuff, the more nodes of Ranvier are enclosed in it and thus the higher the SFAP.

[44] The M-wave can be two or three times larger than the naturally occurring EMG and peaks at higher frequencies, while it can be distinguished because of its greater latency in terms of stimulation and slower time course [Triantis, 2005a].

[45] For example, depending on the particular application, the use of a blanking signal to switch off the recording amplifier (i.e. by disconnecting it from the electrodes with inputs shorted) just before and after stimulation, is an option that can be used to minimise stimulation artifacts, allowing recordings whenever there is no stimulation applied.

anaesthetised New Zealand white rabbits using tripolar cuff electrodes around the tibial nerve with another tripolar cuff being used to apply square biphasic stimulation pulses around the sciatic nerve of the same leg. Therefore, the interference signals that occurred were the stimulus artifact and the M-wave, while the nerve signal recorded was the CAP which is much larger in amplitude than the naturally occurring ENG. An example of the effect of different amplifier gain-ratios (i.e. resulting in different cuff imbalance) to the interference signals at the output of the TT configuration is shown in fig. 2.13. The graph shows that the stimulus artifact and M-wave are close to zero amplitude for different gain-ratios meaning that the value of cuff imbalance associated with each of the two interference signals is different (i.e. both signals cannot be balanced at the same time).

Concluding this chapter one last point should be discussed: the key difference between the two ENG signals of fig. 2.10a and 2.13 is that the former is the outcome of naturally occurring neural activity recorded with some of the nerve fibres "firing" action potentials (i.e. SFAPs) when the S1 dermatome is rubbed, while the latter is a solitary action potential (i.e. a CAP) constructed, as a result of a stimulus pulse, by the superposition of many fibre action potentials firing at the exact same time. This results in two differently looking ENG signals being recorded by the cuff. It is also true that a whole nerve root contains a mixture of fibres having widely different diameters, action potential durations and conduction velocities [Keynes and Aidley, 2001, p. 17]. The pk-pk amplitude of the mechanically-evoked ENG of fig. 2.10a is defined by the activity in the fastest fibres; the fibres with the largest diameters (i.e. action potentials in fibres with smaller diameters have a larger delay and do not contribute to the amplitude of the nerve signal [Struijk et al., 1999]). Conversely, the single action potentials that add up to form a CAP like that of fig. 2.13 include all axon contributions and the amplitude of the CAP will vary depending on how many fibres are firing together [Vanhoestenberghe, 2007].
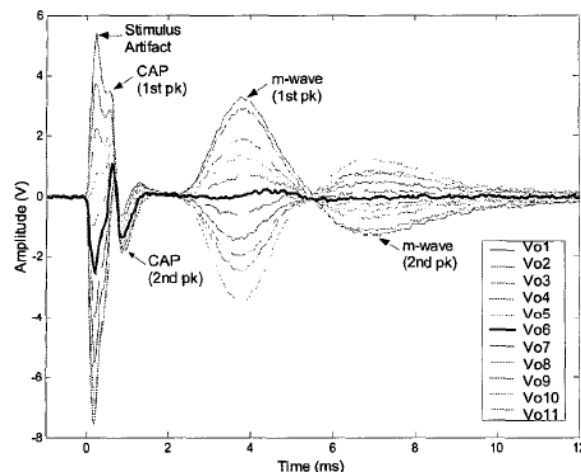
Figure 2.13: An example of an in-vivo ENG signal recording (i.e. a CAP) using the TT amplifier configuration (c.f. §2.3.3.2). The 11 superimposed signals represent measurements for each fixed amplifier gain setting, showing the interference stimulus artifact and M-wave signals, as also the CAP. The peaks of the stimulus artifact and the M-wave reach a minimum for different gain values, i.e., the bold line corresponds to near-zero cuff imbalance value for the M-wave only. Note that the output signal amplitude is in volts due to the gain of the amplifier. Graph taken from [Triantis et al., 2003].

41

2.4 Summary

A much needed background on neurophysiology was first given before subsequently presenting the topic of neural signal recording in some detail. Particular emphasis on the chapter was given in recording neural information using implanted tripolar cuff electrodes and the properties of the cuff were explained. Discussion was focused around cuffs because they are non-invasive to the nerve and appropriate for long-term implantation. In addition, with cuffs, tripolar amplifier configurations can be used that minimise EMG interference and amplify the desired neural signal. In that respect, several recording configurations were presented and their advantages/disadvantages were outlined. As a result, a recording configuration that would offer better neutralisation performance in comparison to the QT but on the other hand is more power efficient than the TT and the AT is considered highly attractive for neuroprosthetic systems that offer improved performance via closed-loop feedback control and thus require to be actively powered. Ideally, the property of the cuff to linearise the fields of external sources allows for the neural signal to reach a maximum at the centre of the cuff and the interference to be neutralised using an appropriate amplifier configuration. More on this important property of the cuff is discussed in the next chapter where minimisation of EMG interference is demonstrated with a novel interference neutralisation approach in an in-vitro preparation.

CHAPTER
THREE

The Modified QT[1]

3.1 Introduction

In this chapter a passive technique for removing myoelectric interference pick-up in neural recording tripoles is presented. The ability to neutralise interference is demonstrated through an in-vitro preparation using the QT as a bridge that can be balanced by adding impedance to one of its outer electrodes. As discussed in Chapter 2, imbalance is simply unavoidable with the conventional QT, and this technique is based on a modified version of the QT configuration – hereafter written as "mQT" – which allows compensating for imbalance that is causing EMG interference to be present at the output of the recording amplifier; we call this the phenomenon of EMG "breakthrough". The operating principle behind the mQT is the utilisation of various passive interference neutralisation (or trimming/nulling) elements, placed at the front-end of the amplifier, in order to eliminate the two main causes of interference present in such a system; namely the myoelectric (or EMG) and the CM interference. In the following sections of this chapter the reader will be introduced to the mQT recording configuration, the advantages/disadvantages it has to offer, as also various results obtained from a series of saline[2] bath experiments, indicating that the technique looks promising.

3.2 Neural recording rationale

Naturally-occurring nerve activity can provide input signals to neuroprosthetic devices. This is advantageous because the natural sensors usually remain viable despite most disabling trauma or disease, they are self-repairing[3], and the nerve interface can be implanted at some more convenient proximal site. The feasibility of this idea has been demonstrated by [Hansen et al., 2002] with a chronic implant for the correction of foot-drop. However, it is difficult to design implanted devices that utilise this method using electrodes that do not penetrate the nerve: the signals are of microvolt level, barely above the noise from the source resistance, and yet the energy available for the amplifier (e.g. in battery powered implants) is usually very limited. Neural recording is also subject to two forms of interference [Donaldson et al., 2003]: CM interference due to potential differences between the amplifier's reference electrode and average potential of the

---

[1] The contents of Chapter 3 were partially presented in [Pachnis et al., 2007].

[2] A salt solution of certain conductivity simulating the composition of body fluids.

[3] Axons in the PNS have the capability of regenerating when damaged [Mathers, 1985, p. 21].

recording electrodes (i.e. $V_{out}=G_{diff}V_d+G_{CM}V_{CM}$ with $V_{CM}=(V_++V_-)/2$), and potential gradients parallel to the nerve but due to external sources. The latter is assumed to be myoelectric interference since it is likely to be due to local muscles. As discussed in Chapter 2 (c.f. §2.3.4.1) action potentials in muscle have mV amplitude, large compared to the neural signal, and most importantly their spectra overlap [Popovic et al., 1993; Nikolic et al., 1994]. Similarly, CM interference can render the output ENG signal unusable in terms of obtaining sensible information from it, or even saturate the amplifier if the CM source amplitude is very high. So minimising these two forms of interference is important.

Recording whole-nerve activity in the body, rather than in an acute preparation, was demonstrated first by [Hoffer et al., 1974] and separately by [Stein et al., 1975] in the mid-1970s. They inserted the nerve into an insulating tube (i.e. a cuff) containing ring electrodes in the QT configuration, open at its ends to allow the nerve to pass through. This basic structure has been used with several amplifier configurations (c.f. §2.3.3) and has been modified over the years into a number of variants, as researchers have striven to improve performance.
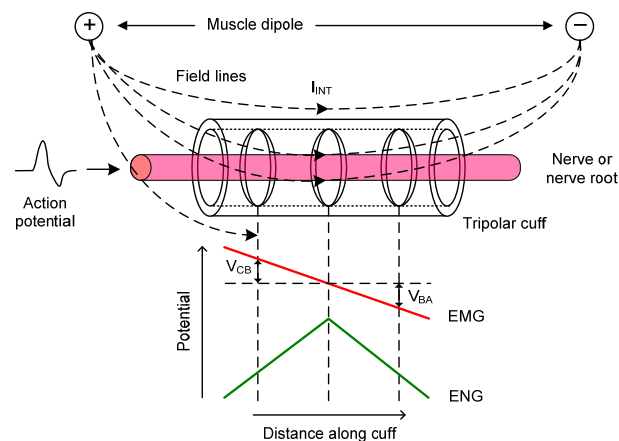
Figure 3.1: Comparison of the linearised potential in the tripolar cuff due to EMG and ENG sources. The external interference source, here represented by a muscle dipole, causes ionic currents to flow through the cuff (isopotential lines not shown). Because of its equal amplitude but opposite phase the EMG signal is (ideally) cancelled at the output of a chosen amplifier configuration, as $|V_{CB}|=|V_{BA}|$. The ENG signal peaks at the middle electrode resulting in $V_{amp\_in}{\approx}V_{ENG}$ (refer to [Donaldson et al., 2003] for proof).

For the nerve signal, the main point of the cuff is that it reduces the volume of tissue in which the action currents flow and, therefore, increases the potential differences between the electrodes. For the EMG interference, the fact that the cuff is a tube of uniform cross-sectional area means that the gradient inside, due to ionic current flowing through the tissue inside the cuff from each external source, is approximately constant, and therefore the potential differences between the pairs of electrodes are equal and cancel. How they are cancelled depends on the amplifier configuration but the principle is that out-of-cuff signals cancel while neural signals do not. This principle is illustrated in fig. 3.1 which shows the way signals of interest are ideally registered by the cuff. The steepness of the

induced EMG potential gradient depends on the length of the cuff (and hence on the outer electrode separation), since longer cuffs result in greater interference reduction [Rahal, 2000c], as the resistance of the tissue inside the cuff is then higher and therefore less ionic current flows through the cuff due to external fields. Nevertheless, it is the property of the cuff to linearise the fields of external sources that is important [Struijk and Thomsen, 1995]. This linearisation is a neat idea but is actually only approximately true, as discussed next.

3.3 Neutralising interference with mQT

3.3.1 Definition of imbalance

Ideally, the QT is immune to electric fields situated externally to the cuff. If we assume uniform resistivity of the cuff internal tissue, the electric gradient inside caused by such extrafascicular fields, due to the insulating property of a perfectly sealed cuff, must be constant. Ideally, this property results in the EMG voltage of the middle electrode being the average of the voltages at the two end electrodes, if those are symmetrical and identical, and the cuff has a small diameter as compared to its length (i.e. so that the small-bore approximation[4] [Cirmirakis et al., 2010] is held). Hence, the voltage amplitudes of the two outer electrodes are, in relation to the middle electrode, in anti-phase (i.e. equal but opposite, i.e., $|V_{CB}|=|V_{BA}|$ in fig. 3.1). Subsequently, by using this arrangement the voltage amplitudes from the two halves of the cuff are equal and cancel at the output of the recording amplifier. Conversely, the ENG signal is always in phase with maximum amplitude at the centre of the cuff (i.e. middle electrode)[5].

In practise, the abovementioned EMG neutralisation principle will not completely remove the interference if the field inside the cuff is not perfectly linear. This breakthrough of EMG has been attributed by [Rahal, 2000c] mainly to: a) manufacturing tolerances on electrode position, and b) impedance irregularities in the tissue inside and along the cuff, due to the biological changes after implantation (i.e. tissue growth). Another factor that has been reported to cause the deviation of the cuff behaviour from its ideal model is c) "end-effects". The end-effect phenomenon was initially shown by [Rahal et al., 2000a] to reduce the linearity of the interference field inside the cuff close to its edges[6]. Moreover, [Triantis and Demosthenous, 2006] demonstrated that imbalance due to end-effects is also related to the proximity and orientation of the external source relative to the cuff, with the latter having a more severe effect on imbalance[7]. All these factors contribute to what we call *imbalance*, since a perfectly symmetrical (or balanced)

---

[4] In this case the field inside the cuff is uniform with a constant gradient, generally unlike the external field.

[5] A detailed explanation of why this is the case was given in §2.3.4.3.

[6] End-effects are caused by the finite length of the cuff which distorts the isopotential lines due to the silicone rubber having lower conductivity than tissue and surrounding fluid. Hence, the interference field lines entering and exiting the cuff are subject to some curvature, and the linearity of the interference potential inside the cuff is degraded near the cuff edges. As a result, different interference signals (e.g. stimulus artifact and EMG) would appear with different cuff imbalance values [Triantis et al., 2005b].

[7] This can greatly affect the interference neutralisation performance of the mQT and TT, as further discussed in §3.6.1.

cuff would be immune to external fields. The first cause of imbalance can be minimised by good fabrication techniques, the other two are unavoidable[8]. Conversely, the ENG is considered unaffected by imbalance [Struijk and Thomsen, 1995; Triantis, 2005a].

3.3.2 Principle of EMG neutralisation

Despite the TT being intrinsically capable of balancing the cuff and thus achieving (almost) complete EMG neutralisation it requires more power than the QT because it uses more than one amplifier. Conversely its rival, the QT, does not provide the means of compensating for interference, however, its low power requirements make it an attractive alternative in cases like ours, where detection of bladder contraction from the neural signal in the sacral roots needs to be carried out for most of the day and with a battery powered implant. In this section an upgrade to the conventional QT is presented which gives it the ability to null the EMG and CM interferences. The idea was originally proposed by [Struijk and Thomsen, 1995] in which they recognised that EMG interference is due to imbalance in the cuff and they placed a potentiometer across the outer electrodes to allow adjustment. In their experiments, a small improvement was possible using this method of manual trimming. [Donaldson et al., 2003] also suggested adding a second potentiometer, as a variable resistance, to allow CM interference to be removed by equalising the source resistances seen by the amplifier[9]. The idea is illustrated schematically in fig. 3.2 below.
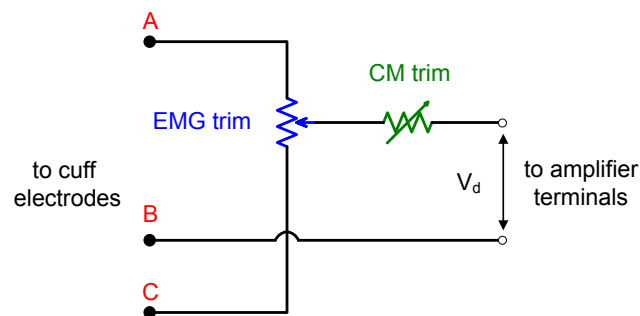
Figure 3.2: Arrangement of trimmers to balance axial and source resistances. The EMG trim potentiometer is placed between the outer electrodes with its wiper connected to the amplifier input with A, B, and C being circuit nodes (c.f. fig. 2.7).

Fig. A.1 of Appendix A shows a model of the tripolar cuff with the three sources of interest – i.e. CM, EMG (labelled I_{INT}), and ENG – contributing to the differential input voltage V_d of the QT amplifier. Imbalance can be due to $R_{t1} \neq R_{t2}$ but it may also be due to $Z_{e1} \neq Z_{e3}$ (i.e. R_t and Z_e are tissue resistances and electrode impedances respectively). Note that Z_{e2} is much less important because it is connected only to the amplifier (high input impedance), whereas current flows through Z_{e1} and Z_{e3}. Assuming that electric and magnetic phenomena happen at the same time, analysis can be based on a lumped circuit

---

[8] However, the effect of imbalance due to end-effects can be lessened by moving the end electrodes sufficiently inside the cuff and away from the edges [Triantis et al., 2005b].
[9] This assumes the ideal case where the source impedances seen by the amplifier are purely resistive, neglecting any capacitive effects.

model. The "EMG" circuit in fig. A.1 is analogous to the Wheatstone bridge in fig. 3.3 in which the LHS comprises two resistors (R_{t1}, R_{t2}) and the RHS two electrode impedances (Z_{e1}, Z_{e3}), which are also the components that form the two ratios for balancing the bridge. The differential input to the QT amplifier is V_d, while the voltage source V_{INT} represents the EMG interference which allows the ionic current $I_{INT,IN}$ to flow inside (and outside $I_{INT,OUT}$; not shown) the volume of the cuff, causing a potential drop across its ends. Thus, the differential input voltage to the QT amplifier is:

$$V_d = \left(\frac{R_{t2}}{R_{t1} + R_{t2}} - \frac{Z_{e3}}{Z_{e1} + Z_{e3}} \right) \cdot V_{INT} \quad (3.1)$$

from which it is clear that when the two ratios are the same (i.e. when $R_{t1}Z_{e3}=R_{t2}Z_{e1}$ and bridge is balanced), the differential input V_d to the amplifier, due to the interference source V_{INT}, is zero and thus no EMG interference is present at the amplifier's input. An EMG trimming impedance, Z_{trim}, consisting of a series or parallel RC combination[10], may be added to one side or other of the outer electrodes (i.e. circuit nodes of the RHS branch of the bridge), to compensate for an imbalance. This nevertheless depends on the particular type of imbalance present in the cuff[11]. Experiments in [Pachnis et al., 2007] and [Cirmirakis et al., 2010] with unsymmetrical and symmetrical tripoles, respectively, have shown that imbalance in either the cuff resistances (R_{t1}, R_{t2}) or the electrode impedances (Z_{e1}, Z_{e3}) will lead to imbalance.
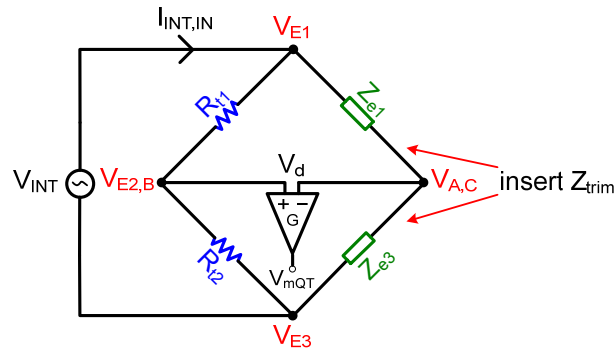
Figure 3.3: The electrodes of QT configuration modelled as a Wheatstone bridge. Balancing the bridge of the lumped circuit is equivalent to cancelling out the effect of the EMG at the input V_d of the differential amplifier. This may be achieved by adding an RC impedance Z_{trim} at the front-end; either in series with Z_{e1} or in series with Z_{e3}.

As shown in the lumped model of fig. A.1, the electrode impedances have capacitive reactance and are thus frequency-dependent. Given that we do not want to increase the noise more than absolutely necessary, we see that a potentiometer is less good than adding an impedance. This is because a purely ohmic term cannot simply cancel out the

---

[10] Other circuit combinations of Z_{trim} are certainly possible. This is further explored in Chapter 5.

[11] As discussed later on, for the purposes of the in-vitro experiment, an imbalance in the tripole was caused by misplacing the middle electrode with respect to the two outer electrodes. Hence, if we assume that the two outer electrodes have the same area, an imbalance is due to the axial resistances at the LHS of the bridge not being equal, owing to the positional asymmetry of the electrodes.

EMG interference completely due to the electrodes having capacitive reactance as well as resistance. Instead, as was demonstrated by [Pachnis et al., 2007], a reactive as well as an ohmic term must be used to achieve EMG neutralisation.

3.3.2.1 Characteristics of the trimming impedance

The natural way to represent an electrode interface for AC analysis is as a resistance in parallel with a capacitance. We should expect the capacitance to be proportional to the area and the resistance to be inversely proportional. Hence, $R=r/A$ and $C=cA$ where A is the electrode area and r and c are taken as constants. The impedance of an electrode interface of area A is therefore $Z_{inter}=[r/(1+j\omega cr)]\cdot 1/A$ which has a phase angle of $-\tan^{-1}(\omega cr)$, independent of area, and a magnitude inversely proportional to the area. In our case, $R_{t1}\neq R_{t2}$, but we assume $A_{E1}=A_{E3}$, and therefore $Z_{e1}=Z_{e3}$.

(a)

(b)

(c)
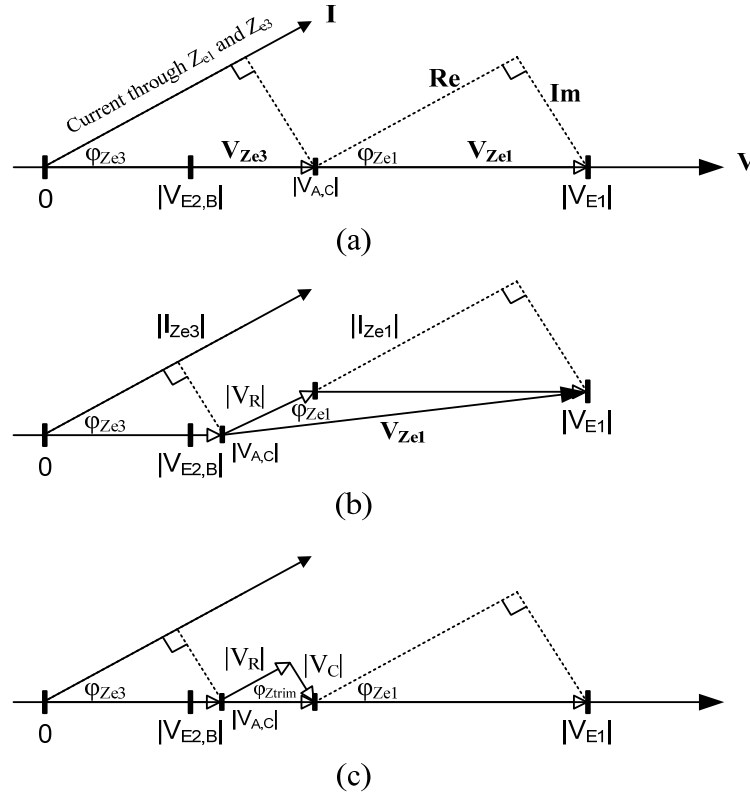
Figure 3.4: Phasor diagrams for bridge of fig. 3.3: (a) $R_{t1}>R_{t2}$ but $Z_{e1}=Z_{e3}$, the current through the electrodes leads the source voltage by $\varphi_{Ze1}=\varphi_{Ze3}$. (b) Effect of adding resistance in series with Z_{e1} moves $V_{A,C}$ to the left but introduces a phase difference between V_{Ze1} and V_{Ze3} (i.e. $\varphi_{Ze3}>\varphi_{Ze1}$ and $V_R=Re[\mathbf{Z_R}\cdot\mathbf{I}]=|V_R|\cdot\cos(\varphi_{Ze1})$). (c) To avoid introducing phase error, the added impedance Z_{trim} must have a phase angle $\varphi_{Ztrim}=\varphi_{Ze1}=\varphi_{Ze3}$, i.e., the same as the electrode impedances Z_{e1} and Z_{e3}. Now, $V_R=Re[\mathbf{Z_{trim}}\cdot\mathbf{I}]=|V_R|\cdot\cos(\varphi_{Ztrim})$ and $V_C=Im[\mathbf{Z_{trim}}\cdot\mathbf{I}]=|V_C|\cdot\sin(\varphi_{Ztrim})$.

If we consider what impedance must be added to such a bridge in order to reach balance, we also see that resistance alone can not achieve balance if the electrodes have reactance as well as resistance. This can be demonstrated by the phasor diagram [DeCarlo

and Lin, 2001], shown in fig. 3.4a where V_{E3} is set to 0 V[12], while the current through the electrodes leads the source voltage by $\varphi_{Ze1}=\varphi_{Ze3}$. The dashed lines show the resistive and reactive parts of the electrode impedances Z_{e1} and Z_{e3}, which in this case divide potential V_{E1} into two equal parts at $V_{A,C}$. Assuming that $R_{t1}>R_{t2}$, potential $V_{E2,B}$ will be smaller than $V_{A,C}$. Adding resistance in the upper RHS arm of the bridge in order to bring potential $V_{A,C}$ closer to $V_{E2,B}$ brings voltage V_R in phase with the current through Z_{e1} but introduces a phase error as is shown in fig. 3.4b (i.e. the added resistance changes the phase angle of Z_{e1}). Moreover, voltage V_{Ze1} is now out of phase with voltage V_{Ze3} but currents I_{Ze1} and I_{Ze3} are in phase. Thus, to move potential $V_{A,C}$ close to $V_{E2,B}$ without introducing a phase error an impedance Z_{trim} should be added having the same phase angle φ as the electrode impedances Z_{e1} and Z_{e3} (fig. 3.4c). Therefore, mismatches in either the cuff resistances or the electrode impedances will lead to imbalance that requires capacitive impedance added to one side. Unfortunately, it follows that while the resistance and capacitance may be trimmed to balance the bridge at a particular frequency, it will be unbalanced at other frequencies due to the frequency-dependence of the two electrode impedances.

In reality, apart from having geometrical asymmetries at the interface (e.g. electrode misplacement, electrode area mismatch) and tissue inhomogeneity inside the cuff, cuff imbalance may also exist due to irregularities on the electrode surface[13], since a perfectly symmetrical cuff with electrode positions made to close tolerance will not necessarily be balanced, as [Cirmirakis et al., 2010] have shown. No matter the reason for imbalance, compensation with a trimming network is only required for either half of the cuff (i.e. the resistance and capacitance always need to be on the same side). In our case, we investigated the effect of adding the trimming impedance Z_{trim} in two possible ways; RC connected a) in series and b) in parallel. Therefore, there are 4 possible combinations in total, as illustrated in fig. 3.5. Moreover, since the parallel and series RC impedances are analogous to each other there is only one impedance per trimming arrangement.
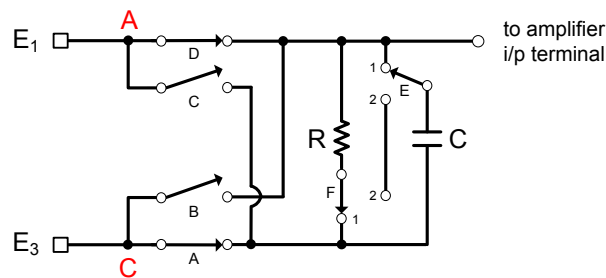
Figure 3.5: Circuit schematic with switches showing the 4 possible trimming combinations in the front-end of the QT amplifier. E_1 and E_3 are connection pads to the outer electrodes of the cuff. R and C are the trimming resistance and capacitance. The middle electrode E_2 (not shown) is connected to the remaining amplifier input.

---

[12] In practice the potential V_{INT}, provided by an audio transformer, is left floating. Refer to §3.4.3 for details.

[13] As discussed in depth in Chapter 5 another important reason for imbalance is the phase angle mismatch in the impedances of the two outer electrodes, as a result of surface roughness.

Control bits			Switches					
Trim	S/P	L/R	A	B	C	D	E	F
0	X	X	O	C	O	C	X	X
1	0	0	O	C	C	O	P1	P1
1	1	0	O	C	C	O	P2	P2
1	0	1	C	O	O	C	P1	P1
1	1	1	C	O	O	C	P2	P2

Table 3.1: Mapping of control bits to switches position. When trim is high, amplifier operates in mQT mode and when low in conventional QT mode. Abbreviations: S=series trim, P=parallel trim, L=RC at left of o/p, R=RC at right of o/p, O=open, C=closed, P1=position 1, P2= position 2, X=do not care.

3.3.2.2 Magnitude and phase of trimming impedance

From eqn. 3.1 we know that when the ratios of the two sides of the bridge are the same the bridge is balanced and $V_d/V_{INT} \approx 0$. However, it is important to show what phase angle the trimming impedance Z_{trim} needs to have, since, as shown above, to balance the bridge a capacitive impedance of a particular magnitude and phase needs to be added. We are going to examine 2 cases:

Case 1: $\varphi_{Ze1} = \varphi_{Ze3}$, $|Z_{e1}| \neq |Z_{e3}|$

$$\frac{Z_{e3}}{\left(Z_{e1} + Z_{trim} \right) + Z_{e3}} = \frac{\left| Z_{e3} \right| e^{-j\varphi_{Ze3}}}{\left| Z_{e1} \right| e^{-j\varphi_{Ze1}} + \left| Z_{trim} \right| e^{-j\varphi_{Ztrim}} + \left| Z_{e3} \right| e^{-j\varphi_{Ze3}}} =$$

$$= \frac{\left| Z_{e3} \right| e^{-j\varphi_{Ze3}}}{\left(\left| Z_{e1} \right| + \left| Z_{trim} \right| + \left| Z_{e3} \right| \right) e^{-j\varphi_{Ze3}}} = \frac{\left| Z_{e3} \right|}{\left| Z_{e1} \right| + \left| Z_{trim} \right| + \left| Z_{e3} \right|}$$

$$\therefore \text{if} \quad \frac{\left| Z_{e3} \right|}{\left| Z_{e1} \right| + \left| Z_{trim} \right| + \left| Z_{e3} \right|} = \frac{R_{t2}}{R_{t1} + R_{t2}} \Rightarrow V_d = 0$$

It is obvious from the above trivial calculations that when the phase angle of the two outer electrodes is the same, the added trimming impedance needs also to have the same phase angle in order to achieve balance, i.e., $\varphi_{Ztrim} = \varphi_{Ze1} = \varphi_{Ze3}$. This verifies our earlier remark which was illustrated graphically with the use of phasors in fig. 3.4. As this will most likely not be the case with real electrodes, it is useful to examine a second case.

Case 2[14]: $\varphi_{Ze1} \neq \varphi_{Ze3}$, $|Z_{e1}| \neq |Z_{e3}|$

$$\text{Let} \quad \varphi_{Ze1} = \varphi_{Ze3} - \frac{\pi}{25} \text{rad}, \quad R_t = \frac{R_{t2}}{R_{t1} + R_{t2}} = \frac{1\text{k}\Omega}{2\text{k}\Omega + 1\text{k}\Omega} = \frac{1}{3}$$

---

[14] The phase angle difference is not important in this example, however, a difference of 7.2 degrees between the two outer electrodes seems to be realistic. Additionally, we assume that the two outer electrodes have a different surface area and therefore their impedance magnitudes are different.

$$\frac{\left|Z_{e3}\right|e^{-j\varphi_{Ze3}}}{\left|Z_{e1}\right|e^{-j\left(\varphi_{Ze3}-\pi/25\right)}+\left|Z_{trim}\right|e^{-j\varphi_{Ztrim}}+\left|Z_{e3}\right|e^{-j\varphi_{Ze3}}}=R_t\Leftrightarrow$$

$$\left|Z_{trim}\right|e^{-j\varphi_{Ztrim}}=\frac{\left|Z_{e3}\right|}{R_t}e^{-j\varphi_{Ze3}}-\left|Z_{e3}\right|e^{-j\varphi_{Ze3}}-\left|Z_{e1}\right|e^{-j\left(\varphi_{Ze3}-\pi/25\right)}\Leftrightarrow$$

$$\left|Z_{trim}\right|e^{-j\varphi_{Ztrim}}=e^{-j\varphi_{Ze3}}\left(\frac{\left|Z_{e3}\right|}{R_t}-\left|Z_{e3}\right|-\left|Z_{e1}\right|e^{j\pi/25}\right)\Leftrightarrow$$

If $A_{E1}=\frac{1}{2}A_{E3}\rightarrow$ let $\left|Z_{e1}\right|=2k\Omega,\quad\left|Z_{e3}\right|=1k\Omega$

$$\left|Z_{trim}\right|e^{-j\varphi_{Ztrim}}=e^{-j\varphi_{Ze3}}\left(\frac{1k\Omega}{1/3}-1k\Omega-2k\Omega e^{j\pi/25}\right)\Leftrightarrow$$

$$\left|Z_{trim}\right|e^{-j\varphi_{Ztrim}}=2k\Omega e^{-j\varphi_{Ze3}}\left(1-e^{j\pi/25}\right)$$

$$\left(1-e^{j\pi/25}\right)=\left(1-e^{j\pi/25}\right)e^{j\pi/50}e^{-j\pi/50}=-\left(e^{j\pi/50}-e^{-j\pi/50}\right)e^{j\pi/50}=$$

$$\overset{\left[\sin x=\frac{e^{jx}-e^{-jx}}{2j}\right]}{=}-2j\sin\frac{\pi}{50}e^{j\pi/50}\overset{\left[-j=e^{-j\pi/2}\right]}{=}2\sin\frac{\pi}{50}e^{j\pi/50}e^{-j\pi/2}=2\sin\frac{\pi}{50}e^{-j24\pi/50}$$

$$\left|Z_{trim}\right|e^{-j\varphi_{Ztrim}}=2k\Omega e^{-j\varphi_{Ze3}}2\sin\frac{\pi}{50}e^{-j24\pi/50}\Leftrightarrow$$

$$\left|Z_{trim}\right|e^{-j\varphi_{Ztrim}}=4k\Omega\sin\frac{\pi}{50}e^{-j\left(\varphi_{Ze3}+24\pi/50\right)}$$

$$\therefore\left|Z_{trim}\right|=4k\Omega\sin\frac{\pi}{50}\text{ rad},\quad\varphi_{Ztrim}=\varphi_{Ze3}+24\pi/50\text{ rad}$$

$$\therefore\frac{Z_{e3}}{Z_{e1}+Z_{trim}+Z_{e3}}=R_t\Rightarrow$$

$$\frac{1k\Omega e^{-j\varphi_{Ze3}}}{2k\Omega e^{-j\left(\varphi_{Ze3}-\pi/25\right)}+4k\Omega\sin\frac{\pi}{50}e^{-j\left(\varphi_{Ze3}+24\pi/50\right)}+1k\Omega e^{-j\varphi_{Ze3}}}=$$

$$=\frac{1k\Omega e^{-j\varphi_{Ze3}}}{\left(2k\Omega e^{j\pi/25}+4k\Omega\sin\frac{\pi}{50}e^{-j24\pi/50}+1k\Omega\right)e^{-j\varphi_{Ze3}}}\overset{\left[2\sin\frac{\pi}{50}e^{-j24\pi/50}=-2j\sin\frac{\pi}{50}e^{j\pi/50}\right]}{=}$$

$$=\frac{1k\Omega}{2k\Omega e^{j\pi/25}-2k\Omega\cdot2j\sin\frac{\pi}{50}e^{j\pi/50}+1k\Omega}\overset{\left[2j\sin\frac{\pi}{50}=e^{j\pi/50}-e^{-j\pi/50}\right]}{=}$$

$$=\frac{1k\Omega}{2k\Omega e^{j\pi/25}-2k\Omega\left(e^{j\pi/50}-e^{-j\pi/50}\right)e^{j\pi/50}+1k\Omega}=\frac{1k\Omega}{2k\Omega e^{j\pi/25}-2k\Omega\left(e^{j\pi/25}-1\right)+1k\Omega}=\frac{1}{3}=R_t$$

51
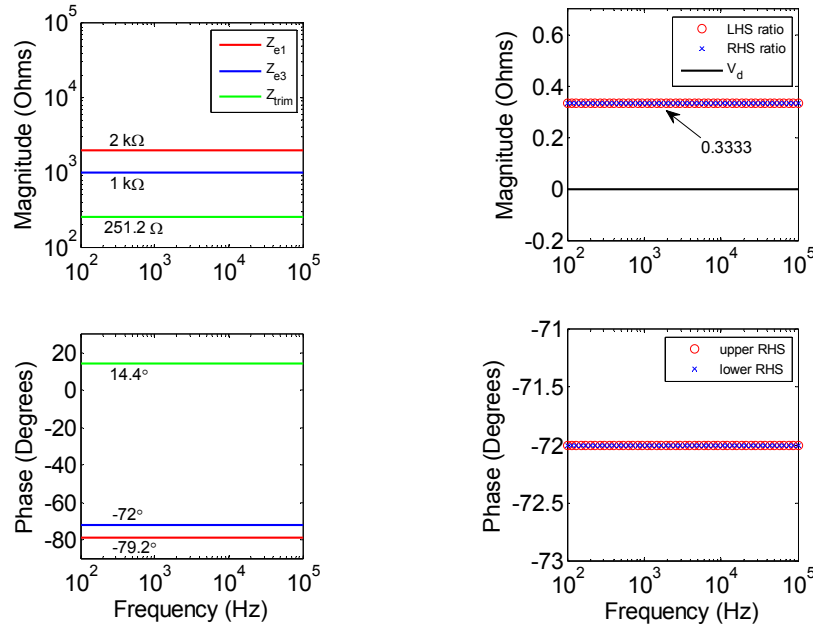
Figure 3.6: Matlab™ simulation illustrating the balance of the bridge arrangement of fig. 3.3. Left graph: magnitude and phase of the two outer electrode impedances Z_{e1}, Z_{e3} and trimming impedance Z_{trim} required to balance bridge. Right graph: by adding impedance Z_{trim} of an appropriate magnitude and phase in series with Z_{e1} the phase of the two electrode impedances now match and the ratio at the two sides of the bridge is equal to 1/3, hence V_d=0.

In this case it is not possible to balance the bridge by finding a solution in terms of φ_{Ztrim} only. It would help explaining why, if one thinks as follows: if we assume a parallel RC network making up the trimming impedance, it is obvious that the phase angle φ_{Ztrim} will depend on both R and C values, which in turn will affect the magnitude $|Z_{trim}|$ of the trimming impedance. Therefore, in order to compensate for the difference in phase of the two outer electrodes, one needs to set an appropriate magnitude and phase to Z_{trim} (i.e. one makes the other). In the first case where $\varphi_{Ze1}=\varphi_{Ze3}$, matching the phase of Z_{trim} to that of the outer electrodes and then maintaining the ratio of $-\text{Im}(Z_{trim})/\text{Re}(Z_{trim})$ constant such that $\varphi_{Ztrim}=\varphi_{Ze1}=\varphi_{Ze3}$ to remain constant, the only requirement for balancing the bridge is then adding an appropriate $|Z_{trim}|$. Conversely, the example calculations for the second case illustrate the difference to the first: as $|Z_{trim}|$ is a constant which is related to the phase angle difference that the two outer electrodes have (i.e. through the $2\sin(\pi/50)$ term), finding the phase angle of Z_{trim} now requires knowing $|Z_{e1}|$, $|Z_{e3}|$, φ_{Ze1}, φ_{Ze3}, and R_t. Plotting the appropriate data of the example calculations in Matlab™ (fig. 3.6) it is shown that the bridge is now balanced because the added magnitude and phase of Z_{trim} have made $\varphi_{(Ze1+Ztrim)}=\varphi_{Ze3}$ and by $|Z_{e1}|=R_{t1}$ and $|Z_{e3}|=R_{t2}$ balance of the bridge is achieved. In that way, at every frequency at which a null is found, Z_{trim} is a function of the two electrode impedances, while it is also related to the imbalance of R_{t1} and R_{t2} at the LHS of the bridge. Additionally, it is important to emphasise that our example assumes an ideal case where the magnitude and phase angle of the electrode and trimming impedances are frequency-independent, something which is not true in real electrodes, nonetheless, the main principle of balancing the bridge remains the same.

Finally, we believe there is only one unique combination of impedance magnitude and phase that can balance the bridge for a particular imbalance and spot frequency.

3.3.3 Common-mode rejection ratio performance

The CMRR performance of an amplifier is important in applications where relevant information is contained in the voltage difference between two signals. No matter how high the intrinsic CMRR performance and input impedances (CM and differential) of an amplifier are, the actual CMRR will be determined by the matching of the source impedances of the two input leads to the amplifier [Casas and Pallas-Areny, 1997]. The CMRR of a tripolar recording amplifier, such as the QT, depends on the impedance imbalance from the cuff (including any blocking capacitors[15]), its current biasing resistor network, and the length of the cable wiring connecting the electrodes to the amplifier [Donaldson et al., 2003]. As such, devices with short cable and low source impedance have a higher CMRR[16].
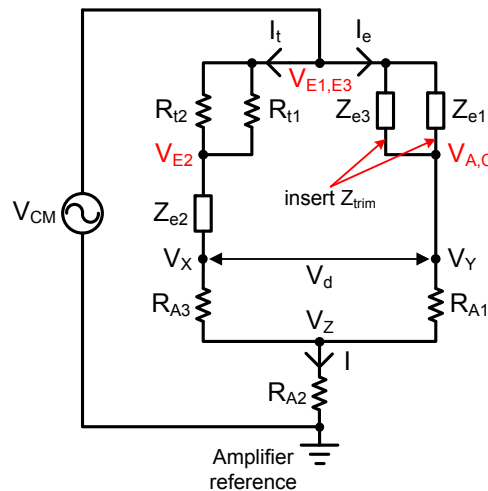
Figure 3.7: CM source analysis equivalent circuit for the QT. R_{t1} and R_{t2} are the tissue resistances inside and along the cuff, Z_{e1} to Z_{e3} are the electrode impedances, and R_{A1} to R_{A3} are the amplifier bias current resistances (c.f. fig. 3.9). The tissue resistances R_{o1} and R_{o2} outside the cuff are assumed to be negligible and therefore have been neglected to simplify analysis. Imbalance of time constants of the two pathways increases the differential input voltage V_d due to CM source V_{CM}: one time constant is due to the two outer electrodes (and trimming impedance Z_{trim}, if used) and the other is due to the axial resistances of cuff plus impedance of middle electrode.

As shown in fig. A.1 of Appendix A, the CM voltage is applied between all electrodes in the cuff and an indifferent (or reference) electrode (c.f. §4.2.2) which is connected to the amplifier reference terminal. Therefore, all three electrodes in the cuff are subject to some CM voltage relative to the reference electrode. Performing a front-end analysis in

---

[15] As a precaution against semiconductor failure which would otherwise allow DC current to pass from the amplifier's power supply to the electrodes causing electrolysis.

[16] Response to CM signal at the differential input voltage V_d of the amplifier rises with frequency because of unequal time constants of source impedances, as was shown by [Donaldson et al., 2003].

terms of the effect of the CM interference on the QT amplifier configuration, it is helpful to rearrange the circuit of fig. A.1 as that shown in fig. 3.7. Also, assuming that the two output tissue resistances R_{o1} and R_{o2} are of negligible value, those can be ignored[17]. Hence we have:

$$\text{Let } R_{t1}//R_{t2} = R_{tt}, \quad Z_{e1}//Z_{e3} = Z_{ee}$$

$$I = I_t + I_e, \quad V_d = V_X - V_Y$$

$$V_Z = \left(I_t + I_e \right) R_{A2} \quad (1)$$

$$V_{CM} - V_Z = I_t \left(R_{tt} + Z_{e2} + R_{A3} \right) \quad (2)$$

$$V_{CM} - V_Z = I_e \left(Z_{ee} + R_{A1} \right) \quad (3)$$

$$\left. {}^{V_X - V_Z = I_t R_{A3}}_{V_Y - V_Z = I_e R_{A1}} \right\} V_d = I_t R_{A3} - I_e R_{A1} \quad (4)$$

$$\text{From } (1) \& (2) \rightarrow V_{CM} - \left(I_t + I_e \right) R_{A2} = I_t \left(R_{tt} + Z_{e2} + R_{A3} \right)$$

$$V_{CM} = I_t \left(R_{tt} + Z_{e2} + R_{A3} + R_{A2} \right) + I_e R_{A2} \quad (5)$$

$$\text{From } (1) \& (3) \rightarrow V_{CM} - \left(I_t + I_e \right) R_{A2} = I_e \left(Z_{ee} + R_{A1} \right)$$

$$V_{CM} = I_e \left(Z_{ee} + R_{A1} + R_{A2} \right) + I_t R_{A2} \quad (6)$$

$$\text{From } (5) \& (6) \rightarrow I_t \left(R_{tt} + Z_{e2} + R_{A3} \right) + I_t R_{A2} + I_e R_{A2} = I_e \left(Z_{ee} + R_{A1} \right) + I_e R_{A2} + I_t R_{A2} \Leftrightarrow$$

$$I_e = \frac{I_t \left(R_{tt} + Z_{e2} + R_{A3} \right)}{\left(Z_{ee} + R_{A1} \right)} \quad (7)$$

$$\text{From } (4) \& (6) \rightarrow \frac{V_d}{V_{CM}} = \frac{I_t R_{A3} - I_e R_{A1}}{I_e \left(Z_{ee} + R_{A1} + R_{A2} \right) + I_t R_{A2}} \quad (8)$$

$$\text{From } (7) \& (8) \rightarrow \frac{V_d}{V_{CM}} = \frac{I_t \left[R_{A3} - \dfrac{\left(R_{tt} + Z_{e2} + R_{A3} \right)}{\left(Z_{ee} + R_{A1} \right)} R_{A1} \right]}{I_t \left[\dfrac{\left(R_{tt} + Z_{e2} + R_{A3} \right)}{\left(Z_{ee} + R_{A1} \right)} \left(Z_{ee} + R_{A1} + R_{A2} \right) + R_{A2} \right]}$$

Assuming: $R_{A2} >> Z_{ee} + R_{A1}$

$$\frac{V_d}{V_{CM}} = \frac{R_{A3} - \dfrac{\left(R_{tt} + Z_{e2} + R_{A3} \right)}{\left(Z_{ee} + R_{A1} \right)} R_{A1}}{\dfrac{\left(R_{tt} + Z_{e2} + R_{A3} \right)}{\left(Z_{ee} + R_{A1} \right)} R_{A2} + R_{A2}} = \frac{R_{A3} \left(Z_{ee} + R_{A1} \right) - \left(R_{tt} + Z_{e2} + R_{A3} \right) R_{A1}}{\left(R_{tt} + Z_{e2} + R_{A3} \right) R_{A2} + \left(Z_{ee} + R_{A1} \right) R_{A2}} =$$

$$= \frac{R_{A3} Z_{ee} - \left(R_{tt} + Z_{e2} \right) R_{A1}}{\left(R_{tt} + Z_{e2} + R_{A3} + Z_{ee} + R_{A1} \right) R_{A2}} \overset{[R_{A1} = R_{A3} = R_A]}{\Leftrightarrow} \frac{V_d}{V_{CM}} = \frac{R_A Z_{ee} - \left(R_{tt} + Z_{e2} \right) R_A}{\left(R_{tt} + Z_{e2} + Z_{ee} + 2R_A \right) R_{A2}}$$

---

[17] As discussed in [Donaldson et al., 2003], this simplifies the CM analysis and it is done as if the cuff were immersed in an isopotential region equal to V_{CM} which is above the reference input to the amplifier (i.e. the potential at the two ends of the cuff in respect to the amplifier reference is the same).

Assuming: $2R_A \gg R_{tt} + Z_{e2} + Z_{ee}$

$$\frac{V_d}{V_{CM}} = \frac{R_A \left[Z_{ee} - \left(R_{tt} + Z_{e2} \right) \right]}{2 R_A R_{A2}} = \frac{Z_{ee} - R_{tt} - Z_{e2}}{2 R_{A2}}$$

Therefore we see that if the source impedances of the two input leads to the amplifier are the same, i.e. $Z_{ee} = R_{tt} + Z_{e2}$, and neglecting effects like: a) stray capacitances (e.g. between cabling, to reference, and to body tissue not close to cuff [Donaldson et al., 2003]), and b) the tissue resistances outside the cuff, then $V_d \approx 0$ and no interference due to CM is present at the differential input of the amplifier. That is, the CMRR performance of the recording amplifier depends on the chosen values of the T of current biasing resistors R_{A1} to R_{A3} (c.f. fig. 3.9), as also on the matching of the input capacitors and resistors of the source such that:

$$\left| Z_{ee} \right| = \sqrt{\left(R_{tt} + \left| Z_{e2} \right| \cos\varphi_{Ze2} \right)^2 + \left(\left| Z_{e2} \right| \sin\varphi_{Ze2} \right)^2}$$

and

$$\varphi_{Zee} = -\tan^{-1} \left[\frac{\left| Z_{e2} \right| \sin\varphi_{Ze2}}{\left(R_{tt} + \left| Z_{e2} \right| \cos\varphi_{Ze2} \right)} \right].$$

In terms of how the trimming impedance Z_{trim} affects the CM performance of the QT, since that is placed either in series with Z_{e1} or with Z_{e3}, it will only cause imbalance to one side of the source impedance to the amplifier, which can still be appropriately compensated for by being matched to the source impedance of the other pathway (c.f. 2nd paragraph of §3.4.2).

Finally, it would be helpful to have an idea of the desired minimum CMRR performance of the recording amplifier system based on the magnitude of the various signals of interest at the front-end. As was shown by [Donaldson et al., 2003] this can be very easily calculated by allocating estimated values for: a) the magnitude of biopotentials (e.g. electrocardiogram or ECG) common to the amplifier inputs of 1 mV, b) an ENG signal across the differential amplifier input of 1 µV, and also c) the ENG signal at the amplifier output being at least 10 times larger than the CM interference. Then the desired minimum total CMRR (i.e. the CMRR of the amplifier, together with the CM input resistance and the electrode impedances[18]) can be calculated as follows:

---

[18] It has been shown by [Casas and Pallas-Areny, 1997] that the total CMRR of an amplifier system can be calculated from:

$$\frac{1}{CMRR_T} \approx \frac{1}{CMRR_A} + \frac{Z_s}{R_c} \left(\frac{\Delta R_c}{R_c} + \frac{\Delta Z_s}{Z_s} \right)$$

where $CMRR_A$ is the intrinsic CMRR of the amplifier, Z_s is the sum source impedance of each input to the amplifier (i.e. $Z_{ee} + (R_{tt} + Z_{e2})$), and R_c is the sum of the two combined CM amplifier and current bias resistors of the amplifier. Conversely, ΔZ_s denotes the difference between the two source impedances and ΔR_c the difference between the two CM input resistors. It is possible by solving the above equation for a targeted $CMMR_T$ and known ΔZ_s to obtain R_c. If we assume that $CMRR_A$ is infinite and that $\Delta R_c / R_c$ to be negligible

$$CMRR_T = \frac{G_{diff}}{G_{CM}} = \frac{\dfrac{V_{out\_diff}}{V_d}}{\dfrac{V_{out\_CM}}{V_{CM}}} = \left(\frac{V_{CM}}{V_d} \right)\left(\frac{V_{out\_diff}}{V_{out\_CM}} \right) \Leftrightarrow$$

$$CMRR_T = \left(\frac{10^{-3}}{10^{-6}} \right)10 = 20\log\left(10^4 \right) = 80dB$$

(3.3)

3.4 Experimental assessment of EMG neutralisation with mQT

The mQT is a simple alternative neural recording configuration that can be used to trim the EMG interference present at the input of a differential amplifier. Albeit the working principle of the mQT is straightforward, careful consideration needs to be given in finding out how well it performs under certain conditions. Therefore, a number of in-vitro experiments were carried out in order to determine how well an mQT performs in terms of: 1) reducing the EMG interference with different RC pairs used for trimming; 2) what range of trimming impedance is required for complete nulling of the EMG interference, which will give the optimum trimming configuration, i.e., parallel or series; 3) how trimming depends on the physiological conditions of the interface (i.e. saline conductivity, degree of imbalance in cuff) and the frequency of the EMG signal[19]; 4) how the amplitude of the EMG interference varies for a fixed trimming impedance value, and as the frequency changes. The following sections describe experiments done with electrodes in a saline-filled tank to explore the idea of balancing the QT passively. The tripolar electrodes were mounted in a book [Brindley, 1972], rather than a cuff, because we are interested in recording ENG from the intra-thecal nerve roots[20]. Fig. 3.8 shows a photo of the actual book electrode used in the experiments. If passive balancing is feasible, we should get low EMG interference with only one front-end amplifier and, therefore, reduced power consumption.

---

compared to $\Delta Z_s/Z_s$ (i.e. as R_c is in the MΩ range), then $CMRR_T \approx R_c/\Delta Z_s$. Therefore, setting the current bias resistors to values equal to those of fig. 3.9 (i.e. an R_{A2} of 50 MΩ is approximately equivalent to an R_c of 100 MΩ after a star-Δ transformation; c.f. [Casas and Pallas-Areny, 1997]) we can achieve a $CMRR_T > 80$ dB if the worst case ΔZ_s is 1 kΩ.

[19] As is shown later via the obtained results, the value of the trimming impedance Z_{trim} is frequency dependent.

[20] The limited amount of space available within the spinal canal makes the book more suitable than the cuff.
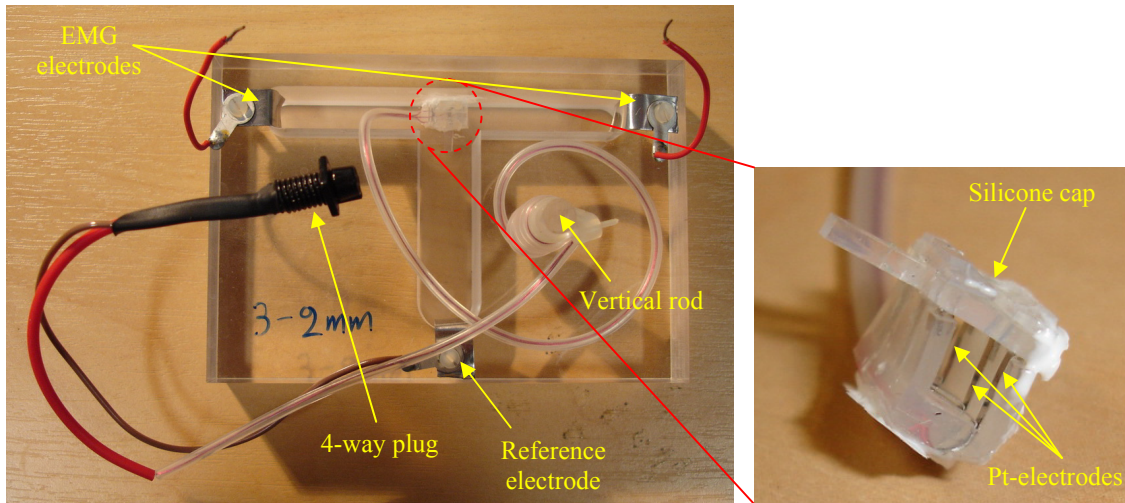
Figure 3.8: The T-shaped tank used as part of the saline experiments (c.f. §3.4.3). The EMG and the reference electrodes, as well as all the cabling are shown. The 3-wire copper cable is coated with medical grade silicone rubber. Insert: blown-up photo of a 1-slot book containing 3 rectangular U-shaped Pt-foil electrodes running along both side walls and bottom of the slot. The slot is closed with a cap. One or more nerve roots may be trapped in a single slot. The asymmetry in the position of the 3 electrodes can be clearly distinguished.

3.4.1 In-vitro realisation

Since the book electrode will be implanted in the spinal canal, the main matter that will come in contact with it may be the CSF. The conductivity of the human CSF according to [Duck, 1990, p. 171] for a frequency range of 0–10 kHz remains constant to a value of σ≈15.45 mS/cm (65 Ω·cm). Nonetheless, since arachnoiditis (i.e. inflammation of the arachnoid mater), nerve inflammation, and connective tissue growth covering the cuff electrode may take place after implantation, we expect the conductivity around the electrodes to change (i.e. rapid changes occur hours to days after implantation [Triantis, 2005a]). [Grill and Mortimer, 1994] demonstrated that the electrical properties of encapsulation tissue around implanted electrodes were functions of the tissue structure and biocompatibility of the implanted materials. The two workers conducted a series of in-vitro and in-vivo experiments in which they found that the resistivity of tissue formed around silicone rubber arrays (i.e. the material used to make our book) was up to 627 Ω·cm (1.595 mS/cm) independent of frequency from 10 Hz to 100 kHz. We decided also to perform experiments using a mid-range saline conductivity and, therefore, did tests with saline of three conductivities: 1.595 mS/cm, 15.45 mS/cm and an intermediate value of 8.52 mS/cm.

3.4.2 Method of removing interference

The principle of balancing the book and source impedances (for rejection of CM interference) of the QT configuration was demonstrated in the lab through a series of

experiments using a saline analogue to biological tissue of an appropriate conductivity[21]. In the experiments, the book (Finetech Medical Ltd.) was intentionally made imbalanced by offsetting the middle electrode in relation to the two outer electrodes (c.f. insert of fig. 3.9), so that the EMG interference source, generated by an audio transformer and applied externally between the ends of the book, produce a differential input to the amplifier. From measurements of the book's dimensions it was confirmed that the distance between electrodes 2 and 3 was more than the distance between electrodes 3 and 4, thus spoiling the symmetry of the tripole. According to the $R=\rho*(L/A)$ formula, where ρ is the electrical resistivity of the electrolyte, L is the separation length of the electrodes, and A is the cross-sectional area of the book, it is obvious that R is proportional to L (i.e. assuming uniform current density inside the book). Thus, measuring the electrode impedances with a multi-frequency LCR meter (Hewlett-Packard, model 4274A), it was found that impedance Z_{BC} was smaller than Z_{AB} (i.e. $R_{t1}>R_{t2}$ in fig. A.1) for all frequencies and all saline conductivities[22]. Therefore, compensating for this particular book imbalance, an appropriate value of impedance Z_{trim} should be added in the upper RHS arm of the bridge. As the mQT was realised and tested on a bench lash-up using discrete circuit components it was convenient for the balancing R and C to be external to the circuit, while the trimming configuration (i.e. series or parallel) was altered with the use of toggle switches whose arrangement was that of fig. 3.5.

Apart from the EMG artifacts, there is also CM interference present at the input of the amplifier that might need trimming. Hence, to reject CM interference the source impedances of the inputs to the amplifier should be made equal. The set-up in fig. 3.9 allows CM interference trimming by using the variable resistor shown, labelled as "CM trim", and neglecting any capacitive effects at the front-end. Since $R_t>R_o$ (c.f. Appendix A), and because the source impedance of the middle electrode is greater than the source impedance of the parallel combination of the two outer electrodes, CM interference can be removed by adding resistance in series to the pathway connecting the outer electrodes to the amplifier (i.e. inverting input in fig. 3.3). Nonetheless, the use of the CM trim can be avoided altogether if the amplifier's CMRR is high (i.e. >80 dB) as was shown by eqn. 3.3. Additionally, as suggested by [Donaldson et al., 2003], the CM interference can be reduced by adding capacitance at the amplifier input, which is connected to the outer electrodes with less noise penalty than adding resistance. Another way of reducing the effect of CM interference is to position the reference electrode in the vicinity of the book (e.g. the reference electrode can be placed at the outside body of the book). With the biasing components of fig. 3.9, the CM input impedance was high [Casas and Pallas-Areny, 1997], and CM trim was not necessary. However, supplying the amplifier bias current with resistors in a different configuration, and of much less resistance than 50 MΩ, trimming with this variable resistance was useful (c.f. §3.5.4). Finally, it should be mentioned that in the case where the use of the CM trim is needed, this will not influence the operation of the EMG trim, due to the high input impedance of the amplifier.

---

[21] The electrolytic conductor in this case was made of Na^+Cl^- solution (using deionised water; not buffered), which offers similar properties to fluids surrounding Pt-electrodes in-vivo.
[22] Outer electrodes open circuit, while assuming that $Z_{e1}=Z_{e3}$.

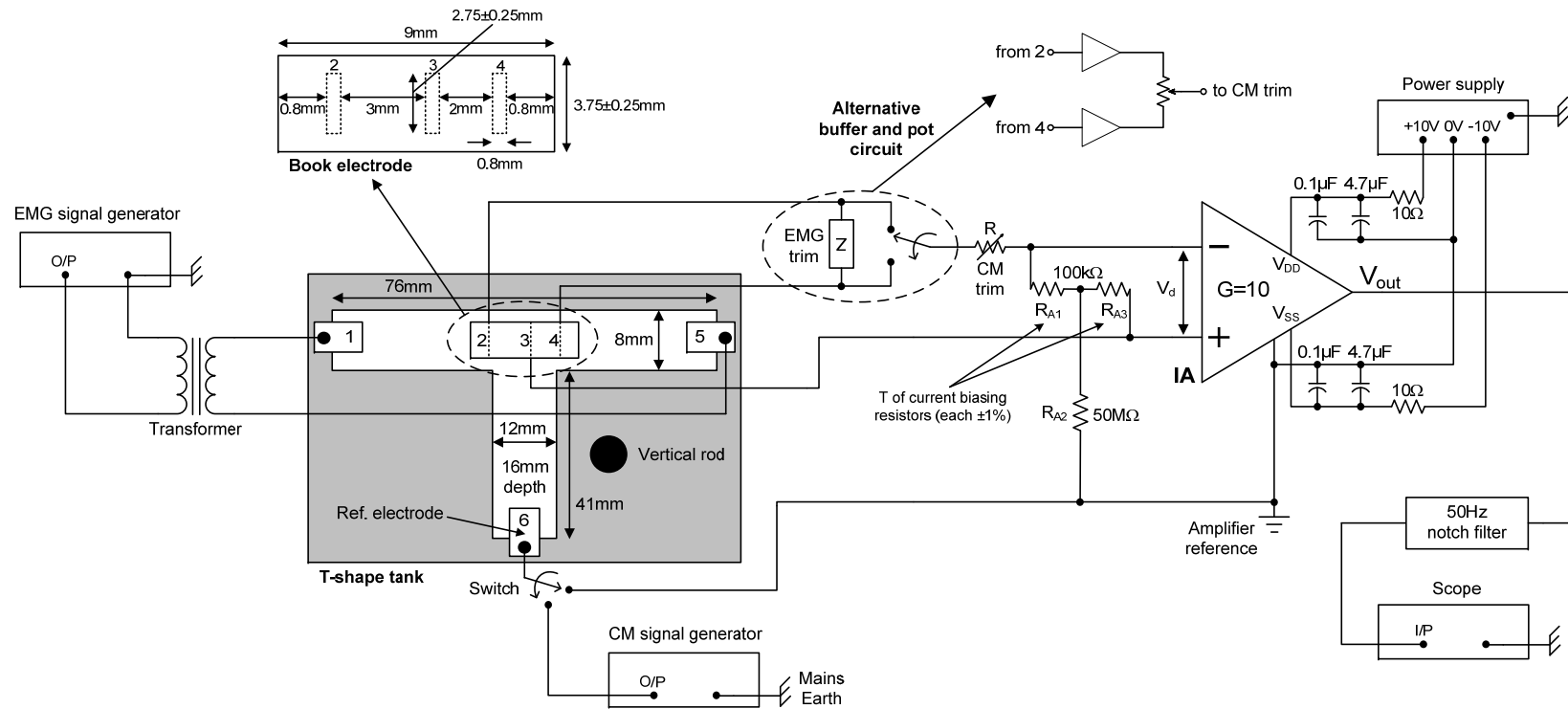Figure 3.9: The apparatus comprises a saline-filled T-shaped tank containing the book electrode, and three other electrodes (numbered 1, 5 and 6) to provide the EMG and CM currents. The instrumentation amplifier is an AMP01 of gain 10 with biasing as shown. The book was purposely made unsymmetrical for the purposes of the experiment (see insert for bottom lateral cut view and approximate dimensions of a tripolar book electrode).

3.4.3 Experimental set-up

The apparatus used for carrying out the experiments is schematically shown in fig. 3.9 with its main component, the mQT amplifier, implemented on a copper strip board together with any other components necessary for its operation (e.g. biasing resistors). The book was fixed at the bottom of a T-shaped Perspex tank[23] made in our workshop, which has an approximate capacity of 20 ml, while the low-resistance enamelled copper wires coming from the 3 Pt-electrodes of the book were strapped to a vertical rod attached to the tank for extra stability. At the 3 ends of the T-shaped tank are 3 stainless steel sheets (7 mm x 20 mm), each fixed to the tank with a nylon screw to avoid corrosion. Two of those electrodes were used to provide the EMG interference (i.e. I_{INT} of fig. 3.1) and the third, positioned away from the interference source electrodes and at the end of the perpendicular arm of the tank, was used as the reference electrode. The reference electrode was used in two ways: 1) it is connected to the amplifier 0 V power supply line (actually mains earth) to define the potential in the saline relative to the amplifier[24], and 2) as means of injecting another signal into the tank in order to be able to study the effect of CM interference. An audio transformer (Oxford Electrical Products Ltd., Part no. A262A1E) was used to provide, via its secondary winding, the interference current in isolation (i.e. a floating EMG input) allowing for a reference electrode to be defined elsewhere in the tank. The book electrodes were connected in a mQT configuration to a differential instrumentation amplifier (Analog Devices, AMP01), while two external variable resistance and capacitance boxes (RS Components Ltd.) were used for providing the trimming EMG impedance to the amplifier's front-end (c.f. fig. 3.9, labelled as "EMG trim"). A 50 Hz notch filter was added to the output of the amplifier to reduce mains interference, and care was taken with decoupling to remove high frequency interference from the supply lines[25]. The amplifier was DC-coupled and had its pass-band limited to about 23 kHz to avoid amplification of high frequency interference harmonics by using an external variable filter (Kemo Ltd., 0.01 Hz–100 kHz dual variable filter type VBF/8). The output signal from the instrumentation amplifier was monitored by a two-channel digital oscilloscope (Agilent mixed-signal oscilloscope, model 54622D) with some averaging used. Finally, any DC offset present at the output of the amplifier, due to electrode potential mismatch, was insignificant (i.e. did not saturate the amplifier) and was removed by the appropriate oscilloscope function.

In terms of dealing with electromagnetic interference during the experiments, each key component of the system, namely: the audio transformer, the T-shaped tank, and the copper strip board was placed in its own metallic enclosure to minimise any interference pick-up from the laboratory surroundings. All cable connections apart from those used to connect: a) the EMG signal generator to the primary of the transformer, b) the trimming

---

[23] The outer body of the book was glued to the T-shaped tank by using one-component silicone sealant (Dow Corning, type 734), to prevent it moving within the tank and influencing the results (c.f. 2nd paragraph of §3.3.1).

[24] This is required otherwise the recording electrodes connected to the amplifier are left floating.

[25] A low-impedance path to ground was formed by using a 4.7 μF tantalum in parallel with a 0.1 μF ceramic capacitor. This is because tantalum capacitors have lower reactance than ceramic at low frequencies.

resistance and capacitance boxes to the amplifier front-end, and c) the book and reference electrodes to the amplifier, were implemented using a two-core twisted co-axial cable, which was appropriately screened. Conversely, a) and b) were connected with a short 4 mm lead wire and c) with a 4-way connector having twisted wires. Care was given not to introduce an earth loop[26], while the enclosure lids were connected to the metallic body with braid copper wire to ensure proper screening. The external boxes that provided the trimming R and C were also screened through their provided earth terminals.

Before conducting an experiment, the tank and book electrodes were thoroughly cleaned with about 500 ml of deionised water, while the EMG source and reference electrodes (i.e. numbered as 1, 5 and 6 in fig. 3.9) were separately cleaned with isopropyl alcohol to keep them free of any contamination, which could then pass to the electrolyte. For each experiment the voltage drop across the book (i.e. V_{AC}, measured with an oscilloscope, reference electrode floating) was adjusted to 30 mV pk-pk at 2 kHz, which is considered low enough in terms of the linear operation of the electrodes at the 500 Hz to 10 kHz bandwidth of interest (c.f. §4.2). All measurements reported below were taken while the reference electrode was connected to the amplifier reference (mains earth) with no applied CM interference, except otherwise noted. Electrolysis was not observed during the experiments and no bubbles, or any other form of evident contamination, was present in the tank.

3.4.4 QT vs. buffered arrangement

In the same experiments, two buffers (National Semiconductor, LF356) with very high input impedance (i.e. 10 TΩ intrinsic impedance) were used together with a potentiometer at the amplifier front-end, instead of the conventional trimming impedance (c.f. insert of fig. 3.9). This was done to lessen the effect of the impedances, Z_{e1} and Z_{e3}, of the two outer electrodes, thus removing the need of a reactive term for nulling the EMG interference. Since now the effect of the electrode impedances should be small, a 10 kΩ potentiometer with no reactive components was arranged for nulling. Additionally, as this configuration closely resembles in principle the TT, it will allow us to perform a comparison against the mQT in terms of the effect of the electrode reactance on the two configurations. Results of this study are shown next.

3.5 In-vitro results

3.5.1 Balance with buffered potentiometer

To observe the imbalance in the axial resistances of the book (i.e. LHS of bridge of fig. 3.3), the high input impedance buffers were used with a 10 kΩ potentiometer. For all conductivities, the potentiometer was adjusted at each frequency to minimise the

---

[26] An earth or ground loop is formed when two points that are supposed to be at the same potential (e.g. 0 V) are actually at different potentials. Hence, a potential difference exists between the two points and unwanted current flows through, which can cause unwanted feedback and possibly induce interference into the system such as CM [Webster, 2010, p. 255].

interference. The results are plotted in fig. 3.10. The actual value of imbalance as a function of frequency is not very important for now, however, we see that for the lowest 1.595 mS/cm saline conductivity curve, imbalance is about 3% and is not very frequency-dependent[27]. This was something we anticipated, since saline is a uniform conductor independent of frequency, and according to [Grill and Mortimer, 1994], this is also valid for tissue formed around silicone rubber electrode arrays. The measured 3% figure can be compared to the geometric asymmetry of the book electrodes shown in the insert of fig. 3.9. The book was made with the centre electrode off the midline by 0.5 mm or 7.6% off the centre between the midline of the outer electrodes (i.e. [0.5−(2.8/6.6)]*100≈7.6%). It is interesting and helpful that electrical imbalance varies more slowly than geometric asymmetry.

The fact that the effect of the electrode impedance is diminished when using the TT is important in neutralising interference, however, the graph of fig. 3.10 clearly illustrates two things: a) that cuff balance and therefore complete EMG neutralisation cannot be achieved with only an ohmic term despite the high input impedance that each electrode sees when the TT is used, and b) imbalance is – although weakly – still frequency depended for all saline conductivities. The implications of this find are discussed more in §3.6.1.
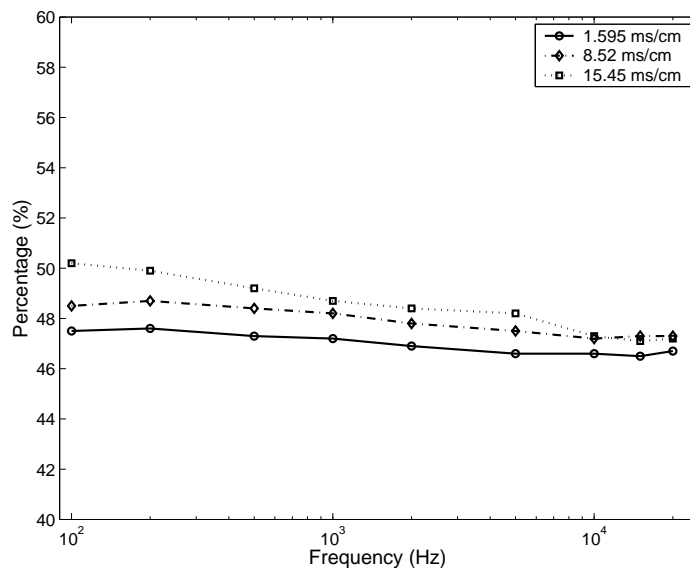
Figure 3.10: Change in book balance with frequency using high input impedance buffers. The potentiometer was reset for each new saline conductivity.

---

[27] Conversely, the balance curve for the highest conductivity changes by about 2% across the 100 Hz to 20 kHz bandwidth because the effect of the electrode impedance reduces with conductivity (i.e. % imbalance becomes smaller), with the capacitive term of the electrode interface becoming more significant in comparison to lower conductivities. At high frequencies, however, that term reduces which is probably why balance tends to a value similar to that of the other conductivities.

3.5.2 Null impedances

After reverting to the unbuffered circuit, the balance was adjusted as close to the null as possible using the resistance and capacitance boxes for all conductivities, with series or parallel connection, and at the frequencies 100, 200, 500 Hz, 1, 2, 5, 10, 15, and 20 kHz. The extreme values for each conductivity and connection are presented in table 3.2. Both trimming R and C were found to decrease with increasing frequency, irrespective of the model used (i.e. series or parallel), meaning that the electrode interface capacitance and resistance follow the same trend (c.f. §4.2.1.2). The impedances were calculated and are plotted in fig. 3.11. As expected, the impedances are nearly the same, whether series or parallel-connected, but with larger differences at low frequencies (i.e. most probably due to the difficulty in finding a null with the scope). It is also evident that increasing the conductivity of the saline, results in the reduction of the impedances of the book electrodes and, thus, a higher value of trimming capacitor is then required at the front-end in order to compensate for the tripole imbalance. Conversely, the required value of the trimming resistor is reduced as saline conductivity increases.

Conductivity (mS/cm)	Extreme values	Series RC		Parallel RC	
		R (Ω)	C (nF)	R (Ω)	C (nF)
1.595	Lowest	23	138	150	121
	Highest	2160	686	6570	299
8.52	Lowest	15	191	136	161
	Highest	1280	5645	1640	324
15.45	Lowest	13	223	107	189
	Highest	615	3366	903	400

Table 3.2: The range of values of the series and parallel RC for obtaining a null for the three saline conductivities.
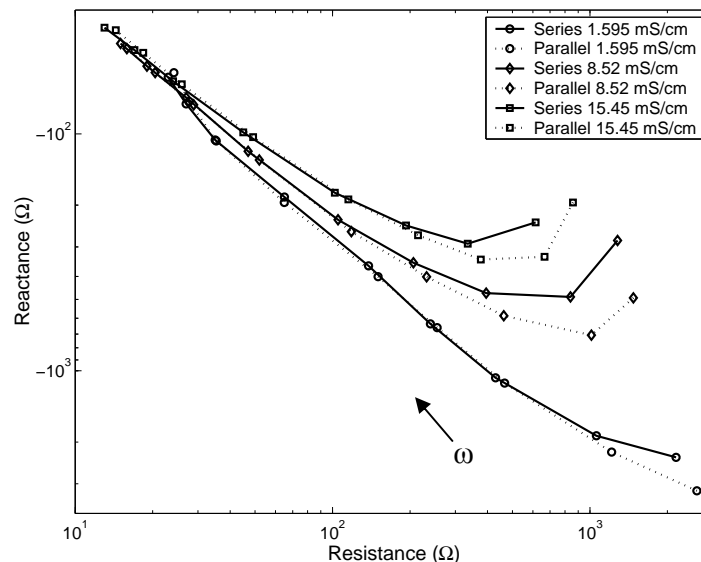
Figure 3.11: Null impedance measured with series and parallel RC at three saline conductivities. Notice that at high frequencies the trimming impedance decreases (i.e. imbalance gets smaller), becoming almost identical for all saline conductivities.

The physical size of the trimming components can be an issue in terms of an integrated circuit (IC) realisation of the technique, especially when dealing with nF size capacitors. As the technique is developed further in the following chapters, it is pointless to discuss layout area issues here. This will be possible once the neutralisation technique has been finalised (c.f. Chapter 5) and the values of the trimming components are once again found through experimental procedures.

3.5.3 Amplitude of interference

The pk-pk amplitudes were measured at all frequencies at the amplifier output for the following four trimming conditions:

- No additional trimming components (c.f. table 3.1, control bits: 0XX);
- Nulled at 2 kHz (mid-band) with resistance and capacitance in parallel (i.e. control bits: 100);
- Nulled at 2 kHz with resistance and capacitance in series (i.e. control bits: 110);
- Nulled at 200 Hz with resistance and capacitance in parallel.
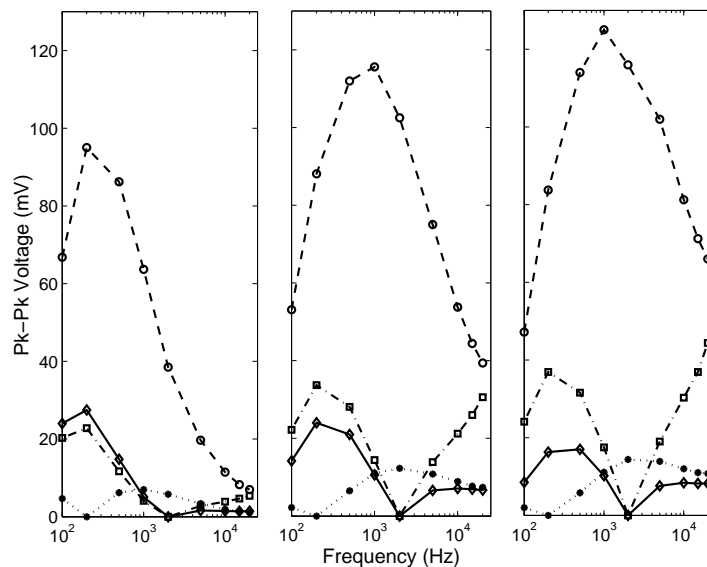
Figure 3.12: Output voltage versus frequency for saline conductivities of 1.595, 8.52 and 15.45 mS/cm, from left to right. Symbols: ○ no trim, ◊ parallel trim at 2 kHz, □ series trim at 2 kHz, * parallel trim at 200 Hz.

When nulled at 2 kHz, parallel connection is generally better than series, as fig. 3.12 illustrates. The least interference occurs when trimming is done at low frequency (200 Hz), where the worst-frequency amplitude is about ten times less than without trimming. This is convenient since EMG is a low frequency phenomenon and therefore balancing the electrodes should be done at the bottom of the range. Even in the case where the EMG interference cannot be completely neutralised, but instead minimised up to a certain extend at the ENG band, the desired information from the nerve signal might still be possible to extract depending on the application (i.e. location of implanted electrodes, maximum amplitude of ENG signal recorded from target nerve fibres, amount of

interference present at that location, etc.) [28]. Data obtained with 3 different saline conductivities clearly reveals the same general trend while it shows that the parallel RC fits better to the frequency response of the electrode-electrolyte interface impedance than the series one (hence the lower EMG breakthrough as frequency changes). Why the parallel RC is better than the series can be attributed to the impedance properties of the electrode-electrolyte interface and will become apparent on the next chapter, where the theory of modelling the impedance of metallic electrodes is presented.

3.5.4 CM interference reduction

The T network of resistors proposed by [Casas and Pallas-Areny, 1997] was used to provide bias current to the amplifier (c.f. fig. 3.9), thus improving its CMRR, while keeping thermal noise to a low level. The extent of improvement was measured against the parallel current biasing resistors (1 MΩ each) and it was found that the T network improved the CMRR of the AMP01 by 15 to 35 dB in the 100 Hz to 2 kHz band (i.e. the improvement was less at higher frequencies), when a source resistance of 1 kΩ was introduced in one of the input pathways.
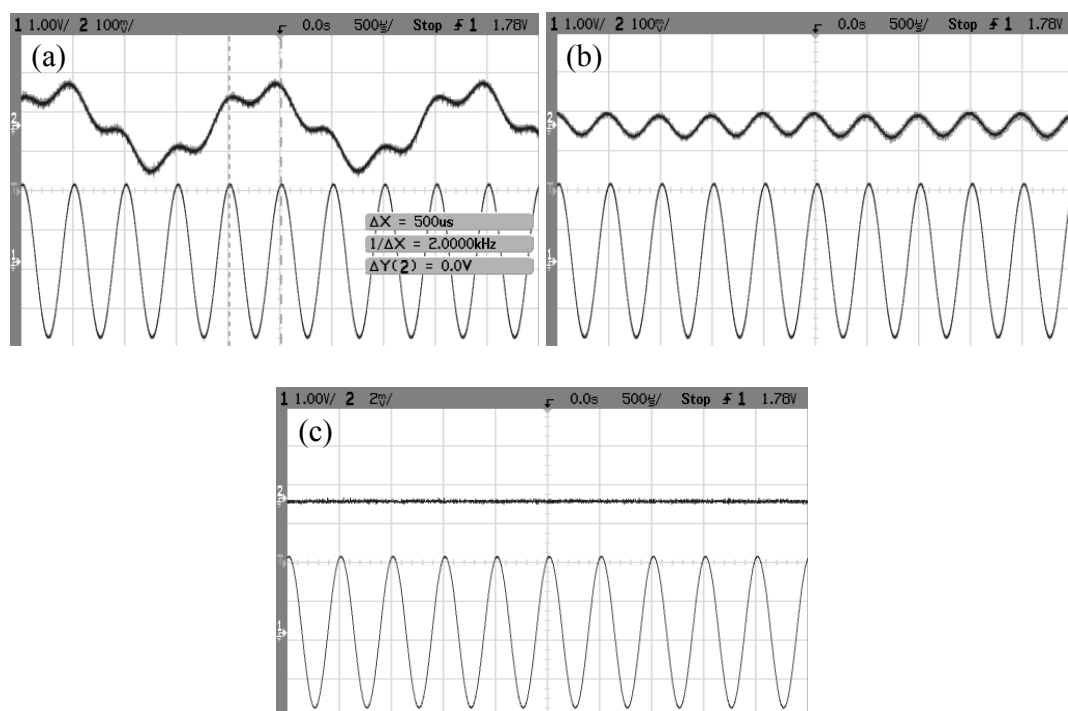
Figure 3.13: Removing CM (500 Hz) and unbalanced-tripole interference (2 kHz) from the amplifier output. (a) Lower trace is 2 kHz input to the transformer; top trace is amplifier output before adjustment. (b) After nulling the CM interference. (c) After balancing the tripole impedances.

---

[28] As an example, the conventional QT configuration has been successfully used in the past with only employing high-order filtering and blanking techniques for removing EMG interference and successfully detecting the ENG activity in a foot-drop correction implant [Haugland and Sinkjaer, 1995].

Fig. 3.13 demonstrates the removal of interference due to CM and tripole imbalance at the amplifier output. The CM interference was a sinusoidal signal of 500 Hz which was injected into the T-shaped tank via the reference electrode, whilst two 1 MΩ parallel resistors (each connected from one input of the amplifier to mains earth) were used to provide bias current to the amplifier. CM interference was removed using a potentiometer connected as a series variable resistor to the parallel connected outer electrodes (c.f. fig. 3.2). Reduction of CM interference was possible in this case, since for this particular book and laboratory set-up, the reactive components of the three electrode impedances and cabling were not significant and satisfactory balance of the source impedances could be achieved by adding a resistive term only.

3.6 Discussion of experimental results

3.6.1 Usefulness of the AT

The buffer measurements (fig. 3.10) are relevant to the TT configuration. The high input impedance of the amplifier diminishes the effect of the electrode impedance and the imbalance is only weakly frequency-dependent. A 3% imbalance as obtained from the buffer measurements (i.e. for 1.595 mS/cm), when there is 30 mV across the outer electrodes, corresponds to 9 mV at the amplifier output which is similar to the worst-frequency amplitudes for the curves in fig. 3.12 when trimming is performed at 200 Hz. The attraction of the automatically balanced TT amplifier (i.e. the AT; c.f. §2.3.3.3) is that a constant imbalance can be cancelled by adjusting the amplifier gains. However, the fact that the curves in fig. 3.10 are not quite frequency-independent shows the limitation of the method: the curve for the highest conductivity changes by about 2% across the frequency range, and so when the gains have settled (to values that will depend on the interference spectrum), interference at some frequencies will still appear (i.e. when multiple EMG sources of different frequency are present at the interface). This is what in-vivo experiments with the AT in rabbits have shown [Triantis et al., 2005b]: when there were two sources of interference present (i.e. in that case the stimulus artifact and an EMG from a nearby muscle), the AT could not minimise both but settle at a gain ratio between the gain ratios that minimised each source alone. The view on the matter, as expressed by [Triantis et al., 2005b], was that the two interference signals were a result of a different cuff imbalance due to the presence of end-effects and inadequancy of the small-bore approximation (c.f. §3.3.1). If we hypothesise the validity of this statement and take into account that imbalance in the cuff with the TT is not so frequency independent as fig. 3.10 illustrates, then it is obvious that both aforementioned factors (i.e. end-effects and frequency dependence of the source impedance) may have a role on tripole imbalance, with interference appearing at the amplifier output.

[Cirmirakis et al., 2010] investigated the effect of changing the applied EMG field in a set-up very similar to that of fig. 3.9. The longitudinal field effect was compared to two amplifier configurations: the mQT and the adjustable TT (aTT) [29]. Two different

---

[29] A TT configuration which was adjusted manually, as opposed to the AT which is automatic.

interfering fields were applied [30] by changing the position of the current injecting electrodes along the top arm of the T-shaped tank, resulting in: a) a symmetrical, solonoidal and b) an unsymmetrical, non-solonoidal electric field applied across the ends of the cuff electrodes. The results were unfavourable for the aTT, showing that if the aTT is nulled in one field, it may produce greater interference breakthrough in another field than the mQT. This result might be due to the effect of screening of tissue inside the cuff that the TT lacks.

3.6.2 Series or parallel trimming for the QT?

The fact that the trimming impedance depends on the frequency of the interference signal has a significant impact when multiple interference sources, of different frequencies, are present at the interface. Hence, finding a trimming impedance that will result in the minimisation of the EMG interference, across the ENG band, is important. Ideally the trimming network would have an impedance-frequency characteristic the same as that measured for the appropriate saline conductivity (i.e. fig. 3.11). The impedance-frequency characteristics for the series RC and parallel RC connections are shown in fig. 3.14, superimposed on the experimental null impedance curves for 8.52 mS/cm. The faint curves show the impedance of the particular RC pairs that gave the nulls at the spot frequencies shown, and while their frequencies are swept. For the series pairs (fig. 3.14a) the impedance curves are vertical lines, for the parallel pairs (fig. 3.14b) they are parts of semi-circles (on linear axes).

The best fit of the RC pair to the null impedance occurs for the parallel combination, nulled at low frequency. This is illustrated by fig. 3.15, which shows the semi-circle of the calculated RC pair and the straighter curve of the electrode null impedance versus frequency, again for 8.52 mS/cm. It is obvious that RC in parallel changes with frequency more like the electrode impedance than the series combination. It, thus, appears that the parallel connection should be superior and, in order to fit the impedance characteristic, nulling should be done at low frequencies. Thus, the amplitude results shown in fig. 3.12 are as expected. Moreover, it is most likely that apart from the series/parallel RC pair, there exist other combinations of passive components which can fit better the characteristic electrode-electrolyte interface impedance, throughout the ENG band. Subsequently, mimicking the frequency-dependence of the electrode impedance with a passive network that will adapt to its frequency response, no tuning would be necessary for balancing the tripole. This idea is further explored in Chapter 5.

At this point one practical difficulty should be recognised. As the imbalance gets smaller, the impedance that must be added to reach the null must be made smaller. This is easily arranged for the resistance but for the reactance, it implies increasing capacitance, tending toward infinity as the reactance tends to zero, and clearly this will be limited by the space available for the trim capacitors.

---

[30] The applied interference signal was a continuous EMG signal recorded with surface electrodes above the medial hamstrings muscles, with 1 kHz sampling rate.

That low frequency nulling is optimum, is a satisfactory discovery, because EMG and ECG interference is mostly at the low end of the ENG band and therefore nulling in their frequency range is appropriate. For either configuration (i.e. series or parallel), the additional resistance will add noise and since the signal-to-noise ratio performance is so poor [Nikolic et al., 1994], the effect of trimming on the noise performance needs further investigation.
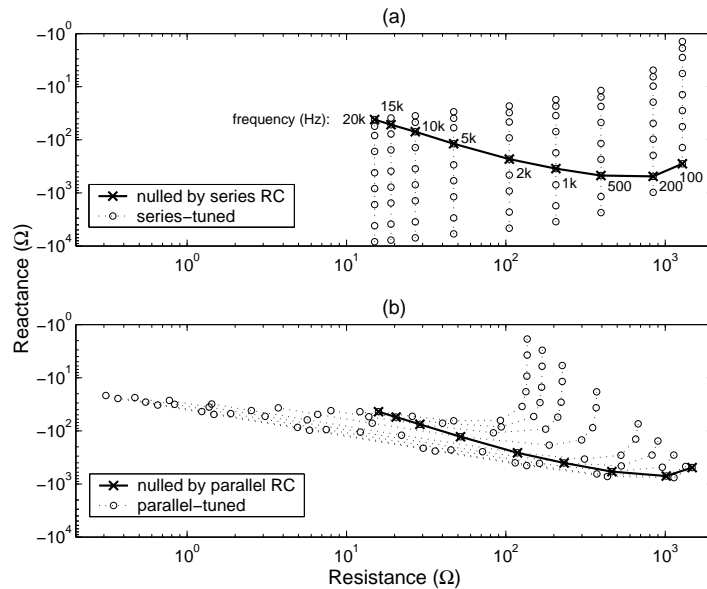
Figure 3.14: Heavy lines show impedances to null the tripole at frequencies shown: (a) series trim; (b) parallel trim. Feint lines show how the impedance of the trim resistor-capacitor pair varies with frequency (at same spot frequencies as for measurement).
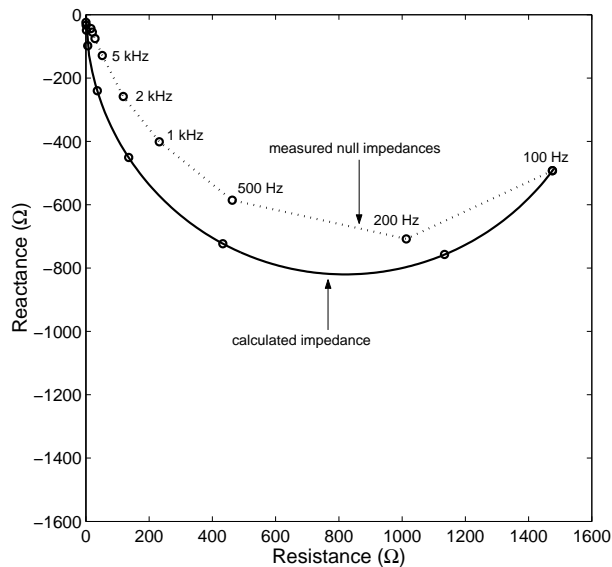
Figure 3.15: Comparison of the change in electrode null impedance (broken line) with impedance of the RC pair that gave null at 100 Hz. The latter curve is part of a circle.

Concluding, an IC version of a tripolar neural recording amplifier employing the here presented passive neutralisation technique is reported in [Demosthenous et al., 2007] and [Demosthenous et al., 2008]. The particular IC was fabricated in a 3 V 0.35 μm BiCMOS technology, occupies an area of 1.5 mm^2, and consumes about 1.4 mW when configured to detect sub-microvolt neural signals.

3.7 Summary

In this chapter the reader was presented with an alternative neural recording configuration based on the conventional QT, which adds the ability to passively remove EMG and CM interference. The technique is suitable for an application that requires minimal current consumption from the amplifier. The analogy between the tripolar cuff or book and the Wheatstone bridge is helpful. This analogy is approximate; a complicated situation with ionic currents flowing in an electric field is here represented by a circuit and, following other researchers, the problem was approximated by considering that the current flows through the lumen as if through two resistances. Fig. 3.10 shows that this is quite a good approximation, but not perfect, and the deviation from the ideal limits the ability of the AT to neutralise all the external interference. We have shown that imbalance in the tripole can be significantly reduced by using passive components, as if the tripole were a Wheatstone bridge that can be balanced by matching the ratios of the two arms. Because the impedance of the electrodes does not change with frequency exactly like a parallel RC, interference is not entirely neutralised but with a tripole that was intentionally made imbalanced, by an amount measured as 3%, it is possible to reduce the interference about ten times at all frequencies, and remove it completely at a chosen frequency in the interfering spectrum. The method requires resistors and capacitors that can be selected and which must be set occasionally as the tissue grows round the electrodes. As EMG is a low-frequency phenomenon it is important to balance the electrodes at the bottom of the ENG range to get the best improvement. The argument presented in §3.6.2 suggests that the variable resistance and variable capacitance should always be in a parallel rather than in a series combination for use at all frequencies, connected to one or other of the outer electrodes.

CHAPTER
FOUR

Impedance Modelling of Metallic Electrodes

4.1 Introduction

From the obtained results of the mQT in Chapter 3 it is apparent that the trimming impedance of our Pt recording electrodes does not change with frequency exactly like a parallel RC. Thus, EMG interference is not entirely neutralised, nonetheless, it can be sufficiently reduced about ten times at all frequencies and removed completely at a chosen frequency in the interfering spectrum. Finding a "universal" trimming impedance that would adapt to the recording electrodes' frequency response, throughout the ENG band, could make the mQT more effective. The motivation is based on the following fact: as there are models that can mimic the frequency response of metal electrodes it should be possible, by constructing a trimming network of an equivalent arrangement to the impedance of electrodes, to fit the characteristic neutralisation impedance[1] and ideally require no adjustment for removing the EMG.

This chapter is devoted to laying out the foundation for the design of the (frequency) adaptive neutralisation recording system, which is discussed in detail in Chapter 5. At first, the reader is introduced to the basic modelling theory of metal electrodes. The discussion, although generalised, is in terms of a recording perspective, i.e., for electrodes used to register the neural signal and not electrodes meant for stimulation. The approach is made in a pure theoretical level based upon electrical equivalent electrode circuit models and their mathematical representations, which are verified when necessary by simulated results having frequency as the independent variable (i.e. through complex impedance and Bode plots) using Matlab™. This chapter by no means claims a full and complete insight into the theory of metal electrodes; besides this would be nearly impossible and beyond the scope of this thesis. However, what it does offer, is a good introduction to metal electrodes and how they can be appropriately modelled. This argument is further strengthened by a real-world example of electrode impedance data fitting at the end of the chapter.

4.2 Impedance of metallic electrodes

The impedance of a single (i.e. monopolar) metallic electrode conductor (e.g. Pt or Pt-Ir) in contact with a volume electrolytic conductor – either fluid (e.g. saline solution), or

---

[1] In this case the impedance required to balance the recording tripole.

solid (e.g. body tissue) – gives rise to the so-called electrode-electrolyte interface; a result of electrochemical reactions due to the ion-electron exchange[2] at the interface. In an attempt to accurately explain and characterise the electrode-electrolyte interface and each different process taking place in it, many models have been devised that simulate the observed electrode behaviour. It is common to model the electrode-electrolyte interface impedance by a 4-element RC network like that depicted in fig. 4.1 [Pollak, 1974a; Weinman and Mahler, 1964]. In particular, this consists of two parts; the impedance of the active (or working) electrode-electrolyte interface, and the resistance of the environmental conductor, both combined into the (overall) electrode impedance Z_e. Included in this model for reasons of completeness is the dc "half-cell"[3] potential developed at the electrode-electrolyte interface of a single electrode under equilibrium conditions (i.e. no influence of constant electric current at the interface). The half-cell potential – the same as the Helmholtz potential difference developed between the electrode and the electrolyte, introduced later on – depends on the composition of the electrode metal and the electrolyte (i.e. composition, concentration, temperature), and for alternating current across the interface it is convenient to neglect it [Mayer et al., 1992]. The difference between the electrode potential E_{ele} and the half-cell potential E_{hc} under the influence of a dc or faradaic current[4], i_{dc}, is known as the "overpotential" η.
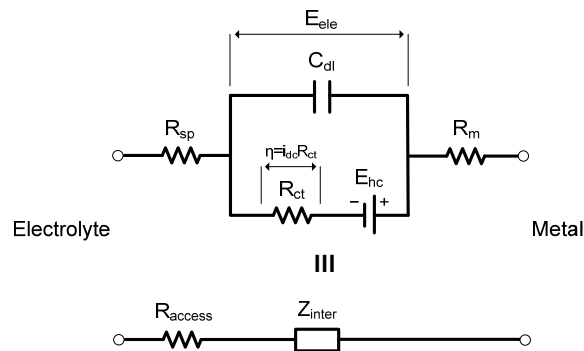
Figure 4.1: Small-signal electrical circuit for describing the electrochemical interface impedance of metallic electrodes. An alternative representation of the model where the access resistance $R_{access}=R_{sp}+R_m$ and the interface impedance $Z_{inter}=C_{dl}//R_{ct}$ is also shown. The overall electrode impedance is $Z_e=R_{access}+Z_{inter}$. When i_{dc} is applied to the interface $E_{ele}=E_{hc}+\eta$, while under equilibrium conditions, $E_{ele}=E_{hc}$.

Each of these elements represents a different physical process at the interface, with vastly different characteristics. However, owing to its simplicity, it is important to signify that this model does not take into account complex mechanisms like the electrolysis[5] of the

---

[2] In the electrode and the connecting lead, electrical charge is carried by electrons, whereas in the electrolyte and in the human body, charge is carried by ions (i.e. atoms that bear an electric charge) [McAdams, 2006, p. 123].
[3] Often termed as "equilibrium" or "reversible" potential in the literature. In this work we adapt the former.
[4] A current creating a reaction at an electrode according to Faraday's law of electrolysis is called a faradaic current [Grimnes and Martinsen, 2000, p. 23].
[5] A chemical decomposition reaction produced by passing an electric current through a solution containing ionic materials that are to be separated. Electrolysis is an irreversible faradaic reaction (i.e. cannot be

electrolyte or the corrosion of the electrode, and assumes linear operation[6] of the working electrode under test. The overall electrode impedance Z_e (i.e. $R_{access}+Z_{inter}$) is the result of the combined action of the equivalent network elements[7] and is given by:

$$Z_e = R_{access} + \frac{R_{ct}}{1+\left(\omega R_{ct}C_{dl}\right)^2} - j\frac{\omega C_{dl}R_{ct}^2}{1+\left(\omega R_{ct}C_{dl}\right)^2} \qquad (4.1)$$
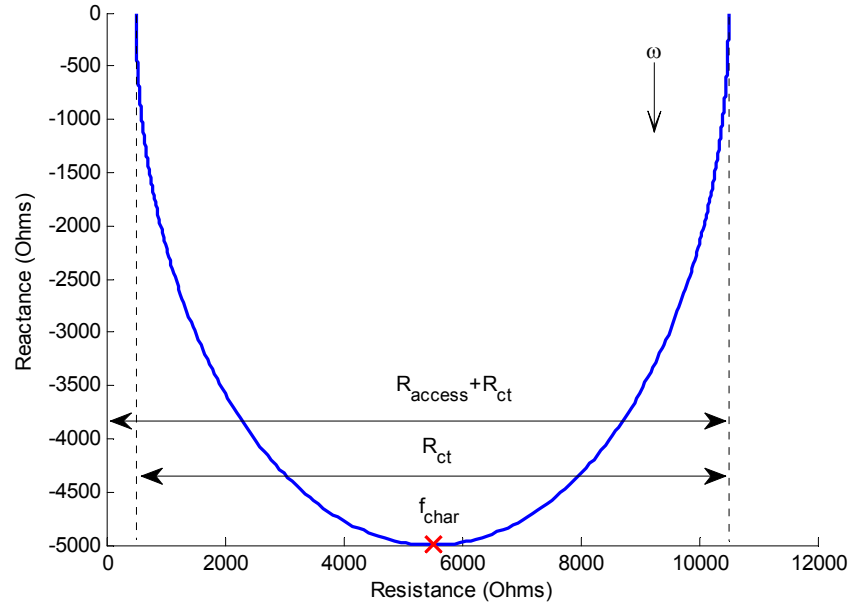
Figure 4.2: Nyquist plot of the electrode impedance of fig. 4.1 with R_{access}=500 Ω, C_{dl}=2 μF, and R_{ct}=10 kΩ simulated in Matlab™ from 1 mHz to 100 kHz. The characteristic frequency f_{char}=7.96 Hz is shown at the peak of the locus, where the negative imaginary impedance reaches a maximum value of $R_{ct}/2$.

---

reversed by changing the direction of current flow) that is harmful to surrounding tissue and therefore must be avoided.

[6] The equivalent circuit of fig. 4.1 for the small-signal impedance of metal bioelectrodes is, in general, non-applicable (i.e. the electrode-electrolyte interface behaves non-linearly) if the signal voltage across the interface due to dc current flow (i.e. the overpotential) exceeds a few hundred millivolts. Indeed, Ohm's law dictates that for a constant voltage applied across a – under conditions – linear electrode impedance Z_e, the resultant proportional current flowing through is assumed to obey the frequency dependence and limits of linearity of that impedance. This can explain the ambiguity in the exact value of the overpotential as [Pollak, 1974b; Pollak 1974c] defines it in the range of about 500 mV for a needle Pt electrode with a diameter of 0.25 mm in 0.9% NaCl solution, while [de Boer and van Oosterom, 1978] at about 700 mV, and [Onaral and Schwan, 1982] at about 120 mV for a 0.0855 cm^2 flat Pt electrode in 0.9% NaCl solution, and relatively independent of frequency and time with the onset of non-linearity defined at the 10% level. Knowing that its value will depend on the electrode type (i.e. area and material) and operational conditions (e.g. electrolyte conductivity and temperature), we can assume that any overpotential below 100 mV should be considered safe to use in terms of linear operation of the electrode.

[7] As per fig. 4.1 these elements are the charge transfer resistance R_{ct}, the double-layer capacitance C_{dl}, the spreading (or bulk) resistance R_{sp} in the electrolyte near the electrode, and the series resistance of the electrode conductor R_m (i.e. connecting wires and metallic part), which is often taken to be of negligible value.

The frequency response of the impedance described by eqn. 4.1 is a semicircular locus with its centre on the real axis (fig. 4.2). A characteristic frequency (eqn. 4.2) can be identified at the top of the semicircle for which the imaginary part of the impedance reaches a maximum[8], while it is also the frequency at which the real part is midway between the low and high frequency x-axis intercepts.

$$f_{char} = \left(2\pi R_{ct} C_{dl}\right)^{-1} \qquad (4.2)$$

It is also worth noting that varying the value of the double-layer capacitance C_{dl}, both the resistive as well as the reactive parts of the interface impedance are altered. Nonetheless, this does not affect the shape of the locus (i.e. the magnitude and phase frequency response of the impedance are obviously affected), however, to obtain the full semicircle one must ensure that $f_{max} \gg f_{char} \gg f_{min}$ (or $\omega_{max}\tau \gg 1 \gg f_{min}$) holds true[9].

In the next two paragraphs we are going to discuss the role of each element of the electrode-electrolyte circuit model of fig. 4.1 by breaking down the impedance in two parts: a) an interface impedance Z_{inter} with capacitive reactance, and b) a series electrolyte resistance R_{access}.

4.2.1 The interface impedance

The first part of the electrode-electrolyte impedance (i.e. capacitor C_{dl} and resistor R_{ct} in parallel) is determined by the rate of transport of charge carriers (i.e. ions in the electrolyte and electrons in the electrode) between the metal and the immediately adjacent layers of the electrolyte[10] [Pollak, 1974a]. This charge exchange arises from the re-arrangement of electrolyte ions at the interface [Fisher, 1996, p. 51]. In particular, a tendency exists for metal atoms M to lose n electrons and pass into the electrolyte as metal ions, M^{+n}, causing the electrode to become negatively charged with respect to the electrolyte; a reaction termed oxidation (i.e. loss of electrons). Similarly, some of the ions in solution M^{+n} take n electrons from the metal and deposit onto the electrode as metal atoms M, causing the electrode to become positively charged with respect to the electrolyte; a reaction termed reduction (i.e. gain of electrons). Conversely, in order for some of the ions in the electrolyte to transfer their charge across the interface, and close to the metal-liquid boundary, many must first diffuse to the electrode-electrolyte interface under the influence of electrostatic (force) attraction [McAdams, 2006, p. 123]. On the liquid side of the metal-liquid boundary, arriving or departing electrons produce a layer of charged particles (i.e. ions), which adsorb (i.e. stick) to the oppositely charged surface

---

[8] The reactance of the electrode interface reaches a maximum value equal to $-R_{ct}/2$, meaning that at the characteristic frequency f_{char} the reactance due to C_{dl} is $X_{dl}=-R_{ct}$ with a phase angle of $-45°$.

[9] Where the time constant $\tau=R_{ct}C_{dl}$ is the dielectric relaxation time of the basic material (i.e. here the interface).

[10] The tissue with its cell walls, membranes etc. is replaced by a homogeneous liquid electrolyte (i.e. contains no boundaries – apart from the walls of the container – or membranes) forming the non-metallic part of the interface. In the literature, for many purposes, this electrolyte can be adequately simulated by a 0.9% solution (9g/1000ml) of Na^+Cl^- (i.e. physiological or "normal" saline). The specific resistance of this solution is about 65 $\Omega\cdot$cm [de Boer and van Oosterom, 1978].

layer in the metal during a transient phase of re-organisation, forming what is known as a "double-layer"[11] at equilibrium [Pollak, 1974a]. As a consequence, there is a layer of positive or negative charge on the metal surface and a layer of equal but opposite charge on the electrolyte side of the interface, both separated by a certain distance with water molecules (i.e. dipoles) acting as an electrical insulator between both types of charges.

4.2.1.1 The double-layer interface model

Many models have been developed which aim to establish the nature of the processes at the double-layer interface. A simple model that attempts to describe these was first proposed by Helmholtz in 1853 and is shown in fig 4.3. At the creation of the electrode-electrolyte interface, ions are attracted or repelled within the electrolyte layer close to the electrode surface and an excess of either anions (i.e. negatively charged ions) or cations (i.e. positively charged ions) is built up[12]. The attracted ions are able to approach the electrode to a certain distance, the boundary of which is denoted by the outer Helmholtz plane (OHP), drawn through the centre of these ions. In this case, the excess charge on the electrode metal is balanced completely in solution by ions situated at the OHP, and the linear potential drop Φ_{ms} across the charge separation layer occurs totally over the region between the metal surface and the OHP. Voltages across the Helmholtz double-layer can reach magnitudes of about 1 V and for some metals even close to 2 V. Although, documenting other developed models of the double-layer interface is beyond the scope of this paragraph, it is important to note that Helmholtz's model was subsequently improved by others (i.e. Gouy-Chapman, Stern, and Grahame to name a few). Among several things, like the definition of the inner Helmholtz plane (IHP) due to specific adsorption[13], most importantly they stated that the potential drop Φ_{ms} is not entirely linear, decaying exponentially with some distance away from the electrode surface and, although it is mainly concentrated in the region closest to the electrode surface, some charge is now held further away from the electrode than the OHP, and into the bulk of the electrolyte (i.e. in the diffusion layer), resulting in an extended potential drop at the interface [Fisher, 1996, pp. 51-54].

---

[11] Considering the electrode and the electrolyte as two parallel layers of charge separated by a small fixed distance, the capacity of the double-layer is given by $C_{dl}=q/E$ where q is the charge accumulated at the interface and E is the steady-state electric field. According to [Bard and Faulkner, 2001, p. 12] C_{dl} is typically in the range of 10 to 40 $\mu F/cm^2$ because of the small double-layer thickness.

[12] Whether the charge on the metal electrode is negative or positive with respect to the electrolyte solution depends on the type of metal used (i.e. electrode material), the composition of the electrolyte, and if a current flows through the interface, to the potential applied across the interface [Bard and Faulkner, 2001, p. 12].

[13] The adsorption is termed "specific" since the interaction with the electrode surface occurs only for certain ions and is often unrelated to the charge on the ion with respect to the charge on the electrode (e.g. anions are adsorbed onto an electrode surface that already carriers a negative charge density). According to [Grimnes and Martinsen, 2000, p. 46] these species do not exchange electrons with the electrode surface but they change the surface charge density.

Following the potential drop Φ_{ms} across the interface, an energy barrier (i.e. steady-state electric field E[14]) between the two equal but oppositely charged layers prevents their instantaneous recombination. However, even at equilibrium (i.e. external current is zero), there is a constant interchange of electrons across the energy barrier due to the aforementioned electrochemical reactions (i.e. oxidation and reduction), giving rise to the so-called dc (or faradaic) "exchange current" [Pollak, 1974a]. These electron transfer reactions experience a charge transfer resistance, R_{ct}, which can be thought of as shunting the non-faradaic double-layer capacitance C_{dl}. Hence, the contribution of the double-layer to the total interface impedance can be represented by a capacitor in parallel with a leaky resistor, mimicking the charge transfer process[15] at the pseudo-capacitive metal-liquid interface (since by definition a capacitance is frequency and potential invariant).
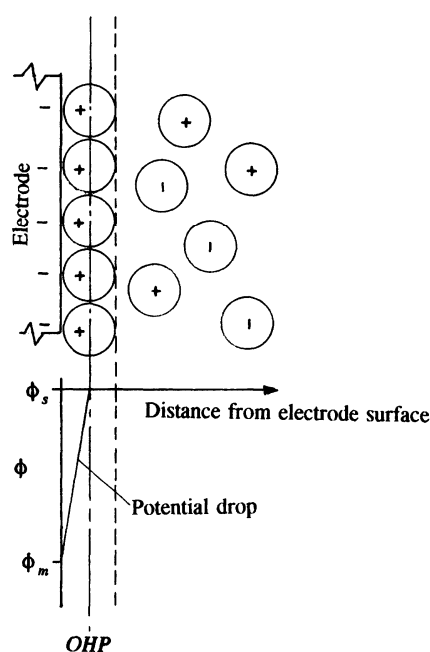
Figure 4.3: The Helmholtz electrical double-layer model. A negatively charged layer appears on one side of the interface (electrode), while positively charged ions are in majority on the opposite side (electrolyte) forming a rigid layer near the electrode. Generally, the metal is negative relative to the electrolyte. The linear potential drop Φ_{ms} across the interface, and the OHP are also shown. Conversely, the IHP, the water dipoles (i.e. dielectric), and the diffusion layer are not shown in this electrode-electrolyte interface model. Figure taken from [Fisher, 1996, p. 52].

From the above discussion we can conclude that the interface impedance Z_{inter} involves a pseudo-capacitive reactance whose R and C values are not constant, and among frequency, depend on several other factors. Those are discussed next.

---

[14] This electric field E is a result of the charge distribution at the double-layer with zero net current flow (i.e. the rate of exchange electron flow in either direction is on average the same) and is generated without the application of any external voltage.

[15] This process is a function of the electrode-electrolyte system and to some extent of the surface structure of the electrode [Pollak, 1974b]. Hence, a good electrode system, from an electrical point of view, will be characterised by a large value of exchange current or a low value of R_{ct}.

4.2.1.2 Sources of non-linearity effects at the interface

The magnitude of the double-layer capacitance depends on many factors. The most important ones (in no particular order) are the composition of the electrolyte (e.g. electrolyte conductivity; C_{dl} increases with higher electrolyte concentration), the type of the electrode conductor (i.e. material and surface condition; C_{dl} increases with surface roughness), frequency (i.e. C_{dl} decreases with increasing frequency), and temperature [Pollak, 1974a]. Another important source of non-linearity is the potential difference across the double-layer interface, and therefore the applied current density[16], since the amount of charge stored (i.e. charge density) in the double-layer region varies with the potential difference across it. The diffusion process[17], which at the lower Hz and sub-Hz frequency ranges and at dc is the main charge transport mechanism in the vicinity of the interface, affects the electrode impedance, because the rate at which the charge transfer reactions are proceeding depends on the concentration of electron donors and acceptors in the double-layer region. If this concentration changes (e.g. by applying an external EMF), the rate of charge transfer at a given potential difference will also change, altering the current (i.e. a new current flow results as opposed to equilibrium conditions) and consequently the impedance of the interface [Pollak, 1974a]. For recording electrodes this voltage dependence is usually small enough to be neglected but in stimulation, where the voltages applied and therefore the operating current densities are quite large, this may not necessarily be the case as distortion of the stimulus waveshape due to irreversible[18] electrochemical reactions may occur.

Shifting discussion to the second component of the interface impedance; the charge transfer resistance R_{ct}, its value for non-faradaic (or ideal) polarisable (or blocking) electrodes is relatively high[19]. As such, is important, because it significantly contributes to the highest impedance that an electrode-electrolyte interface can attain. The value of R_{ct} is high in the low frequency region and is very dependent on current density, decreasing with an increase in current density and frequency [Ragheb and Geddes, 1990; Pollak, 1974b; Mayer et al., 1992]. Other factors that affect the magnitude of the R_{ct} are

---

[16] Current density (typically measured as A/cm^2 for electrodes) is the electric current per unit area of cross section and as such it is inversely proportional to the electrode area. The principal difference between recording and stimulating electrodes is the operating current density and in the case of the double-layer capacitance, C_{dl} increases as the current density and electrode area are increased.

[17] The diffusion process of the interface has been assigned by [Pollak, 1974a] to an electrically equivalent part (i.e. a diffusion impedance Z_d) positioned in series with the interface impedance Z_{inter} of fig. 4.1 and with the author suggesting that this impedance can be modelled by an infinitely long RC transmission line.

[18] Forcing a current through the electrode-electrolyte interface causes electrochemical reactions between the metal and the electrolyte at the electrode surface which can be classified as reversible or irreversible (i.e. depending on the magnitude of the current). Irreversible reactions are undesirable as they decompose the electrode metal which might harm the tissue.

[19] The documented by [Mayer et al., 1992] value of R_{ct} for a $0.1\ cm^2$ area Pt and Pt-Ir electrodes (i.e. the electrode materials we are using) in a 0.9% NaCl at 25°C with zero current density, is 30.3 kΩ and 47.6 kΩ respectively. For reasons of comparison the same source reported a value of 345 kΩ for a 316 stainless steel electrode of equivalent area. Values of the zero current faradaic resistance R_{ct} for other electrode materials, for the same conditions, have been documented by [Geddes and Roeder, 2001] as: 3.82 kΩ for silver (bare), 9.22 kΩ for tin, 7.65 kΩ for nickel silver, 5.5 kΩ for copper (bare), and 17.7 kΩ for carbon (i.e. values have been scaled up for a $0.1\ cm^2$ area electrode).

the state of the electrode-electrolyte interface (i.e. electrolyte conductivity, temperature), the material type of electrode, and also according to [Pollak, 1974b; McAdams et al., 1995b] its surface condition (i.e. roughness) as this can increase the electrode effective area (i.e. R_{ct} decreases with increasing electrode area). It has additionally been suggested that R_{ct} is a major source of observed non-linearities (c.f. §4.3.3.2) at the interface [McAdams and Jossinet, 1994]. Finally, a method for measuring the charge transfer resistance of a single electrode-electrolyte interface is reported by [Mayer et al., 1992].

4.2.2 The electrolyte resistance

The last component of the electrode impedance Z_e is the sum resistance R_{access} of the electrode conductor R_m and the spreading resistance R_{sp} in the electrolyte near the electrode. As most often R_m is considered negligible due to its small value, R_{access} can be measured directly from the spreading resistance[20] between a working electrode and a surrounding sensing electrode. To aid our explanation of the spreading resistance we will refer to fig. 4.4, where a 2D representation of an actual 3D electrolytic cell is shown. Ignoring the reference electrode for now, for a spherical working electrode in contact with electrolyte (e.g. NaCl) and placed at some distance $\Delta r = r_2 - r_1$ from a spherical sensing ring electrode[21] of low impedance, the dc spreading resistance, if the electrolyte is considered to be purely resistive and homogenous (i.e. tissue is not), is given by:

$$R_{DC} = \frac{\rho l}{A} = \frac{\rho(r_2 - r_1)}{4\pi r^2} = \frac{\rho \Delta r}{4\pi r^2}$$

$$R_{12} = \int_{r_1}^{r_2} \frac{\rho}{4\pi r^2} \, dr = \frac{\rho}{4\pi}\left(\frac{1}{r_1} - \frac{1}{r_2}\right)$$

$$R_{sp} = \lim_{r_2 \to \infty} R_{12} = \frac{\rho}{4\pi r_1} = \frac{\rho}{2\sqrt{\pi A}} \qquad (4.3)$$

where ρ is the electrolyte resistivity, l and A the length and cross-sectional area of the conductor, while r_1 and r_2 are the radii of the spherical electrode and the measuring electrode of the cell (i.e. the sensing electrode). The region which determines the spreading resistance is located in the vicinity of the electrode tip surface in contact with the electrolyte, where the current density is high comparing to that of the electrode core. Therefore, the "thickness" of the (volume) conductor determining the spreading resistance is Δr. Integrating to find the resistance between surface radii r_1 and r_2, and taking the limit with respect to a supposedly very distant sensing electrode, we end up

---

[20] The resistance encountered by current spreading out onto the electrolyte volume.

[21] The separation distance of the working and sensing electrodes affects the value of R_{sp}. Thinking from an electrode perspective, although most of R_{sp} appears close to the surface of the working electrode the total R_{sp} depends, among other things, on the radius of the sphere electrode as well as the distance from the sensing electrode. If the latter is reduced, R_{sp} is also reduced since the spreading current is confined into a smaller space with respect to the sensing electrode, inside the volume conductor. Conversely, the current decreases linearly (i.e. resistance increases linearly, as will be discussed later) with increasing distance from the surface of the working electrode (i.e. assuming a semi-infinite homogenous volume conductor).

with eqn. 4.3. Thus, if the secondary electrode of the cell is very distant from the working electrode, the spreading resistance R_{sp} is dominated by the radius r_1 of the working electrode alone.
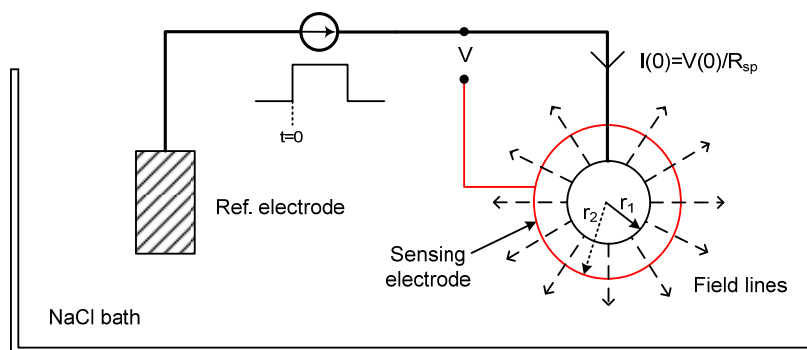

Figure 4.4: Spreading resistance R_{sp} of a sphere monopole with radius r_1 in contact with an electrolytic volume conductor. The intensity of the perpendicular spreading current vectors, denoted here by the field lines stemming from the electrode tip surface, depends on the magnitude of the current pulse I and the conductivity of the electrolyte. The sensing potential V is measured at t=0 using a bigger diameter spherical ring electrode placed near the working electrode tip surface (i.e. within a radius r_2). The equipotential lines developed when a current I enters the working electrode are not shown. The reference electrode is made bigger than the sphere electrode; typically >100 times as suggested by [Mayer et al., 1992].

A diagram illustrating the spreading resistance experimentally being measured between a spherical working electrode and a large reference electrode[22] (in order to form a closed circuit cell) is also combined in fig. 4.4. The measurement of the resistance has to be done in such a way so that the shunting effect of the double-layer capacitance C_{dl} overrides the influence of the dominant charge transfer resistance R_{ct}. Assuming the validity of the simple model of fig 4.1, it is possible to measure R_{sp} by applying a current pulse I(t) between the working electrode and the reference electrode while measuring the inflicted voltage drop V(t) at the vicinity of the working electrode tip surface, using a low impedance potential sensing ring electrode, at t=0[23]. To avoid confusion, as the sensing electrode is not part of the cell (i.e. no current can flow due to the high input impedance of the amplifier) radius r_2 here is drawn for illustration purposes only (i.e. to aid our explanation of the spreading resistance so $R_{12}=R_{sp}$ and calculated as if the sensing

---

[22] The working electrode must be made smaller with respect to the reference electrode so the effective cell impedance of the monopolar system is primarily due to the current flowing into the smaller electrode under test. With no current through the electrolytic cell, it does not matter whether the electrodes are large or small; the half-cell equilibrium potentials E_{hc} are the same (i.e. assuming the material is the same for both the working and reference electrodes). But with current flow, the current density and therefore the voltage drop will be much higher at the small electrode. Therefore, in general, the properties of the small electrode will dominate the measurement results. In the literature, reference electrodes that do not influence the impedance of a cell are called passive, neutral, or indifferent [Grimnes and Martinsen, 2000, p. 39].
[23] At t=0 the double-layer capacitance C_{dl} has not been charged and therefore has not developed a potential drop across it, essentially acting as a shunt. In reality, however, the resultant R_{sp} value obtained using the aforementioned measuring technique is based on the simplistic model of fig. 4.1 and therefore will not be entirely accurate (i.e. the voltage drop measured at t=0 might not only be due to R_{sp} but also due to some other non-faradaic process).

electrode was a spherical reference ring electrode surrounding the working electrode with the volume conductor in between). For reasons of completeness, another way of measuring R_{sp} would have been to inject a high-frequency current, measure the inflicted voltage drop between the working and reference electrodes with a high-input impedance differential amplifier, and obtain R_{sp} by calculating the asymptotic high-frequency impedance which should correspond to eqn. 4.3.

From eqn. 4.3 it is apparent that the spreading resistance R_{sp} depends on two factors; the area of the electrode and consequently the electrode geometry (i.e. R_{sp} is inversely proportional to radius r_1 for a spherical working electrode with an indifferent electrode completing the cell), and the conductivity of the electrolyte. Moreover, unlike R_{ct} and C_{dl}, the value of R_{sp}, and subsequently that of R_{access}, being a function of the electrode geometry and possible current constrictional effects, depends upon the cross-sectional area (i.e. two-dimensional) of the electrode conductor and not on the overall surface area (i.e. three-dimensional), which can increase with surface roughness[24]. It is also worth noting that the spreading resistance is frequency-independent over a wide range, which covers practically all frequencies of interest in physiological applications and where skin-effect[25] phenomena are not significant, while also being the only element of fig. 4.1 which is voltage (and thus current density) independent [Pollak, 1974b].

Concluding, another interesting point deserves mention. Plotting eqn. 4.3 in Matlab™ (fig. 4.5) reveals the property that doubling of the radius r_1 decreases the spreading resistance by half. As such, half of it lies between r_1 and $2r_1$, one quarter between $2r_1$ and $4r_1$, and so on. Therefore, if we measure the resistance of a spherical electrode using the aforementioned sensing electrode technique and with an indifferent distant electrode, we will find that the spreading resistance increases with distance from the surface of the electrode, however, as distance increases the increment gets smaller. [Ragheb et al., 1992] who studied the effect of the distance between a sphere monopole and an indifferent electrode, on the spreading resistance, reached to the same conclusion, i.e., the measured resistance increased asymptotically as the distance between the electrodes was increased. Moreover, the same study has shown that when the indifferent electrode is more than 20 times the radius r_1 distant from the working electrode, the measured resistance is essentially that which would be measured with the indifferent electrode at infinity (i.e. within 5% of the value predicted).

---

[24] The spreading resistance R_{sp} for the sphere electrode decreases with increasing diameter of the electrode (i.e. for other electrode shapes it is inversely proportional to some characteristic length of the electrode), while the interface impedance Z_{inter} decreases with the square of the diameter [Pollak, 1974a; de Boer and van Oosterom, 1978]. Thus, R_{sp} will be the dominant element of the electrode impedance Z_e when the working electrode area becomes large. Moreover, [Ragheb et al., 1992] has shown that electrode surface roughness does not affect the actual value of R_{sp}, but the frequency at which the measured impedance comes within 5% of the high-frequency asymptotic R_{sp} (i.e. which [Ragheb et al., 1992] called the transition frequency).

[25] Skin-effect phenomena begin to appear at high frequencies where the distribution of current within a conductor occurs is such a way that the current density near the surface of the conductor is much greater than that at its core, thus causing the apparent conductivity of the electrolyte to decrease and R_{sp} consequently to increase.
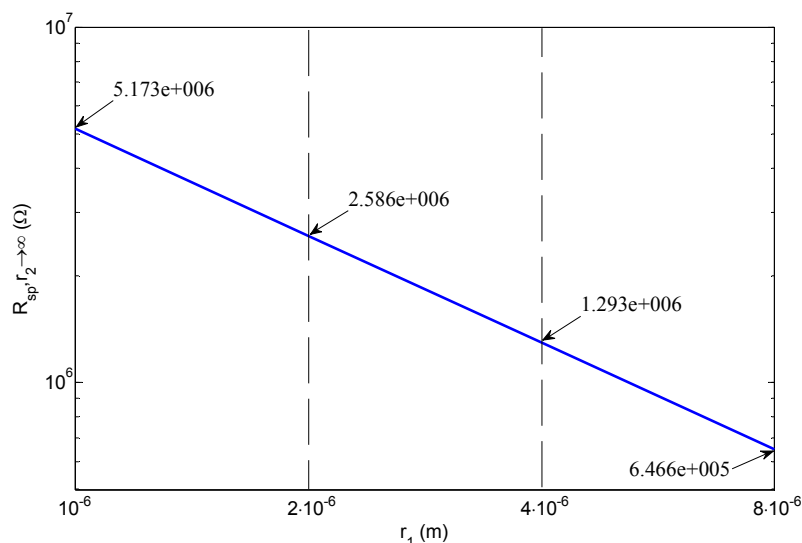
Figure 4.5: Spreading resistance R_{sp} as a function of sphere electrode radius r_1 for $\rho=65$ $\Omega \cdot$m.

4.3 Modelling the electrode-electrolyte impedance

4.3.1 The Randles and Cole models

The circuit of fig. 4.1, although a good approximate equivalent to the actual electrochemical reactions taking place at the electrode-electrolyte interface, is too simple to model the impedance found with real electrodes at all frequencies. In particular, when other workers tried to visualise impedance data of real electrochemical systems on a Nyquist plot they expected the locus to be a semicircle with the centre on the real axis (c.f. fig. 4.2). Instead, what they observed was the arc of a circle with the centre some distance below the real axis. These "depressed" semicircles have been explained by a number of phenomena, depending on the nature of the system under investigation. However, the common thread among these explanations is that some property of the system is not homogeneous or that there is some distribution (or dispersion) of the value of some physical property of the system. The polarisation impedance[26] and the observed frequency dispersion[27] of Pt electrodes and of other metals, has been investigated over an

---

[26] Polarisation is a term used by Fricke in 1932 to describe the observed constant phase angle impedance of electrodes and postulated that it was due to its "spontaneous depolarisation"; a phenomenon which was not explained by the author. Although many researchers have used Fricke's terminology for describing the unexplained effects taking place at the electrode-electrolyte interface – like frequency-dependence, non-linearity, noise, and so on – its use in that context is flawed [McAdams et al., 1995b]. Another more meaningful this time definition is given by [Bard and Faulkner, 2001, p. 22] according to which polarisation is defined as "the departure of the electrode potential from its equilibrium value (i.e. the half-cell potential E_{hc}) upon the passage of faradaic current". As such, an electrode immersed in an electrolyte is polarised when its potential is different from its open-circuit potential (i.e. ideally polarisable electrodes do not allow the passage of dc current). The degree of polarisation is measured by the additional voltage drop across R_{ct}, i.e. the overpotential η, which was defined at the beginning of this chapter.

[27] The term "frequency dispersion" is used in the literature to denote the observed frequency dependent properties of the electrode interface, like the magnitude and phase frequency response of the electrode

extended frequency range, and many models have been suggested to describe the processes at the electrochemical interface and the observed frequency dependence [Onaral and Schwan, 1982]. Two of the most well-known models are the Randles and the Cole circuit models, which are shown in the fig. 4.6 below.

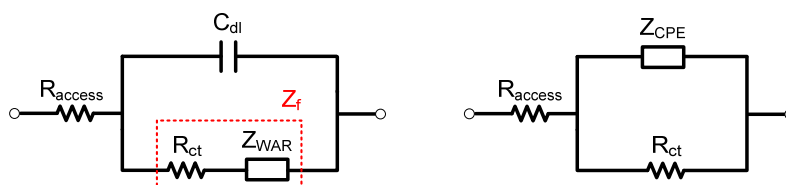Figure 4.6: Randles (left) and Cole (right) circuit models of the electrode-electrolyte interface impedance Z_e. The polarisation impedance is Z_{WAR} and Z_{CPE} respectively.

The Randles circuit model, proposed by J. E. Randles in 1947 [Bard and Faulkner, 2001, p. 376], consists of an electrolyte resistance R_{access} in series with the parallel combination of the double-layer capacitance C_{dl} and an impedance of a faradaic reaction[28] Z_f which accounts for the more complex electron transfer reactions taking place at the interface. More specifically, the circuit was used for modelling of interfacial electrochemical reactions in presence of semi-infinite linear diffusion of electroactive particles to flat electrodes (i.e. non-blocking systems)[29]. In this model, the impedance Z_f consists of an active charge transfer resistance R_{ct} and a specific electrochemical element of diffusior Z_{WAR}, called the *Warburg* element[30], which represents a kind of resistance to mass transfer (e.g. diffusion). As a result, the impedance Z_{WAR} can be used to mimic the influence of the diffusion of ions towards or away from the interface, while, in contrast to the model of fig. 4.1, this model can now describe the behaviour of more complicated electrolytic reactions (e.g. electrolysis or corrosion at low frequencies) which take place at the surface of the working electrode. Fig. 4.7 shows a typical impedance plot obtained under conditions when an electrolytic reaction is taking place at the electrode. At high frequencies the electrode impedance is simply that of the electrolyte resistance since the double-layer capacitance C_{dl} provides a path of negligible resistance to the current (i.e. capacitive current is inversely proportional to the magnitude of the double-layer capacitance). However, as the frequency is reduced, the effect of charge transfer resistance R_{ct} in parallel with the C_{dl} gives rise to the characteristic semicircular

---

impedance as a result of the variation of the series polarisation capacitance/resistance (c.f. §4.3.3.1) with frequency.

[28] Diffusion and charge transfer obey Faraday's law in contrast to the charging of the double-layer capacitance which is a non-faradaic process (i.e. does not permit the flow of dc current) [McAdams et al., 1995b].

[29] According to [Orazem et al., 2006]: "The Randles circuit provides an example of a class of systems for which, at the zero-frequency or dc limit, the resistance to passage of current is finite, and current can pass. Many electrochemical and electronic systems exhibit such non-blocking or reactive behaviour.".

[30] The Warburg impedance, named after Warburg who first derived the expression for this impedance, allows for the frequency dependence of diffusion of the chemical reactants (i.e. ions) to the electrode interface from the bulk of the electrolyte, which takes place at a finite rate, thus giving rise to an impedance to current flow through the electrode system, especially at low frequencies [McAdams et al., 1995b]. This diffusion process is a factor determining the total electrode impedance and its use in a model depends on the operational conditions of the working electrode as well as on frequency.

impedance locus. At still lower frequencies (i.e. usually sub-Hz), the faradaic impedance Z_f and consequently the electrode impedance, being dominated by the Warburg element, show a large rise[31].
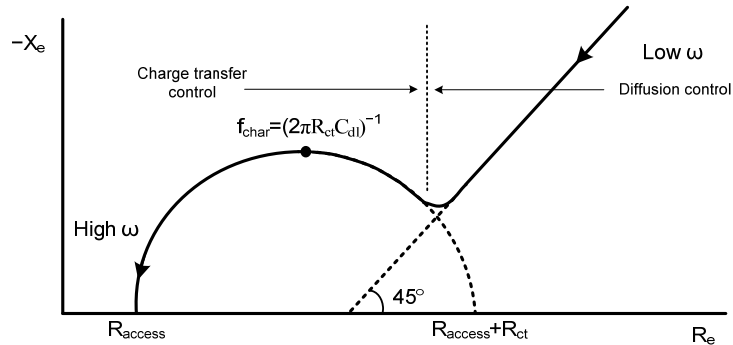
Figure 4.7: Nyquist plot of an electrochemical cell impedance modelled by the Randles circuit model. At high frequencies no electrolytic reactions take place and the characteristic impedance is mainly due to the charge transfer process at the interface. As frequency is reduced the Warburg impedance Z_{WAR} becomes dominant and the current flow through the interface is due to the diffusion of ions to the interface from the bulk of the electrolyte. Plot reproduced from [McAdams et al., 1995b].

Another circuit model used for describing the electrochemical interface impedance was introduced by K. S. Cole in 1940 [McAdams and Jossinet, 1995a]. The polarisation impedance Z_{CPE} in Cole's model is equated to the double-layer capacitance of fig. 4.1, representing the interface capacitance impedance (i.e. a capacitance with distributed properties) distorted by surface roughness effects and specific adsorption. Both circuit models can represent electrode impedance data significantly well (as will be shown in the next chapter), nonetheless, unlike the Warburg impedance, the CPE exhibits no transition from intensive to extensive behaviour[32] as the frequency decreases – i.e. no diffusion process is included because such a process tends not to be observed for many biomedical electrode systems over the range of frequencies typically used [McAdams, 2006, p. 125]. Also, due to the material of the electrodes used (i.e. Pt which is highly polarisable) and frequency range of interest (i.e. 500 Hz to 10 kHz ENG band), the use of a Warburg impedance, meaning the Randles model, or perhaps a model that combines both Z_{WAR} and Z_{CPE} elements (thus replacing C_{dl} for describing the distributed capacitance of the electrochemical double-layer), does not significantly contribute to the overall impedance of our recording electrodes. That is, for our electrode material, bandwidth of interest, and electrode potentials E_{ele} present during neural activity, the current flow at the interface is (mainly) due to a non-faradaic charge transfer process[33] and certainly not due to a

---

[31] The Warburg impedance drops out at high frequencies because the time scale is so short that diffusion cannot manifest itself as a factor influencing the current at the interface [Bard and Faulkner, 2001, p. 381].

[32] There are two kinds of processes: intensive which can be thought of as localised, occurring in a specific volume that is negligible compared to the volume of the entire system (e.g. charge transfer or double-layer capacitance), and extensive that are distributed over a large volume, and which can include the entire test system (e.g. diffusion) [Barsoukov and Macdonald, 2005, pp. 85, 87, 436-437].

[33] For current flowing through the double-layer capacitance under AC conditions, no charge actually crosses the electrode-electrolyte interface (i.e. no net current flows and therefore there are no reactions), as

faradaic diffusion-controlled reaction which can be neglected at high frequencies. There are of course many models, as also variations of the Cole and Randles models that can appropriately mimic the impedance of metal electrodes. Nonetheless, if we intend to make an IC implementation of the adaptive neutralisation approach, which was briefly discussed at the beginning of the chapter, we shall be aiming to use a simple model (i.e. few components) that will be easy to adjust in order to compensate for any changes (e.g. tissue growth) at the interface that would cause imbalance. For all the abovementioned reasons, the trimming impedance Z_{trim} will be based on the Cole model and as such the following discussion is about that.

4.3.2 Analysis of the Cole model

The complex impedance circular arc locus of certain biological tissues has been found to be well modelled by the empirical expression proposed by Cole in 1940 to describe the electrical properties of cell membranes [McAdams and Jossinet, 1995a]:

$$Z = R_\infty + \left(R_0 - R_\infty \right) \Big/ \left[1 + \left(j\omega/\omega_0 \right)^\alpha \right] \qquad (4.4)^{[34]}$$

where the subscripts for the resistances relate to frequency (i.e. R_∞ is the high frequency intercept and R_0 the low frequency intercept of the locus with the real axis), ω_0 ($=1/T_0$) is the angular turnover frequency, T_0 can be considered an average time constant[35] and α is a dimensionless numerical constant with a value between zero and one. Comparing the circuit model of fig. 4.1 against eqn. 4.4, and bearing in mind that the double-layer capacitance C_{dl} has now been substituted with a pseudo-capacitive impedance Z_{CPE}, the following relations hold:

$$R_\infty = R_{access} \qquad (4.5a)$$

$$R_{ct} = \left(R_0 - R_\infty \right) \qquad (4.5b)$$

$$Z_{CPE} = K \left(j\omega \right)^{-\alpha} \qquad (4.5c)$$

$$T_0^\alpha = R_{ct}/K \qquad (4.5d)$$

---

the AC source pushes and pulls electrons in and out of the electrode at the source frequency. Instead, ions in the electrolyte are attracted or repelled by charges on the electrode.

[34] This is an exact analogue, at the impedance level, of the Cole-Cole complex dielectric constant expression found in [Cole and Cole, 1941].

[35] Albeit the circuit of fig. 4.1 proclaims a single RC time constant it has been shown by [de Boer and Oosterom, 1978] that the response of an electrode system cannot be accurately represented by a circuit containing only one time constant; a result of the fact that C_{dl} and R_{ct} are not ideal. They also demonstrated that a series Z_{CPE}, R_{sp} circuit resulted in a more accurate description of the electrode voltage and current step response, in comparison to the RC network of fig. 4.1, essentially pointing to circuits employing an "average" distribution of time constants, as per eqn. 4.5d.

where K is a measure of the magnitude of Z_{CPE} (i.e. $|Z_{CPE}|_{\omega=1}=K\omega^{-\alpha}=K$) and has units[36] of $\Omega \cdot s^{-\alpha}$, while the time constant T_0 of the electrode impedance is now governed by the charge transfer resistance R_{ct} together with the pseudo-capacitance K and has units s^{α}. The impedance Z_{CPE} is defined by an empirical equation (i.e. eqn. 4.5c), representing the impedance of the double-layer capacitance C_{dl} in the presence of surface roughness effects, whose importance as a modelling element requires further discussion and will be revisited later in the chapter, as well as in Chapter 5. Substituting eqns. 4.5a to 4.5d into eqn. 4.4 we end up with the following expression:

$$Z_e = R_{access} + \left(R_{ct} \right) \Big/ \left[1 + \left(R_{ct}/K \right) \left(j\omega \right)^{\alpha} \right] \qquad (4.6)$$

which is also the expression for the electrode impedance Z_e of the Cole circuit model of fig. 4.6 derived by means of simple circuit analysis.

It is known that in polar coordinates $j^{-\alpha}=e^{(-j\alpha\pi/2)}$ and using the Euler-de Moivre identity this equates to $\cos(\alpha\pi/2)-j\sin(\alpha\pi/2)$. The expression of eqn. 4.5c for the Z_{CPE} can then be rewritten in terms of series resistance R_{CPE} (real) and reactance X_{CPE} (imaginary) parts as:

$$R_{CPE} = K\omega^{-\alpha} \cos\left(\alpha\pi/2 \right) \qquad (4.7a)$$

$$X_{CPE} = -K\omega^{-\alpha} \sin\left(\alpha\pi/2 \right) \qquad (4.7b)$$

$$C_{CPE} = \left(1/K \right)\omega^{-m} \operatorname{cosec}\left(\alpha\pi/2 \right) \qquad (4.7c)^{[37]}$$

where eqn. 4.7c is derived from eqn. 4.7b in the form of a reactive capacitance C_{CPE} with $m=1-\alpha$. The phase angle of this impedance is then given by:

$$\varphi_{CPE} = \tan^{-1}\left(X_{CPE}/R_{CPE} \right) = -\alpha\pi/2 \text{ rad} \qquad (4.8a)$$

$$\psi_{CPE} = \left(90° - \varphi_{CPE} \right) \deg = \left(1-\alpha \right)\pi/2 = m\pi/2 \text{ rad} \qquad (4.8b)$$

Eqn. 4.8a, also known as "Fricke's rule" or "Fricke's law", is very important as it shows that the phase angle of the impedance of eqn. 4.5c is independent of frequency and depends only on the α constant. That observation has led to this impedance being termed a constant phase angle or constant phase element (CPE). Other terms in the literature include polarisation or diffusion impedance, Warburg impedance, and distributed circuit elements [McAdams and Jossinet, 1995a]. Additionally, eqn. 4.8b, termed the "loss angle", measures by how many degrees the centre of the semicircular impedance Z_e arc is depressed. In particular, when α=1, the Z_{CPE} represents a purely capacitive impedance element having units of capacitance (as opposed to α=0 for a purely resistive one),

---

[36] If a capacitor $C=1/j\omega Z_C$ has units of F=C/V=A·s/V=s/Ω then a pseudo-capacitor $K=(j\omega)^{\alpha}Z_{CPE}$ will have units of Ω/s^{α}, where s denotes seconds. Therefore, K is inversely proportional to capacitance.

[37] According to [Hsu and Mansfeld, 2001], eqn. 4.7c is incorrect as it results in an equivalent parallel combination of R_{ct} and C_{dl} with some error in the value of C_{dl}. Instead, the correct equation used to convert K into C is $C=(2\pi f_{char})^{-m}/K$. This is possible since the real part of the $R_{ct}//C_{dl}$ impedance and the characteristic frequency f_{char} are both independent of α.

corresponding to the interface double-layer capacitance C_{dl}, and therefore its impedance locus is a semicircular arc whose centre lies on the real axis with the high frequency intercept angle φ_{CPE} being equal to $-90°$ (c.f. fig. 4.2). Conversely, if $\alpha<1$, the locus has the form of a "depressed" semicircular arc whose centre lies below the real axis while the intercept angle φ_{CPE} this time is less than $-90°$.

Simulating eqn. 4.6 in Matlab™ we obtain the Nyquist plot shown in fig. 4.8. The deviation of the semicircle from the Z_{CPE} behaviour at low frequencies is due to the faradaic charge transfer control owing to the presence of the parallel resistance R_{ct} with the non-faradaic impedance Z_{CPE}. At high frequencies the impedance can be represented with a straight line at an angle φ_{CPE} to the real axis. Finally, the characteristic frequency f_{char} (eqn. 4.9), governed by the time constant of the system, is now at 3.082 Hz.

$$f_{char} = \sqrt[\alpha]{K\left(2^{\alpha}\pi^{\alpha}R_{ct}\right)^{-1}} \qquad (4.9)^{[38]}$$
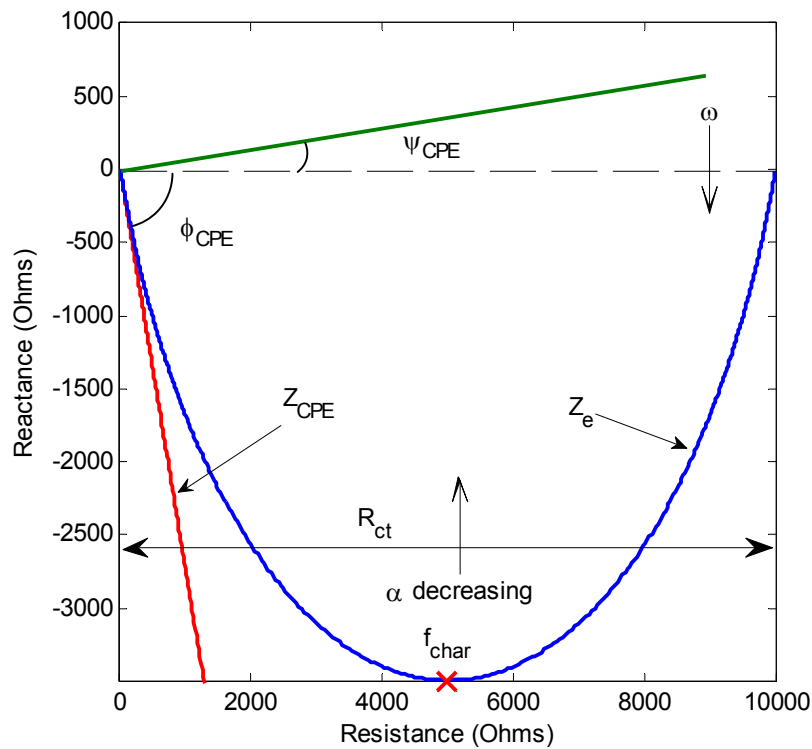
Figure 4.8: Nyquist plot of the electrode impedance of Cole circuit model of fig. 4.6 for $R_{access}=0$ Ω, $K=100$ kΩ/s$^{\alpha}$, $\alpha=0.777$, and $R_{ct}=10$ kΩ simulated in Matlab™ from 1 mHz to 100 kHz. Also shown is the Z_{CPE} impedance locus (eqn. 4.5c) having a constant slope of -2.74, i.e., $\varphi_{CPE}\approx-70°$ (on square axis). Because of the Z_{CPE}, the centre of the semicircle is now depressed by a loss angle $\psi_{CPE}\approx20°$.

---

[38] Realising that eqn. 4.2 is inversely proportional to the time constant $R_{ct}C_{dl}$ of the interface, eqn. 4.9 is derived using eqn. 4.5d, resulting in a reactance of the electrode interface that reaches a maximum value equal to $-[R_{ct}\sin(\alpha\pi/2)]/[2+2\cos(\alpha\pi/2)]$.

4.3.3 The importance of CPE

The CPE is a very important part of an electrode-electrolyte interface both because its use allows a fairly accurate description of the electrical properties of the interface, as also for its historical significance in electrochemical impedance measurements. The following is an overview of some of the most noteworthy early findings that eventually led to the development of circuit models like those of fig. 4.6. Meanwhile, the interested reader may find the following reference on the historical evolution of circuit models for the electrode-electrolyte interface useful: [Geddes, 1997].

4.3.3.1 The electrode polarisation impedance

In 1896 Wien stated that the electrode-electrolyte interface included both capacitive and resistive components and he represented the electrode "polarisation"[39] impedance by the series combination of a resistance R_{pol} with a capacitance C_{pol}, while he showed that for many electrode systems, both are frequency dependent and decrease with increasing frequency. He also found that for a given electrode system over the limited frequency range investigated (i.e. 64 to 256 Hz), the phase angle of the polarisation impedance to be approximately constant [McAdams and Jossinet, 1995a].

Driven by Wien's results, Warburg showed in 1899 that an electrode-electrolyte interface can be equated to a series combination of polarisation resistance and polarisation capacitance (i.e. Z_{WAR}), the values of which are frequency and current density dependent [Ragheb and Geddes, 1990; Geddes et al., 1971]. For low current density[40], Warburg's classical model characterises the electrode impedance Z_e as a series combination of a resistance R_{pol} with a capacitance C_{pol} both varying inversely approximately as the square root of frequency and states that at each frequency, the capacitive reactance is approximately equal to the resistance. His theory led to the following relationships for platinised Pt electrodes [McAdams and Jossinet, 1995a]:

$$C_{pol} \propto f^{-0.5}$$
$$R_{pol} \propto f^{-0.5} \qquad (4.10)$$

---

[39] The quotes in this case are used to distinguish the meaning of the term polarisation impedance that was used in a different context back in the old days when fellow workers were actually trying to measure and understand this peculiar impedance of metal electrodes (i.e. the electrode impedance Z_e), even sometimes in a very limited frequency band. The polarisation electrode impedance is traditionally expressed in terms of a series arrangement of a polarisation resistance R_{pol} with a polarisation capacitance C_{pol}. However, the fact that a series RC model provided a reasonably good representation of the electrode impedance this does not necessarily mean that it was also conceptually accurate. For instance, [Geddes et al., 1971] proved the validity of the series RC model using effectively one 4.47 mm diameter stainless steel electrode in which it is known that the charge transfer resistance R_{ct} is high, and therefore rightfully exhibited a constant phase angle behaviour in the frequency range of investigation (i.e. 30 Hz to 10 kHz). Nonetheless, the term polarisation impedance in contemporary literature refers to the response exhibited by a CPE (e.g. Z_{CPE}) and not to the whole electrode impedance Z_e.

[40] In particular, [Geddes et al., 1971] used 0.025 mA/cm^2 (rms) as the lowest value to prove Warburg's postulation.

Hence, as $R_{pol}=X_{pol}=-(1/2\pi f C_{pol})=k/\sqrt{f}$ (where k is a constant), the phase angle of the polarisation impedance is frequency independent and has a value[41] of $-45°$ [Ragheb and Geddes, 1990; Onaral and Schwan, 1982; Geddes et al., 1971].

To see whether Warburg's proposed theory was generally applicable with other electrode types and frequency span, Wolff in 1926 made measurements on various electrode systems over wide frequency ranges and found that R_{pol} and C_{pol} were indeed generally both linear functions of $f^{-0.5}$ at frequencies higher than 20 kHz. Nonetheless, he discovered that C_{pol} was proportional to $f^{-0.3}$ in the range of 200 to 10 kHz [Wolff, 1926; McAdams and Jossinet, 1995a].

In 1930, Zimmerman investigated the influence of temperature (i.e. from $0°$ to $95°C$) and electrolyte concentration on the polarisation capacitance and resistance of the electrode-electrolyte interface, over a frequency range from 60 Hz to 4 kHz. In particular, for small-area gold and Pt electrodes in a wide range of concentrations of sulphuric acid, C_{pol} increased and R_{pol} decreased with increasing temperature and concentration [Geddes, 1997].

Fricke in 1932, being concerned with all these findings, recognised that for a frequency range from 100 Hz to 3.5 kHz the polarisation capacitance and resistance did not always vary as the square root of frequency, but are better described as power functions, while the phase angle is constant over a wide range of frequencies [Onaral and Schwan, 1982; Geddes, 1997]:

$$C_{pol} \propto f^{-m}$$
$$R_{pol} \propto f^{m-1} \qquad (4.11)$$

He thus formulated a relationship between the phase angle and the power factor as $m=1-\alpha$ (c.f. eqn. 4.8a). In other words, C_{pol} and R_{pol} are a power-law function of frequency. Additionally, it can be seen that Warburg's relationships (i.e. eqn. 4.10) are a special case of Fricke's relationships for $m=0.5$. In the case where m is restricted to positive values in the range $0<m<1$, then the polarisation impedance decreases with increasing frequency, in accordance with what is found for tissue [McAdams and Jossinet, 1995a].

Schwan in 1963 and 1966 explored the frequency range from 20 Hz to 200 kHz and noted that the power factor m in Fricke's formulation for the polarisation capacitance changes with frequency from a value of about 0.3 to 0.5 as the frequency increases from 20 Hz to 200 kHz. Nevertheless his data agreed well with Fricke's rule, which assumes a frequency independent power factor m [Onaral and Schwan, 1982]. [de Boer and van Oosterom, 1978] carried out experiments in the 10 Hz to 20 kHz frequency range using platinum needle electrodes with an effective surface area of 0.05 mm^2 submerged in 0.9% NaCl solution and found the impedance profile of their electrodes to obey the empirical

---

[41] In reality, X_{pol} is usually greater than R_{pol} and as such the phase angle is greater than $-45°$.

eqn. 4.5c with a frequency dependence of $f^{-0.75}$. Simpson in 1980 extended the range of measurements down to 1 Hz and observed Fricke's rule to be obeyed at these frequencies for various levels of DC bias currents [Simpson et al., 1980]. Onaral and Schwan in 1982 measured the frequency-domain impedance behaviour of platinum electrodes in 0.9% NaCl down to 1 mHz and observed that Fricke's phase angle rule is applicable down to 10 mHz. Using a low current density, they found that C_{pol} and R_{pol} both decreased monotonically with increasing frequency from 1 mHz to 1 kHz. Furthermore, they observed that the polarisation impedance locus of their measured Pt electrode formed depressed semicircular arc that could be approximated by an equivalent expression of eqn. 4.4. They also suggested that this impedance could be represented by an electrical circuit model comprising a constant phase angle impedance Z_{CPE} in parallel with a shunt resistance [Onaral and Schwan, 1982].

Warburg's series RC model is capable of describing the electrical properties of an electrode-electrolyte interface and has been verified that it can do so by several investigators such as [Ragheb and Geddes, 1990; Onaral and Schwan, 1982; Geddes et al., 1971] who wanted to study the properties of metal electrodes. At a first instance one could notice that Warburg's series RC model does not account for the behaviour of the electrode-electrolyte interface at very low frequencies (i.e. at 0 Hz, the Warburg model predicts an infinite impedance); sometimes a result of the limited AC measuring methods used at the time (i.e. R_{ct} is dominant at low frequencies where the polarisation impedance becomes larger than this shunt). Nonetheless, as discussed in the beginning of this chapter, it is well known that such an interface can pass direct current, making Warburg's model not consistent with experimental evidence. As such, electrochemists have presented equivalent circuits in which the faradaic leakage resistance R_{ct} has been placed across the polarisation element (e.g. Cole model). More specifically, at high frequencies the interface impedance Z_{inter} is well represented by eqn. 4.5c, whereas at low frequencies by eqn. 4.6 less the R_{access} resistance. Finally, in the case of the models of fig. 4.6 it is important to note that when $\alpha=0.5$ then the CPE impedance Z_{CPE} behaves effectively like a Warburg element Z_{WAR}, however, that does not mean that the electrical circuits of fig. 4.6 are the same. More specifically, this CPE has nothing to do with diffusion controlled charge transport but originates from the coupling of the electrolyte resistance to the double-layer capacitance (i.e. for a perfectly polarisable electrode), as was shown[42] by [Scheider, 1975]. At each instance, Z_{CPE} and Z_{WAR} represent different interfacial electrochemical reactions that depend on different physicochemical parameters at the electrode interface, but in essence have one thing in common; an impedance (faradaic and non-faradaic respectively) with a phase angle independent of frequency.

4.3.3.2 Effect of current density on interface impedance

According to [Weinman and Mahler, 1964] and [Geddes et al., 1971] an accurate description of electrode impedance must include the frequency as well as the current density used for measurement. In particular, the electrode-electrolyte interface behaves

---

[42] As elaborated by [Nyikos and Pajkossy, 1985] "(Scheider) derived by conventional dimensional analysis that if the impedance is a CPE and if it originates from the coupling mentioned then 1/K of eqn. 4.5c should be proportional to $\rho^{\alpha-1}$ with ρ being the electrolyte resistivity.".

non-linearly if the excitation current exceeds a critical value; the "limit current of linearity" at a given frequency [Onaral and Schwan, 1982]. This is an important feature as electrodes often introduce non-linear characteristics that are erroneously ascribed to the biological system under study. When an electrode-electrolyte interface is operated with increased sinusoidal current density, the resistance R_{pol} decreases, the capacitance C_{pol} increases, and the increase occurs at higher current densities as the frequency is increased[43]. Schwan in 1963 defined a "limit current of linearity"[44] as the current at which the electrode-electrolyte resistance R_{pol} and capacitance C_{pol} deviated by 10% from the values observed at low current densities. The linearity limit marks the current density below which R_{pol} and C_{pol} are nearly constant at a particular frequency (i.e. with current density being the independent variable), and thus the current density below which linear system theory can be used to model the electrode-electrolyte interface [Ragheb and Geddes, 1990]. This will depend on the effective area and the material type of the electrode under investigation, as different metals exhibit a different current-carrying capability, as demonstrated by [Ragheb and Geddes, 1990]. Hysteresis effects are observed as current values beyond the limit of linearity are applied, i.e., polarisation impedance values do not only change with current density but are also dependent on previously applied currents. Additionally, as shown by [Simpson et al., 1980], the onset of the limit current of linearity for an electrode at a particular frequency is independent of the applied DC bias current (i.e. within the overpotential limits for linear operation of the electrode). Finally, another important fact needs mentioning. It is known that the current density under a surface plate electrode is not uniform, with larger densities at the edge. The fractal properties of the electrode surface (c.f. Chapter 5, part 1) also create local areas of high current density. The onset of non-linearity may therefore be gradual, and start very early (i.e. at much lower voltages than about 100 mV) at very limited areas on the electrode surface [Grimnes and Martinsen, 2000, p. 50].

Results from [Geddes et al., 1971] show that with a low current density, the Warburg series-equivalent resistance and capacitance of a single electrode-electrolyte interface were found to vary almost inversely as the square root of frequency. With high current densities however, the Warburg concept does not hold in that, at a critical frequency value, the resistance decreases and capacitance increases as current density is increased [Weinman and Mahler, 1964; Geddes et al., 1971], and the manner in which each varies with frequency does not permit a power function approximation (i.e. one which is linear on a log-log plot). Hence, the Warburg equivalent circuit model is applicable at low current densities (and thus low overpotentials across the interface) only. Additionally, the

---

[43] According to [McAdams, 2006, p. 129] "as the applied current amplitude is increased, the charge transfer resistance R_{ct} decreases rapidly, causing the diameter of the impedance locus to decrease. As the low frequency end of the arc is dominated by R_{ct}, the effects of such non-linearity will be first evidenced at these frequencies".

[44] The non-linearity rule was formulated by Schwan in 1968 as $i_L \sim f^{1-m}$ where m is Fricke's power factor (c.f. eqn. 4.11), but need not be constant with respect to the frequency as may change with frequency more or less pronouncedly for a given electrode system. The frequency dependence of the limit current of linearity holds true to frequencies as low as 1 mHz [Onaral and Schwan, 1982]. Accordingly, the presence of m in the expression of an electrode system's non-linear behaviour is therefore simply due to the presence of a very non-linear resistance in parallel with a relatively linear, frequency-dependent Z_{CPE} [McAdams, 2006, p. 129].

magnitude of the impedance of an electrode-electrolyte interface decreases with increasing current density, revealing an important difference between stimulating and recording electrodes[45]. Conversely, as was shown by [Geddes, 1997], the phase frequency response is very little affected by increasing current density, while it decreases (i.e. tends towards 0°) with increasing frequency.

4.4 Electrode impedance data fitting

It will be good to demonstrate what we have discussed so far regarding the constant phase angle property of metal electrodes with an actual example. Towards that purpose a suitable electrochemical cell had to be constructed. The cell should be made in such a way so that its phase angle response should exhibit a clear CPE behaviour at the bandwidth of investigation. Therefore, the approach of the "cut-wire" electrochemical cell was adopted [Liu et al., 2008].

4.4.1 The electrochemical cell

A 90% Pt-10% Ir enamelled wire (70 μm in diameter) was placed in a small acrylic tube with a 3.7 mm diameter bore and then was filled with epoxy resin. Once cured, a low-speed diamond saw (South Bay Technology Inc., model 650) with a 400 μm blade width was used to make a cut part-way through the middle of the tube and wire forming two aligned flat electrode surfaces of same size. The cut was then filled with a drop of 0.9% NaCl solution to complete the cell. A schematic representation of the cut-wire cell together with its electrical circuit equivalent is shown in fig. 4.9 and 4.10 respectively.
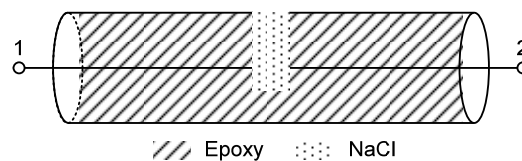
Figure 4.9: The cut-wire electrochemical cell. The impedance of the two flat electrodes in contact with the aqueous volume conductor was measured between terminals 1 and 2 using a previously calibrated, precision impedance analyser (Wayne Kerr Electronics, model 6520BD1, 20 Hz-20 MHz) with a test voltage of 30 mV from 100 Hz to 100 kHz.
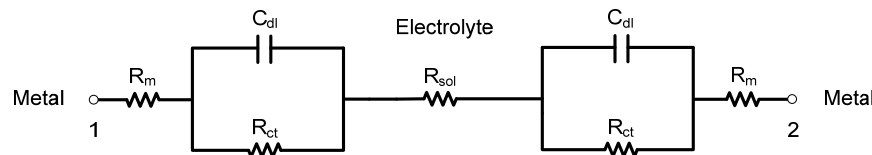
Figure 4.10: Electrical circuit model of the cut-wire cell. Shown are the two interface impedances Z_{inter} in series with the solution resistance $R_{sol}=2R_{sp}$. The resistance R_m of the metal wire conductors is considered to be of negligible value, as such $R_{access}=R_{sol}$.

---

[45] During stimulation, a high electrode impedance would result in a large applied voltage leading perhaps to undesired electrochemical reactions. Conversely, during recording, a small implanted electrode would mean that the small extracellular signals might be lost in noise exhibited by the electrode and the surrounding electrolyte area (i.e. the load impedance).

4.4.2 Polarisation impedance modelling

Having a suitable circuit model of the cut-wire cell the next step is to put it to the test by trying to fit its measured impedance. Additionally, in place of the double-layer capacitance C_{dl} we are going to use the much discussed CPE. Thus, having the opportunity to examine the empirical Cole eqn. 4.5c in terms of whether it can indeed represent actual electrode impedance data satisfactorily. Before proceeding with the fit it would be suitable to define a number of assumptions regarding the cut-wire cell. These are the following:

a) Since both electrodes were made out of the same wire material we can assume that they exhibit identical electrode impedances Z_e.

b) Because the electrolyte in this case is homogenous and the two electrode surfaces perfectly aligned we can represent both spreading resistors as $R_{sol}=2R_{sp}$.

c) As the material of the electrodes is highly polarisable, and also due to the very small diameter of the electrodes, the charge transfer resistance R_{ct} is expected to be large and effectively can be ignored (i.e. there is essentially no faradaic path across the interface).

d) The spreading resistance R_{sp} of the cell is expected to be smaller in comparison to having the same two aligned electrodes some distance apart in a volume conductor of bigger proportions. This is a result of the very small size of the cell, i.e., the spreading current is confined into a smaller space with respect to the other electrode of the cell, inside the volume conductor.

e) From previous discussion it has become apparent that Z_{CPE} is dominant at high frequencies (c.f. §4.3.2, fig. 4.8). Additionally, the smaller the electrode the more the interface impedance Z_{inter} will dominate the electrode impedance Z_e over R_{sp} (c.f. §4.2.2). Taking into account that: a) R_{ct} is considerably high, and b) because of that R_{ct} is not the dominant element at the frequency of investigation, the cell should exhibit a clear constant phase angle characteristic. If this postulation is indeed correct then a Z_{CPE} in series with R_{sp} should result in a satisfactory fit on the measured impedance of the particular cell.

Attempting to perform a fit on the impedance profile of one[46] electrode wire, the plot of fig. 4.11 is obtained. Shown is the magnitude and phase of the electrode wire impedance Z_{cw} (blue curve) fitted in two different ways; a) using an electrode impedance Z_e made out of a Z_{CPE} (i.e. using eqn. 4.5c) in series with an electrolyte resistance R_{sp} (red curve; K=115 MΩ/s$^{+\alpha}$, α=0.81, R_{sp}=2.2 kΩ), and b) using a Z_{CPE} only (green curve; for same K and α). Looking at the plot the following comments can be made. The empirical Cole CPE model offers indeed a constant phase angle (i.e. $\varphi_{CPE}=-\alpha*\pi/2$ rad$\approx-73°$) but it does not result in a satisfactory fit, especially at high frequencies where we expect $R_\infty \rightarrow R_{sp}$. Conversely, once combined with the series solution resistance the fit is improved. This verifies our earlier postulation that an acceptable fit should be possible without the need of a charge transfer resistance R_{ct} as part of the fitting impedance.

---

[46] Since the impedance of the two electrode wires has been assumed to be the same, results have been modified so any values given from now on in text have been reduced to that of one electrode.
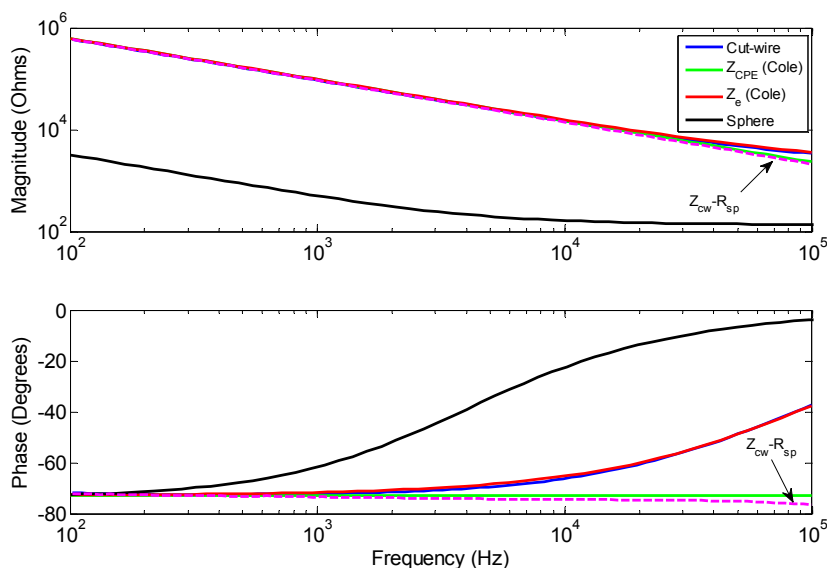
Figure 4.11: Matlab™ plot showing the impedance magnitude and phase of the electrode wire (blue), sphere electrode (black), and the fitting curves of Z_{CPE} (green) and $Z_e=Z_{CPE}+R_{sp}$ (red). Performing a fit on the electrode wire impedance Z_{cw} using Z_e resulted in a satisfactory fit without the need of a shunt interface resistance R_{ct}. Plotting $Z_{cw}-R_{sp}$ (magenta) reveals the accuracy of the fit. Also, due to the small size of the cut-wire cell the phase angle is constant over a wider range of frequencies, despite $R_{sp\_cw} \gg R_{sp\_sphere}$. All measurements were carried out at a room temperature of 23 °C with electrodes immersed in 0.9% NaCl solution.

Finally, to signify the accuracy of the fit, the 2.2 kΩ spreading resistance R_{sp} was subtracted from the impedance of the electrode wire Z_{cw} and was also plotted on fig. 4.11 (dotted magenta curve)[47]. The resulting phase angle should ideally be a straight line matching that of the Cole Z_{CPE}, however, this is not the case, especially at high frequencies. Hence, the use of a high value shunting resistance R_{ct} across the interface could have been useful in fitting the low frequencies of the electrode wire impedance to improve the fit, when opting for a slightly higher value (i.e. about 1°) for the CPE phase angle[48]. Another point revealed by this plot is that our Pt electrode is not ideally polarisable but instead relatively polarisable meaning that apart from the charging and discharging of the double-layer capacitance, there is some electron transfer taking place at the interface (i.e. with this phenomenon being dominant at low frequencies, $\ll 100$ Hz), as well as having free charge carriers "crossing" the double-layer or flow in the bulk of the electrolyte. Additionally, the value of α used in the fit departs from 0.5, meant for describing an impedance of an electrode-electrolyte interface when the charge transport is controlled by diffusion, proving in practice the earlier remarks that our electrode system is not governed by a faradaic diffusion-controlled reaction at the frequencies of ENG activity we are interested in.

---

[47] Whenever possible the value of R_{sp} should be verified independently of the regression (c.f. §5.7.3.2).

[48] By increasing the phase angle, the impedance fit at high frequencies was better for a lower value of R_{sp}. Subsequently, to compensate for the introduced error in the fit at low frequencies a shunting resistance R_{ct} of very high value was used (i.e. the smaller the value of R_{ct} and therefore the radius of the semi-circle, the higher the frequency at which the phase angle tends towards 0° due to R_{ct}). In particular, the fit was improved throughout the band by using an $R_{ct}=20$ MΩ, and setting K=115 MΩ/s$^{+\alpha}$, α=0.82, $R_{sp}=2$ kΩ.

In an attempt to prove another important point, the magnitude and phase response of a spherical 90% Pt-10% Ir electrode (860 μm in diameter) manufactured[49] in our laboratory (c.f. fig. 5.5) is plotted on the same graph (black curve). The impedance of the spherical electrode was measured in accordance to what we have discussed in §4.2.2 (i.e. using an indifferent electrode) and in a cell having a volume conductor of a much greater scale comparing to the cut-wire, but same conductivity. The fact that the phase angle of the sphere electrode is the same as that of the cut-wire at low frequencies is purely coincidental. Additionally, due to the bigger surface area, the impedance magnitude of the sphere electrode is less than that of the electrode wire. Conversely, its phase angle tends quicker towards zero, making R_{sp} the dominant factor at those frequencies[50]. This remark is backed-up by fig. 4.12. This would normally mean that the value of the R_{sp} of the sphere electrode is larger than that of the electrode cut-wire, i.e., $R_{sp\_sphere} \gg R_{sp\_cw}$ owing to the geometry of the situation due to the tiny cut-wire cell – knowing that the spreading resistance depends on the geometry of the cell and not on the working electrode alone. Nonetheless, the opposite is true here (i.e. R_{sp_sphere}=135 Ω; c.f. fig. 5.38) due to the larger cross-sectional area (i.e. bigger radius) of the sphere electrode (c.f. eqn. 4.3). Therefore, it seems that the effect of size of the working electrode has more impact on R_{sp} than the geometry of the cell. Concluding, although most of the solution resistance is close to the electrode tip surface where the current spreads out, as the cut-wire cell is smaller in size the current is now confined into a tiny area around the surface of the electrode. As a result, the cut-wire cell exhibits a CPE behaviour over a wider range of frequencies.
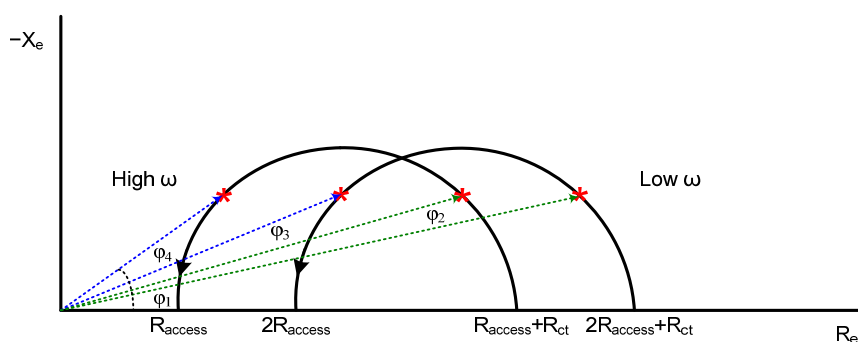
Figure 4.12: Plot illustrating the effect of the R_{access} value on the phase angle of the electrode impedance Z_e. Coloured arrows denote impedance magnitudes at high (blue) and low (green) spot frequencies. Increasing R_{access} will alter the phase angle both at high and low frequencies, however, at low frequencies the effect will be less severe, i.e., $\varphi_4-\varphi_3>\varphi_2-\varphi_1$.

---

[49] By melting a 90% Pt-10% Ir Teflon insulated wire of 0.175 mm diameter using a small handheld flaming torch (Micro-Weld Ltd., Micro-flame gas generator - type A).

[50] The absolute value of the phase angle, as well as the surface texture of the two electrodes, is not of interest at present. Nonetheless, due to the manufacturing process we expect the surface of the electrode wire to be smoother than that of the sphere electrode. Although this does not affect the value of R_{sp}, it consequently explains the large value of K used for fitting the electrode cut-wire impedance (i.e. K_{cw}=115 MΩ/s$^{+\alpha}$ as opposed to K_{sphere}=683 kΩ/s$^{+\alpha}$), since K is inversely proportional to the surface area of the electrode and decreases with surface roughness.

4.5 Summary

In this chapter the electrode-electrolyte interface of metallic electrodes was described and basic modelling theory was presented with emphasis being given on the sources of non-linearity effects. Because an electrode-electrolyte interface is a non-linear circuit element that can be operated over a very wide frequency and current density range, it is unlikely that a single model can be created for it, nonetheless, under restricted frequency and current density range conditions, models like those of fig. 4.6 can be used. Undoubtedly, an important element of the polarisation impedance of electrodes is the CPE. Up until now the CPE has been presented as a theoretical concept backed up by a circuit model and a descriptive empirical equation that was used to assist in describing the observations that various workers have made on the polarisation impedance of metallic electrodes. At the end of this chapter we have demonstrated through a real-world example that the interface impedance at high frequencies (and before the electrolyte resistance becomes dominant) is well represented by the empirical eqn. 4.5c, whereas it is known due to the direct-current behaviour of the interface that at low frequencies the need for an equivalent circuit model incorporating a resistance in parallel with the CPE impedance is necessary. Finally, the CPE (or alternatively the Warburg element) is, in reality, not realisable with ordinary lumped electric circuit components. There are however electric circuit models which can approximate the properties of a CPE and thus adequately describe the overall behaviour of the interface impedance. Such circuit models are presented in the next chapter where practical system design considerations like the origin and realisation of the CPE in a phantom model are discussed.

CHAPTER
FIVE

Adaptive Neutralisation Using the mQT

Part 1: Rationale, Theory and Simulation

5.1 Introduction

In Chapter 3 the reader was introduced to a passive neutralisation technique where myoelectric interference from neural recording tripoles was removed using RC models – either series or parallel – placed at the front-end of the QT amplifier configuration. This passive method offers complete neutralisation of the EMG interference at a spot frequency. We called this configuration the mQT. However, performance of the mQT was suboptimal due to the frequency-dependence of the electrode impedance and consequently the breakthrough of interference in the ENG band was not uniform (c.f. fig. 3.12). Using the electrode impedance modelling theory of Chapter 4, here we present an improvement where (ideally) interference is removed at all frequencies by appropriately modelling the impedance of our recording electrodes. Using this approach the trimming impedance Z_{trim} (i.e. the impedance required to balance the tripole; c.f. fig. 3.3) now "adapts" to the impedance profile of our recording electrodes and the neutralisation performance of the mQT in the ENG band is improved without the need for continuous adjustment[1]. We call this improved configuration the adaptive mQT. The main idea was developed using Matlab™ and initially tested in Cadence™ circuit simulator for evaluation. Subsequently, it was implemented using discrete circuit components and tested in an in-vitro preparation using NaCl solution as the electrolyte/tissue substitute.

This chapter is broken down in two parts; part 1 contains the theoretical background and the initial development of the system solely in simulation, while part 2 covers the hardware design aspects and the in-vitro testing strategy and verification of the adaptive

---

[1] The fact that the EMG breakthrough at the output of the conventional mQT amplifier configuration depends on the frequency of the interference signal, as well as on the proximity and orientation of the interference fields with respect to the recording tripole has a significant impact when multiple interference sources of different frequencies are present at the recording site (c.f. §3.6.1). Despite, as will be shown later, a single adaptive trimming impedance can be used to neutralise EMG at multiple frequencies, interference will still appear as the source impedance changes due to tissue growing around the tripole. Therefore, in practice, adjustment of the elements of the new adaptive trimming network would still be required. Nonetheless, the new approach offers an improvement over the conventional mQT in that it instantaneously removes the EMG in the whole ENG band and it does so more efficiently, i.e., without any adjustment.

mQT configuration. More specifically, part 1 consists of two main sections. The first section documents the initial attempt to model the trimming impedance Z_{trim} as a 5-component network using the Randles circuit of fig. 4.6. Recognising the possibilities and limitations of this approach, the second section explores different ways of modelling the frequency-dependence of metal electrodes and in particular the exhibited phase angle response in the form of a CPE. We begin by introducing the reader to the very important single-pore model which is an accurate, yet simple, physical representation of the CPE. A thorough overview of the literature on modelling the CPE using transmission lines and fractals then follows from which 3 methods are further explored in detail using Matlab™. Part 1 concludes by utilising the chosen CPE model – Schrama's RC ladder network – in a trimming impedance network for EMG neutralisation in a Matlab™ simulation where useful conclusions are drawn. Part 2 of Chapter 5 begins with an assessment of the adaptive mQT configuration in a model-based Cadence™ simulation for neutralising EMG interference present in the recording tripole. A PCB implementation of the CPE then follows and actual measurements are compared against simulation results. Chapter 5 finally concludes with the design of a discrete system and an in-vitro experiment where it is demonstrated in practice that the new adaptive neutralisation approach can potentially offer improved results in the way EMG interference is neutralised in recording tripoles.

5.2 Null impedance data fitting[2]

Realising that the simplistic RC models of the mQT offered limited neutralisation performance (c.f. §3.6.2) we needed to come up with models that better resemble the impedance profile of our recording Pt electrodes. Towards that purpose a passive trimming network that would fit the characteristic null impedance curve, in the entire ENG band, would ideally balance the tripole more efficiently. The benefits of such an approach are twofold: a) the solution would be considered "adaptive"[3] without increasing power consumption; b) it would assist in establishing feasibility of the design (e.g. size of passive components, added noise from the new network) and most importantly interference neutralisation performance – in other words can this adaptive network offer improved performance in comparison to the conventional mQT? The following paragraphs document the theoretical reasoning behind this matter with results obtained both from Matlab™ simulations and from an in-vitro preparation.

5.2.1 Methodology

Although the structure of an electrode-electrolyte interface is of complex nature, its behaviour can be equated to electrical circuit components, as was clearly demonstrated in Chapter 4. One approach to modelling the impedance required to balance our recording tripole is to consider the electrode-electrolyte interface as a black box, and by gathering

---

[2] The contents of §5.2 were partially presented in [Pachnis et al., 2008].

[3] It is a good point at this early stage of the chapter to perhaps emphasise here that the word "adaptive" is not used in the context of closed-loop control theory. Instead, what we mean is that our balancing network is able to "adapt", in terms of frequency response and due to its component topology, to the impedance of our recording electrodes.

some sort of data about it, find the electrical circuit network that fits the given data in the frequency range of interest. The data that we want our model to represent is the real and the imaginary part of the null impedance curve (i.e. bold curve of fig. 3.14). Finding the adaptive passive trimming network values involves first providing a model that will be suitable for representing the previously obtained experimental neutralisation data. Subsequently, performing complex nonlinear least-squares procedures, available in numerous electrochemical impedance spectroscopy data fitting computer software on a given model, it is possible to extract the circuit component values that will result in an adequate fit. How well the model will fit the data depends on the topology and selection of its components. The best model will be an electrical equivalent network that exhibits the same frequency response, while at the same time it is relatively simple and best adapted to variations on the target data. In addition, a correct model should closely resemble the physical and electrochemical properties of the given data, and therefore, by having knowledge of the electrode-electrolyte interface, its given topology should also be possible to correlate and justify.

The series and parallel RC circuits used to perform neutralisation of the EMG in Chapter 3 are too simple to mimic the impedance found with real electrodes, as impedance spectra is obviously more complicated. Conversely, it is known that both electrical circuit models of fig. 4.6 can represent such an impedance profile, and by using data fitting computer software, it is possible to extract the circuit component values. Fitting was performed with ZView™ software package (Scribner Associates Inc.) using the Randles electrical circuit model (c.f. §4.3.1), while the Warburg impedance Z_{WAR} was represented by a parallel RC arrangement[4], as shown in fig. 5.1. Additionally, it should be noted that the specific circuit model may not uniquely represent the complex impedance frequency response of our system.
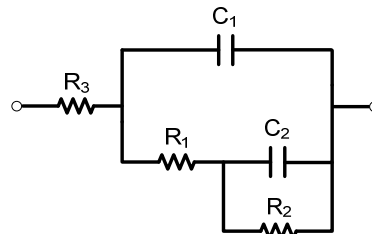
Figure 5.1: The Randles circuit model of fig. 4.6 used for fitting the null impedance locus of fig. 3.14 (bold curve), where $C_2//R_2=Z_{WAR}$, $C_1=C_{dl}$, $R_1=R_{ct}$, and $R_3=R_{access}$. Typically $R_1>>R_3$.

The component values of the network are shown in table 5.1, while the fit impedance curve superimposed to the original null impedance data is shown in fig. 5.2a with the respective magnitude and phase plots shown in fig. 5.2b. It is important for the circuit components of the trimming network to be small in size, thus avoiding excess noise and silicon area, if the method is to be integrated. Looking at the size of the components we

---

[4] At first instance, the Randles circuit was used instead of the Cole to carry out the data fitting. In particular, representing the faradaic Warburg impedance using a simple parallel RC arrangement containing a leaky resistor seemed more sensible at the time. A non-faradaic capacitance C_1 had then to be used to achieve the fit.

see that it is easy to integrate the resistors, however the size of the capacitors is comparable to those used for the trimming parallel RC impedance (c.f. table 3.2), which may be difficult to incorporate in an implantable device.

	R_1	R_2	R_3	C_1	C_2
	423 Ω	1230 Ω	12.7 Ω	195 nF	290 nF
% error in the fit	11%	6%	14%	3%	10%

Table 5.1: Simulated component values of the Randles circuit model of fig. 5.1 obtained from ZView™ for an ionic conductor (NaCl solution) having conductivity equal to 8.52 mS/cm. The error figures are the estimated percentage error in the same units as the component values and show the accuracy of the fit, e.g., in this case R_1 can take a value of 423±46.5 Ω.

Figure 5.2a: Complex plane showing how the impedance of the Randles circuit model of fig. 5.1 (○ solid line) fits the null impedance (+ dashed line) for an electrolyte conductivity of 8.52 mS/cm.

Figure 5.2b: Magnitude and phase of the impedance loci of fig. 5.2a.

98

In one of his studies on the impedance characteristics of metal electrodes (like Pt and Au) Pollak showed [Pollak, 1974b; Pollak, 1974c] that the electrode impedance at very low frequencies 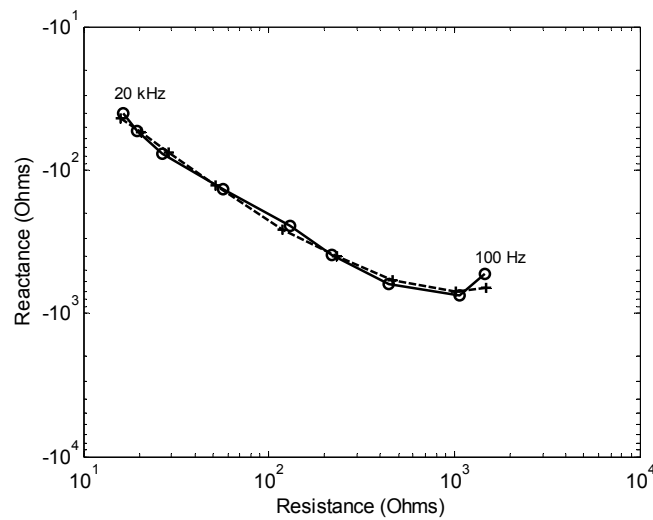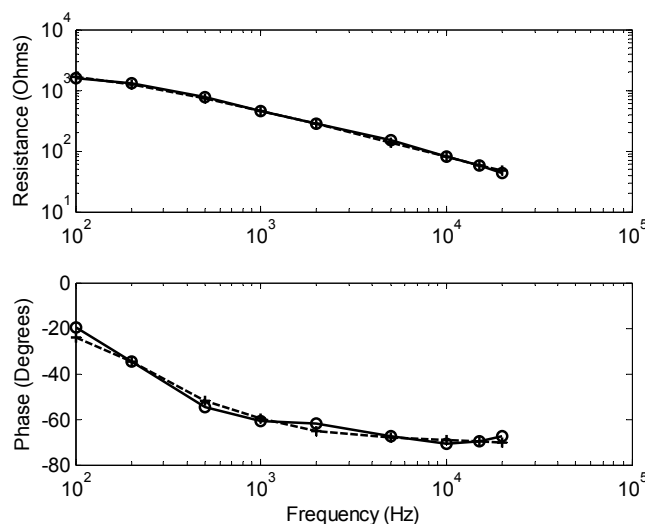turns out to be almost purely resistive in character and mainly determined by the exchange current density of the electrode-electrolyte system. Hence, the high value of the interfacial impedance magnitude of fig. 5.2b at low frequencies is to be expected. In the intermediate frequency range the polarisation impedance Z_{WAR} together with the double-layer capacitance C_{dl} are the decisive factors, while the phase angle of the impedance lies in the region between −45° and −90°. This is clearly noticeable in the phase plot of fig. 5.2b, where the phase angle is within that limit. At still higher frequencies the electrode impedance becomes resistive again, with the access resistance R_{access} of the electrolyte being the most important factor (thus the relatively constant phase[5]). Moreover, the frequency at which this (last) transition occurs decreases with decreasing diameter of the electrode (although the impedance of large-area electrodes is resistive over most of the frequency range). This is also true with decreasing electrolyte conductivity as the capacitive reactance of the electrode and the electrolyte resistance then increase.

Looking at the above magnitude and phase plots we can summarise a number of useful points. Finding a "universal" trimming impedance that will neutralise the EMG interference in the ENG band seems feasible by modelling the impedance required to balance the tripole. Moreover, this can be done without the requirement of adjustment since the trimming impedance now adapts to the frequency response of our recording electrodes.

5.2.2 In-vitro verification

The same apparatus used for carrying out the in-vitro experiment of Chapter 3 was also used in this experiment for validating the performance of the new trimming network (c.f. §3.4.3). The trimming circuit of fig. 5.1, positioned at the front-end of the QT amplifier, was realised using discrete circuit components of approximate value (i.e. about 4% tolerance) as in table 5.1. During the voltage amplitude measurements of the EMG breakthrough at the amplifier output, the voltage drop across the electrode tripole was mostly kept constant at about 30 mV in order to stay safely within the linear region of the electrode impedance. The small value of the EMG signal caused some noise problems in the low frequency region where the source impedance is high. This was addressed by averaging the output response of the amplifier using the appropriate digital oscilloscope function. Fig. 5.3 shows the pk-pk breakthrough voltage at the output of the mQT

---

[5] Comparing fig. 5.2b with fig. 4.11 we see that the magnitude frequency response follows the same trend, nonetheless, the phase angle follows an opposite one. If, for our recording tripole, we assume both outer electrodes to exhibit an impedance with identical phase angle, this has to match the phase angle of the trimming impedance Z_{trim} (c.f. §3.3.2.2), which at high frequencies is less significant (i.e. since both $Re(Z_{trim})$ and $Im(Z_{trim})$ decrease; c.f. fig. 3.11 or fig. 5.2a). At the same time the trimming resistance and capacitance needed to balance the tripole decrease due to C_{dl} and R_{ct} of the interface decreasing with frequency (c.f. §4.2.1.2). As such, the ratio $Im(Z_{trim})/Re(Z_{trim})$ increases – i.e. $Im(Z_{trim})$ is decreasing slower with frequency comparing to $Re(Z_{trim})$ – with the phase angle tending to −90° and the electrolyte resistance $R_3=R_{access}$ being the dominant factor at those frequencies (hence the relatively constant phase, as per fig. 5.2b).

amplifier for an electrolyte conductivity of 8.52 mS/cm with no trim, parallel trim at 200 Hz, and with the new adaptive network. The latter should require no adjustment since its impedance fits the characteristic trimming impedance of the specific electrode tripole.
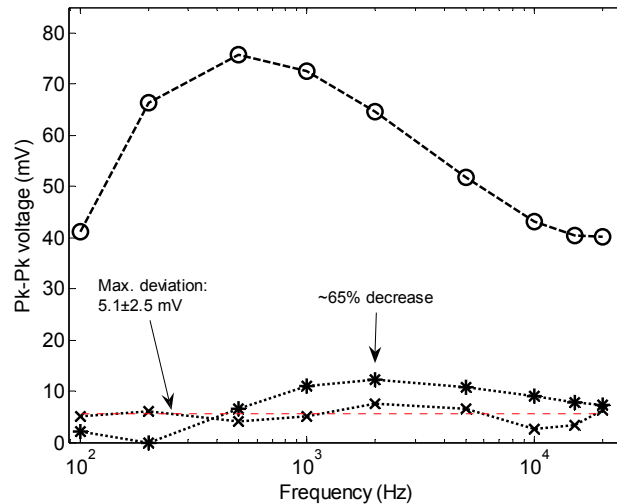
Figure 5.3: Output voltage of the mQT amplifier configuration versus frequency. Symbols: ○ no trim, * parallel trim at 200 Hz, x adaptive trim. The electrolyte conductivity was 8.52 mS/cm.

In the amplitude response of fig. 5.3 for the adaptive trim setting, the null is not as low as we would like since that should ideally have been zero. This result can be accounted for by two key reasons: a) the double-layer capacitance C_{dl} and the faradaic impedance (i.e. R_{ct} and Z_{WAR}) of the network of fig. 5.1 were implemented by ideal, frequency-independent, ordinary lumped discrete components whereas it is known that in real metal electrodes those elements are non-ideal since their actual value depends, among other things (c.f. §4.2.1.2), on frequency; b) using the parallel RC arrangement in place of the polarisation impedance Z_{WAR} does not effectively model the surface porosity and roughness of electrodes, while clearly such a network does not exhibit a constant phase. Finally, there was some error in the fit (c.f. table 5.1) in terms of how well the particular component values of the model of fig. 5.1 fit the target data (i.e. estimated accuracy of the fit), while there was a small deviation between the simulated and the actual discrete component values used. For all the abovementioned reasons an imperfect fit seems inevitable. There is however an improvement in terms of the deviation of the EMG breakthrough as shown by fig. 5.3 where, at best case, it can be about 65% less at the amplifier's output.

Undoubtedly, the parallel RC used in place of the polarisation impedance Z_{WAR} is too simple to mimic the observed phase angle of real metal electrodes, which is frequency-independent and has a constant value over a wide frequency range (e.g. −45° for a Warburg element). Instead, it has been suggested in the literature that a semi-infinite transmission line can be used to model the effects of uneven surface topology that lead to frequency dispersion – a term often used in electrochemistry to denote a frequency dependence which deviates from that of an idealised model of the interface – and

consequently to the observed CPE behaviour[6] of metal electrodes. Moreover, by modelling the CPE with a transmission line we believe can also address the first of the two abovementioned problems. Three different methods of obtaining a more accurate CPE are given in §5.3.4.

5.2.3 Adaptive mQT evaluation

The problem when trying to make an electrical model of the physical or chemical processes in tissue is that often it is not possible to mimic the electrical behaviour with ordinary lumped, physically realisable components such as resistors, capacitors and inductors. Examples of the difficulties involved in such a task are modelling the CPE as a semi-infinite number of lumped components, and the double-layer interface in the electrolyte in contact with an electrode surface whose capacitive properties are known to be voltage and frequency-dependent. Thus, neutralising the multiple – in reality – sources of EMG interference present at the recording site is more difficult to address. Despite the difficulties, the use of a simple parallel RC network in place of Z_{WAR}, although conceptually incorrect, worked well as an initial "proof of concept", helping us to realise whether or not the adaptive neutralisation approach with the mQT is advantageous.

Knowing the relative simplicity of the 5-component Randles circuit of fig. 5.1 arranged for trimming, it is unknown how easy it will be to tune each component in order to adapt for the changes at the interface and moreover how varying one component affects the value of the others in terms of balancing the recording electrodes. To make things worse, as tissue grows around the electrodes the recording configuration will become unbalanced and as such the trimming network will require adjustment, even if an adaptive trimming impedance Z_{trim} is used. Additionally, it should be mentioned that although this study was based around Pt electrodes it has been shown by [Pollak, 1974c] that the magnitude and frequency dependence of the electrode impedance of highly polarisable electrodes is, in general, similar[7]. This is convenient, as the proposed solution does not strictly depend on the electrode material.

Although an acceptable fit was possible with the Randles circuit model for one tissue conductivity, a more adequate fit can be obtained using circuit models which can account for more complex representations of the electrode-electrolyte interface. More specifically, appropriately modelling the effects of uneven surface topology (i.e. surface porosity/roughness) that lead to the observed frequency dispersion of the electrode impedance can offer significant advantages in fitting (i.e. a circuit model that is easier to tune and adapts better to the electrode impedance data), as is shown later in the chapter.

---

[6] As correctly pointed out by [Jorcin et al., 2006], the frequency dispersion is generally attributed to a "capacitance dispersion" expressed in terms of a CPE, especially in ideally polarisable electrodes. In a paper by [Kurtyka and de Levie, 1992] it was demonstrated via a numerical simulation that a non-homogeneous interfacial capacitance gives rise to frequency dispersion. Additionally, [Pajkossy and Nyikos, 1992] have even demonstrated (again via a numerical simulation) the appearance of a CPE behaviour by assuming wide interfacial capacitance distribution (i.e. non-uniform capacitance density) on a planar electrode.

[7] Comparisons of the magnitude and phase characteristics performed in [Pollak, 1974c] show that highly polarisable materials like platinum, gold, tungsten, stainless steel, and even nickel exhibit essentially a similar frequency behaviour.

5.3 Frequency dispersion of electrode impedance

A way of making the passive neutralisation technique of Chapter 3 adaptive, by modelling the electrode-electrolyte impedance profile of our recording electrodes was presented, albeit with moderate results. The reasons for this were discussed in §5.2.2 and §5.2.3 where a justification for the source of poor results was given mainly in the way the CPE behaviour of our electrodes was (inadequately) represented by a simplistic parallel RC network. Additionally, it was concluded that the 5-component circuit used to compensate for interference was not easy to tune and therefore not practicable. Seeking for ways to improve the interference neutralisation performance of the mQT so that no adjustment is required, we realised that we need to use models that better resemble the electrochemical properties of our recording Pt electrodes. Fig. 5.4 shows a typical 3-component model of the electrode impedance Z_e that can be used for such purpose. An important component of the model is the polarisation impedance Z_{CPE}, referred to as constant phase angle or element, since the phase angle exhibited by blocking electrodes like Pt is independent of frequency.

The so-called frequency dispersion (or frequency-dependence) of the impedance of a metal electrode-electrolyte interface is a well known experimental fact, observed in the absence of faradaic processes and being attributed to the inhomogeneity (i.e. roughness) of the electrode surface. The presence of surface roughness (e.g. a porous layer) at the interface influences the ideal capacitive behaviour of electrodes and consequently the shape of their impedance curves (i.e. the rougher the surface, the larger is the deviation from ideal capacitive impedance and the greater the frequency dependence). Nonetheless, such an electrode pseudo-capacitive response can be appropriately modelled by a CPE impedance Z_{CPE}.
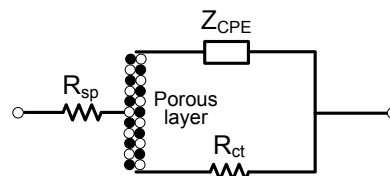
Figure 5.4: Equivalent small-signal electrical circuit of a porous electrode-electrolyte interface. R_{sp} is the spreading resistance in the tissue near the electrode (i.e. series resistance of the electrode conductor R_m is ignored). The pseudo-capacitive polarisation impedance is Z_{CPE} which is used to model the non-linear effects of the electrode interface. In text, Z_{CPE} shunted by the charge transfer resistance R_{ct} is the interface impedance $Z_{inter}=R_{ct}//Z_{CPE}$.

In the following sections we will explain qualitatively how to emulate a CPE and by using it as part of an electrode-electrolyte interface model, accurately describe the frequency response of metal electrodes. The fundamental difference with the electrode impedance data fitting example of §4.4 is that we are now aiming to depart from the empirical eqn. 4.5c of Cole and construct a real CPE which can be implemented in hardware. Modelling the ideal CPE as part of the electrode-electrolyte interface impedance Z_{inter} has already been discussed in Chapter 4, however, here we will take this a step further. We begin by documenting the background theory and properties of the CPE and the work that others have done on rationalising it and appropriately modelling it. For this

purpose, great emphasis is given on the effects of geometrical inhomogeneities of the electrode surface.

5.3.1 The mystifying CPE impedance

The impedance of a cell consisting of a working solid electrode immersed into an electrolyte with a distant and indifferent electrode should ideally be represented by a series RC circuit provided no charge passes between the working electrode and the electrolyte (i.e. in the absence of faradaic reactions). As such, $Z_e(\omega)=R-j/\omega C$, where R represents the ionic resistance of the electrolyte, and C represents the capacitance of the ideally polarisable electrode-electrolyte interface. However, this ideal representation does not give an adequate description of the ac response of the interface as a real electrode surface is not perfectly flat and the impedance of cells of this type can be accurately described[8] by $Z_e(\omega)=R+K(j\omega)^{-\alpha}$.

The ideally polarisable small signal ac impedance of metal electrodes, like Pt, is proportional to $(j\omega)^{-\alpha}$ over a wide range of angular frequencies ω (e.g. [Bates et al., 1988] indicates frequencies below ≈50 kHz) where the polarisation impedance Z_{CPE} is dominant and therefore can be successfully described by the empirical eqn. 4.5c of Cole, where $j=\sqrt{-1}$, K is a measure of the magnitude of this pseudo-capacitive impedance and independent of ω (i.e. a constant), and finally α takes values between 0 and 1 indicating the departure from pure capacitive behaviour[9]. Thinking in terms of the model of fig. 5.4, since in polarisable electrodes R_{ct} is very high, it is obvious that Z_{inter} will have a fractional power frequency dependence (FPFD) on ω, while it is worth noting that this dependence is a general characteristic observed for both liquid and solid ionic electrode conductors.

As an example, fig. 5.5 illustrates the constant phase angle φ_{CPE} exhibited, in a limited frequency range, by a 90% Pt-10% Ir sphere electrode; the electrode whose impedance was plotted in fig. 4.11. The same electrode was later used as part of the in-vitro experiment (c.f. §5.7.3.4). Three regions can be distinguished with the help of the phase plot. At relatively low frequencies the phase is constant meaning that there is a linear relation between Z' and −Z''. Progressing to intermediate frequencies (second region) a smooth inflection arises due to the effective distributed RC of the porous interface, coming into a third region where the distributed double-layer capacitance of the interface is manifested by the resistance of the electrolyte.

Many workers have attempted to explain the physical processes and the observed frequency dispersion exhibited by metal electrodes in solid or aqueous electrolytes and sought to relate the FPFD exponent α – hereafter written as frequency exponent α – to the degree of roughness and the geometry of the electrode surface (i.e. α approaches 1 as the electrode surface is made smoother; then Z_{CPE} of fig. 5.4 is equal to the double-layer

---

[8] As was illustrated by the fitting example of fig. 4.11.

[9] The exponent α is fractional and its experimental value for ideally polarisable electrodes is between 0.5 and 1 [Scheider, 1975], usually lying in the narrower region between 0.75 and 0.95 [de Levie, 1990]. Others [McAdams, 2006, p. 125] mention that α typically has a value of 0.8 for many biomedical electrode systems. In general, with solid electrodes in aqueous electrolytes in the audio and sub-audio frequency range one should expect the frequency response of Z' and −Z'' to be no longer proportional to $\omega^{-0.5}$ (c.f. eqn. 4.10) but to some other power of ω, while values of $\alpha<0.8$ are usually observed with porous electrodes.

capacitance per unit area). On the contrary, the CPE coefficient K depends on the electrode area and the electrolyte conductivity (i.e. K decreases with increasing electrolyte conductivity and surface irregularities, as rough electrodes have a larger surface area comparing to smooth ones[10]). Additionally, it is often found that the value of α can decrease with increasing temperature [Bates et al., 1986; Wang and Bates, 1986, fig. 4].
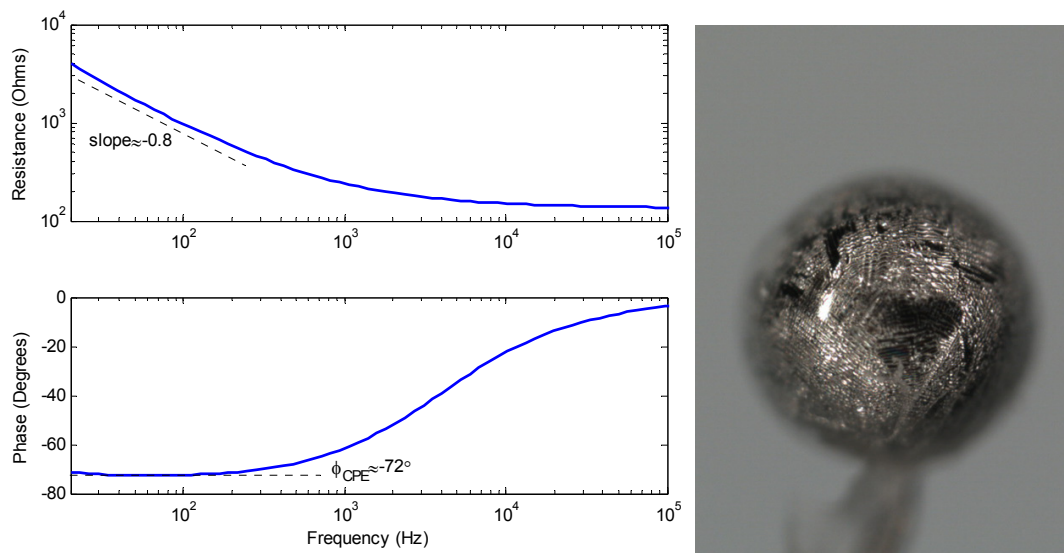

Figure 5.5: Resistance and phase of a sphere electrode (surface area≈2.32 μm^2) plotted against frequency (i.e. 20 Hz to 100 kHz). The real part of the sphere electrode impedance has a slope which according to eqn. 4.7a falls with frequency at a rate of α≈0.8 (on square axes). For this particular electrode, at frequencies higher than about 4 kHz the impedance is dominated by the resistance of the 0.9% NaCl electrolyte. At right is a photo of the sphere electrode magnified 32x by an optical microscope. The microscopic grooves on the electrode surface are responsible for the observed frequency dispersion and CPE behaviour of the electrode impedance.

Finally, it has been demonstrated by several workers[11] that the frequency dispersion of electrodes in solid or aqueous electrolytes is intimately related to the roughness of the interface with efforts being made to model the surface unevenness (e.g. pores/grooves, hills and valleys) as distributed RC elements [Scheider, 1975; Wang and Bates, 1986], and fractals [Liu, 1985; Nyikos and Pajkossy, 1985; Sapoval, 1987]. Although surface roughness might not be the only physical explanation to be accounted for[12], in this work

---

[10] Although it may be obvious, one might think that by roughening the surface of a metallic electrode we decrease its size (i.e. the real area of the electrode decreases by removing metal), and therefore we increase its impedance. However this is not true, as what we actually achieve is to increase the effective (active) surface area of the electrode due to the formation of microscopic hills and valleys on its surface, while the geometric (macroscopic) area remains almost the same. Therefore, by roughening the electrode surface we increase its interfacial capacitance (i.e. K is inversely proportional to the double-layer capacitance; c.f. §4.3.2) and at the same time reduce the phase angle of the electrode impedance as the electrode surface stops acting as a perfect capacitor.

[11] Refer to §5.3.3.1.

[12] After reviewing the majority of the literature on the topic, the main view that prevails is that with solid biomedical electrodes, irregularities on the surface alone can be the cause of frequency dispersion and non-ideal behaviour (e.g. capacitance dispersion) of the interfacial impedance. Another likely cause could be specific adsorption [McAdams, 2006, p. 125]. According to [Pajkossy, 2005], there are currently two trends

we assume that irregularities of the surface (i.e. geometrical inhomogeneities), and therefore non-uniform potential and current distribution, is the *main* factor affecting the CPE behaviour of metal electrodes[13]. In addition, the geometry of a solid electrode is never perfectly smooth, and therefore at this early stage it is useful to establish the kind of geometric irregularity that we will be dealing with in this work. According to [de Levie, 1990; Pajkossy, 2005] there are 3 size ranges of geometric irregularities: a) the large, *macroscopic*, surface roughness features which are visible to the naked eye (say >0.1 mm); b) the *microscopic* roughness due to scratches, pits, grooves, pores etc. in the size range of about 10 nm to 100 μm which can be made visible by optical or scanning electron microscopes (e.g. fig. 5.5); c) the *atomic scale* roughness, due to the presence of steps, kinks, and dislocations making the surface uneven on the atomic scale (say <10 nm). Since, the frequency dispersion and CPE behaviour of solid electrodes is, according to the literature, linked to the microscopic geometry of an electrode surface, the use of the term "roughness" in this work will always denote geometric irregularities of microscopic nature. Conversely, macroscopic aspects of cell design can be found in many electrochemical engineering textbooks, whereas geometries at the atomic scale, although often related with microscopic roughness (i.e. a mechanically coarsened surface carries a great number of dislocations), these deal with energetic inhomogeneities as a result of roughness (e.g. activation energies of adsorption-related processes are linked to surface energetics) [Pajkossy, 2005]. Thereby, both macroscopic and atomic scale roughness will not be explicitly dealt with in this work.

5.3.2 The single-pore model

One way of understanding the origin of the CPE is through the single-pore model of a rough interface, shown in fig. 5.6 together with its equivalent circuit. Such circuit offers an input impedance Z_T whose ratio $Im(Z_T)/Re(Z_T)$ is independent of ω. More specifically, the roughness of the interface can be modelled with pores on the surface of the electrode while the value of frequency exponent α can be related to the shape (i.e. geometry) of the pores [Wang and Bates, 1986]. The impedance of each pore is approximated as a non-uniform RC ladder network[14] with a distributed resistance r(x) and capacitance c(x) which

---

for this non-ideal behaviour: a) physicochemical effects (i.e. adsorption-related processes) within the double-layer with roughness being implicitly irrelevant (i.e. the activation energies of adsorption-related processes are related to surface energetics and rough surfaces are energetically inhomogeneous), b) microscopic roughness having an effect (i.e. coupling of solution resistance with interfacial capacitance) in the solution bulk region rather than the interface. As per the experimental investigations of Pajkossy presented in [Pajkossy, 2005], the former cause seems to prevail. Other possible causes are beyond our concern, nonetheless, some can be found in [Jorcin et al., 2006; section 1] and [Research Solutions & Resources, last accessed in March 2010], if required.

[13] Owing to the pseudo-capacitive nature of a rough interface, it is true that the (dispersive) interfacial impedance can be successfully approximated by a CPE. As rationalised by [Pajkossy, 2005], due to surface roughness, current density inhomogeneities appear along the surface and, as a result, the effective solution resistance varies along the interface, i.e., it is larger for surface elements in the bottom of voids/pores and smaller on the top of protrusions. Thereby, solution resistance and interfacial capacitance are inseparably coupled and as such this effect can be interpreted in terms of the CPE coefficient K and frequency exponent α.

[14] Both (discrete) ladder networks and transmission lines with distributions of RC-pairs in this work have the exact same meaning – i.e. ladder networks are typically used in filter theory while transmission lines are

are functions of the distance x into the pore. By considering the electrode-electrolyte interface to be represented by a distribution of pores (i.e. a distribution of CPEs) along the surface of the electrode metal, the exhibited value of the frequency exponent will be a result of the weighted average of the distribution, since the members of the distribution will most probably have different frequency exponents [Bates et al., 1986]. According to [Wang and Bates, 1986], if each pore is assumed to have an impedance given by eqn. 4.5c, and the various pores are described by a distribution in the frequency exponent α, then the resultant impedance can still be described roughly by eqn. 4.5c with some effective value of α. This is especially true when the distribution is not too broad.
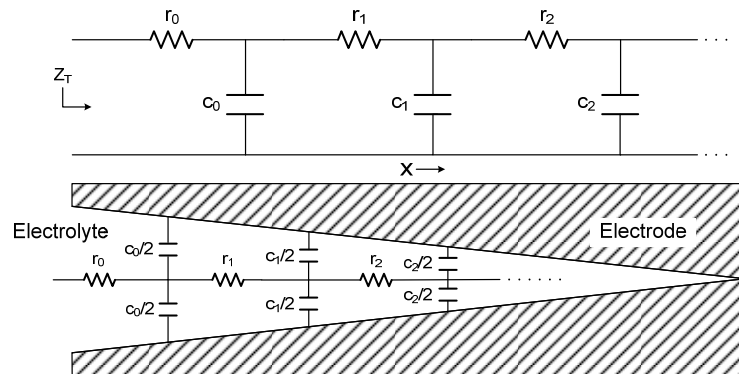

Figure 5.6: A non-uniform/tapered RC ladder network model for a one-dimensional V-shaped pore of semi-infinite depth inside an electrode surface. The specific resistivity of the electrolyte in the pore and the double-layer capacitance per unit area at the interface increases and decreases respectively with the distance x down the pore. The smaller the angle of the V-shaped pore (i.e. the lower its distributed interfacial double-layer capacitance), the smaller the frequency exponent α. An RC ladder network of this form with an input impedance Z_T based on Schrama's continued fractions can be used to emulate the frequency response of a CPE (c.f. §5.3.4.3).

The single-pore model is based on a one-dimensional potential distribution[15] which represents a pore of average (i.e. semi-infinite) pore length. In this work, as a first approximation, we assume a uniform distribution of various pore sizes on the electrode surface that are only of conical shape and, inside each pore, there are no pores of smaller

---

used in the context of energy transfer to model e.g. optical fibres, waveguides and microstrips. For consistency reasons from now on we will only use the term "ladder network" to denote a series chain of unbalanced L half sections with position-dependent or –independent Rs and Cs. Conversely, the term "transmission line" will only be used where necessary, e.g., to accurately reference others' work. Besides, a transmission line with distributed Rs and Cs per unit length of the line can be approximated by a ladder network when divided into small (lumped) circuit elements corresponding to a unit length, as has been pointed out by [Wang, 1987]. Finally, realisation of a CPE by an RC ladder network is not very easy, while only a CPE with α=0.5 is (at first instance) achievable [Biswas et al., 2006].

[15] In the case of pores, the potential distribution can be characterised by only one coordinate along the pore axis. In particular, the assumption of virtually infinite length in the z-direction (i.e. perpendicular to the paper) reduces the problem to two-dimensions [de Levie, 1965]. A further assumption that each V-shaped pore may be described as a non-uniform RC ladder network having a longitudinal impedance which varies with distance x down the pore can reduce the problem to being a one-dimensional one. This involves the neglect of the curvature of the equipotential lateral surfaces inside a pore (i.e. small pore angle; therefore the equipotential surfaces are parallel planes and the potential inside the pore is assumed to be only a function of x) since the potential distribution is not one-dimensional in pores with a greater angle (say 10 to 30 degrees) [Pajkossy and Nyikos, 1988].

sizes (i.e. current penetration depends on both the size and the location of the pore [Wang, 1988b]). Moreover, the electrolyte solution is homogeneously distributed inside the pore, while we ignore the effect of the layer of electrolyte just outside the pore, where the equipotential planes are still distorted by the electrode surface rugosities, contributing to the over-all frequency-dependence, which cannot be "captured" by a one-dimensional transmission line [de Levie, 1990]. Thereby, the single-pore model of fig. 5.6 provides a single CPE which is representative to the average physical characteristic of a particular electrode surface. Hence the given model name.

Thinking in terms of the validity of the single-pore model of fig. 5.6 and whether it can be utilised for the representation of the CPE, one may simply think as follows. The transfer of electric charge across the interface between the electrode and the electrolyte encounters an impedance which consists of the ohmic resistance in the electrolyte and the interfacial capacitance. Physically, the electric current encounters ohmic resistance in both substances (i.e. access resistance) and a capacitance across the interface (i.e. double-layer capacitance). At high frequencies this ionic current can penetrate very little inside the pore since the interface distributed capacitance is shorted. Therefore, the high frequency phase angle response cannot be represented with a CPE. This is true, since at high frequencies the phase angle is not constant but, instead, tends to zero due to the presence of the electrolyte resistance (c.f. fig. 5.5). The model of fig. 5.6 takes this into account.

Before moving into discussing the various ways of modelling and implementing a real CPE it would be first appropriate to present what has been achieved by other workers on the topic. The contribution of surface roughness and pore shape on the electrical properties of the interface is taken into consideration in this discussion.

5.3.3 Modelling the roughness of electrodes

5.3.3.1 Studies on the electrochemical impedance

Work on the CPE impedance and the various parameters characterising its behaviour was essentially initiated in the mid-1970s when [Bottelberghs and Broers, 1976] investigated the interfacial behaviour of Na_2WO_4–Na_2MoO_4 solid electrolytes in contact with Pt paint and polished Pt disc electrodes in air, oxygen, and nitrogen atmospheres in the range of 0.1 Hz to 32 kHz and at temperatures between 500 and 660 °C. They observed a particular type of impedance behaviour (which they termed constant phase angle impedance) with different frequency exponents α for the painted Pt electrodes[16], but did not use models to analyse this behaviour. Instead, they hypothesised (correctly) that the highly inhomogeneous current distribution effects – a surface which is rough cannot be expected to have a uniform current density – might be the culprit.

Around the same time, [Armstrong and Burnham, 1976] studied the effect of roughness on the impedance of the interface between a solid electrolyte (i.e. two types were used; a single crystal and a sintered disc of β alumina) and a blocking electrode (i.e. gold) in the frequency range of 1 to 10 kHz. The surfaces of the two electrolytes were polished and

---

[16] Apparently, the CPE behaviour was not involved with polished Pt electrodes. Perhaps, the use of Pt paint on electrodes created a highly polarisable rough interface, thus emphasising the effect of the CPE at those frequencies.

then progressively roughened using coarser grades of diamond resulting in the formation of grooves and pits. Showing results of ac impedance measurements and scanning electron micrographs of the electrolyte surface after different polishing treatments, the two workers concluded that the variation in the phase angle is caused by the different extents of surface roughening (i.e. the rougher the surface, the lower the phase angle and consequently the value of the frequency exponent α; c.f. eqn. 4.8a). This was true for the sintered disc but not for the single crystal of β alumina, whose phase angle remained unaffected[17] from the roughening process in the frequency range studied (within experimental error).

The relationship between the microstructure of a Pt metal-solid electrolyte interface and its CPE impedance was investigated for various surface preparations (i.e. polished or saw-cut surfaces) of single crystal and polycrystalline β and β″ alumina by [Bates et al., 1986]. Impedance measurements were performed on cells in vacuum from 0.1 Hz to 10 MHz and at temperatures from −134 to 400 °C, indicating that the frequency exponent α depends in general on the texture of the metal-electrolyte interface and in particular on the size and distribution of features on the surface of the electrolyte, and also on temperature. In principal, it was found that larger values of the frequency exponent α were associated with smaller features (i.e. width of pits or scratches)[18], however, different values of α were observed for the single crystals and the polycrystalline specimens with comparably sized features. The latter might be due to a difference in the distribution of features on the surface of the (solid) electrolytes. With regards to the temperature dependence of the frequency exponent [Bates et al., 1986] have shown that although α is larger for smooth cell contacts at low temperatures, it approaches the same value for smooth and rough contacts at high temperatures. The conclusion was that this decrease in α might be a result of damage to the metal contacts with increasing temperature.

Rammelt and Reinhard [Rammelt and Reinhard, 1990] studied the applicability of CPE to the estimation of roughness of solid metal electrodes. To this end the impedance spectra from 0.1 Hz to 20 kHz of a polycrystalline iron disk working electrode of a 0.5 cm^2 area (and of other various metals, like different types of steel and Pt) was measured at room temperature in a pH 1 H_2SO_4 (i.e. sulphuric acid) solution, and under various mechanical surface polishing pretreatments with emery paper of different grain size. They found that the frequency exponent α (and consequently the phase angle of the CPE)

---

[17] According to [Armstrong and Burnham, 1976] this phase angle deviation probably arises from the pulling out of crystallites from the surface of the crystal instead of causing pitting from roughening. For the single crystal of β alumina, only the magnitude of the double-layer capacitance per unit area was affected by the roughening process (i.e. the series capacitance of the sample was reduced while the complex impedance slope was constant at about 90°). This might be due to the real surface area of the electrolyte, or perhaps, the effective area of contact between the electrolyte and the gold, decreasing with surface roughness.

[18] This contradicts the caption remark of fig. 5.6, i.e., the smaller the angle of the V-shaped pore, the smaller the frequency exponent α. Most probably the terms "angle" and "width" have a different meaning in this case, where "width" perhaps denotes the latitudinal surface width of the pore when looking into it. Thereby, it is important to emphasise that according to footnote 10 and figure caption 5.6, the double-layer capacitance C_{dl} depends both on the surface texture (e.g. angle of pore) as well as on the surface area of the electrode, i.e., the distributed interfacial capacitance C_{dl} of a single-pore decreases but the overall equivalent C_{dl} exhibited by an electrode increases with surface roughness. This is true, since according to [Wang and Bates, 1986] "the impedance of an interface containing many pores can be calculated by placing the impedance of the individual pores in parallel" and this is the reason why overall C_{dl} increases.

unequivocally reflected the roughness of solid electrodes, being independent of the electrode material, and that the impedance of the working electrodes is in the form of depressed[19] rather skewed arcs.

5.3.3.2 The transmission line approach

Many attempts have been made to interpret the effect of surface geometry and structure on the magnitude and phase of the interface impedance. One of the first modelling treatments was done by de Levie who postulated that the impedance of pores on the electrode surface could be represented by transmission lines. His hypothesis was that microscopic roughness of the electrode surface is directly related to the frequency dispersion. This was also later linked by [Scheider, 1975] to the uneven current distribution on the electrode surface as a result of its rough interface, viz. current flow will not be perfectly normal to the surface causing uneven charging of the double-layer capacitance. According to [McAdams et al., 1995b], de Levie's pore model successfully explained qualitatively many aspects of the interface impedance, however, the many assumptions and approximations made, limited its ability to represent accurately measured impedance data.

De Levie studied the effect of electrode surface roughness and used pores in form of long cylindrical channels [de Levie, 1963], and V-shaped grooves and conical pits [de Levie, 1965] to model the impedance of pores in a blocking metallic electrode. In [de Levie, 1963] he represented a long channel pore of uniform diameter using a uniform semi-infinite transmission line where the solution in the pore was assumed to be homogeneous so that its conductivity does not depend on the distance down the pore[20], while in [de Levie, 1965] he represented V-shaped grooves using a tapered transmission line model relating, for ideally polarisable electrodes, the apparent phase angle of the cell impedance to the geometric parameters of the groove (i.e. groove depth and angle). As per de Levie's arguments, each electrolyte-filled porous channel can be approximated by an RC transmission line; the resistance per unit length r is determined by the resistivity of the electrolyte and the channel cross-section, while the corresponding capacitance c by the double-layer capacitance per unit area and the interfacial area per unit length of channel [Wang, 1987]. For the long channel pore the impedance was found to be that of a Warburg element, meaning de Levie's model could only interpret CPE behaviour[21] where $\alpha=0.5$, unless the r and c elements of the transmission line have specific spatial dependence (i.e. position-dependent r and c) as in the case of a tapered line. Finally, two graphs that illustrate the effect of different pore shapes on the measured electrode impedance are shown in fig. 5.7. Geometry of the voids, and therefore the type of current density distribution on the electrode surface, is important for the frequency-dependence of the CPE impedance. In addition, notice that the V-shape pore (i.e. void no. 5 on the RHS graph of fig. 5.7) – resembling to the single-pore model – exhibits a clear CPE in a wide frequency range (comparing to the rest of the voids).

---

[19] With increasing roughness the diameter of the impedance semicircular arc does not only decrease (i.e. because R_{ct} decreases) but the semicircles become more and more depressed.

[20] According to [Kramer and Tomkiewicz, 1984] de Levie suggested that each pore in a porous electrode may be thought of as having a uniformly distributed electrode and electrolyte resistance throughout its length.

[21] It is later shown that a uniform RC ladder network does indeed exhibit a CPE behaviour with $\alpha=0.5$.
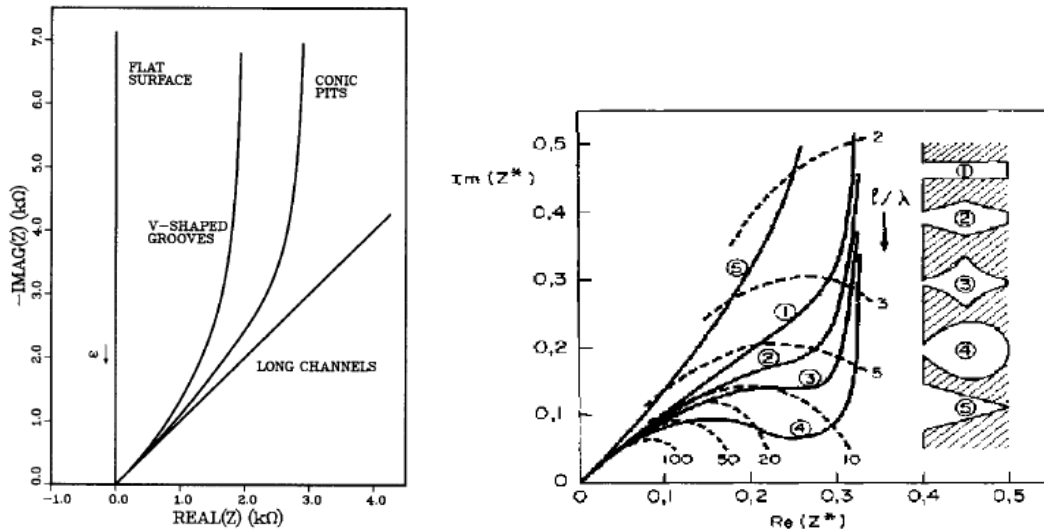
Figure 5.7: Graphs of the complex impedance of an interface with pores of different shape; (left) impedance loci of pore shapes studied by de Levie. His long channel model discussed in text is shown by the straight line forming a 45° angle with the real axis. The impedance of an ideal capacitive metal-electrolyte interface is shown by the vertical line denoting the absence of frequency dispersion. Graph taken from [Wang and Bates, 1986]; (right) Keiser and co-workers important extension work to pores of various specific shapes. Notice that not all voids exhibit CPE behaviour in the same frequency range. ℓ is the pore length and λ is a form factor (refer to the original reference, written in German). Graph taken from [Keiser et al., 1976].

In relation to the abovementioned work, [Kramer and Tomkiewicz, 1984] introduced the first random 3D network model to simulate the porous metal-electrolyte interface in respect to the long channel pore model by de Levie. By using computer simulation, they constructed a 3D cubic lattice model and calculated its complex impedance in the frequency range of 1 Hz to 1 MHz using passive elements. A comparison of the random network model (i.e. various distributions of pore location, depth, and/or width) with the long channel pore model yielded a qualitative agreement between the two (i.e. similarity in the shape of the impedance spectrum). Nonetheless, a major difference between the two models was the fact that in the random network the pores interact with each other as in a true porous electrode, while in the de Levie model each pore is kept separate from the others. Despite this, the qualitative agreement between the two models illustrates that de Levie's single-pore model is valid and need not be of complicated structure (e.g. have crosslinks between the pores) in order to emulate the frequency response of a rough electrode surface satisfactorily.

In general, RC networks can be utilised for realising an impedance approximating $(j\omega)^{-1/2}$ over a wide frequency range $\omega_0 < \omega < \infty$, where ω_0 depends on the parameters of the RC network and those of the terminating impedance, while the number of elements of the network increases as the bandwidth increases. In particular, there is a plethora of publications on the theory of distributed and lumped RC networks which provide a constant angle impedance, nonetheless, documenting those is out of the main focus of this chapter (and work). However, a good starting point for the interested reader can be the work of [Roy and Shenoi, 1966].

5.3.3.3 Introduction to the fractal geometry approach

In a different method to modelling the roughness of the electrode-electrolyte interface, several workers have adapted Mandelbrot's work on the theory of fractals[22] [Mandelbrot, 1982] in an attempt to derive an expression that would relate the roughness of the electrode surface to the interface impedance, after realising, that the geometry of a practical interface often contains the same or similar structural features at various scales (i.e. self-similar interface). According to several developed fractal models, the impedance due to the fractal nature of the interface, and in particular the frequency exponent α, is related to the fractal dimension of the interface, while this relation is model-dependent. Thereby, the most relevant features of the time or frequency behaviour of the interface can be described without the need for a detailed knowledge of its geometric fine structure but with a global description of the effect of interfacial roughness. Such fractal models can be broadly classified, as per [McAdams et al., 1995b], into three categories: hierarchial, fractal branching of single pores [Liu, 1985]; fractal distributions of surface pore diameters [Sapoval, 1987]; fractal scaling of the interface [Nyikos and Pajkossy, 1985]. Here, only the work of Liu and separately of Nyikos and Pajkossy is discussed. Documenting other fractal models, or certain variations of the above, will not be taken up here, nonetheless, if necessary, a review of the models developed for describing the impedance of fractal electrodes may be found in [Nyikos and Pajkossy, 1990] and [Pajkossy and Nyikos, 1990].

For reasons of comprehension an example of a particular fractal object, shown in fig. 5.8, will now follow. The term "fractal" was given by the father of fractal geometry, Benoit Mandelbrot in 1975, and is used for objects that are: a) irregular, yet b) look the same under different scales of magnification; in other words illustrate (at least approximately) self-similarity. To create a fractal you start with a simple shape and duplicate it successively (using the method of recursion) according to a set of fixed rules. For example, imagine a line segment of length ℓ, as in fig. 5.8, being divided into three equal parts (step 0). We form an equilateral triangle pointing outwards using the middle third of the line as its base and remove the base leaving a broken but continuous line (step 1). The line is now composed of four linear segments, each of length $\ell/3$, while the total length of the curve is $4\ell/3$. Repeating the above process for each of the four line segments a more complex line is obtained (step 2) which consists of 16 straight segments each of length $\ell/9$, so that the total length is $(4/3)^2$ times ℓ. Keep repeating this process n times (step n) leads to a line with 4^n segments of length $\ell/3^n$, and with a total length of $(4/3)^n$ times ℓ. The result is a fractal von Koch "monster" curve[23] – due to having an infinite length, while its area remains finite – named after Helge von Koch who first described it in a 1904 paper. Examples of fractals include the von Koch snowflake constructed from three von Koch curves of fig. 5.8, while coastlines, clouds, lighting, and vegetables (e.g. cauliflower and broccoli) are regarded as real-life examples of fractals, being statistically self-similar.

---

[22] According to which, a single parameter – the fractal (or Hausdorff) dimension d – is capable of characterising a rough interface without the need of a detailed description.

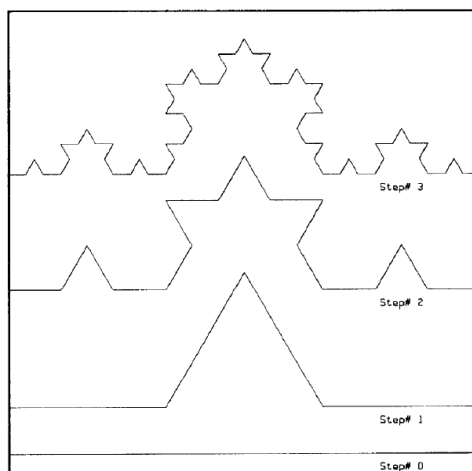[23] Not all fractal models are "monster" curves.

Figure 5.8: The first few steps of the recursive construction of the triadic von Koch curve. The curve is continuous and nowhere differentiable due to the infinite number of zigzags between any two points on the curve, while its parts are similar to each other and to the whole, i.e., it illustrates an infinitely repeating self-similarity when it is magnified. Refer to text for a detailed description of construction. Figure taken from [Nyikos and Pajkossy, 1985].

At this point it would be appropriate to define another important quantity in respect to fractals; the fractal dimension d of objects. More specifically, in fractal geometry the fractal dimension is a measure of irregularity of the boundary of the object and a (statistical) quantity that gives an indication of how completely a fractal appears to fill space, as one zooms down to finer and finer scales of magnification. Every time the resolution is improved by a factor A the number of discernable segments increase by a factor N, i.e., $N=A^d$ and the fractal dimension of the object is $d=\ln N/\ln A$ [Liu et al., 1986]. In the case of the von Koch curve the fractal dimension is $d=\ln 4/\ln 3 \approx 1.26$[24]. Therefore, d is equal to 1, 2 and 3 for a line, an area and a volume, respectively – the fundamental elements of Euclidean geometry – indicating that the von Koch curve has properties intermediate between those of a one- and two-dimensional object, while it should be mentioned that for de Levie's single-pore model d=1.

5.3.3.4 Fractal models of a rough interface

Le Mehaute and co-workers [Le Mehaute and Crepy, 1983] were the first to notice the possible use of fractals for describing the electrochemical behaviour of porous interfaces, and the first to try to relate the frequency exponent α with the fractal dimension (of the surface) d_s of a rough interface[25]. Le Mehaute gave the word "fractance" to describe such

---

[24] For the von Koch curve A=3 to obtain self-similarity when blowing up the curve by a factor A (i.e. the length of the magnified segment will be 3 times that of the original curve). In general, an object is considered to be fractal when $N=A^d$ results to a certain d value which is in the full range between 0 and 3.

[25] To avoid confusion, there are two ways of expressing the fractal nature of the electrode-electrolyte interface, i.e., the fractal dimension d, and the fractal dimension d_s of the electrode surface area, both related as $d_s=2+d$. This relation was developed by Pfeiffer and co-workers in 1983 who have shown that surfaces in heterogeneous catalysis are naturally rough in the microscopic scale, and the roughness can be described in terms of a fractal dimension between 2 and 3 [Liu et al., 1986].

an impedance and proposed the relation $\alpha=1/d_s$, nonetheless, his presented theory was not completely free of arbitrary steps and in certain cases not well justified. Despite its flaws, the introduction of the fractal concept as a possible mathematical tool for calculating electrode impedance was at the time overwhelming.

Inspired by the observation of de Levie that polished metal surfaces often have grooves of jagged edges, [Liu, 1985] proposed a fractal Cantor bar-like model to represent the interface between a rough blocking electrode (i.e. R_{ct} is neglected) and an electrolyte having the property of CPE, where the frequency exponent α is related to the fractal dimension d and therefore to the geometry of the interface, as $\alpha=1-d$. The fractal dimension of a rough surface as measured by the area under different length scales (i.e. different magnification) can be found to be $d_s=2+d$. Consequently, we can relate the exponent directly to the fractal dimension of the electrode surface d_s, i.e., $\alpha=3-d_s$ with $2<d_s<3$ (e.g. $d_s=2$ for a smooth surface).

Although Liu's model relates the surface geometry and the frequency exponent α, it is not a realistic model of an actual interface because any real surface will not be regular with a well-defined scaling ratio, as in the case of Liu's symmetrical fractal model, but randomly disordered (i.e. real surfaces can have a range of scaling ratio and they are self-similar in a statistical sense). The effect of disorder by applying random scaling and branching on Liu's fractal model was examined by [Kaplan and Gray, 1985] who found Liu's relationships between α and d_s for the regular fractal to still hold for the random fractal surface, while it was speculated this relation to also hold approximately true for real surfaces [Liu et al., 1986]. In the same valid seeking manner [Kaplan et al., 1986] further examined the inverse Cantor bar structure, defined by interchanging the metal and electrolyte to see "...whether the system still exhibits the CPE property". Under certain conditions the inverse Cantor bar yielded the same exponent as was found for the Cantor bar in [Liu, 1985], however, its frequency response was not determined.

Few year later, [Bates et al., 1988] examined the theory that relate the frequency exponent α with the fractal dimension d_s of the surface of a rough interface and found no obvious correlation between the two from experiments[26] using aqueous 0.1 M sulphuric acid electrolytes, and metal (i.e. Pt) and semiconductor (i.e. low-resistivity silicon with and without gold coating) electrodes. This was also consistent with the earlier findings of [Kaplan et al., 1987] who mathematically came to the conclusion that the frequency exponent α is not just a function of the fractal dimension d_s of the electrode surface. A similar conclusion was also reached by [Keddam and Takenouti, 1988][27]. In addition to

---

[26] Impedance measurements were made at frequencies from 0.1 Hz (and in some cases from 1 mHz) to 50 kHz with an ac pk-pk voltage of 50 mV or less, applied to the cell. Values of the frequency exponent α were determined by least-squares fit of the empirical CPE impedance (i.e. eqn. 4.5c) to $Re(Z_e)$ and $Im(Z_e)$ of the measured electrode impedance at frequencies (i.e. below than $\approx$100 Hz) where the effect of the electrolyte resistance was not dominant. The fractal dimension d_s of the surface of roughened electrodes (on scales less than 1 μm) was accordingly obtained with a profilometer. The electrode surface had previously been roughened by polishing with emery paper and alumina powder of varying grit size.

[27] As commented later by de Levie on this matter [de Levie, 1990], there is a factor of randomicity involved on the interfacial properties of even single-crystal electrodes. Therefore, one would not necessarily expect to find a simple correlation between the observed value of α and just one aspect of

their obtained results [Bates et al., 1988] also hypothesised that the shape of the protrusions on the surface of an electrode is one of the more important factors determining the value of the frequency exponent α. In particular, rounded or flattened protrusions give large exponents (α>0.9), while sharp protrusions give small exponents (α≈0.8 to 0.9). Despite of those findings, if the fractal dimension of the interface is defined in a way consistent with the current penetration concept[28] as in Liu's model, a simple relation such as α=3−d_s can exist [Wang, 1988b].

Nyikos and Pajkossy [Nyikos and Pajkossy, 1985] have mathematically shown through a theoretical treatment that microscopic surface roughness on blocking electrodes is of CPE form and that a blocking electrode with fractal self-similar surface behaves as a CPE. Although still fractal, their approach was different from Liu's; according to [Wang, 1988a], in Liu's model each groove subdivides into smaller grooves from one stage to another, whereas in the model of Nyikos-Pajkossy the electrode contains a distribution of grooves of various sizes, inside of which there are grooves of smaller sizes, in essence exploiting the symmetry properties of fractals (i.e. self-similarity). Using fractal geometry Nyikos-Pajkossy assumed that the electrode interface has a profile which follows the same self-similar scaling arguments, as the example von Koch curve of fig. 5.8, and assigned an effective fractional dimension d_s, which may take any value between 2 and 3, to the irregular electrode surface in order to characterise the surface structure in terms of the fractional exponent α, as α=1/(d_s−1). Hence, α can be regarded as a measure of surface irregularity and roughness. The main advantage of this approach was that "...it is completely irrelevant whether the irregularities are grooves, cracks, pores, whiskers or other structures as long as they obey a certain average symmetry", i.e., the surface is – at least statistically – self-similar no matter what the actual irregularities. This is true since the fractal dimension is a global property insensitive to structural features, nonetheless, their fractal impedance model did not include faradaic reactions[29] and diffusion processes[30] at the time. Additionally, in [Pajkossy and Nyikos, 1986] they verified their model experimentally[31] using Na_2SO_4 solutions (i.e. specific resistivities between 50 μS and 1 mS) and compared actual measured impedance data of fractal electrodes against Liu's theoretical model from [Liu, 1985]. Obtained results confirmed the accuracy of their fractal model and highlighted, by comparison on the same plots, the departure from their rival's.

---

interfacial randomicity, such as the fractal dimension of the interfacial profile, especially when the comparison involves a variety of electrode materials as in [Bates et al., 1988] case. A year later, [Pajkossy, 1991] described another method based on the Cottrell diffusion-controlled current measurement (i.e. change in electric current with respect to time) for the determination of fractal dimension, relating it this time to the frequency exponent α, as α=(d_s−1)/2.

[28] Liu's model involves the flow of ionic current from stage to stage, similar to the current penetration concept in the pore model, implying that Liu's fractal can be transformed into a pore.

[29] So that the true interfacial impedance is purely capacitive, denoting the use of a "blocking" electrode model.

[30] Explicit expressions for the effects of diffusion were later presented by de Levie in [de Levie, 1990].

[31] Two different working electrodes with a well-defined fractal dimension of the surface d_s were designed using copper plate segments placed on a PCB, resulting in d_s=2.50 and d_s=2.73.

Results of the Nyikos-Pajkossy publication sparked opposition between the supporters of Liu's model. In particular, Wang [Wang, 1988a; Wang, 1988b] compared Liu and Nyikos-Pajkossy fractal models by means of numerical calculations. He showed that Nyikos-Pajkossy fractal blocking electrodes prepared in [Pajkossy and Nyikos, 1986] do not give a FPFD impedance and consequently a constant phase angle behaviour. Additionally, his results contradicted the claims of the Nyikos-Pajkossy fractal model and directly questioned the agreement of their experimental data with theory found in [Nyikos and Pajkossy, 1985] stating that "...the discrepancies originate from the use of invalid assumptions in their theory..." – e.g. interfaces having an electrolyte-metal boundary in the shape of a generalised von Koch curve do not have a CPE impedance as Nyikos-Pajkossy claimed. Moreover, [Keddam and Takenouti, 1988] also carried out an experimental verification which seemed to contradict with the Nyikos-Pajkossy fractal model. The response from Nyikos-Pajkossy came immediately in [Pajkossy and Nyikos, 1988] claiming that Wang's calculation method was inappropriate either to prove or disprove their theoretical result and clarified the arguments in question in a way different from that of their previous publication[32]. While the debate with Wang continued [Wang, 1989], Nyikos-Pajkossy work has also received some support[33] [de Levie, 1990; Maritan and Toigo, 1990].

As a last piece to the puzzle, in 1990 Nyikos-Pajkossy published an excellent paper [Pajkossy and Nyikos, 1990] where, apart from offering a different kind of proof to their previously derived $\alpha=1/(d_s-1)$ equation, they most importantly provided a unified method which reproduced the results of 16 published fractal models, including the ones already discussed above. The key concepts in their methodology were symmetry and scaling laws[34]. Concluding, they have made a very important statement; the impedance spectrum of fractal blocking electrodes is determined by the whole cell construction rather than by the working electrode alone, in other words, the CPE is caused by inhomogeneities of the potential field of the solution which is determined by cell geometry (i.e. working and reference electrodes, in a two-electrode system) rather than by the working electrode alone, revealing, according to Nyikos-Pajkossy, the discrepancy of Wang's results to theirs. Therefore, a cell has to be designed in such a way in order to avoid a non-homogeneous current distribution at the metal-electrolyte interface, as an improper cell design can lead to frequency dispersion [Kurtyka and de Levie, 1992]. This last statement aptly calls out towards our earlier remark made in this work – which incidentally is the dominant view to date behind the frequency dispersion of electrodes – i.e. a geometrically inhomogeneous surface, and therefore current density inhomogeneities

---

[32] One of the arguments from [Pajkossy and Nyikos, 1988] was that Wang's method for calculating the impedance of a generalised von Koch curve blocking electrode – the fractal interface Nyikos-Pajkossy used to prove their model – is conceptually inadequate since a ladder network cannot serve as a topological model for two or three dimensional potential distributions, even if branched ladders are used.

[33] In a personal communication with L. Nyikos on February 2009 it became apparent that the conflicting results of [Nyikos and Pajkossy, 1985] and [Liu, 1985] are both correct but apply to self-similar and self-affine (i.e. scaling differently along different directions) interfaces, respectively.

[34] Equations connecting admittance functions of electrodes of different sizes for which there exist symmetry operations transforming the electrodes onto themselves. Therefore, relating system size and frequency rescaling to obtain self-similar potential and current density distributions [Pajkossy and Nyikos, 1990].

along the surface, is the major source for the frequency dependence of electrodes. In fact, as was experimentally shown by Pajkossy in [Pajkossy, 1994] using Pt electrodes and in [Pajkossy, 2005] using Au, Pt, and Ag electrodes, chemical inhomogeneities of interfacial origin (i.e. electrolyte ion adsorption effects) is also another important factor which should not be neglected. Nevertheless, it is this very statement and its blunt acceptance that will lead us to a solution that is both simple and plausible for the task.

5.3.4 CPE emulation

We would like to be able to mimic the behaviour of a CPE in a hardware implementation with the intention of using it in the mQT recording configuration for neutralising EMG interference. Thereby, for a design to be suitable for the purpose, it needs to fulfil a certain number of criteria which are the following:

- The CPE must exhibit a constant phase angle at least within the 500 Hz to 10 kHz ENG bandwidth of interest.
- A simple network with components which are easy to adjust to remove interference.
- Small size of passive components in order to keep silicon area and thermal noise to a minimum.
- A two-terminal device which can work in a fully floating arrangement.

A number of 3 different CPE modelling approaches, all based on RC ladder networks, will now follow. One can construct RC ladder networks with or without branching whose arrangement may or may not resemble the actual geometrical structure of a porous electrode surface and the topology of the current flow in an electrochemical cell. In this case, closely matching the geometrical surface structure of our recording electrodes is not necessary. The outcome is circuit models with an input impedance whose phase angle is independent of frequency, i.e., the key property of a CPE.

5.3.4.1 Polydimensional branching ladder networks[35]

In a paper published in 1975, Scheider, concerned with the frequency dispersion of the small-signal impedance between a blocking gold electrode and an electrolyte solution (mostly solutions containing chloride ions) used branched ladder networks with distributed properties and shown those to have input impedance of the form of a CPE [Scheider, 1975]. Although a thorough discussion of branched ladder networks and the actual link of those to the electrode surface roughness and current distribution was not attempted by Scheider, the author demonstrated that such networks can be used to obtain circuits with FPFD on ω. In what follows, it is shown (via a computer simulation) that this is indeed the case.

---

[35] The contents of §5.3.4.1 were partially presented in [Pachnis et al., 2009a].
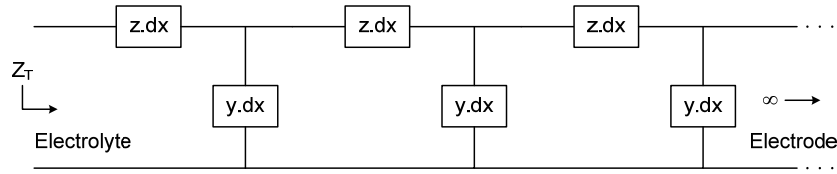
Figure 5.9: A generalised transmission line describing a one-dimensional pore of infinite length. z, y are lumped and therefore the specific resistivity and the double-layer capacitance of the interface are independent of the distance x down the line.

It is possible for one to make use of continued fractions to express the total impedance of an infinitely long transmission line (fig. 5.9) at a certain frequency range, as follows:

$$Z_T = z + \cfrac{1}{y + \cfrac{1}{z + \cfrac{1}{y + \ldots}}} = z + \cfrac{1}{y + \cfrac{1}{Z_T}} \qquad (5.1)^{36}$$

where z and y are the series impedance and parallel admittance per unit pore length x, respectively. In general, both the series z and the parallel y components of the network may be replaced by other transmission lines, which may themselves be branched [Scheider, 1975]. Solving for Z_T and subsequently for the resulting quadratic equation, we obtain the following expression:

$$Z_T = \frac{z}{2} + \sqrt{\frac{z^2}{4} + \frac{z}{y}} \qquad (5.2)$$

Although the line is infinitely long, assuming that the z, y components are lumped and the electrolyte homogeneous[37], by taking the limit of dx→0, z, y→0 but z/y is now a finite quantity. Hence, the above expression simplifies to:

$$Z_T = \sqrt{\frac{z}{y}} \qquad (5.3)$$

which is the characteristic input impedance of the now transformed line into a ladder network. Substituting for z=R (pure resistance) and y=jωC (pure capacitance) we have:

---

[36] Any two-terminal RC network can be written as the parallel combination of a number of series RC circuits. The total impedance is calculated numerically stage by stage starting from the electrode side toward the electrolyte side (from right to left). Thus, the continued fraction expression is obtained if we solve the following: $Z_{T,k}=z_k+(Z_{T,k-1}//Z_{c,k})$ where $Z_c=1/y=1/j\omega C$ and k is the stage number.

[37] Thereby, approximating the behaviour of the distributed double-layer capacitance and specific resistivity of the interface pore system by substituting the distributed Rs and Cs per unit length of the line with lumped ones of a discrete ladder network, while by assuming the solution in the pore to be homogeneous, those are independent of the distance x down the pore (i.e. the effect of frequency is ignored).

$$\varphi_{Z_T} = \tan^{-1}\frac{-\sqrt{\frac{R}{C}}\,\omega^{-\frac{1}{2}}\sin\left(\frac{1}{2}\frac{\pi}{2}\right)}{\sqrt{\frac{R}{C}}\,\omega^{-\frac{1}{2}}\cos\left(\frac{1}{2}\frac{\pi}{2}\right)} = -\tan^{-1}\frac{\sin\left(\frac{1}{2}\frac{\pi}{2}\right)}{\cos\left(\frac{1}{2}\frac{\pi}{2}\right)} = -45° \qquad (5.4)$$

Hence, for a semi-infinite, uniform, zero-order RC ladder network (c.f. fig. 5.10a) the phase angle remains constant to −45°. A Warburg impedance can thus be approximated with a uniform RC ladder network, as was done so by de Levie in 1963 for his long channel pore. If instead of a resistor we substitute $z=K(j\omega)^{-1/2}$ (i.e. empirical CPE equation with $\alpha=0.5$; essentially a zero-order ladder network) we then have a first-order series-branched ladder network (c.f. fig. 5.10c) with (in this example) CR branches. This results in a new phase angle of:

$$\varphi_{Z_T} = \tan^{-1}\frac{-\sqrt{\frac{K}{C}}\,\omega^{-\frac{3}{4}}\sin\left(\frac{3}{4}\frac{\pi}{2}\right)}{\sqrt{\frac{K}{C}}\,\omega^{-\frac{3}{4}}\cos\left(\frac{3}{4}\frac{\pi}{2}\right)} = -\tan^{-1}\frac{\sin\left(\frac{3}{4}\frac{\pi}{2}\right)}{\cos\left(\frac{3}{4}\frac{\pi}{2}\right)} = -67.5° \qquad (5.5)$$

A first-order branch may itself be branched, and this is branching of order 2 and so on. Thereby, using the same approach, for a second-order all series-branched ladder network we end up with a phase angle of:

$$\varphi_{Z_T} = \tan^{-1}\frac{-\left(\frac{K^{\frac{1}{4}}}{C^{\frac{1}{8}}}\right)\omega^{-\frac{7}{8}}\sin\left(\frac{7}{8}\frac{\pi}{2}\right)}{\left(\frac{K^{\frac{1}{4}}}{C^{\frac{1}{8}}}\right)\omega^{-\frac{7}{8}}\cos\left(\frac{7}{8}\frac{\pi}{2}\right)} = -\tan^{-1}\frac{\sin\left(\frac{7}{8}\frac{\pi}{2}\right)}{\cos\left(\frac{7}{8}\frac{\pi}{2}\right)} = -78.75° \quad (5.6)$$

Finally, if the parallel elements (i.e. capacitors in this case) are replaced with the input to another ladder network, we respectively have a parallel type of branching (c.f. fig. 5.10b).
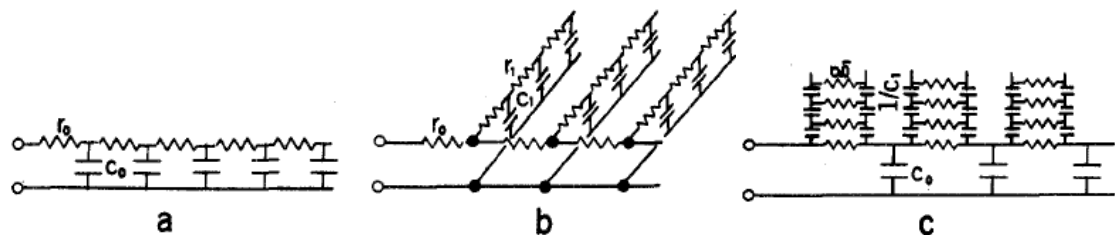

Figure 5.10: Branched ladder networks which exhibit CPE behaviour. The degree of branching may be unlimited. (a) zero-order RC ladder network; (b) first-order parallel-branched RC ladder network; (c) first-order series-branched network with CR branches. Figure taken from [Scheider, 1975].

Based on the theory so far, the concept of uniform branched ladder networks has offered a mechanism for producing a generalised Warburg impedance with a phase angle other than −45° while obviously the branch parameters (i.e. RC values) may differ from those of the zero-order ladder. Simulating eqn. 5.2 in Matlab™ confirms the stated theory of CPE emulation using branched transmission lines/ladder networks in the bandwidth of interest (i.e. 500 Hz to 10 kHz). Results for 3 different orders of branching are shown in fig. 5.11. The average phase angle deviation in the bandwidth of interest for all 3 networks is about 1.8°. In this case no termination impedance was used while the number of stages required is directly proportional to the chosen R and C values of the network which shape its frequency response[38]. At high frequencies the capacitors act like a short (i.e. admittance is increased) and the phase angle is no longer constant but tends to 0°. This can be rectified by reducing the capacitance of each stage which reduces the admittance at higher frequencies. Conversely, at low frequencies surface roughness effects no longer dominate and the phase angle tends to −90°. If that happens too quickly, this can be again rectified by increasing the resistance. Additionally, according to [Scheider, 1975], because of strong damping in RC networks[39], these discrete ladder networks need not be long to be effectively infinite equivalent.
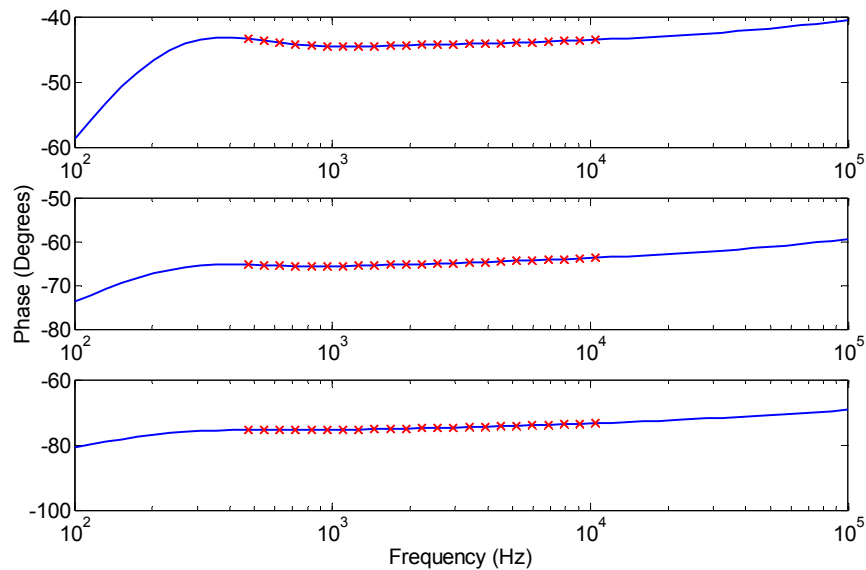

Figure 5.11: Phase angle for a 200 stages zero-order (top), first-order (middle), and second-order (bottom) all series-branched, uniform transmission line. In this example, R=4 kΩ and C=20 pF. The phase angle is relatively constant in the 500 Hz to 10 kHz bandwidth of interest (marked with x). Conversely, the impedance magnitude (not shown) depends on the values of the RC components of the line and it is inversely proportional to frequency. The phase angle tends to −90° at low frequencies because no resistive terminating load was used.

---

[38] E.g. if the number of stages is increased (say from 20 to 200), the value of R and C components decreases and increases respectively.

[39] As is also discussed in terms of thermal noise contributed by the RC ladder network in §5.8.4, each stage in the ladder acts as a LPF and therefore, at high frequencies, stages towards the end of the ladder are rendered insignificant in terms of impedance contribution. In fact, only the first couple of stages in the ladder (i.e. about the first five) are the most important and as such any tolerances in the RC values of subsequent stages is not critical for the desired impedance frequency response of the ladder.

Indeed, by changing the order of the ladder network we can obtain an electrical impedance with a different constant FPFD and therefore different phase angle of discrete steps which is only limited by the extent of the series/parallel branching. The intervals between values of the frequency exponent α which can be synthesised by such networks is $1-[1/2]^{\theta+1}$, where θ is the order of branching [Scheider, 1975]. This results in a very large and complicated in structure network which possibly cannot be used in an implanted device. Furthermore, in order to achieve a fit on the past Z_{trim} data and thus balance the electrodes we need either to vary the RC values of the network (i.e. balancing the recording tripole involves compensating for both magnitude and phase) or, more conveniently in terms of tuning complexity, use negative impedance conversion techniques (revisited in part 2). Conversely, one key property of these branched ladder networks is that the frequency dependence is completely determined by the branching type, and it is not affected by the magnitude of any of the circuit elements. Thus, many ladder networks, each with circuit elements of widely different magnitude, may be connected with their inputs in parallel, and if the branch type of all networks is the same, the frequency dependence of the entire system will be homogeneous [Scheider, 1975]. This is convenient since for our application we need a method where the targeted phase angle does not depend upon the values of the RC network.

5.3.4.2 Hierarchial branching ladder networks

In order to understand the relation between the roughness of the electrode-electrolyte interface and its ac response [Liu, 1985] constructed a model of the interface based on the Cantor bar fractal model[40] [Mandelbrot, 1982]. The cross-section of the interface is shown in fig. 5.12 in which the electrolyte side is shown in black, while grooves of self-similar structure in the electrode surface are seen as protrusions on the electrolyte side. The surface of the electrode is thus imagined as a succession of rectangular grooves. Each groove subdivides into two branches, and the branches are similar to the whole groove when magnified by a factor A, A>2 (since at the base of each groove lie N=2 others of a width A times smaller[41]). Viewed from the electrolyte side, the interface has the fractal dimension d=lnN/lnA<1 for a model with N grooves each of which subdivides into N branches at every level, while the magnification factor A for self-similarity satisfies A>N. A smooth surface has few grooves (small N), and each branch has a large reduction ratio in area (large A) [Liu, 1985]. Therefore, its d is small and α is close to unity (i.e. the greater the fractal dimension d, the rougher the electrode surface, the smaller the pore angle, and consequently the frequency exponent α). As each groove of the model of fig. 5.12 has the self-similar structure in that it subdivides into two branches, and the branches are similar to the whole groove when magnified by a factor A>2, the fractal dimension of the particular Cantor bar is d=ln2/lnA<1 and therefore α=1−d with 0<d<1.

---

[40] In the Cantor bar model, the fractal nature of the circuit is related to the scaling of the resistors, as well as the circuit topology.

[41] Where A is essentially the factor by which the effective area of the interface is reduced at each subdivision of the Cantor bar [Bates et al., 1986].
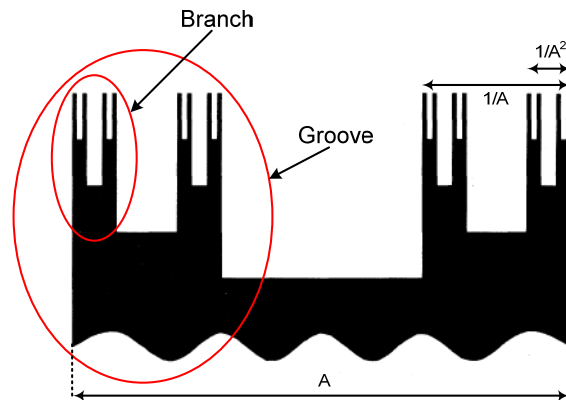
Figure 5.12: The Cantor bar model for a rough metal-electrolyte interface. Two grooves, each with four stages of branching, are shown. The electrolyte side shown in black is forming protrusions into the scratches of the metal electrode shown in white. The rough surface is modelled by assuming that every groove is itself similarly grooved and continuing this process infinitely produces the symmetrical fractal. The number of branches may be generalised to N as long as A>N. Notice that the surface is not everywhere rough. Figure taken from [Liu, 1985].
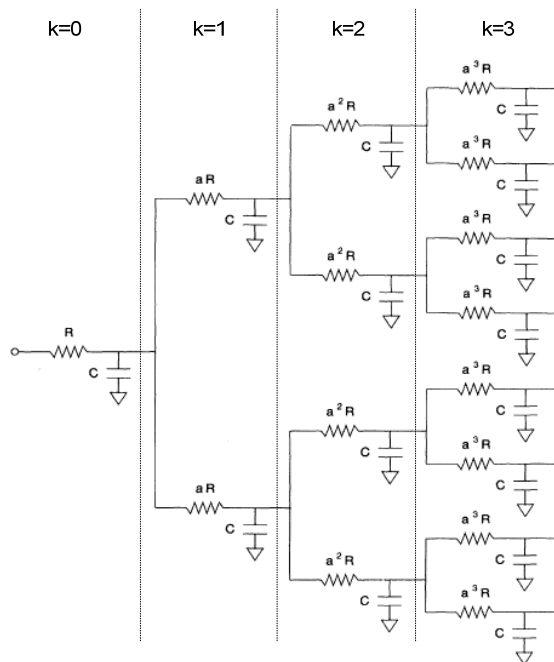
Figure 5.13: Equivalent circuit for the groove of a rough interface which models the double-layer charging behaviour of the interface in fig. 5.12. The first 4 stages of branching are shown with a total of 8 sub-grooves at k=3. R is the electrolytic resistance and C the interfacial double-layer capacitance. The magnification factor in the figure is A=a to avoid confusion in notation with the frequency exponent α. In this model, uniform channels are cut into the electrode surface in such a way that the cross-sectional area is reduced by a factor A and the number of channels with same cross-sectional area grows by a factor N=2 from stage to stage. Figure taken from [Liu, 1985].

The electric circuit equivalent of the interface in fig. 5.12 consists of a branching RC network shown in fig. 5.13 with each resistor R connected to ground by a capacitor C.

The circuit, which branches out at every new stage of the Cantor bar, takes into consideration the resistance between the electrode and the electrolyte, with the common ground being the metal electrode (i.e. ohmic resistance in the electrode is negligible and therefore neglected), as well as the capacitance of the interface (i.e. double-layer capacitance) [Liu, 1985]. At each stage, the circuit subdivides into N branches and the resistance R increases by the factor A at every stage of branching because of the reduction in cross-sectional area (i.e. the resistors of each branch of the kth stage are A times larger than those of the k−1 stage, while at the kth stage there are N^k grooves of width A^{-k}) whereas the capacitance C, which is the same at every stage[42], represents the combined effect of the interfacial capacitance of the two lateral faces of the branch [Kaplan and Gray, 1985].

Despite real electrode surfaces will not have the regularity of the Cantor bar model the advantage is that its ac response can be exactly calculated. At stage k=0 the total impedance of the sides of the groove is taken to be $1/j\omega C$ and the electrolyte contained within the groove has a resistance R. At the kth stage the groove is A^k times narrower while the contribution to the capacitance at each stage from the exposed sides remains constant since the grooves in Liu's self-similar model have unity height [Blunt, 1989]. Thereby, the impedance between the input terminal and the ground of the network has the form of an infinite continued fraction of the form [Liu, 1985]:

$$Z(\omega) = R + \cfrac{1}{j\omega C + \cfrac{2}{AR + \cfrac{1}{j\omega C + \cfrac{2}{A^2R + \cfrac{1}{j\omega C + ...}}}}} \qquad (5.7)^{43}$$

where the continued fraction has been written up to the third stage of iteration (i.e. k=2). The magnification factor A can be obtained from α=1−lnN/lnA as $A = \sqrt[(\alpha-1)]{1/N}$ while the real part of eqn. 5.7 was shown by [Liu, 1985] to have a low frequency solution with CPE behaviour. Hence, the self-similarity property of the interface represented by the network in fig. 5.13 gives rise to a FPFD on ω.

Ladder networks of various sizes can be connected according to the branching geometry of the interfacial structure in order to appropriately describe it. To calculate the impedance of Liu's fractal model for a groove, the fractal interface is represented by an

---

[42] The number of interfacial capacitors increases in proportion with the number of branches but since these lateral faces are assumed to be the same size at every stage, C is constant. In addition, the area of the horizontal faces is reduced by the factor A at each stage, and thus its contribution to the capacitance becomes negligible at higher stages, i.e., only the lateral faces are assumed to act as capacitance [Kaplan and Gray, 1985].

[43] It is easy to show that following the same approach as for the derivation of eqn. 5.1 and using an RC ladder network equivalent to that of fig. 5.13 (i.e. with elements calculated by eqn. 5.8) then eqn. 5.7 is obtained.

infinite branching RC network like that of fig. 5.13. Since the impedance of a pore can also be approximated with a ladder network or a transmission line this implies that Liu's fractal model can be transformed into a pore [Wang, 1988a]. More specifically, when the points of equal potentials (i.e. the nodes between stages) of the network are folded together, it becomes an RC ladder network like that of fig. 5.9 with elements [Wang, 1987]:

$$r_k = r\left(A/N\right)^k$$
$$c_k = cN^k \qquad (5.8)$$

where r and c are the values of the resistor and capacitor at the first stage of the branching network, k is an integer running from 0 to ∞ denoting the stage number (from left to right of fig. 5.13), and N is the number of new branches at each node. From one stage to the next, the resistance of each resistor is increased by a factor A, satisfying A>N. Simulating either the continued fraction of eqn. 5.7[44], or eqn. 5.8 (in the form of an RC ladder network with increasing r_k, c_k per increasing number of stages) in Matlab™, the graphs of fig. 5.14 are obtained[45]. In this example, 10 stages of RC branching were simulated using eqn. 5.7 with R=1 kΩ, C=10 pF, N=2, A=8 (i.e. α≈−60°), and without using a termination load. The straight line of slope −α of the real part of the input impedance Z(ω) plotted in fig. 5.14a shows a clear CPE behaviour at those frequencies. From fig. 5.14b, the phase angle is invariant to the magnitude of the input impedance while it remains relatively constant at about −58.5° (i.e. max deviation is about ±1.2°) in the bandwidth of interest. Notice that even a few hierarchies of grooves generate CPE behaviour over a wide range of frequencies. It is possible by varying the R, C, A, and N parameters to obtain any phase angle in the 0<α<1 range, however, a complete investigation of how those analytically affect the frequency response of Liu's model (like it was done by [Blunt, 1989] using a generalised model of self-affine surfaces) is beyond the scope of this section – the fact that a CPE can be obtained with a given set of parameters is sufficient for our purpose and to be able to draw appropriate conclusions as far as the usability of this model is concerned.

---

[44] By solving the recurrent relation $Z_k=[1/(j\omega C+2/Z_{k+1})]+A^k\cdot R$ in Matlab™ where k is the stage number running from ∞ to 0, i.e., from the last stage towards the first.

[45] It should be mentioned that eqn. 5.7 and eqn. 5.8 produce identical inputs impedances, however, the stage-to-stage impedances are, as expected, not the same. This is true, since the continued fraction of eqn. 5.7 needs to be evaluated in full in order to produce the correct impedance result.
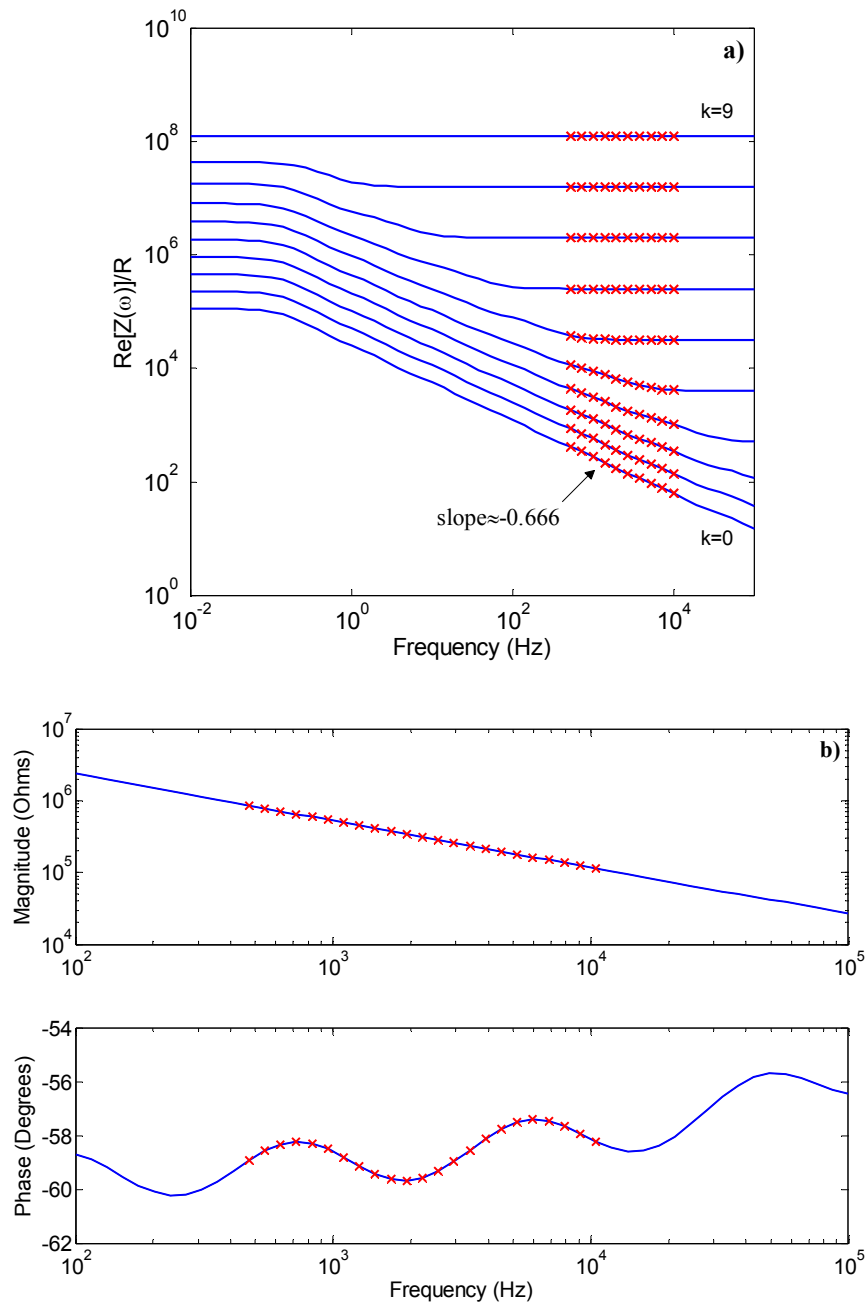
Figure 5.14: a) The real part of the input impedance of circuit in fig. 5.13 plotted as a function of frequency and stage number; b) The magnitude and phase angle frequency response of the input impedance for a 10 stages branched RC network constructed with R=1 kΩ, C=10 pF, N=2, and A=8. An RC ladder network with elements obtained by eqn. 5.8 gave an identical response. Ringing appears in the phase angle because the distribution function of the capacitances is discrete. Marked with red x is the 500 Hz to 10 kHz ENG bandwidth of interest.

5.3.4.3 Non-uniform RC ladder networks[46]

In 1957 Schrama proposed a semi-infinite RC ladder network which had the following generalised impedance based on continued fractions for describing linear relaxation processes [Schrama, 1957]:

$$Z_T = S \cdot \left(h + \frac{1}{j\omega} \right)^\alpha = r_0 + \cfrac{1}{c_0 j\omega + \cfrac{1}{r_1 + \cfrac{1}{c_1 j\omega + \cfrac{1}{r_2 + \cfrac{1}{c_2 j\omega + ...}}}}} \qquad (5.9a)$$

$$r_k = S \cdot \left[2h^\alpha \frac{\Gamma(1-\alpha)\Gamma(k+\alpha)}{\Gamma(\alpha)\Gamma(k+1-\alpha)} - h^\alpha \delta_{k0} \right] \quad \text{where} \quad \delta_{ij} = \begin{cases} 1, & \text{if } i=j \\ 0, & \text{if } i \neq j \end{cases}$$

$$c_k = S^{-1} \cdot \left[h^{1-\alpha}(2k+1) \frac{\Gamma(\alpha)\Gamma(k+1-\alpha)}{\Gamma(1-\alpha)\Gamma(k+1+\alpha)} \right] \qquad (5.9b)$$

where k is a stage in the ladder network (i.e. corresponding to the distance x into the pore and here is taken to be zero at the opening of the pore), α is the same as the frequency exponent of eqn. 4.5c, h is an arbitrary real positive small number[47], Γ denotes the gamma function, δ is the Kronecker delta, and S is the scaling factor[48]. Schrama derived eqn. 5.9b[49] such that the resulted input impedance Z_T of his RC ladder network is proportional, at least in a limited frequency range, to $(j\omega)^{-\alpha}$ while we found the coefficient K of eqn. 4.5c to be also equal to the scaling factor S. Moreover, there is no indication of what value h might be assigned to or how small it can be. Simulating the LHS of eqn. 5.9a in Matlab™ for a set of small values of h (fig. 5.15) it was possible to obtain a linear impedance locus Z_T, and therefore a good CPE behaviour in the bandwidth of interest, by setting $h=10^{-6}$. Conversely, if a very small value of h is chosen (e.g. $h=10^{-7}$) the low frequency end of the phase angle response is affected (i.e. tends towards 0° faster) and as a consequence more RC ladder stages need to be added to compensate for this effect (since in that case r_k, c_k are smaller to begin with).

---

[46] The contents of §5.3.4.3 were partially presented in [Pachnis et al., 2009b].

[47] We need h to prevent r_k or c_k from becoming infinite at k=0.

[48] The scaling factor S was used for appropriately scaling the values of r_k and c_k components of the Schrama ladder network and its use is discussed later in §5.6.1. For now, it is important to note that the phase angle frequency response of $Z_T(\omega)$ was not affected much in the bandwidth of interest by this scaling operation.

[49] The derivation of eqn. 5.9b is shown analytically in the Appendix of [Wang, 1987].
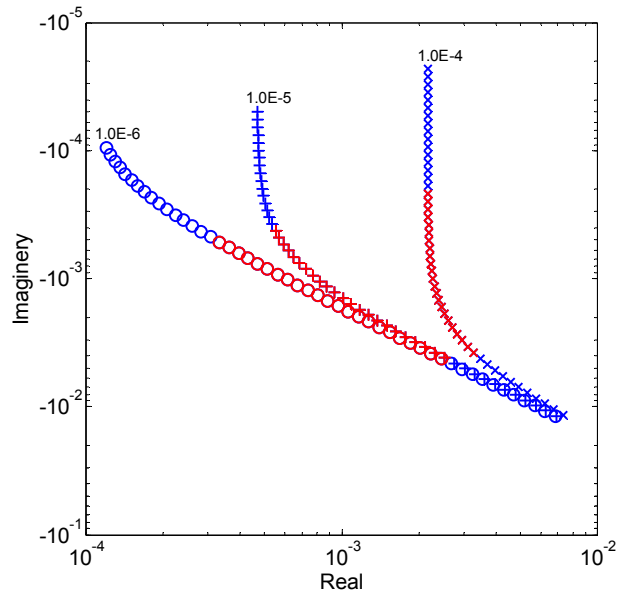
Figure 5.15: Nyquist plot based on the given value of h for obtaining a linear impedance Z_T over the bandwidth of interest (500 Hz to 10 kHz; marked in red). Setting h=10^{-6}, results in a good CPE representation. A value of α=0.666 was used for the frequency exponent.
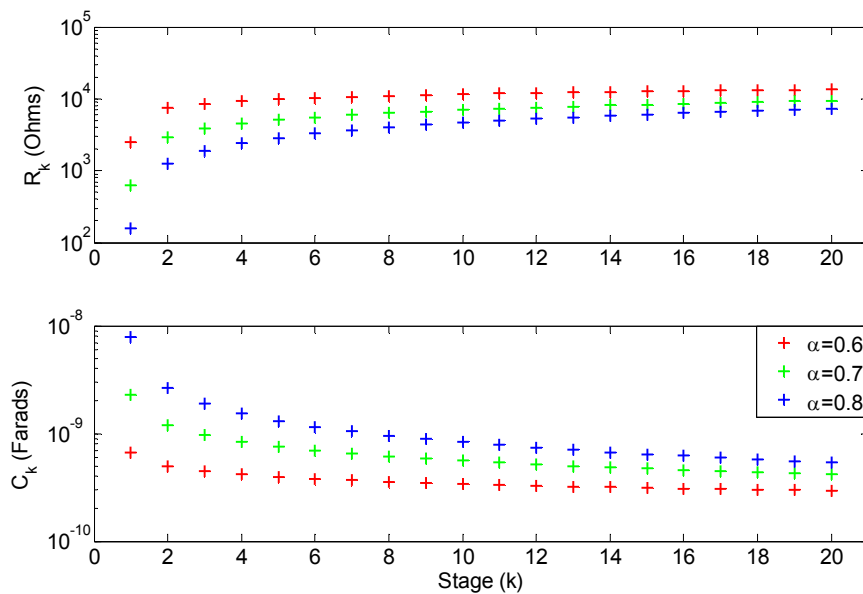
Figure 5.16: Values of resistors r_k and capacitors c_k for a 20 stages RC ladder network, as specified by eqn. 5.8b. In this simulation, 3 different values of the frequency exponent α have been used, while the scale factor S was set to 10^7.

Having concluded on the value of h it is possible to calculate r_k and c_k using eqn. 5.9b. As is shown in fig. 5.16, for a 20 stages RC ladder network the value of r_k increases and that of c_k decreases with increasing number of stages k, signifying that Schrama's continued fractions result in a non-uniform RC ladder which resembles the single-pore model of fig. 5.6. Furthermore, according to [Wang, 1987] and verified in this work using Matlab™, when the frequency exponent α>0.5, r_k increases and c_k decreases with k,

126

exactly as in fig. 5.16. However, for α<0.5 this trend is reversed; now r_k decreases and c_k increases with k (not shown in fig. 5.16). For α=0.5 both r_k and c_k become independent of k and the impedance becomes that of a Warburg element, i.e., φ=−45°.

Schrama's eqn. 5.9a was subsequently simulated in Matlab™ using the calculated values of r_k, c_k for α=0.666 (i.e. φ_{CPE}=−α*π/2 rad≈−60°), k=20 and S=10^7. Also, since the RC ladder network is relatively long and thus its impedance magnitude is high at low frequencies, a terminating resistive load[50] of 1 kΩ was used whose value affects the low frequency phase angle response of Z_T(ω). Fig. 5.17a shows the impedance loci from the last stage of the ladder network up to the first (i.e. locus pointed by the arrow), demonstrating the change in impedance as each stage is sequentially added to the ladder. Fig. 5.17b is plotted in the same manner but this time for the phase angle. In the former graph the impedance locus of the input stage is linear at mid-frequencies and this is reflected in the latter graph as a constant phase angle at the same frequency band. For reasons of simplicity only results for a single frequency exponent value are shown, however, it is possible to acquire a CPE angle for any value in the 0<α<1 range.
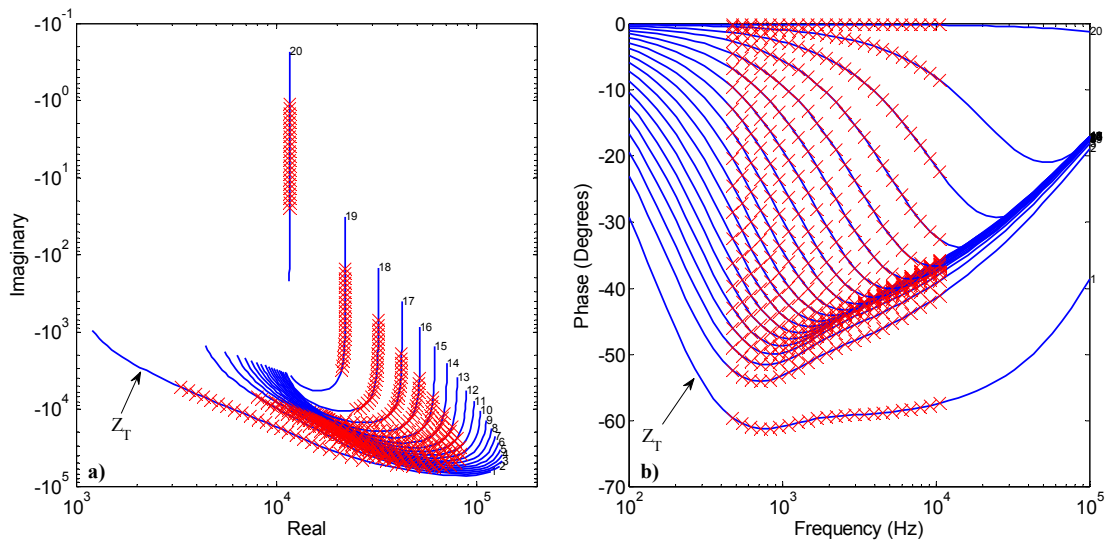
Figure 5.17: a) Nyquist plot showing impedance loci for 20 sequentially added stages of Schrama's RC ladder network (from last to first – top to bottom). Each stage represents a slice of the pore/groove from inside the electrode wall towards the electrolyte. The input impedance of the ladder Z_T is linear in the 500 Hz to 10 kHz bandwidth of interest (marked with x); b) Phase angle exhibited by Schrama's ladder network. At the input impedance Z_T, the phase angle is approximately constant in the bandwidth of interest, denoting a CPE with a frequency exponent of α=0.666.

For reasons of comparison, the magnitude and phase angle of the input impedance Z_T was plotted in fig. 5.18 against Cole's empirical eqn. 4.5c for the same frequency span, K coefficient – scaling factor S, and frequency exponent α. It is obvious that Schrama's

---

[50] The value of the termination impedance defines the boundary condition at the bottom of the pore. If the termination impedance is infinite this means that a pore is terminated by a wall (of electrode), whereas when it is zero the pore contacts the bulk solution.

ladder network is a very good approximation to the (ideal) empirical CPE eqn. 4.5c, in the bandwidth we are interested in.
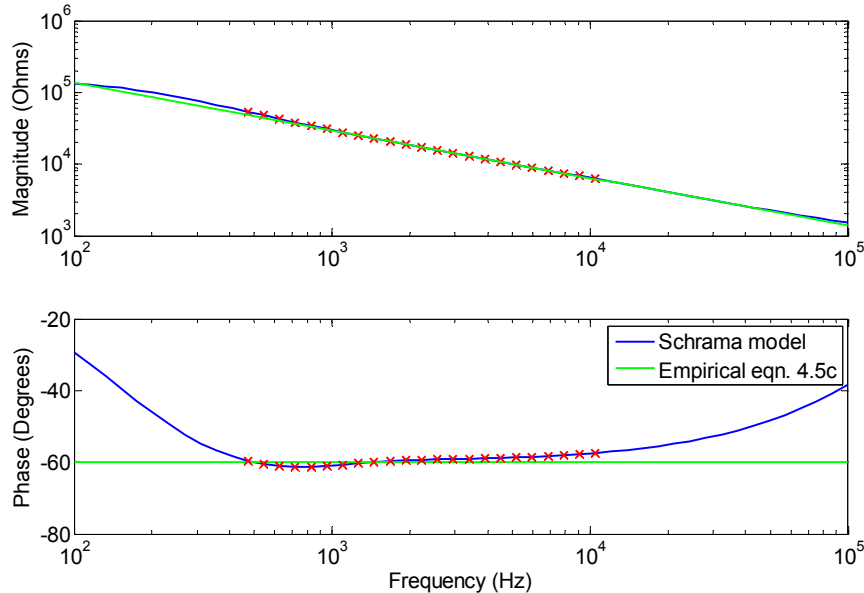
Figure 5.18: Comparison of the magnitude and phase of Schrama's RC ladder network impedance Z_T against Cole's empirical Z_{CPE} (500 Hz to 10 kHz bandwidth of interest marked with x). The same scaling factor – CPE coefficient $S=K=10^7$ and frequency exponent $a=0.666$ were used.

One important issue is the number of stages required for the RC ladder network to have. In this example 20 stages were sufficient to achieve a relatively constant phase angle in the bandwidth of interest, however, one may think as follows: if we take a V-shape pore and cut it to k slices, each slice representing a stage of the RC ladder network with different distances from the opening of the pore, the resistance r_k is determined by the resistivity of the electrolyte in the pore and the cross-section and thickness of the kth slice, while capacitance c_k is determined by the double-layer capacitance per unit area and the electrolyte-metal boundary area on the two edges of the slice [Wang, 1988b]. If the number of slices (i.e. number of stages) is large enough, $Z_T(\omega)$ should be a good approximation to the impedance of the pore. This can be achieved by making sure that further increase of the number of stages does not change $Z_T(\omega)$ over the frequency range of interest. Moreover, it must be emphasised that by adding more stages to the ladder we only affect the low frequency end of the phase angle response, i.e., it tends towards 0° slower.

Another matter needs further discussion regarding fig. 5.18. The low-frequency phase angle response of Schrama's ladder network could be further improved (i.e. flattened) by adding more stages to the ladder, nonetheless, this is not the case for the high-frequency end; the double-layer capacitance is shorted resulting in the phase angle tending towards zero and the input impedance losing its constant FPFD on ω. This is however acceptable since this kind of frequency response has been observed with real Pt electrodes. Physically this means that for these frequencies the ac current cannot reach the terminating load of the ladder network, i.e., in other words, at high frequencies the

current penetration depth inside the pore is small. In case, however, there is a need to extend the high frequency response of the CPE beyond 10 kHz this can be achieved by reducing the admittance to the metal electrode (i.e. ground) for those high frequencies, ultimately in favour of increased thermal noise. This trade-off is revisited again analytically in part 2 of this chapter.

5.3.4.4 CPE method evaluation

There are in general two approaches that someone could follow in emulating the CPE behaviour of electrodes; constructing a circuit model that will mimic either the frequency behaviour, or the geometrical/topological structure of the electrode. Thus, as is to be expected, an equivalent circuit can describe the frequency behaviour but may have nothing to do with the actual geometrical or topological structure of the electrode. For our purpose we have decided to follow the former where we treated the roughness of the electrode interface as a distribution of one-dimensional pores of semi-infinite length and tried to approximate its exhibited CPE frequency response by using an RC ladder network[51] in which the potential drop along the pore axis is being reproduced by the resistor chain of the ladder, while the equipotential lateral surfaces of the pore by the interfacial double-layer capacitance which is reduced as we move down the length x of the pore (i.e. the cross-section of the pore becomes smaller with increasing depth). The single-pore model of fig. 5.6 emulates the frequency behaviour of a single CPE which is representative of the physical characteristics of an average distribution of pores on a particular electrode surface and therefore it is appropriate for modelling the phase angle frequency response of the electrode interface impedance.

Choosing between a fractal and a single-pore model representation for the CPE, we have adopted the latter and thereby assumed all surface discrepancies in the interface microstructure to be in a V-shape form. Although de Levie in [de Levie, 1990] has criticised the use of ladder networks/transmission lines and stressed their limited accuracy in representing surface pores[52], those have proved to be a popular way of emulating the CPE behaviour in recent years. The major attractiveness of the single-pore model and consequently of the ladder network/transmission line circuit used to model it, lies in its one-dimensional–simple structure nature and the fact that it is a system for which we have an analytic result that may be used to derive expressions for the impedance in different frequency ranges. Conversely, it is obvious that a valid description of the electrochemical behaviour of a single scratch or pore requires at least a two-dimensional approach, which greatly increases, apart from the structural, also the mathematical complexity of the system [de Levie, 1990].

---

[51] Modelling the pore of the electrode surface is done with an RC ladder network as opposed to a CR where capacitors are series elements and conductances are parallel elements, in which case the first term of eqn. 5.2 would have been negative. That concept would have been useful if the series element was a measure of the inverse capacitance per unit length [Scheider, 1975].

[52] Those models become poor approximations for wide and shallow pores, i.e., when the pore diameter becomes larger than the effective ac signal penetration depth, or when the signal penetration depth becomes larger than the pore length.

The treatment of Nyikos-Pajkossy is based on purely dimensional arguments, i.e., a set of equations which relate the system size and the frequency dependence of the CPE impedance, whereas the models of Liu [Liu, 1985] and Sapoval [Sapoval, 1987] are based on ladder networks/transmission lines. For Liu's model, the interfacial impedance can be calculated using the RC ladder network approximation whereas for Nyikos-Pajkossy model (i.e. the von Koch curve) this is not possible since that cannot be described by a one-dimensional network. For such a system the dc or ac potential and current distribution can be represented by an RC impedance mesh [Nyikos and Pajkossy, 1985]. Thus, despite fractal models of rough interfaces having provided a possible explanation for the observed CPE behaviour, their structure is too complicated to be of any use in our case.

Another important matter is what factors affect the high and low frequency cut-offs of the CPE. In other words, what parameters define the frequency range of the dispersion in which the CPE dominates? The CPE behaviour of electrodes has the form of eqn. 4.5c over several decades of frequency ω (i.e. usually more than four decades; i.e. 10^{-4}–10 kHz). Undoubtedly, the frequency range of this exhibited behaviour depends on the topology (e.g. cell geometry, as current distribution is affected) and surface microstructure of the electrode. However, it is important to understand how the latter actually transforms into the frequency domain in which the power law dependence is observed. In the case of the single-pore model, the frequency limits of the CPE behaviour are determined by geometric data: pore diameter, electrode thickness and inter-electrode spacing [Pajkossy, 2005]. An infinitely long pore exhibits no characteristic size along the pore axis and its impedance is a CPE. With a finite length pore, however, the impedance is not a CPE in the full frequency range. In the case of RC ladder networks we can change the cut-off limits by selecting appropriate value for the RC elements and number of stages of the ladder. Conversely, for fractal models, physically the frequency range should depend on the range of length scale in which the surface exhibits self-similarity [Liu et al., 1986]. Finally, equivalently important is the effect of surface roughness and its link by various workers to the conductivity of the electrolyte. As studied by others and mentioned by [de Levie, 1965]: "the effect (of surface roughness) increased with decreasing solution conductance", while according to [Scheider, 1975]: "in very concentrated electrolytes, (the frequency exponent) α is sometimes observed to be not constant, but to change gradually over the entire frequency range of observation".

Out of the 3 methods studied in §5.3.4, Schrama's RC ladder network offered the best results. In particular, the R and C values are readily calculated based upon the desired phase angle, the network is simple in structure (i.e. always zero-order), it is easier to adjust parameters to compensate for variations at the interface, and most importantly we can achieve a good CPE emulation with an acceptable number of stages. Therefore, a single-pore model in the form of Schrama's RC ladder network has been chosen to emulate the CPE of a rough electrode interface that is required to balance the recording tripole. Some of the key advantages over the two other modelling approaches are summarised in table 5.2.

(1) The phase angle of the input impedance of the network in terms of the frequency exponent α, i.e., $\varphi_{CPE}=-\alpha\pi/2$ rad.
(2) "Fixed" RC values are selected upon the desired frequency cut-offs of the phase angle.
(3) Where $\theta\geq0$ is the order of branching.
(4) Where k_{total} is the total number of stages in a ladder network with $\theta=0$. All branching stages have the same k_{total}.

RC ladder network	[1]CPE angle	[2]RC values	No. of stages	Comments
Uniform	$\alpha=0.5$	Fixed	200	Only $\varphi_{CPE}=-45°$
Polydimensional branching (Scheider)	[3]Discrete steps at $\alpha=1-[1/2]^{\theta+1}$ intervals	Fixed	[4]$\sum_{n=1}^{\theta+1}(k_{total})^n$	Highly complex network
Hierarchial branching (Liu)	$0<\alpha<1$	Fixed	10	φ_{CPE} depends on N, A, R, and C parameters
Non-uniform (Schrama)	$0<\alpha<1$	Calculated given α	20	Easiest to adjust

Table 5.2: Comparison of different methods for emulating a CPE.

5.3.5 CPE and passive EMG neutralisation

Having successfully implemented a CPE based on Schrama's RC ladder network it is now possible to arrange it for passively neutralising EMG interference at the tripole, however, before doing so, a number of questions need answering. In particular, how the constructed CPE can be arranged for the purpose of balancing the tripole, and whether the new approach can offer improved performance[53] in respect to the conventional mQT. We will use fig. 5.19 in our discussion. The figure shows 3 different sets of impedance magnitude and phase angle curves at spot frequencies (i.e. denoted by the black markers), obtained from the in-vitro experiments of Chapter 3 for 3 NaCl concentrations (c.f. fig. 3.11), representing a different conductivity on the recording site based upon the degree of tissue growth around the electrodes. A circuit equivalent to the interface impedance Z_{inter} of fig. 5.4 was constructed using 20 stages of Schrama's RC ladder network for the Z_{CPE}, in an attempt to perform a fit on the past neutralisation data. As illustrated by fig. 5.19 the fitting network can represent such data. Notice that the high frequency phase angle response at about 10 kHz can be improved by reducing c_k (i.e. reducing admittance to ground at high frequencies) of the RC ladder network. Moreover, arranging for trimming does not seem to require an access resistance R_{access} placed in series with Z_{inter} since, for reasons already explained (c.f. 2nd to last paragraph of §5.2.1), the phase angle of the trimming impedance loci in fig. 5.19 does not tend to 0° at high frequencies.

The values used for the fitting impedance Z_{inter} are shown in table 5.3. The value of the frequency exponent is the same for all 3 electrolyte conductivities σ, while the fitting values of the scaling factor S and the charge transfer resistance R_{ct} did vary significantly. This is something to be expected since the same electrode tripole was used throughout the experiments, whereas it is known that the frequency exponent α is most sensitive to the texture of the interface. Hence, if we assume that all 3 electrodes of a recording tripole are of the same size, symmetrically placed and, as in this case, immersed in a uniform

---

[53] By "improved performance" here mean less EMG breakthrough throughout the ENG band without the mQT requiring continuous adjustment.

electrolytic conductor, the imbalance must be caused by surface discrepancies between the two outer electrodes, despite their identical surface treatment (i.e. manufacturing process and electrode preparation before experiments). Moreover, as quite correctly pointed out by [McAdams et al., 1995b] "it is naive, however, to think that surface effects will only distort the non-faradaic impedance (i.e. Z_{CPE}) and will have no effect on R_{ct}", something assumed by the model of fig. 5.4 which does not explicitly include the effects of interface geometry on R_{ct}, and continues "...it is more realistic that surface effects will affect the parallel combination of Z_{CPE} and R_{ct} giving rise to skewed or distorted arcs[54]". Concluding, we should emphasise that the proposed neutralisation technique is now a 3 "degrees of freedom" problem (i.e. 3 components to tune) in comparison to 2 of the previous simplistic parallel RC impedance Z_{trim} used in Chapter 3 (c.f. §3.6.2). The outcome of this, is increased performance with only 1 component penalty (i.e. that of the frequency exponent), which once it is known for a particular electrode tripole, the problem is reduced down to 2 again. The problem of component tuning of the new frequency adaptive network is explicitly dealt with in §5.8.2.
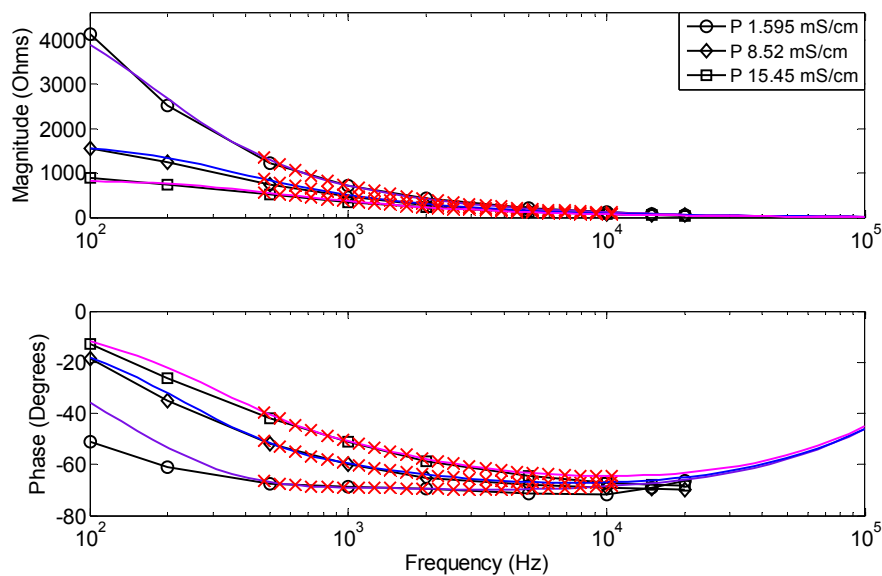
Figure 5.19: Fitting measured neutralisation impedance data (c.f. fig. 3.11) using an interface impedance Z_{inter} (c.f. fig. 5.4) constructed with 20 stages of Schrama's RC ladder network in parallel with resistance R_{ct}. Bandwidth of interest is marked with x. The same electrode tripole was used in all measurements.

NaCl σ (mS/cm)	1.595	8.52	15.45
S (Ω/s^{+a})	0.8 M	0.61 M	0.45 M
α	0.8	0.8	0.79
R_{ct} (Ω)	12 k	2.2 k	1 k

Table 5.3: Values of the interface impedance Z_{inter} arranged for fitting.

---

[54] In the literature "skewed" and "depressed" semicircular arcs have a different meaning. Skewed arc plots for the impedance have been observed, e.g., in corrosion study of carbon steel in neutral chloride solutions [Maritan and Toigo, 1990].

This approach offers two important advantages over other neural recording configurations, like the mQT and AT: it can be considered (frequency) adaptive without the addition of a close-loop mechanism and therefore increased power consumption, while most importantly, it now neutralises interference in the entire ENG band. In practice, the proposed neutralisation technique needs to be used in conjunction with either a negative impedance converter (NIC), or with an audio transformer having a large selection of turns ratios (i.e. for use in acute in-vivo ENG recordings). This is important in order to be able to alter the magnitude of the hardware Z_{CPE} to a value that would be appropriate for trimming while at the same time maintaining the phase angle of the CPE. The idea of the NIC has been explored in Cadence™ circuit simulator with very satisfactory results, while we expect the alternative option of the transformer to offer better signal-to-noise ratio due to its intrinsic ability to reduce noise by the number of the turns ratio. Results towards the hardware implementation of a CPE are shown in part 2 of this chapter.

5.4 Summary of part 1

In part 1 of this chapter a novel approach was presented where removing the EMG interference in neural recording tripoles can be done passively, and at all frequencies, by appropriately modelling the impedance profile of our recording electrodes. The improvement lies in the physical interpretation of the trimming impedance Z_{trim} by replacing the double-layer capacitance C_{dl} of the parallel RC of the conventional mQT with a CPE based on the single-pore model to account for the surface roughness effects of the interface. Apart from providing a critical literature review on the CPE, a number of methods for appropriately emulating its behaviour have also been presented. Schrama's RC ladder network was successfully utilised to represent a CPE, hence, essentially mimicking the frequency response but not the geometrical/topological structure of an electrode surface. Although the single-pore model does not account for the random distribution of pores as in a true porous solid, or for the complicated surface topology, it is simple in structure and provides an impedance with a constant phase angle in the ENG band, which was the requirement. This choice was also due to practical reasons, since a different model-based Z_{CPE} would not be realisable both in terms of application (i.e. easiness of tuning, compensating for the changes at the neural interface), as also implementing the idea on silicon. As the trimming impedance now adapts to the electrodes' frequency response, no continuous tuning is necessary. Simulation results have demonstrated this to be feasible. Therefore, fig. 5.19 is very important in that it allowed us to understand two things; the trimming with the new proposed network is possible and, most importantly, that now tuning is not required. Results from an in-vitro experiment using this improved neutralisation approach are presented in part 2.

Part 2: CPE Realisation and In-Vitro Verification

5.5 Introduction

In part 1 of Chapter 5 we concluded on a method for emulating the frequency response of a CPE which is appropriate for our purpose, i.e., modelling the neutralisation impedance necessary to balance the recording tripole. After a thorough exploration of 3 different approaches for modelling the CPE (c.f. table 5.2 for a brief comparison), we ended up using Schrama's continued fractions (c.f. eqn. 5.9a and 5.9b) for describing the input impedance of a V-shape pore in the form of a 20 stages non-uniform ladder network. This was done for two key reasons: a) the particular model resulted in a network which was simple in structure in comparison to the other 2, allowing a potential IC implementation to be feasible, and b) it was the easiest of the 3 to adjust offering only 1 additional "degree of freedom" for compensating for any imbalance in the recording tripole (c.f. §5.3.5). In part 2 of this chapter the particular CPE model is realised in hardware and used, as a proof of concept, in an in-vitro experiment.

5.6 CPE realisation

Implementing the CPE in hardware is very important towards verifying, in practice, the accuracy of the selected CPE model. Although there have been numerous studies and modelling attempts of the electrode-electrolyte interface impedance of metal electrodes over the years (e.g. [Franks et al., 2005] being a recent one), to the best of our knowledge, none of those ever attempted to model the polarisation impedance of the electrode-electrolyte interface using a practically realisable (in the form of an RC ladder network) CPE, let alone building one with a frequency exponent α other than 0.5. A paper that reports the fabrication process and performance of a hardware non-implantable phantom CPE in the form of a capacitive probe (i.e. 12 cm long and 6 mm wide, made from double-sided copper-cladded PCB) in a polarisable medium (i.e. tap water) is the only find at the time of writing which documents a realisable CPE. The hardware CPE was studied as a circuit device in a fractional differentiator circuit and details of its fabrication together with test results can be found in [Biswas et al., 2006]. In the section to follow we fill the gap by emulating the frequency response of a CPE having variable phase (i.e. by changing the frequency exponent α) in a hardware PCB implementation.

5.6.1 Hardware PCB

The validity of the simulated 20 stages scaled Schrama RC ladder network was investigated against actual measured data obtained from a number of PCB realisations. Although the chosen number of stages was sufficient to give us a relatively flat phase response at the lower frequency end, the resulted mΩ and mF values of eqn. 5.9b for the r_k and c_k components of the ladder network were not practical.
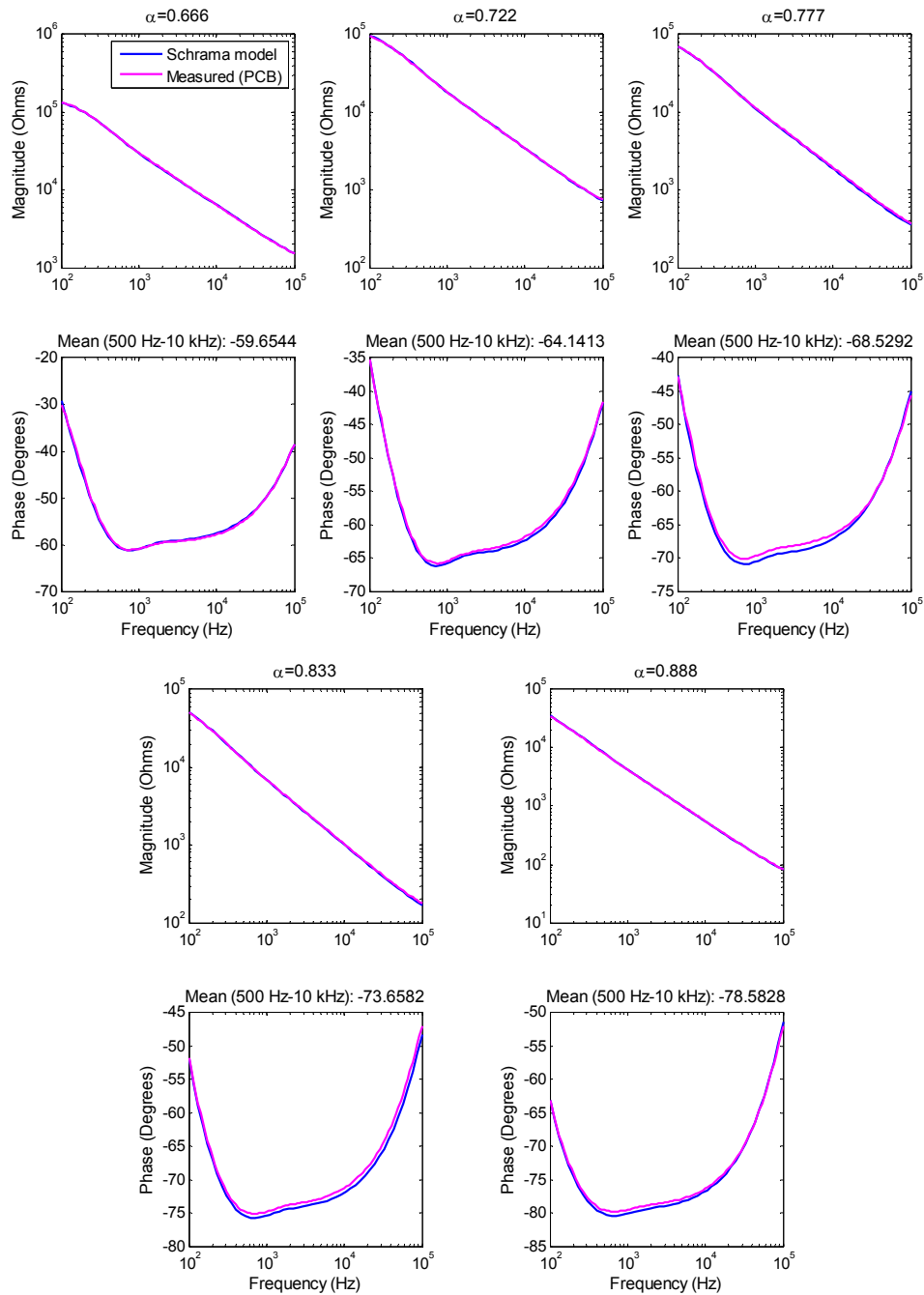
Figure 5.20: Comparison of actual measured PCB magnitude and phase angle data against calculated values using Schrama's model from 100 Hz to 100 kHz and for 5 different values of frequency exponent α. The mean phase angle value measured in the 500 Hz to 10 kHz band for each PCB is also given.

According to [Schrama, 1957], we can multiply all the resistors and divide all the capacitors in the network by a particular factor (i.e. the scaling factor S); in effect scaling the r_k and c_k components (and thus the magnitude of Z_T) but still (approximately)

retaining the same phase angle frequency response[1]. Therefore we multiplied the RHS of eqn. 5.9a by a factor $S=10^7$ resulting in scaling r_k up to kΩ (1.01 min, 10.58 max) and c_k down to pF (375 min, 1488 max) for $\alpha=0.666$ (i.e. $\varphi_{CPE}\approx-60°$), making an IC implementation of the design possible in terms of layout area (c.f. §5.8.3). For reasons of comparison, measurements of the input impedance obtained with an impedance analyser (Wayne Kerr Electronics, model 6520BD1, 20 Hz-20 MHz) for 5 PCBs are shown in fig. 5.20 superimposed on the respective simulated CPE obtained using Schrama's model. The impedance analyser was calibrated according to the instructions from the manufacturer before measurements took place in order to improve accuracy and minimise errors. It is obvious that the measured PCB data match the simulated results sufficiently well, while the error in the mean phase angle over the ENG bandwidth of interest is very small (i.e. about 1.4° to 0.3°). The pre-determined (via simulation) RC values[2] required for the construction of a 20 stages ladder network for a set of CPEs with fixed frequency exponent α are documented in Appendix B. Because of the way the RC values were arranged, each PCB was designed with a number of six slots per stage and populated with resistors (in series; a short was used for any unused slot(s)) and capacitors (in parallel) whose values were within less than 1% of the targeted value. Also shown in fig. 5.21 is a stack of 5 PCBs implementing the phase angle of CPEs from −60° to −80° in 5° steps. Again, any CPE in the 0<α<1 range can be realised. A rotary switch (Grayhill Inc.; not shown in fig. 5.21) was used to select the desired CPE.
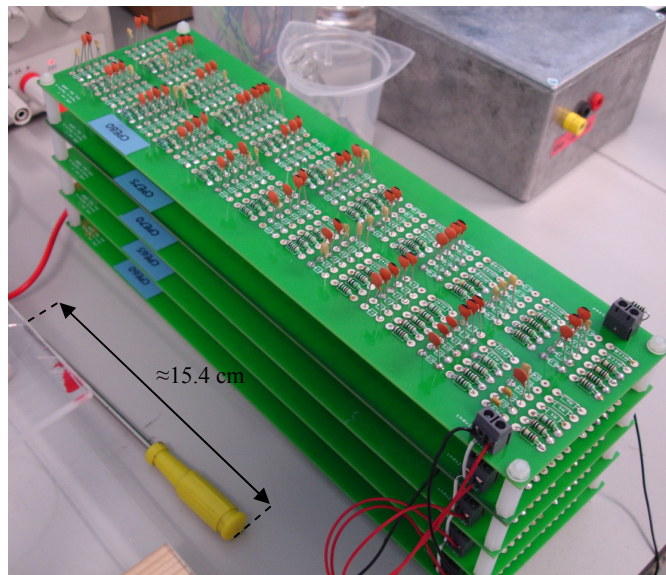
Figure 5.21: Stack of PCBs emulating the frequency response of 5 CPEs with a phase angle in the range of −60° to −80° in 5° steps. Screw driver at the bottom left is shown for size comparison.

---

[1] It is easily shown that the generalised impedance (LHS of eqn. 5.9a) corresponds to a ladder network in which all the resistances are S times as large and all the capacitances 1/S times as large as those of eqn. 5.9b.

[2] The RC values were calculated in Matlab™ using Schrama's continued fractions (c.f. eqn. 5.9a and 5.9b).

5.6.2 PCB issues

Implementing the CPE in hardware involves the resolution of certain issues so that the PCB design meets certain criteria such as size, frequency response, and exhibited thermal noise. In this section we discuss the 3 aforementioned issues in detail.

5.6.2.1 RC tolerance

Matching the RC component values of the PCB to those of simulation is important in obtaining an accurate frequency response for the CPE in the ENG bandwidth of interest. This remark is especially true for the first few stages of the particular ladder networks (i.e. about the first five stages as various Matlab™ simulations have indicated). To better understand the effects of (mis)matching, component tolerance was investigated in simulation were a variation of up to 10% in various ways (i.e. component values increasing/decreasing or even remaining constant at different stages – see table 5.4) revealed no significant change in the desired frequency response of the ladder network. Results of this investigation are shown in fig. 5.22. A similar comparison was performed by [Wang and Bates, 1986] for their transmission line where they allowed r(x) and c(x) to fluctuate by about ±20% randomly at all x (i.e. x≡distance into the pore). They found the resultant impedance could still be described by eqn. 4.5c quite well with the same value of frequency exponent α. Although a particular mismatch (i.e. 10%) is here applied to all stages, for reasons that will be discussed later in the chapter (i.e. §5.8.4), the stages closer to the input are more significant in dictating the frequency phase angle response of the CPE.
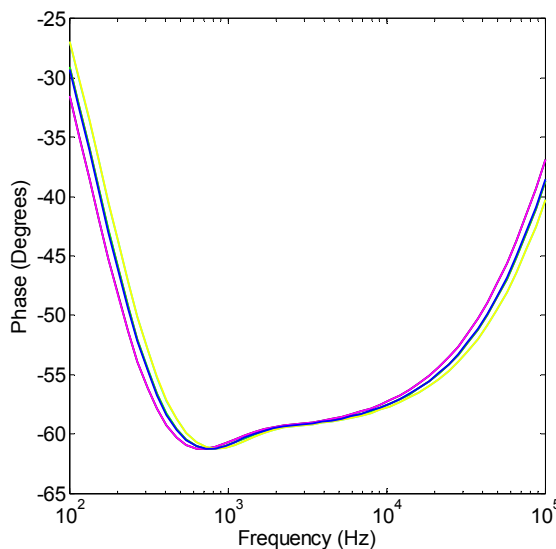
Line Colour	Type of deviation
blue	R−, C−
red	R↓, C↑ by 10%
green	R↑, C↓ by 10%
black	R↑ by 10%, C−
cyan	R↓ by 10%, C−
magenta	C↑ by 10%, R−
yellow	C↓ by 10%, R−

Table 5.4: List of RC deviations applied to the ladder network.

Figure 5.22: Matlab™ simulation illustrating the effect of RC component tolerance on phase angle of a 20 stages Schrama ladder network with α=0.666 (i.e. $\varphi_{CPE}≈−60°$).

5.6.2.2 Noise vs. integration

The size of the RC elements in a Schrama ladder network will also determine the exhibited noise of the network. In particular, noise versus the ability to integrate is a trade-

off since, as we increase the scale factor S, resistance of r_k increases (and thus the thermal noise), but at the same time capacitance of c_k reduces resulting in a smaller layout area. The spot noise voltage density is shown in fig. 5.23. As a figure of merit, the ladder network that gave fig. 5.17 exhibits a calculated RMS voltage noise of 1.02 μV in the 500 Hz to 10 kHz bandwidth of interest. This value is close to the absolute maximum amplitude of ENG (c.f. §2.3.4.1; subject to interface geometry) which might be of a limiting factor towards using this technique in a fully implantable in-vivo preparation.
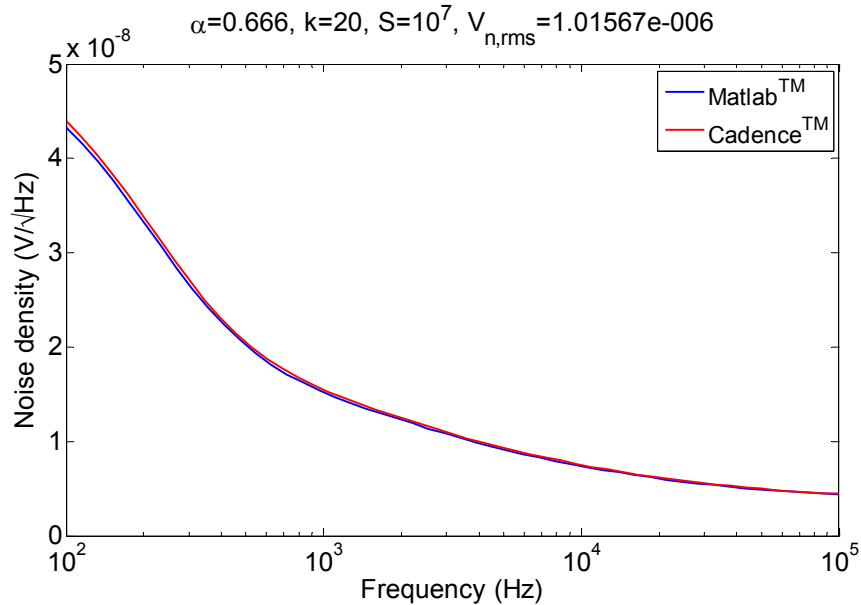

Figure 5.23: Spot noise of a 20 stages Schrama RC ladder network with α=0.666 (i.e. $\varphi_{CPE} \approx -60°$). The voltage noise per square root hertz was calculate manually in Matlab™ and was also plotted in Cadence™ CAD circuit simulator for comparison.

5.6.2.3 Number of stages vs. frequency response

In the last paragraph of §5.3.4.3 we touched on the topic of improving the high frequency response of the CPE by extending the bandwidth beyond 10 kHz. As briefly discussed there, this can be achieved by reducing the admittance to ground for the high frequencies by further reducing c_k (i.e. using a larger scaling factor S) without at the same time altering the value of r_k. The problem is that by doing so we improve the high frequency response of the CPE but the low frequency end is now ruined, tending quicker (i.e. at frequencies higher than about 500 Hz) towards 0°, since at those frequencies the interfacial capacitance is effectively open-circuit with the series resistance of the ladder – or of the electrolyte in the pore – taking over. This effect can be rectified by adding more stages to the ladder network with the disadvantage of increasing its size as well as the thermal noise[3]. Fig. 5.24 illustrates this with a Matlab™ simulation. Additionally, as will

---

[3] This is because admittance to ground has previously been reduced and fewer stages towards the bottom end of the ladder network are now screened (i.e. less resistors are bypassed). Another problem that needs mentioning is that by increasing the scale factor S and the number of stages k, the stage to stage capacitance difference (i.e. passed the 20th stage) can be in certain cases less than 1 pF which might be tricky to implement in terms of accuracy.

be shown later (c.f. §5.8.4) through another simulation, having more than 20 stages in the ladder for a given set of r_k and c_k does not affect the exhibited RMS noise. Therefore, the frequency response of the CPE can be expanded below 500 Hz without an additional noise penalty. Nonetheless, in the case of having c_k altered and admittance to ground reduced as in the above example, RMS noise does increase (from 1.02 μV to about 1.72 μV) due to resistors from the added stages not being shorted to ground at high frequencies.
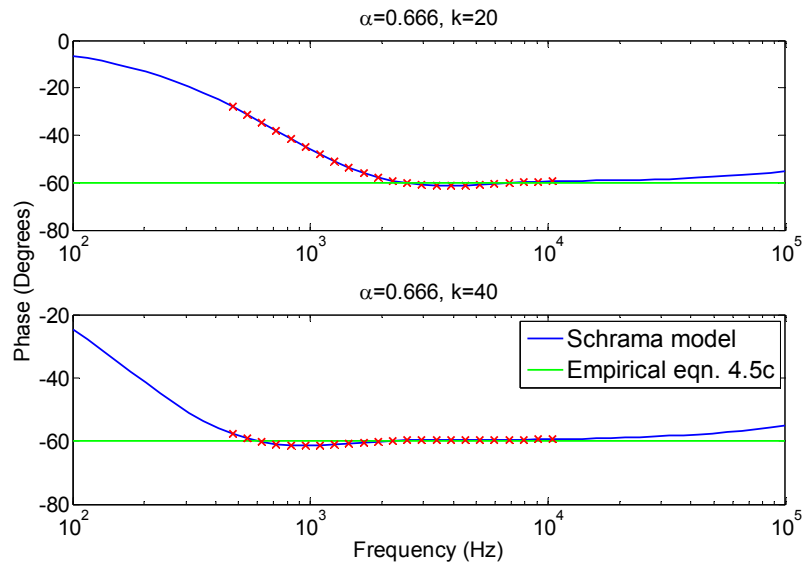
Figure 5.24: Improving the high frequency response of the CPE in comparison to that of fig. 5.18. By reducing the values of c_k 5 times and retaining those of r_k it is possible to extend the frequency range where the phase angle remains constant, nonetheless, the low frequency response is now ruined (top graph). Increasing the number of stages of the ladder network (i.e. from k=20 to k=40) it is possible to restore the low frequency end of the CPE bandwidth, where an approximately constant phase angle is achieved (bottom graph).

5.7 Adaptive mQT[4]

In §5.3.5 a 20 stages non-uniform RC ladder network, constructed using Schrama's continued fractions, was used as part of an interface impedance Z_{inter} and a fit was performed on past neutralisation data (i.e. the impedance locus needed for balancing the tripole in the ENG band). Simulation results were very satisfactory in that the network was able to adapt (in terms of frequency) to the target data, meaning that tuning is no longer required to balance the tripole, i.e., in other words, using a network whose frequency response matches that of the trimming impedance Z_{trim} can improve the mQT in terms of tuning. Additionally, a PCB realisation of the CPE was made with actual measurements matching exceptionally well the predicted Matlab™ simulations (c.f. fig. 5.20). In the present section we are taking this a step further by actually utilising the CPE impedance as an RC ladder network in a cuff model-based simulation for neutralising interference present in the tripole. Therefore, at first instance, this solely involves the

---

[4] The contents of §5.7 were partially presented in [Pachnis et al., 2010].

verification of the proposed technique in simulation using Cadence™ in order to further evaluate its performance. If the assumption of using a trimming impedance Z_{trim} in the form of the 3-component circuit of fig. 5.4 is correct, then as previous simulation results have indicated (c.f. fig. 4.11 and fig. 5.19) no tuning will be necessary. Towards testing the validity of this remark a suitable model of the tripolar cuff is required.

It has become apparent from the in-vitro experiments reported in Chapter 3 that imbalance in the mQT can be due to tissue growth irregularities among the two halves of the cuff, or perhaps, due to geometrical asymmetries at the interface (i.e. electrode misplacement, electrode area mismatch, or differences in the surface textures of electrodes). Therefore, in order to compensate for an imbalance in the tripole a trimming impedance Z_{trim} of the right magnitude *and* phase needs to be added (c.f. §3.3.2.2). Additionally, we need to have independent control over the magnitude and phase of Z_{trim} to reach balance. To achieve so, we used a negative impedance converter (NIC) circuit [Sedra and Smith, 1991, p. 73].

5.7.1 The NIC circuit

A single-ended NIC circuit is shown in fig. 5.25. The particular circuit can be used to multiply or divide an inductive or capacitive impedance with the use of an op-amp (e.g. [De Marcellis et al., 2007] used the NIC for capacitance multiplication in an integrated LPF). In an ideal op-amp the differential input voltage $V_d = V_{(+)} - V_{(-)} \rightarrow 0$ for $G_{diff} \rightarrow \infty$ and as such $V_{in} = V_{(+)} = V_{(-)}$. If the op-amp has high input impedance it is easy to show that the equivalent input impedance Z_{eq} of the NIC is proportional to the ratio of the 3 biasing impedances.

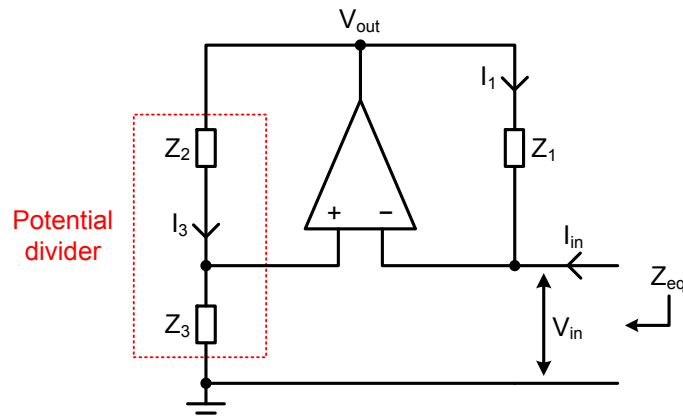Figure 5.25: A NIC circuit with one of its inputs grounded (i.e. single-ended). Shown here is the voltage-inversion (VNIC) configuration where the op-amp acts as an "over-helping" voltage source (as opposed to swapping the input terminals and obtaining the current-inversion (INIC) "over-impeding" configuration). All variations of the NIC circuit used in this work are based on the VNIC configuration.

$$I_{in} = -I_1 = -\frac{(V_{out} - V_{in})}{Z_1} \Leftrightarrow -I_{in}Z_1 + V_{in} = V_{out}$$

$$V_{in} = \frac{Z_3}{Z_3 + Z_2}V_{out} = \frac{Z_3}{Z_3 + Z_2}\left(-I_{in}Z_1 + V_{in}\right) \qquad (5.10a)$$

$$\frac{V_{in}}{I_{in}} = Z_{eq} = -\frac{Z_3 Z_1}{Z_2}$$

or

$$I_3 = \frac{(V_{out} - V_{in})}{Z_2} \Leftrightarrow I_3 Z_2 + V_{in} = V_{out}$$

$$I_3 = \frac{V_{in}}{Z_3} \Rightarrow V_{out} = V_{in} + \frac{V_{in}}{Z_3}Z_2 = V_{in}\left(1 + \frac{Z_2}{Z_3}\right)$$

$$I_{in} = -I_1 = -\frac{(V_{out} - V_{in})}{Z_1} \Leftrightarrow I_{in}Z_1 = -V_{in}\left(1 + \frac{Z_2}{Z_3}\right) + V_{in} \qquad (5.10b)$$

$$\frac{V_{in}}{I_{in}} = Z_{eq} = -\frac{Z_3 Z_1}{Z_2}$$

As eqn. 5.10 reveals it is possible to change the magnitude of impedance Z_3 (i.e. the load) by appropriately selecting impedances Z_1 and Z_2. Nonetheless, it might not be immediately obvious how the NIC succeeds in doing so. We will try to explain this now. The op-amp in the circuit of fig. 5.25 simply tries to compensate for the voltage drop across Z_1 which is connected between the output and the inverting input of the op-amp (i.e. VNIC configuration). By generating current I_1 (and current I_3) that is proportional to the voltage drop across impedance Z_1, the op-amp acts as a supplementary voltage source which aids the (ideal in this case) input voltage source V_{in} towards providing a suitable current I_{in} that is equal but opposite to I_1. This is achieved by the op-amp incorporating both negative (via Z_1) and positive (via Z_2 and Z_3) feedback. The op-amp continuously compares via feedback a fraction of its own output (i.e. via the potential divider) with the voltage drop across impedance Z_1, and tries to keep the difference close to zero (i.e. $V_d \rightarrow 0$) by adjusting the output voltage V_{out}. Thus, V_{out} is always larger (in absolute value) than the voltage drop across Z_1; some is used to compensate for the voltage drop across Z_1 (i.e. $V_{out}=V_{Z1}/[(Z_3/(Z_3+Z_2))-1]$) while the rest is added to the input voltage source V_{in} – the op-amp is misled! As a result, the voltage drop across impedance Z_1 is essentially reversed while the current I_{in} continues to flow in the same direction. In other words the op-amp over-compensates for the voltage drop across Z_1 by providing the appropriate voltage (or current), and depending on the ratio V_{in}/I_{in}, achieves an input impedance Z_{eq} which is a function of the 3 biasing impedances. Furthermore, as the NIC applies an inversion between voltage V_{in} and current I_{in} of the input source, the phase of

Z_{eq} is 180° phase shifted (−ve sign in eqn. 5.10)[5]. For our purpose we needed to use a chain of two NIC circuits (or we can replace impedance Z_2 with another "floating" NIC circuit). Therefore, impedance Z_{eq} will be positive for even number of stages and negative for odd number of stages[6].
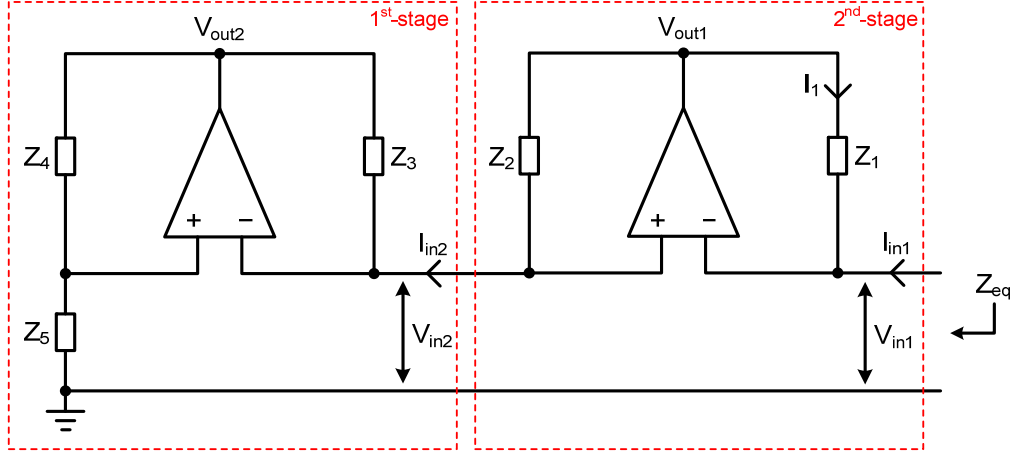

Figure 5.26: A positive single-ended impedance scaler made by two cascaded NIC circuits.

A NIC circuit offering an input impedance Z_{eq} with no phase inversion is shown in fig. 5.26. Typically, the 1st NIC stage carries out the impedance conversion while the 2nd NIC stage recovers the phase angle of load impedance Z_5. Nonetheless, apart from the phase angle recovery, the 2nd NIC stage can also be used to further multiply or divide the load.

$$V_{in_1} = V_{in_2} = -\frac{Z_5 Z_3}{Z_4} I_{in_2} \Leftrightarrow I_{in_2} = -\frac{Z_4}{Z_5 Z_3} V_{in_1}$$

$$V_{out_1} - V_{in_2} = I_{in_2} Z_2 \Leftrightarrow V_{out_1} - V_{in_1} = -Z_2 \frac{Z_4}{Z_5 Z_3} V_{in_1}$$

$$I_{in_1} = -I_1 = -\frac{\left(V_{out_1} - V_{in_1}\right)}{Z_1} = -\frac{-Z_2 \dfrac{Z_4}{Z_5 Z_3} V_{in_1}}{Z_1}$$

---

[5] Writing the input impedance of the NIC circuit in polar exponential form we have: $Z_{eq} = -\dfrac{|Z_{CPE}|e^{j\varphi_{Z_{CPE}}}|Z_1|e^{j\varphi_{Z_1}}}{|Z_2|e^{j\varphi_{Z_2}}}$, while if Z_1 and Z_2 were resistances then $\varphi_{Z_1} = \varphi_{Z_2} = 0°$ and $Z_{eq} = -\dfrac{|Z_{CPE}|e^{j\varphi_{Z_{CPE}}}|R_1|e^{j0}}{|R_2|e^{j0}} = \left(\dfrac{|Z_{CPE}||R_1|}{|R_2|}\right)e^{j(\varphi_{Z_{CPE}}+0-0)}e^{j\pi\,rad} = \left(\dfrac{|Z_{CPE}||R_1|}{|R_2|}\right)e^{j(180°+\varphi_{Z_{CPE}})}$. Therefore, $|Z_{eq}| = \dfrac{|Z_{CPE}||R_1|}{|R_2|}$ and $\varphi_{Z_{eq}} = 180° + \varphi_{Z_{CPE}}$ where the last term is the phase angle of the CPE RC ladder network.

[6] In case of an ideal op-amp, interchanging the input terminals of a NIC circuit like that of fig. 5.25 – in other words using either the VNIC or the INIC configuration – has no effect on the sign of the input impedance Z_{eq}. In fact, the principle of operation remains the same. The difference exists in that the over-compensating op-amp either adds or subtracts, depending on the chosen NIC configuration, a voltage to or from the voltage of the input source V_{in}.

$$\frac{V_{in_1}}{I_{in_1}} = Z_{eq} = \frac{Z_5 Z_3 Z_1}{Z_2 Z_4} \qquad (5.11)$$

Due to the way the mQT amplifier is connected to the cuff, in order to balance the recording tripole a trimming impedance Z_{trim} which is floating must be used (c.f. fig. 3.3). Therefore, a floating version of the NIC circuit is also required. Such a circuit has been proposed by [De Marcellis et al., 2007], and is reproduced in fig. 5.27 for the convenience of the reader[7].
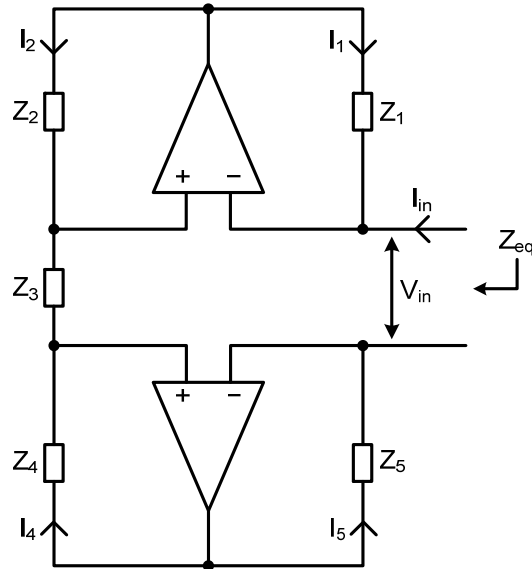
Figure 5.27: A single stage floating NIC circuit. The floating impedance Z_3 at the middle of the structure is multiplied by the selected impedance ratio.

Taking the circuit of fig. 5.25 and redoubling the structure with respect to impedance Z_3 (i.e. the impedance we want to convert) we obtain the floating version of the NIC circuit. Since the structure in fig. 5.27 is now floating we can safely assume that the feedback currents I_1 and I_5 (as also I_2 and I_4) will be equal (but opposite). Therefore we can redraw fig. 5.27 as per fig. 5.25 with impedances Z_2+Z_4 and Z_1+Z_5 connected between the op-amp's output and its non-inverting and inverting inputs, respectively. Following the same steps as for the derivation of eqn. 5.10, the input impedance Z_{eq} of eqn. 5.12 is obtained for the floating arrangement. Finally, an analytical derivation of the input impedance of the floating arrangement of fig. 5.27 is given in Appendix C.

$$Z_{eq} = -Z_3 \left(\frac{Z_1 + Z_5}{Z_2 + Z_4} \right) \qquad (5.12)^8$$

---

[7] For the interested reader, an alternative floating NIC circuit that was ultimately tested (in simulation) but at the end was not used is this work can be found in [Antoniou, 1972], if required.

[8] Comparing eqn. 5.12 with eqn. 15 from [De Marcellis et al., 2007] the reader may notice that those are not the same. In a personal communication with A. De Marcellis on June 2009 it became apparent that eqn.

5.7.1.1 NIC biasing arrangements

The NIC circuit is a simple in operation circuit but the reader should make no mistake – as with every increasingly complex configuration (i.e. going from a single stage to using a chain of NICs) there are cases where things can go wrong. One such case will be analysed in this section for the support of discussion and to ease any future attempts of realising this circuit. In particular, care must be taken in appropriately selecting the biasing impedances (or in this example resistances) of the 2nd NIC stage which is responsible for the phase angle recovery. Using the circuit of fig. 5.26, we redraw the circuit in fig. 5.28 and set resistances $R_1=R_2=R_4=10$ kΩ and $R_3=100$ Ω to perform a "divide by 100" conversion of a load resistance $R_{load}=2.3$ kΩ. We have chosen those values for two reasons: a) the value of R_{load} corresponds to the actual input impedance magnitude of a 20 stages Schrama RC ladder network with $\varphi_{CPE}=-80°$ (i.e. $\alpha=0.888$)[9] at 2 kHz in the ENG band; b) in that way we can understand first-hand if an accurate conversion of that scale can be achieved by offering a very small equivalent +ve resistance after the NIC (i.e. about 23 Ω). The set reduction ratio in this case is rather pessimistic since in reality we will not need to downconvert the magnitude of the CPE more than about 15 times in order to match that of our Pt electrode cell (c.f. §5.7.3.4). Conversely, a reduction ratio set value will certainly depend on the amount of imbalance present in a tripolar cuff.

The reported voltages depicted at various points on the circuit of fig. 5.28 were the result of actual measurements[10] taken from a discrete realisation of the circuit. Two basic high input impedance op-amps (National Semiconductor, LF355) were used for the conversion task, while to measure the input impedance of the overall NIC circuit a variable gain instrumentation amplifier (Analog Devices, AMP01) was used. A test resistor R_{test} of a known value (i.e. 1 kΩ) was placed in series to the input of the NIC circuit having the voltage drop across it being measured[11] with the AMP01 set to operate

---

15 from the aforementioned reference was wrong and eqn. 5.12 is indeed valid. The discrepancy in the derivation of those two different expressions lies in the assumption that the currents flowing at the input are not equal, i.e. $|I_1|\neq|I_5|$, whereas for the floating NIC this argument is not true and $|I_1|=|I_5|$.

[9] The reader is reminded that as the frequency exponent α goes up (i.e. as the phase angle increases), the R – stage to stage – components of the ladder network are reduced (because the pore cross-section is increased), while conversely the C components are increased (because the interfacial double-layer capacitance is increased). Hence, the overall magnitude of the RC ladder network is reduced as α increases. This argument can be readily verified by looking at the table of pre-calculated RC values of Appendix B (i.e. for a normalised scaling factor S).

[10] The reported pk-pk voltage signal values shown on fig. 5.28 were measured manually using a digital oscilloscope and therefore their values are approximate and not necessarily matching exactly (as shown later) those of the hand calculation. Moreover, albeit on the schematic a signal might look like being a perfect sine wave, in this case, some of the signals were slightly distorted (e.g. V_{out2}) making their exact measurement difficult.

[11] Oscilloscope probes can also be used to directly measure the voltage difference across R_{test} (i.e. by either using the math oscilloscope operation between two channels or using a single differential probe instead) without causing an issue to the operation of the NIC circuit, as the highest frequency of input impedance measurement is 100 kHz. This requires the use of an additional oscilloscope channel as opposed to using a differential amplifier to measure the voltage drop (i.e. except in the case where a single differential probe is used). Moreover, the effect of the probes' parallel 1 MΩ resistance/12 pF capacitance to the operation of

at unity gain (i.e. in order to maximise its GBW). Therefore, the input current to the NIC, being proportional to the output voltage of the AMP01, can be calculated and with that the input impedance of the circuit. This input impedance measuring method is revisited in more detail in §5.7.3.1. An input sinusoidal test voltage V_{test} of 900 mV was used for exciting the circuit with its magnitude being chosen on the basis of causing a desired distortion in respect to the utilised power supply rail and selected biasing resistors. A smaller in amplitude V_{test} might not have caused this distortion, however, it would be rather difficult to accurately measure the induced mV signals (i.e. much less than about 20 mV) throughout the circuit using a digital oscilloscope (Tektronix Inc., 4 channel model TDS 2004B, 60 MHz) with a maximum channel gain of 2 mV per division. Finally, it should be also mentioned that signals were recorded with some averaging being applied by the oscilloscope.
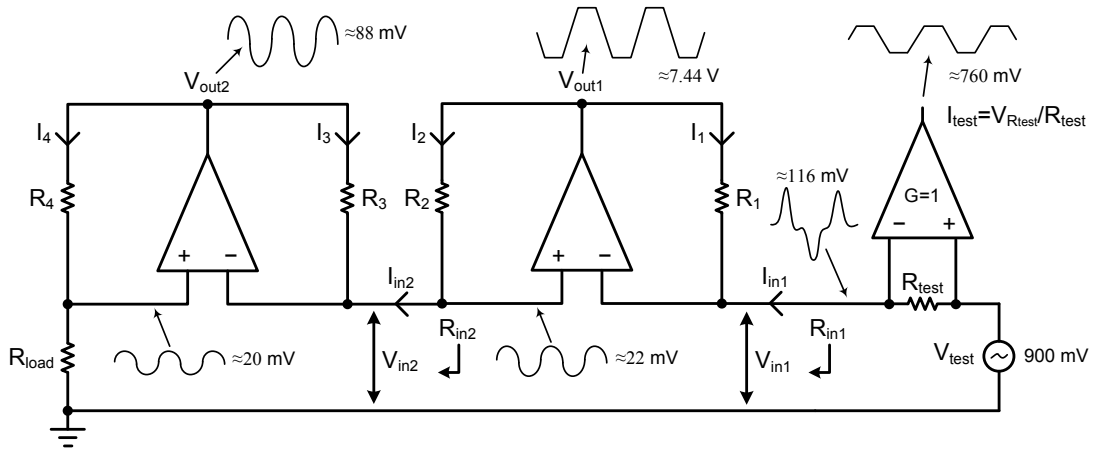
Figure 5.28: A two stage single-ended NIC circuit performing resistance conversion. In this case choosing inappropriate (i.e. too high) values for the biasing resistors of the 2nd NIC stage causes the op-amp of the 2nd stage to saturate. All voltages were measured from a discrete realisation of the circuit and their reported values are in pk-pk. $R_1=R_2=R_4=10$ kΩ, $R_3=100$ Ω, $R_{load}=2.3$ kΩ, $R_{test}=1$ kΩ, VDD=+5 V, VSS=−5 V, and $V_{test}=900$ mV (i.e. power rails not shown). Note that V_{out2} is 180° out of phase with V_{out1} which in turn is 180° out of phase with I_{test}.

Assuming ideal op-amp operation for the 1st NIC stage we have:

$$\frac{V_{out2}-V_{in2}}{R_3}=\frac{V_{out2}-V_{in2}}{100\Omega}=I_3=-I_{in2} \Leftrightarrow V_{out2}=V_{in2}-100\Omega\cdot I_{in2}$$

$$V_{in2}=\frac{R_{load}}{R_4+R_{load}}V_{out2}=\frac{2.3k\Omega}{10k\Omega+2.3k\Omega}\left(V_{in2}-100\Omega\cdot I_{in2}\right)\Leftrightarrow$$

$$\frac{V_{in2}}{I_{in2}}=R_{in2}=-\frac{230k\Omega}{10k\Omega}=-23\Omega \quad \therefore I_{in2}=\frac{22mV}{-23\Omega}\approx-956uA$$

$$V_{out2}=20mV-100\Omega\cdot(-956uA)\approx116mV$$

the NIC circuit was also investigated in Cadence™ circuit simulator and the circuit confirmed working without any issues (i.e. the capacitive reactance to ground was too large to be of any issue, especially at the ENG frequencies we are interested in).

$$\therefore I_4 = \frac{V_{out2} - V_{in2}}{R_4} = \frac{116mV - 20mV}{10k\Omega} = 9.6uA$$

i.e. the current I_{in2} that flows to the input of the 1st NIC stage is about 100 times more (in absolute value) than the feedback current I_4 flowing in the potential divider. The input resistance R_{in2} is now 100 times less than the load, i.e., at 23 Ω. Note that there is also a 180° phase difference between I_{in2} and V_{out2}. Similarly, proceeding with the analysis of the 2nd NIC stage we have:

$$V_{R_{test}} = V_{test} - V_{in1} = I_{in1} \cdot R_{test} \Leftrightarrow I_{in1} = \frac{900mV - 116mV}{1k\Omega} = 784uA$$

$$\frac{V_{in1}}{I_{in1}} = R_{in1} \Leftrightarrow V_{in1} = 784uA \cdot 23\Omega \approx 18mV$$

$$\frac{V_{out1} - V_{in1}}{R_1} = \frac{V_{out1} - V_{in1}}{10k\Omega} = I_1 = -I_{in1} \Leftrightarrow V_{out1} = V_{in1} - 10k\Omega \cdot I_{in1}$$

$$\therefore V_{out1} = 18mV - 10k\Omega \cdot 784uA \approx -7.82V$$

Despite having the 1st NIC stage successfully converting the load resistance down to 23 Ω the 2nd NIC stage which is responsible for the phase angle recovery (thus the reason for setting $R_1=R_2$) causes a distortion of the signals due to the high value of the particular biasing resistors. The amplitude of the output voltage V_{out1} becomes higher than the 5 V power rail, causing the voltage, and therefore the proportional input current I_{in1}, to be clipped. This clipping causes issues to the correct operation of the NIC circuit. In this example, selecting lower value of resistances for the 2nd NIC stage (e.g. $R_1=R_2=1$ kΩ) or setting R_3 of the 1st NIC stage to a higher value (so that $R_{in2}>>23$ Ω) can minimise or even eliminate this signal clipping. Hence, as illustrated through this example, appropriately choosing the values of the biasing resistors for any of the two NIC stages is important for the correct operation of the circuit.

5.7.1.2 NIC testing results

The operation of the NIC circuit was verified both in Multisim™ (Analog Devices Edition) and Cadence™ circuit simulators as well as by successfully implementing, using discrete circuit components, an active LPF having a very small cut-off frequency with a chain of two single-ended NIC circuits which performed capacitance multiplication (i.e. 100 pF to 4 μF). In this section for the convenience of time and space we report a single simulation result in Cadence™ to illustrate that the NIC circuit actually works the way it is supposed to.

Due to the way the NIC circuit achieves the impedance conversion we need to set $Z_3=Z_{CPE}$ while for converting the magnitude without affecting the phase of the CPE we use resistors in place of the impedances, i.e., $Z_1=R_1=1$ kΩ and $Z_2=R_2=10$ kΩ to perform, in this example, a "divide by 10" of a Z_{CPE} with $\alpha=0.666$ (i.e. $\varphi_{CPE}\approx-60°$). Fig. 5.29

shows the simulation result with a two stage floating version of the NIC (c.f. fig. 5.27)[12] employing the aopac07 FET input op-amp cell by XFAB™ XC06 (i.e. 0.6 μm CMOS process). The circuit schematic and data sheet of the particular op-amp are given in Appendix D. In the log-log scale plot it is easy to see that the magnitude of the Z_{CPE} is reduced by 10 times after the NIC. Conversely, the phase is not affected much in the 500 Hz to 10 kHz ENG bandwidth. The reason for the deviation of the phase angle at high frequencies (i.e. >10 kHz) is due to the inability of the 2nd NIC stage (i.e. the phase angle recovery stage) to handle the reduced impedance load from the 1st stage, since that now approaches a value comparable to the output impedance of the op-amp – in other words the downconverted Z_{CPE} is starting to "load" the op-amp of the 2nd stage. In addition, as was emphasised by [De Marcellis et al., 2007], the large frequency range of impedance conversion also depends on the op-amp's performance in terms of (finite) DC gain, input impedance, and bandwidth. In practice, the usefulness of the NIC can be limited by its tendency to oscillate due to the use of +ve feedback. If necessary, stability could be improved by adding a capacitance to the resistive feedback network, but only at the cost of reducing the frequency range over which the conversion is produced[13].
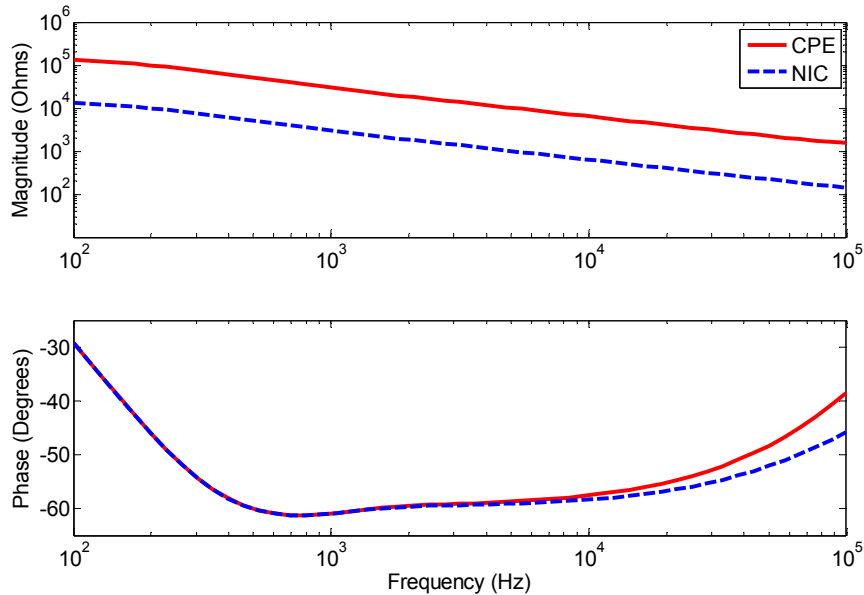
Figure 5.29: Cadence™ simulation of the floating NIC using the aopac07 op-amp cell from XFAB™ to perform a "divide by 10" of a 20 stages Schrama RC ladder network Z_{CPE} with $\varphi_{CPE} \approx -60°$. The magnitude is reduced after the NIC while the phase angle is maintained in the ENG bandwidth of interest (i.e. 500 Hz to 10 kHz).

---

[12] Therefore setting $Z_1=R_1=1$ kΩ, $Z_5=R_5=1$ kΩ, $Z_2=R_2=10$ kΩ, and $Z_4=R_4=10$ kΩ for the 1st stage (i.e. for simulation this is necessary, however, resistors do not need to be balanced at both sides in a true floating arrangement), while for the 2nd stage $Z_3=Z_{eq,1st\text{-}stage}$ and $Z_1=Z_2=Z_4=Z_5=R=1$ kΩ in order to recover the phase angle of the CPE. A supply rail of VDD=5 V was used.

[13] In our case there is no issue of instability since the NIC is not utilised to compensate against the effect of a component in another circuit (e.g. cancelling out the effect of source resistance in a current source). In particular, having the NIC supplying surplus current can potentially generate positive feedback (i.e. when $Z_{eq}<R_{source}//R_{load}$) causing the op-amp to saturate, thus rendering the system unstable.

5.7.2 Model-based simulation (adaptive mQT on cuff model)

Before proceeding with the in-vitro verification of the adaptive mQT using the NIC circuit so to achieve independent control over the magnitude and phase of a chosen CPE impedance, it would be appropriate to assess its performance in simulation. The model of the tripolar cuff used in this simulation is shown is fig. 5.30. The principle was to cause a deliberate known imbalance in the tissue resistances and compensate for that imbalance by adding an impedance of appropriate magnitude and phase. More specifically, if the model is seen as a Wheatstone bridge having resistances R_{t1}, R_{t2} at one arm and electrode impedances Z_{e1}, Z_{e3} at the other, the mid-point differential voltage across the two arms of the bridge should be zero if that is balanced (i.e. the ratio of the two arms is the same). Setting R_{t1}=2 kΩ, R_{t2}=1 kΩ and Z_{e1}=Z_{e3} we have a ratio of 1/3 and 1/2 respectively. Hence, the percentage imbalance in the tripole is 17%[14]. To test the ability of the NIC to downconvert the magnitude of an impedance used for trimming without affecting its phase and while the NIC is connected to the cuff model, we used an impedance Z_{RC} with a magnitude of 100 times larger than Z_{CPE} but same phase $\varphi_{CPE}\approx-60°$. If the idea works, after a "divide by 100" of the floating NIC, Z_{RC}=Z_{CPE} and adding an impedance Z_{trim}=$Z_{e1,3}$ to the upper right arm of the bridge should match the ratio and achieve balance.
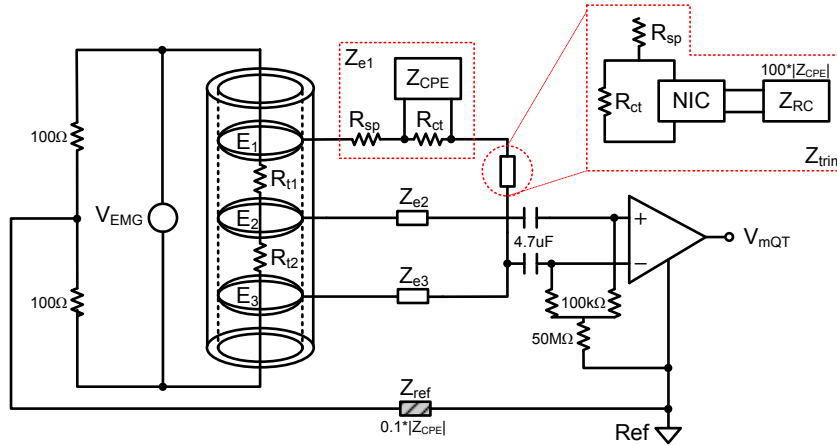
Figure 5.30: EMG model of the mQT recording configuration. The impedance Z_e of Pt electrodes E_1, E_2, E_3 is the circuit of fig. 5.4 with Z_{CPE} being a 20 stages Schrama RC ladder network with $\varphi_{CPE}\approx-60°$. The internal to the cuff tissue resistances are R_{t1}=2 kΩ and R_{t2}=1 kΩ causing a known imbalance. The impendence Z_{RC} arranged for trimming has a magnitude of 100 times more than Z_{CPE} but same phase. Using the floating NIC, Z_{trim}=Z_e. The reference electrode impedance Z_{ref} is connected to the cuff via two 100 Ω external to the cuff tissue resistances. The decoupling capacitors and the T-network of biasing resistors are also shown. V_{EMG}=10 mV, R_{sp}=500 Ω and R_{ct}=50 kΩ.

The amplifier reference is connected via an impedance Z_{ref} of a magnitude 10 times less than Z_e (i.e. representing a reference electrode of bigger size to that of recording

---

[14] Knowing that a ratio of 1/3 corresponds to 33% and 1/2 to 50% of balance for the tissue resistances and electrode impedances respectively, the overall percentage imbalance in the tripole is defined as the difference of the two ratios, i.e., $|[R_{t1}/(R_{t1}+R_{t2})]*100-[Z_{e1}/(Z_{e1}+Z_{e3})]*100|=|(1/3)*100-(1/2)*100|\approx17\%$.

electrodes Z_e[15]) to two 100 Ω, external to the cuff, tissue resistances indicating that the reference electrode is implanted in the vicinity of the cuff. The 4.7 µF capacitors are used in series with the electrodes for safety, blocking any direct current from the recording amplifier from flowing through the electrodes and causing electrolysis in the event of a semiconductor failure (i.e. safeguard under single-fault conditions in respect to the blocking capacitors). Using those blocking capacitors also avoids the problem of having different DC electrode potentials at the two inputs of the amplifier as a result of faradaic current flowing through their polarisable interface (i.e. also known as the overpotential η; c.f. §4.2), resulting in a DC offset appearing at the output. It is also important to state that the trimming network is currently not fail-safe (i.e. current can flow from the NIC to electrodes). For simulation, the reference was connected to the middle of a VDD=5 V power supply.

The output voltage of the mQT is shown in fig. 5.31 from 100 Hz to 100 kHz. At 500 Hz the EMG breakthrough with compensation is 6829 times less, while at 10 kHz it is 107 times less, when an EMG source of 10 mV is applied across the cuff. Knowing however that most of the energy of the ENG will be concentrated around the 2 kHz frequency or below (c.f. §2.3.4.1), this is a rather satisfactory result. Concluding, the effect that an ENG voltage source has on the neutralisation performance of the adaptive mQT has also been studied. More specifically, a floating V_{ENG}=1 µV was positioned between the middle point of the two tissue resistances and the electrode impedance Z_{e2}. Simulation results indicated no issues in recording of the ENG signal.
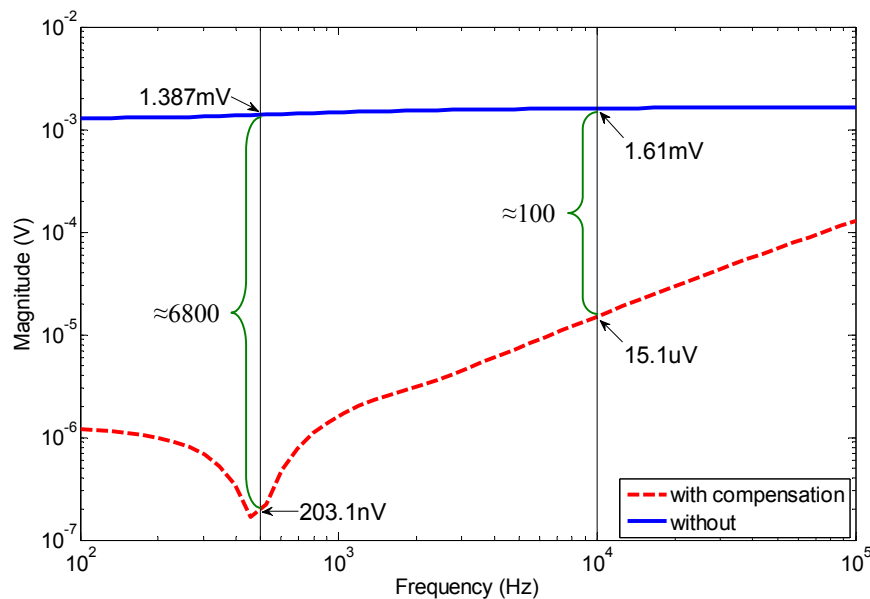
Figure 5.31: Cadence™ ac simulation of the mQT output with (dotted) and without (solid) compensation in the form of the added trimming impedance Z_{trim}. Input is a 10 mV signal applied across the tripolar cuff.

---

[15] Note that increasing the impedance of the reference electrode to that of the cuff electrodes does not significantly affect the response at the differential input of the amplifier with respect to CM voltage [Donaldson et al., 2003].

5.7.3 Experimental verification

Having accessed in simulation the operation of a novel proposed technique which employs a NIC circuit to perform the neutralisation of EMG interference picked up by the recording tripole, we can now proceed with the in-vitro verification. In the first instance we need to make sure that the NIC circuit can – in practice – convert the magnitude of a real CPE (i.e. a 20 stages Schrama RC ladder network) without affecting its exhibited phase angle at the bandwidth of interest. As is shown later, this can be successfully achieved.

Knowing that both ends of the trimming impedance Z_{trim} added to either side of the outer electrodes must not be tied to a fixed potential, a floating version of the NIC circuit like that of fig. 5.27 is required. During the laboratory experiments the operation of the floating NIC circuit could not be verified using discrete circuit components. The main reason was the already discussed discrepancy of deriving eqn. 5.12. Additionally, there was no attempt at the time to "drive" the input V_{in} of the floating NIC circuit using an audio transformer, as it should have been done. Having difficulties getting the floating NIC circuit to work the testing plan had to be quickly revised. Instead, a single-ended version of the NIC circuit can be used to balance a Wheatstone bridge arrangement having an electrochemical cell at one side of the arm of the bridge and an impedance, made out of a circuit like that of fig. 5.4 with the Z_{CPE} obtained after a single-ended NIC circuit, at the other side. The actual arrangement is shown in fig. 5.32. If the idea works, we should be able to match exactly the impedance Z_{cell} of the electrochemical cell with our added impedance Z_{trim} and therefore achieve balance. Although in practice we do not actually neutralise interference in the tripole in the exact same way (i.e. a floating NIC circuit must be used while there are two electrode impedances actively taking part in balancing the tripolar arrangement), this approach is technically identical and therefore can conveniently prove the operating principle of the proposed technique.

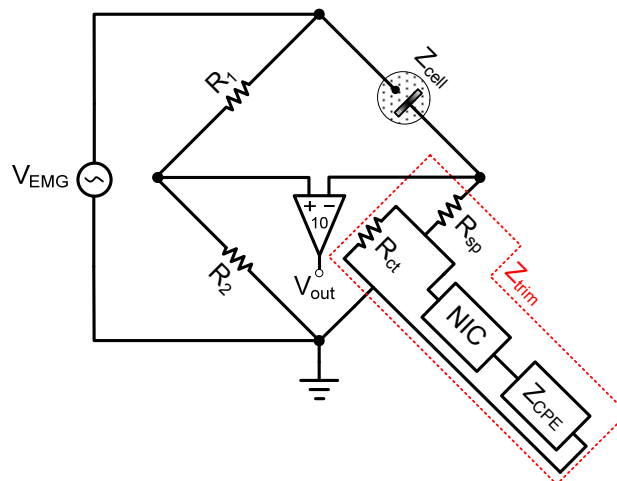

Figure 5.32: Balancing a Wheatstone bridge arrangement using a single-ended NIC circuit to match the impedance Z_{cell} of an electrochemical cell. Also, $R_1=R_2=1$ kΩ with ±0.1% tolerance. The output V_{out} of the differential amplifier will be zero if the ratio of the two arms of the bridge is the same, i.e., when $R_1=R_2$ and $Z_{cell}=Z_{trim}$.

5.7.3.1 CPE magnitude conversion

A schematic diagram showing the circuit arrangement for measuring the input impedance of the NIC circuit in the form of a test voltage and current is shown in fig. 5.33. The particular measuring scheme was needed since in this case the available impedance analyser (Wayne Kerr Electronics, model 6520BD1, 20 Hz-20 MHz) could not be used to measure the input impedance of such an active circuitry. Focusing our discussion to fig. 5.33, a test resistor R_{test}=1 kΩ was selected to ensure that R_{source}+R_{test}<|Z_{in}| in order to avoid any "loading" effects on the V_{test} signal generator but at the same time R_{test} was not made very small in order to moderately limit the input current to the circuit, thus producing a measurable (i.e. sufficiently high) voltage drop across R_{test}. An instrumentation amplifier (Analog Devices, AMP01) set to operate at unity gain was used to measure the test current I_{test} flowing through the test resistor R_{test} and into the circuit (i.e. by measuring the voltage drop across this known-value resistor), while a JFET input op-amp (National Semiconductor, LF355) connected as a buffer was used to measure the voltage drop after R_{test} (i.e. the actual input voltage of the circuit under measurement). Knowing the value of the test voltage applied to the input of the NIC and the test current drawn by the circuit, as a result of the applied voltage, it is possible to obtain the magnitude (i.e. V_{in}/I_{test}) and phase angle (i.e. phase difference between V_{in}(t) and I_{test}(t) signals) of the input impedance Z_{in} of the circuit from the sinusoidal signals V_{in}(t)=V_{in}·cos(ωt+φ−n) and I_{test}(t)=I_{test}·cos(ωt+φ), where n in this case denotes the phase angle difference between the (leading) current I_{test}(t) and voltage V_{in}(t).
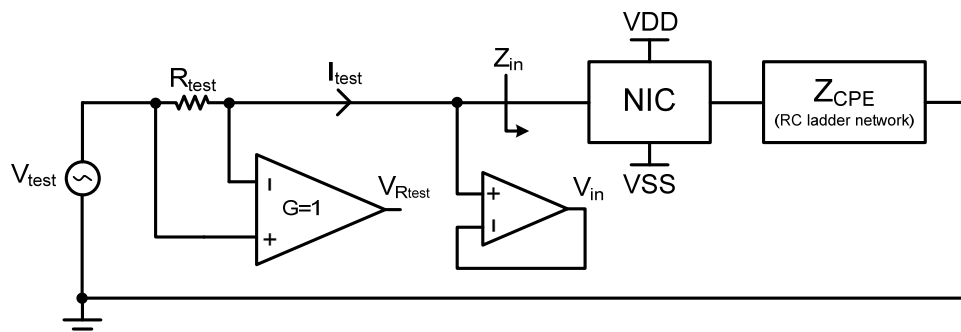
Figure 5.33: High-level schematic of the NIC input impedance measurement arrangement[16]. R_{test}=1 kΩ, VDD=+5 V, VSS=−5 V. Z_{CPE} is a 20 stages Schrama RC ladder network having a phase angle φ_{CPE}.

---

[16] An alternative circuit based on the inverting amplifier configuration can be used for measuring the input impedance of a device which has one of its input terminals connected to ground (i.e. single-ended). The high-level schematic of this arrangement is shown at the bottom left of this footnote. This arrangement, however, cannot be used to measure the impedance after the NIC circuit, as demonstrated from real measurements performed using discrete circuit components. This is because in our case the circuit whose impedance we are trying to measure is active and as a result I_{test}≠I_{in}. This is true since some current from the power supply of the NIC will also flow to the inverting input of the op-amp (i.e. I_{in}=I_{test}+I_{VDD}−I_{VSS}). Instead, what we end up measuring is the impedance of the ladder network as if it has not been downconverted by the NIC circuit. Nevertheless, this arrangement can be successfully used to measure the input impedance of a passive device (e.g. an RC network) since then I_{test}=I_{in} and Z_{in}=V_{test}/($V_{Rfeedback}$/$R_{feedback}$). This has also been verified in Cadence™ circuit simulator. Finally, representing the measuring circuit as a potential divider with resistances R_{NIC} (i.e. the input resistance after

Frequency (Hz)	$\varphi_{CPE}=-60°$		$\varphi_{CPE}=-80°$	
	Magnitude (Ω)	Phase (°)	Magnitude (Ω)	Phase (°)
500	4750	−64.8	781.8	−80.6
1 k	2917	−63.4	421.8	−80.6
2 k	1820	−62.6	228.3	−80.6
3 k	1355	−61.5	156.0	−81.0
5 k	1014	−61.2	93.00	−79.9
8 k	739.5	−61.1	51.40	−79.5
10 k	625.2	−60.6	36.11	−79.2

Table 5.5: Magnitude and phase data measured for two PCBs with $\varphi_{CPE}=-60°$ and $\varphi_{CPE}=-80°$ after a two stage NIC circuit performing a "divide by 10" impedance scaling. A V_{test}=60 mV pk-pk was used.

Table 5.5 shows actual measurement results of the magnitude and phase angle at spot frequencies for two different 20 stages Schrama RC ladder networks; one with $\varphi_{CPE}=-60°$ and the other with $\varphi_{CPE}=-80°$. The input impedance was measured after a two stage single-ended NIC circuit (c.f. fig. 5.26) having a reduction ratio of 1/10, by utilising the measuring technique discussed above. In particular, the phase angle was measured in two ways: a) using an analogue phase meter (Feedback Ltd., model APM612) that automatically compared signals V_{Rtest} and V_{in}, displaying the phase difference between the two; b) using the time-axis cursors of the digital oscilloscope to manually calculate the phase difference of the two signals in question as: $\theta=(\Delta t/T)\cdot 360°$ (where Δt is the time difference between the two signals and T is the period). Although both approaches offered identical results, as the phase meter was of analogue type, the oscilloscope ultimately offered better resolution and precision, especially at high frequencies. As such, the magnitude and phase angle data of table 5.5 were obtained using the oscilloscope.

For means of comparison the data of table 5.5 were plotted in Matlab™ (fig. 5.34) against actual measured data obtained from the two PCBs taking part in the magnitude downconversion (i.e. the impedance of a 20 stages RC ladder network Z_{CPE} before the NIC circuit). The measured magnitude after the NIC circuit was then manually multiplied back by a factor of 10 to cancel out the effect of the reduction ratio of the NIC (i.e. 1/10) so comparison of the two magnitudes in terms of their differences, as a result of the conversion, can be carefully performed. We see that results match very closely, and this is especially true for the magnitude data. As the intrinsic conversion phase angle error of

---

the NIC) and $R_{feedback}$ we see that the virtual ground essentially isolates the two resistors and thus current $I_{in}=-I_{out}$ depends solely on R_{NIC} (which the op-amp tries to match) and not on $R_{NIC}+R_{feedback}$ as would be the case in an actual potential divider circuit.
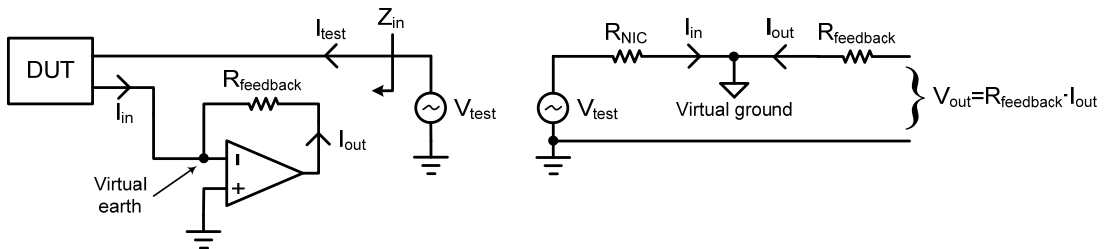
a two stage single-ended NIC was measured (i.e. using a resistive load) to be less than 1°, any mismatch in the phase angle data should mainly be due to human error while taking readings off the oscilloscope (i.e. finding the exact difference in time between the adjacent zero crossings). Another source of error might be due to the non-idealities of the NIC op-amps (e.g. high but not infinite input impedance and open-loop gain). For further comparison, magnitude and phase angle data from 100 Hz to 12 kHz obtained using the analogue phase meter have also been plotted on the same graphs. It is clear that the phase angle is also maintained at frequencies lower than 500 Hz. The only limitation existed at frequencies higher than about 12 kHz where the particular Z_{CPE} impedance downconverted by the 1st NIC stage was starting to "load" the output of the 2nd NIC stage (as already explained for fig. 5.29). This was true for the PCB having $\varphi_{CPE}=-80°$ since, as the frequency exponent α increases, the impedance magnitude of the Z_{CPE} reduces (c.f. fig. 5.20) and therefore it is easier to present an impedance whose magnitude (once downconverted) is closer to the output impedance of the 2nd NIC stage, in comparison to a PCB exhibiting a smaller phase angle (i.e. $\varphi_{CPE}=-60°$) and thus higher magnitude.
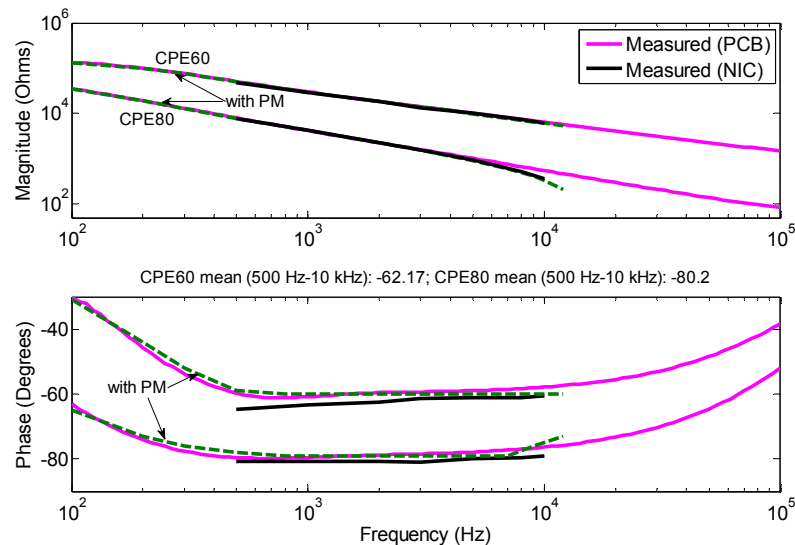
Figure 5.34: Magnitude and phase angle of two CPEs before and after a NIC circuit reducing down the magnitude by 10 times. The phase angle is within reasonable limits and not affected much by the downconversion, i.e., the error in the mean phase angle in the ENG bandwidth of interest for the PCB with $\varphi_{CPE}=-60°$ and $\varphi_{CPE}=-80°$ is about 2° and 0.3°, respectively. Magnitude after the NIC has been multiplied back by a factor of 10 for comparison. Shown with the green dotted line is the magnitude and phase angle measured with the analogue phase meter for a slightly wider bandwidth (i.e. 100 Hz to 12 kHz).

5.7.3.2 Electrochemical cell

The electrochemical cell was made from two metal electrodes; a small spherical Pt electrode (i.e. the working electrode) and a much greater in size reference electrode which was used to complete the cell[17]. The electrolyte solution of the cell was a 0.9%

---

[17] Hence the impedance contributed to the overall cell by the reference electrode is minimal and therefore the measured cell impedance is, essentially, dominated by that of the working electrode alone.

NaCl in contact with air used throughout the experiments. Two different types of working electrodes[18] were made in our laboratory by melting insulated Pt wire (i.e. either pure Pt or mixed with Ir) using a small handheld flaming torch (Micro-Weld Ltd., Micro-flame gas generator - type A), while the reference electrode was a thin sheet of medical grade stainless steel. Each of the two melted wires was placed inside a glass pipette which was subsequently filled with silicone sealant (Homebase Ltd., kitchen & bathroom, translucent silicone rubber) providing additional insulation and fixing the wire into position so that it will not move around when inside the pipette and electrolyte. Both the reference and working electrodes were placed in a plastic beaker with the reference electrode being fixed at the side wall using one-component silicone sealant (Dow Corning, type 734), while the working electrode was positioned approximately at the middle of the beaker. The beaker was subsequently filled with electrolyte up to the top. The glass pipette was held by blue tack in a vertical position through a horizontal sheet of Perspex, which was fixed to a wooden stand. Only the tip of the wire where the metal sphere was situated was exposed to the electrolyte; the rest being insulated.
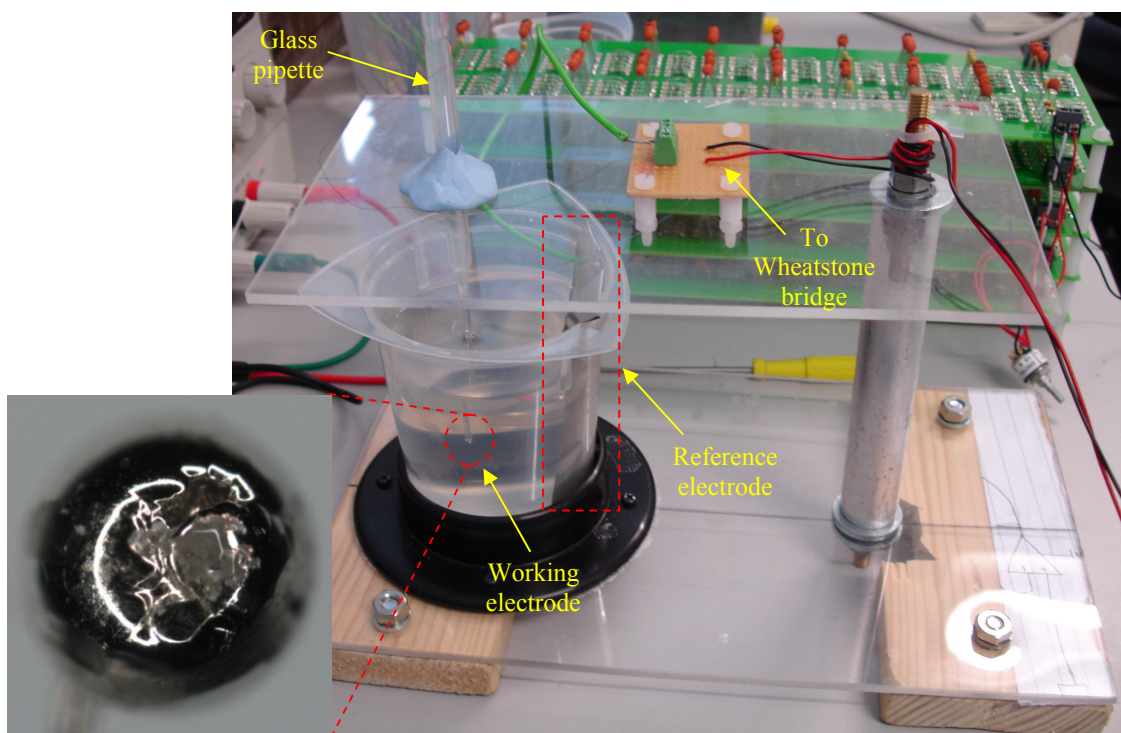
Figure 5.35: The electrochemical cell apparatus. A plastic beaker containing the electrolyte solution (i.e. 0.9% NaCl; $\sigma \approx 15.45$ mS/cm) with the reference and working electrodes making up the cell. At left is a photo of the 100% Pt sphere electrode magnified 32x by an optical microscope, where the formation of cratering/pitting is evident on the electrode surface.

---

[18] One electrode was a 90% Pt-10% Ir wire of 0.175 mm nominal outside diameter and the second electrode was a 100% Pt wire of 0.076 mm nominal outside diameter. The 90% Pt-10% Ir sphere electrode (i.e. as a result of having the wire melted) had a diameter of ≈ 860 μm (i.e. surface area≈ 2.32 μm^2) while the 100% Pt sphere electrode had a diameter of ≈ 740 μm (i.e. surface area≈ 1.72 μm^2). The surface textures of the two sphere electrodes were quite different when examined under an optical microscope. Refer to detailed description in text.

A photo of the electrochemical cell is shown in fig. 5.35. At the insert is a magnified photo of the 100% Pt sphere electrode. For reasons of completeness, it should be mentioned that the 90% Pt-10% Ir sphere electrode was introduced before in this work (i.e. §4.4.2 and §5.3.1) and a magnified photo of it is shown in fig. 5.5. All subsequent impedance data of the working electrode were obtained using the Wayne Kerr Electronics impedance analyser, unless otherwise mentioned.

The CPE behaviour of the 100% Pt working sphere electrode can be quantified by plotting the real and the imaginary parts of the impedance as a function of frequency in logarithmic coordinates. This plot yields insight into possible mechanisms or governing phenomena of the electrochemical system and will allow, for example, the values of the frequency exponent α and CPE coefficient K to be obtained directly without regression of equivalent circuits. For aiding our analysis we have also plotted the impedance modulus and phase as a function of frequency. In particular, fig. 5.36a shows the magnitude and phase angle, while fig. 5.36b shows the real and the imaginary parts of the same impedance data. Comparing the impedance magnitude of fig. 5.36a to that of fig. 5.20 we see that the magnitude of the sphere electrode is less than any of the magnitude of the PCBs – the same applies for the 90% Pt-10% Ir sphere electrode (c.f. fig. 4.11). The frequency dependence of –Im(Z) shown in fig. 5.36b is proportional to $\omega^{-\alpha}$ ($\alpha \approx -0.82$) for frequencies up to 20 kHz. However, this is not the case for Re(Z). According to [Jorcin et al., 2006]: "As the imaginary part of the impedance is independent of the electrolyte resistance, the slope is constant in the whole frequency range.". Therefore, the slope of –Im(Z) for an ideally polarisable electrode should be constant[19]. Also, –Im(Z) is identical to the adjusted for R_{sp} modulus presented in fig. 5.36a. That –Im(Z) is not exactly constant in the full frequency range can be accounted for the fact that our working electrode does not show ideal blocking behaviour (i.e. the shunt charge transfer resistor R_{ct} is not infinite), or that the CPE is in parallel with some other reactive process. In addition, both real and imaginary impedance data should show the same CPE behaviour at low frequencies (i.e. according to eqn. 4.7a and 4.7b both –Im(Z) and Re(Z) should have the same slope). Nonetheless, the slope of Re(Z) is slightly different owing to the fact that the CPE of this working electrode is not exactly constant even at low frequencies (c.f. phase plot of fig. 5.36a). Once again, non-ideal blocking electrode behaviour might be a worsening factor of this effect.

---

[19] In case there is a large relative deviation of the slope with frequency then there must be some source of error in the measurement (or some exogenous system behaviour, e.g., actual physical inductance of the connecting wires and, possibly, of the blocking electrode itself at high frequencies), which is not desirable. As an example, the plot of –Im(Z) vs. Re(Z) (c.f. inset of fig. 5.36b) is characterised by an inductive loop at very high frequencies (i.e. about 1 MHz) which is not visible in the current plot (i.e. someone needs to zoom in order to see it). Additionally, it has been suggested by [Orazem et al., 2006] that the absence of a clearly identifiable asymptote in Re(Z) may be attributed to high frequency instrumental artifacts.
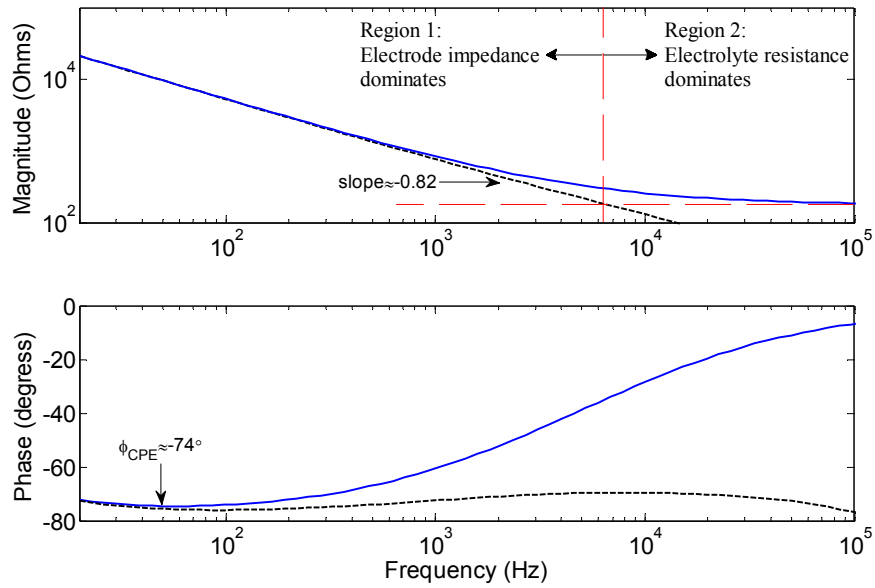
Figure 5.36a: Impedance modulus and phase of the 100% Pt sphere electrode at ≈25 °C in physiological saline, as a function of frequency. Subtracting R_{sp} from the measured impedance, a linear relationship of log|Z| vs. log(f) with a slope≈−0.82 (on square axes) and an almost constant phase angle emerge (black dotted lines). An input test voltage of 50 mV was used in the cell impedance measurements.
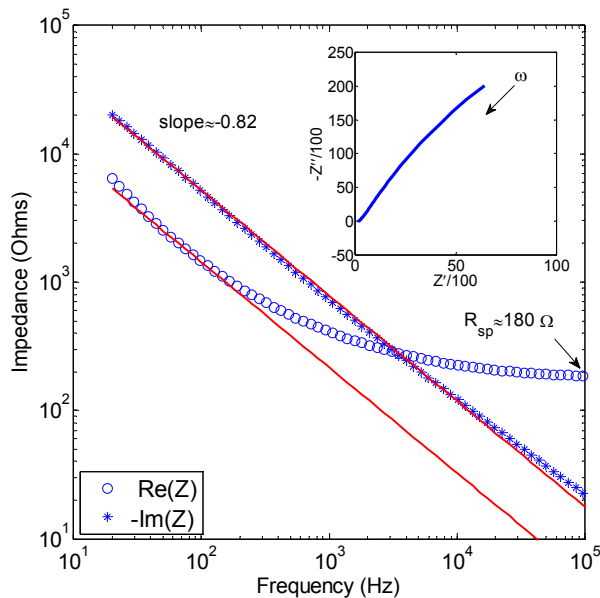
Figure 5.36b: Real and imaginary parts of the same impedance against frequency. The solid lines through the data points are graphs of $Re(Z)=K\omega^{-\alpha}\cdot\cos(\alpha\pi/2)$ and $Im(Z)=-K\omega^{-\alpha}\cdot\sin(\alpha\pi/2)$ with $K=1.083$ MΩ/s$^{+\alpha}$ and $\alpha\approx0.82$ at low frequencies. At high frequencies, $Re(Z)$ approaches a constant value determined by the dc resistance of the electrolyte, with its approximate value being readily verified by using eqn. 4.3. The inset is the graph of $-Im(Z)$ vs. $Re(Z)$.

Plotting the fitting lines of $Re(Z)$ and $-Im(Z)$ on fig. 5.36b using, respectively, eqn. 4.7a and 4.7b in order to find their slopes, revealed that the value of the CPE coefficient

K is not exactly the same. To obtain the same K for both Re(Z) and −Im(Z) we first need to correct for the ohmic electrolyte resistance of the electrode impedance. Instead, we can extract K from eqn. 4.7b since the imaginary part of the impedance is independent of the electrolyte resistance. This remark was also supported by [Orazem et al., 2006] who also proposed eqn. 4.7b for finding the effective CPE coefficient K[20]. Concluding, the slope of an impedance electrode curve, and therefore the phase angle and frequency exponent α, does not greatly depend on the amplitude of the applied input signal (c.f. §4.3.3.2). This has been also experimentally demonstrated by [Biswas et al., 2006] for their fabricated CPE.

5.7.3.3 Procedure

After submerging the sphere electrode into the electrolyte we allowed 3 min. for the electrode-electrolyte interface to reach steady state. All electrochemical impedance measurements were carried out at room temperature (i.e. at about 25 °C) and using an input test voltage having an amplitude which is considered appropriate for the linear operation of the electrode (i.e. well below 100 mV). Moreover, we assume that our sphere electrode is ideally polarisable in an indifferent electrolyte[21] and in the absence of faradaic and diffusion processes. We additionally assume that electrode surface roughness is in the form of pores and that the pore system of the sphere electrode to be isotropic, i.e., invariant with respect to the pores' direction. All pores are of V-shape (c.f. fig. 5.6) and therefore their frequency response can be appropriately modelled by a Schrama RC ladder network.

Water quality of the electrolyte medium was found to be a key point of purity; a satisfactory reproducibility of results could be obtained when deionised and chemical grade NaCl instead of tap water and table salt, respectively, was used. Moreover, small amounts of contaminant can greatly affect the polarisability characteristics of the working electrode, and it has been suggested in the literature [Scheider, 1975] that impurities can give faradaic character to systems which, in their pure state, would polarise ideally. Therefore, care was taken for the electrolyte to be free of any form of contamination (e.g. dust particles) by renewing it often and always after each experimental run. Equally, the working electrode was thoroughly cleaned with deionised water before each run. As with the results obtained in Chapter 3, drifting of measurements was observed with time. Generally, the variability of the electrode parameters with time has been acknowledged in the literature to vary by tens of percent without any obvious reason (i.e. knowing from actual measurements performed that the conductivity and temperature[22] of the electrolyte

---

[20] Having calculated K from both eqn. 4.7a and 4.7b, a fit using the Schrama model was performed on the magnitude and phase data of fig. 5.36a, showing that K obtained through eqn. 4.7b resulted in a better fit. If there is no correction for the series electrolyte resistance R_{sp} the degree of error in the fit will depend on the value of R_{sp} being negligible or not.

[21] An electrolyte solution whose constituents are not electroactive (i.e. that can take part in an electrode reaction or that can be adsorbed on the electrode) in the range of applied potentials being studied.

[22] No special effort was made to stabilise the temperature of the electrolyte, which could vary for each experimental run and cause some variability of the results. Conversely, the real-time temperature variation of the electrolyte during a run was small (i.e. about 1 °C or less).

remain very much the same during an experimental run), especially in the first minutes [de Boer and van Oosterom, 1978]. This variability with time of sample immersion might as well be due to some electrochemical processes taking place at the interface [Orazem et al., 2006]. Perhaps, using an electrolyte other than NaCl, or buffering the existing one with a pH of approximately 7.0 (i.e. neutral) might make the electrochemical cell more stable. This was not attempted at the time of experiments.
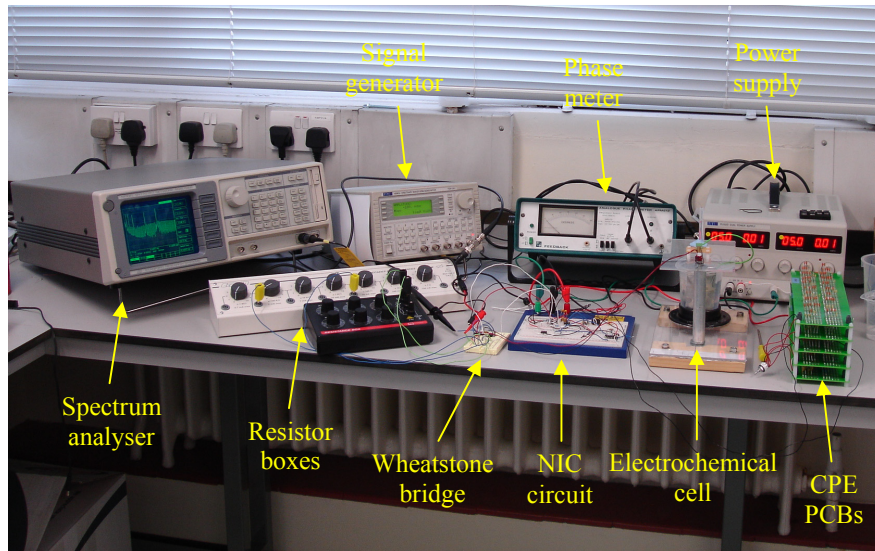
Figure 5.37: Instrumentation set-up for impedance matching of the electrochemical cell.

The arrangement shown in fig. 5.32 was used for verifying the proposed neutralisation technique, as previously discussed. A two stage single-ended NIC configuration connected to one of the 5 pre-constructed CPE PCBs was put together using LF355 op-amps. In order to have control over the magnitude reduction ratio applied by the NIC to the Z_{CPE}, a trimmer potentiometer (or pot for short) of an appropriate value was used as a variable biasing resistor. The trimming impedance Z_{trim} was completed with resistors R_{sp} and R_{ct} which were implemented via two external variable resistor boxes (RS Components Ltd.). The LF355 series op-amp was chosen because it offered a high gain bandwidth of 2.5 MHz with a typical input resistance of 1 TΩ, plus it was immediately available in our laboratory. The EMG input applied across the Wheatstone bridge was a multi-frequency sinusoidal signal (i.e. 500, 1 k, 2 k, 5 k, and 8 kHz) loaded to a digital signal generator (TTi, model TGA1241)[23]. The differential output of the Wheatstone bridge was measured using a high speed FET-input instrumentation amplifier (Burr-Brown, INA111) set to operate at a gain of 10. The output of the amplifier was subsequently connected to an FFT spectrum analyser (Stanford Research Systems, model SR760) to be able to observe the total EMG breakthrough in the bandwidth of interest. Finally, a dual power supply (TTi, EL302D) was used to power all active circuitry via decoupling capacitors. The NIC and Wheatstone bridge circuits were implemented on

---

[23] 5 sine wave signals of different frequencies were generated in Matlab™ and subsequently added together to produce the composite sinusoidal signal. The data was then loaded to the digital signal generator using the serial data cable and software provided by the vendor (TTi, Waveform manager plus).

prototyping breadboard. A photo of the whole instrumentation set-up is shown in fig. 5.37.

In order to find the component values of the balancing to the electrochemical cell, impedance Z_{trim}, a fit was perform on Z_{cell} using the much discussed 3-component model of fig. 5.4. After a successful fit, the values of R_{sp} and R_{ct} can be extracted and having selected a particular PCB whose phase angle is close (i.e. since in our case could not be exact) to the phase angle of the working sphere electrode (at the low end of the ENG band) the only thing that is left to decide upon is the reduction ratio applied by the NIC circuit. The way the fit was performed was straightforward; the component values were adjusted manually[24] in Matlab™ – albeit using sensible values at first, obtained as previously discussed (c.f. fig. 5.36b) – depending on the desired frequency response of Z_{trim}, and until an adequate fit on Z_{cell} was obtained by visual inspection. Since we wanted to use the same RC values of the Schrama ladder network towards balancing the bridge it was important to maintain the CPE coefficient K–scaling factor S of the PCB the same to those used for making each PCB (i.e. thus keeping the same component size which is suitable for integration and acceptable exhibited noise; c.f. §5.6.2.2). Due to that aspect it was found that sometimes R_{sp} and R_{ct} had to be set to values which normally (i.e. in the case of having the phase of the selected PCB and working electrode match) would not be appropriate for fitting the impedance of the working electrode forcing, in a way, the fit.

5.7.3.4 Electrochemical cell impedance matching

According to measurements performed by [Mayer et al., 1992] and reported in Chapter 4 of this work, Pt is less polarisable than Pt-Ir but at the same time our 100% Pt working electrode has a smaller surface area than the 90% Pt-10% Ir (i.e. about 1.35 times less and therefore higher faradaic charge transfer resistance R_{ct}). Hence we can empirically assume that the blocking characteristics of the two sphere electrodes are about the same. Additionally, comparing the two sphere electrodes in terms of their exhibited CPE it seems that, the alloyed with Ir, Pt sphere electrode has a slightly more constant phase angle at low frequencies comparing to the pure Pt sphere electrode, most probably due to the structural characteristics of the electrode surface during manufacturing and less to the fact of having the Pt alloyed. For that reason it was decided to use the 90% Pt-10% Ir sphere electrode of fig. 5.5 as the working electrode for carrying out the experimental verification.

A plot of the fit on the working electrode impedance Z_{cell} is shown in fig. 5.38. Since the 3-component electrode impedance Z_e model of fig. 5.4 was used to perform the fit there are 4 unknowns: a) the electrolyte resistance R_{sp}, b) the charge transfer resistance R_{ct}, and c) the magnitude and d) phase of Z_{CPE}. For reasons already discussed in the last paragraph of the previous section, the value of the CPE coefficient K and the frequency exponent α had to be set to values that were the same to one of the 5 pre-constructed CPE PCBs. The best PCB out of those 5 that was chosen to perform the fit had $K=S=10^7$ and

---

[24] At the time of writing, a Matlab™ code has been created that can extract all the necessary fitting parameters automatically, thus obtaining the fitting impedance by only providing the target data (i.e. in this case the electrochemical cell impedance Z_{cell}).

α=0.833 (i.e. $\varphi_{CPE}{\approx}{-}75°$); the reason will become apparent shortly. The fit was achieved by setting R_{sp}=135 Ω and R_{ct}=100 kΩ. Because no actual NIC circuit was used here to downconvert the impedance magnitude of the CPE we had to simulate its operation manually in Matlab™ (i.e. by dividing the magnitude of the CPE by an appropriate factor – in this case 15.5)[25]. As can be seen from fig. 5.38, the fit is satisfactory in the 500 Hz to 10 kHz ENG bandwidth of interest. Also plotted on the same figure is a fit using an electrode impedance Z_e which is comprised of R_{sp} in series with Z_{CPE}. This last fit is almost identical to the 3-component fit, denoting that R_{ct} is not necessary in order to achieve a good fit at those frequencies. The same remark was previously proven in Chapter 4 by performing a fit using the Cole CPE model (and not Schrama) on a different electrochemical cell (i.e. the cut-wire cell; c.f. §4.4.2).
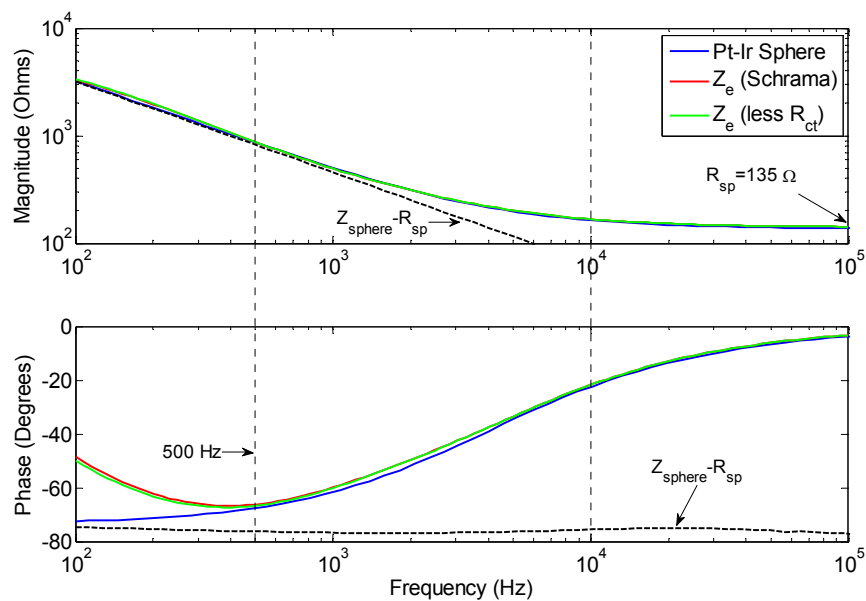
Figure 5.38: Matching the impedance of the 90% Pt-10% Ir sphere electrode using the electrode impedance Z_e model of fig. 5.4, where R_{sp}=135 Ω and R_{ct}=100 kΩ. A 20 stages Schrama RC ladder network with K=S=10^7 Ω/s$^{+\alpha}$ and α=0.833 was used as Z_{CPE} (c.f. Appendix B). The magnitude of Z_{CPE} was multiplied by 1/15.5 to achieve the fit. The vertical dotted lines denote the ENG bandwidth of interest. The fit was satisfactory even without an R_{ct} being used in the fitting model. Refer to text for a detailed description.

The CPE is an extremely flexible fitting parameter. The fact that a satisfactory fit was achieved by setting α=0.833 (i.e. $\varphi_{CPE}{\approx}{-}75°$) instead of α=0.8 (i.e. $\varphi_{CPE}{\approx}{-}72°$; the exhibited constant phase angle of the 90% Pt-10% Ir sphere electrode at low frequencies, as was indicated in fig. 5.5) requires further investigation. In particular, using K=10^7 and α=0.8 the fit was found not to be satisfactory. Subtracting R_{sp} from the impedance of the

---

[25] The reader should not neglect the fact that in a Schrama RC ladder network the exhibited impedance magnitude and phase are independent and that changing the magnitude of the PCB via an NIC circuit will not affect the phase of the Z_{CPE} in the bandwidth of interest. However, having the Z_{CPE} as part of an electrode impedance Z_e, changing the magnitude of the Z_{CPE} will also affect the phase angle of the overall electrode impedance Z_e. Hence, we cannot simply perform a fit on the phase of Z_e by adjusting α, R_{sp} and R_{ct}, and then adjust the magnitude conversion factor of the Z_{CPE} to achieve a fit.

160

sphere electrode Z_{sphere} and plotting the new data, a linear impedance magnitude and an almost constant phase angle was revealed[26] (i.e. black dotted lines in fig. 5.38). At frequencies shown, the corrected modulus is dominated by the contribution of the imaginary part of the impedance, approaching zero (i.e. at frequencies >100 kHz) according to $|Z_{sphere}-R_{sp}|\sim f^{-\alpha}$ [Orazem et al., 2006]. Although the CPE is not entirely constant in the whole frequency range (i.e. perhaps due to the electrode not being ideally polarisable, or due to the electrolyte being used), its mean value in the 500 Hz to 10 kHz bandwidth of interest is about $-76.5°$, i.e., 4.5° off the $-72°$, as was originally assumed. Therefore, in order to be confident about the value of the CPE frequency exponent α of an electrode one must subtract the value of R_{sp} and visually inspect the phase angle, preferably obtaining a value by taking the mean over the bandwidth of interest. Indeed, performing a fit on Z_{sphere} using a Z_{CPE} with $\alpha=0.85$ resulted in a better fit[27]. Nonetheless, we had to settle with using $\alpha=0.833$ despite the error in the fit, since none of the two sphere electrodes actually had a phase angle that precisely matched that of any of the 5 CPE PCBs that were available.

5.7.3.5 Results

Having acquired all the necessary component values of the trimming impedance Z_{trim} it is now possible to proceed with balancing the Wheatstone bridge arrangement of fig. 5.32. At first, the magnitude of the input signal applied across the Wheatstone bridge was measured in the following way. The output of the INA111 instrumentation amplifier was recorded using the spectrum analyser with the lower RHS arm of the bridge being shorted (i.e. the trimming impedance Z_{trim} was bypassed). Since $R_1=R_2$, the voltage V_{out} measured at the output of the amplifier will then be $V_{out}=10 \cdot V_{EMG} \cdot [(1/2)-(0/Z_{cell})]$. Conversely, once the bridge was balanced the output voltage of the amplifier was divided by 10 in order to obtain the normalised magnitude of the EMG breakthrough at the output.

Measurements of the input and output voltage as a function of frequency are shown in fig. 5.39 (i.e. with some averaging being used), while the corresponding EMG reduction factor is reported in table 5.6. All 5 frequency components had approximately the same magnitude (i.e. as an indication, there was a maximum difference of about 15% among the 500 Hz and 8 kHz components). At the time of recordings, a frequency component (i.e. most probably noise from the surroundings of our laboratory) was present at 250 Hz, causing harmonics at multiples of that frequency (i.e. 500 Hz, 750 Hz, 1 kHz, etc.). In addition, the output signal spectrum resembles that of the power spectral density of pink 1/f noise, which is inversely proportional to frequency having a slope of -1 (marked in fig. 5.39 by the arrow for comparison to the slope of the output signal). Looking at fig. 5.39 we notice that the EMG breakthrough is less than what is applied across the

---

[26] The value of R_{sp} was obtained at high frequencies (i.e. >100 kHz) from the impedance magnitude of the sphere electrode, where the resistance of the electrolyte dominates the impedance, and was found to be about 135 Ω.

[27] That the CPE of the Schrama RC ladder network is not constant at low frequencies (i.e. at the same frequencies as the sphere electrode) is not the source of error in the fit. From theory, a CPE has a constant phase angle throughout the band with resistors R_{sp} and R_{ct} dictating how fast the phase will tend towards 0° at high and low frequency cut-offs, respectively.

Wheatstone bridge in the whole interfering spectrum[28], while the mean interference floor of the output of the amplifier (i.e. defined as the mean interference of the input in the entire spectrum shown over the mean reduction of interference at spot frequencies) is set at about 4.3 µV.
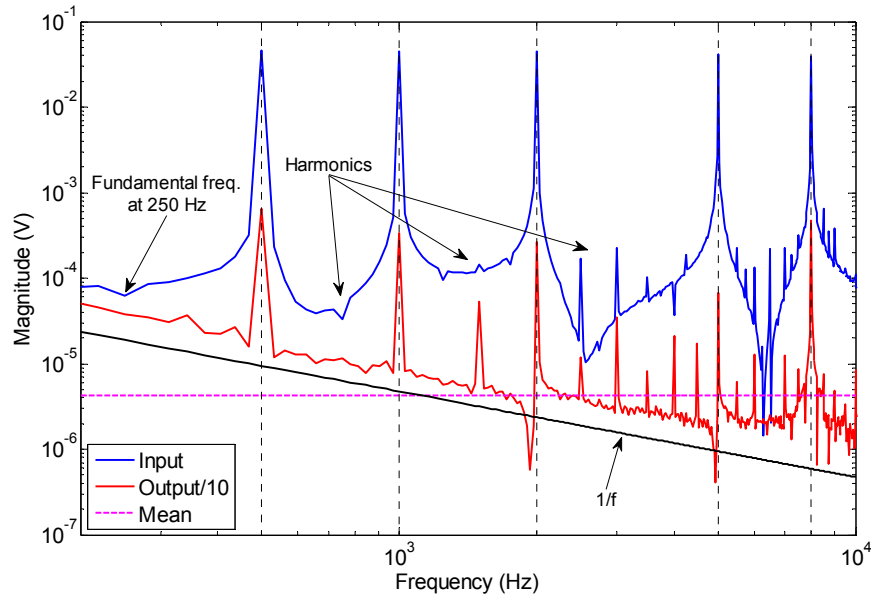
Figure 5.39: Comparison of the Wheatstone bridge input and output spectra. Input is a composite sinusoidal signal at 500, 1 k, 2 k, 5 k, and 8 kHz spot frequencies denoted by the vertical dotted lines. At those frequencies, the worst case EMG reduction is by a factor of 70 at 500 Hz. In the same plot, the mean interference floor is marked by the horizontal (magenta colour) dotted line.

Frequency (Hz)	Input (mV)	Output (µV)	Ratio
500	45.75	656	70
1 k	45.25	332	136
2 k	44.31	267	166
5 k	41.00	68.2	601
8 k	39.02	467	83.5

Table 5.6: Input and output interference magnitudes and reduction factor between the two at the 5 spot frequencies.

The performance of the frequency adaptive trimming network impedance Z_{trim} can be considered to be satisfactory. A mean reduction of about 100 times less (i.e. if we do not take into account the 5 kHz spot frequency) EMG breakthrough at the output of the recording amplifier when the frequency of an interference signal lies in the 500 Hz to 8 kHz range means that 1 mV can be reduced down to about 10 µV, which is one to two orders of magnitude higher than the ENG signal we wish to detect with our electrodes (c.f. §1.4). Although there is evident reduction of interference in the entire spectrum of fig. 5.39, the bridge is not fully balanced. This can be accounted for by three key reasons.

---

[28] With the only exception at about 6.3 and 6.5 kHz where the magnitude of the input signal is approximately 820 and 140 nV, respectively, below that of the output.

Firstly, the CPE data we used to produce the fit of fig. 5.38 came directly from the Schrama model and not from data of the actually chosen, for balancing the bridge, PCB. From measurements (c.f. fig. 5.20) we know that there are differences between the two. Therefore, some error in the fit is in this case inevitable. Secondly, the fit of fig. 5.38, despite being good, is undoubtedly not perfect due to the use of a PCB with $\alpha=0.833$ (i.e. instead of $\alpha=0.85$) which we had available. Looking at fig. 5.38, we see that there is a small difference between the actual electrode and fitted impedance data, especially noticeable for the phase angle data and with the difference becoming larger (i.e. about 2°) at low frequencies (i.e. <5 kHz). This error is evidently portrayed in the spectrum plot of fig. 5.39, where the interference reduction is less at the lower end of the band. We speculate that a PCB having a phase angle of $\varphi_{CPE} \approx -76.5°$ (i.e. $\alpha \approx 0.85$) might have offered better reduction if used for balancing the Wheatstone bridge arrangement instead. Finally, we should not neglect the conversion error introduced by the NIC circuit (c.f. fig. 5.34). From simulations (c.f. fig. 5.29) we know that the phase angle is most likely to be mismatched at the high end of the band owing to the non-idealities of the NIC op-amps (e.g. relatively high output impedance). The result of this mismatch is increased amount of EMG breakthrough at those frequencies (c.f. fig. 5.31). Perhaps this would somewhat explain the lower figure of reduction obtained at the 8 kHz spot frequency.

5.8 Usability of the technique

Having characterised the performance of the frequency adaptive mQT in part 2 of Chapter 5, it would only be appropriate to conclude the chapter with a discussion on the actual usability of the technique in an implanted device.

5.8.1 Expediency

For the purpose of testing the technique in-vitro the impedance of the electrochemical cell was conveniently measured using an impedance analyser and through regression procedures we obtained the component values of the fitting network. In an implanted device, however, we will not be having the same degree of flexibility; the impedance of the tripolar electrodes could certainly be measured before implantation (e.g. the impedance phase angle of the two outer electrodes in physiological saline) but this sort of impedance data would only be good for use as an initial estimate of the tuning parameters (i.e. phase angle of CPE) of the balancing network. Additionally, having the electrodes implanted, their impedance with time will change as connective tissue grows around them. If we assume that the only information available from the implant to the outside world is the recording amplifier's amplitude of raw ENG covered in EMG interference, by tuning the components of the balancing network we should be aiming to minimise the interference across the whole ENG spectrum, obtaining just the neural signal. Nevertheless, how easy will it be to compensate for an imbalance in the tripole by tuning (say) the value of 3 components while looking at the output voltage? The time required to adjust those is also important; a clinician and most certainly a patient would like the procedure to be a matter of few minutes (i.e. 10 to 15) for the technique to be acceptable in terms of practical use. For instance, if a stimulation induced EMG is utilised towards the tuning procedure with a muscle twitch occurring every second, and the average of 10

seconds obtained being the interference signal to be minimised, then a clinician would require at least 11 minutes to go through all possible combinations, if each of the components had 4 possible settings.

In reality, the components for scaling the magnitude of Z_{CPE} and setting the value of the appropriate series solution resistance R_{sp} would require having many more settings than just 4. As the most suitable type of device for these two is a linear trimmer pot, the possible combinations would tend to infinity. Conversely, we can probably get away with having 2 to 3 component settings for choosing an appropriate CPE phase angle. Nevertheless, it would have been somewhat helpful to know the relationship that each of the components have (if any) between two or more distinct tuning settings. The idea is illustrated schematically in fig. 5.40.
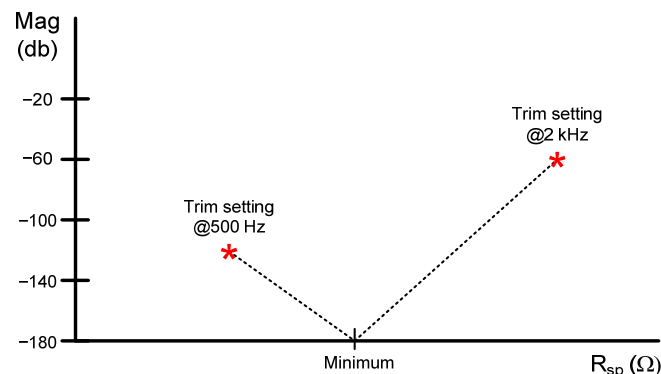
Figure 5.40: Concept graph illustrating a linear relationship of the EMG magnitude as a function of the resistance R_{sp}. Following the linear relationship between two trimming settings a mean interference floor (i.e. marked here as minimum) can be achieved at all frequencies in the ENG band. Absolute magnitude values are for illustration purposes only.

In this example a linear relationship is shown to exist between the output voltage magnitude of the recording amplifier at two trimming settings (i.e. one at 500 Hz and another at 2 kHz) and the value of the series R_{sp} resistance. Since, for the bandwidth of interest and the electrode material we are using (i.e. highly polarisable Pt), the trimming network effectively consists of R_{sp} being in series to Z_{CPE}, it is easy to predict what will happen to the trimming impedance locus when the value of R_{sp} changes, affecting only the real part of that impedance (e.g. as the value of R_{sp} increases, the magnitude of the trimming impedance also increases while the phase angle tends quicker towards 0°, at the high frequency end of the band). However, it is naïve to believe that the relationship between the trimming settings and the output voltage magnitude will in practice be linear, let alone that a minimum can be achieved as a function of R_{sp} only; simply because balancing the recording tripole depends upon 2 other parameters (i.e. the magnitude and phase of the CPE) whose values affect the overall trimming impedance. Nevertheless, if such a relationship can emerge, even a non-linear one, it could undoubtedly become a very useful tool towards the tuning of components to minimise interference. Unfortunately, data that would help us determine such kind of relationship were not obtained during the in-vitro experiment and thus the idea had to be shelved, at the time of writing.

5.8.2 The "knobs" problem

It is important to elaborate on the method of tuning the components of the balancing network (i.e. trimming impedance Z_{trim}). For the purposes of this discussion let us suppose that each component is a "knob" which can be turned to change the component's value. The 3-component network of fig. 5.4 has 4 tuning knobs in total: a) the series electrolyte resistance R_{sp}, b) the shunt interface charge transfer resistance R_{ct}, c) the phase angle of the CPE (i.e. pre-constructed ladder network), and finally d) the magnitude of the CPE (i.e. biasing trimmer pot of the NIC circuit). From simulation results which involved two different electrochemical cells (c.f. fig. 4.11 and fig. 5.38) it seems that we can achieve a fit without using R_{ct} in the model, if the working electrode we attempt to fit is blocking and the bandwidth of interest is from 500 Hz to 10 kHz. This reduces the number of knobs we need to worry about tuning down to 3 and eventually to 2, once the frequency exponent α has been found for a particular cuff electrode (i.e. assuming that α is dominated by electrode surface roughness effects)[29]. The aforementioned postulation was also witnessed during the in-vitro experiment of balancing the Wheatstone bridge arrangement of fig. 5.32, where introducing an R_{ct} via one of the external variable resistor boxes made no significant difference to the output voltage magnitude of the multi-frequency sinusoidal signal that we used for the measurements. Finally, whether a series solution resistance is actually needed for balancing the recording tripole still requires further investigation. From previous in-vitro data (c.f. §5.3.5) there was evidence that this is not necessary in the ENG band. Nonetheless, we should not neglect the fact that our saline solution is a uniform electrolytic conductor. Therefore, at present, it is not easy to determine this with absolute confidence[30]. Most probably an R_{sp} in series with a Z_{CPE} will in practice make the trimming impedance Z_{trim}.

Instead of trying to guess the component values of the balancing network by observing whether the magnitude of the output EMG breakthrough is minimised, or trying to find these through manual or automatic (e.g. least-squares) regression procedures, we can extract their values directly from the Nyquist plot of the measured electrode impedance data (i.e. providing that such data can be acquired while the electrodes have been implanted). Assuming that by having a particular impedance data set, we can work out the trimming impedance required for balancing the tripole, the tuning problem can be approached as follows. The 3-component model of fig. 5.4 requires values for 4 parameters, if electrodes are not ideally blocking. The asymptotic values of the impedance modulus at low (sub-Hz) and high (usually >100 kHz) frequencies provide values for the faradaic and ohmic electrolyte resistance, respectively[31], while the CPE frequency exponent α and the CPE coefficient K, which will allow us to calculate the phase angle of the CPE PCB (i.e. through eqn. 4.8a) and the required magnitude that the

---

[29] Performing a fit on previous experimental trimming data obtained with different conductivities of saline (c.f. table 5.3) demonstrated that α remains the same for a particular cuff electrode.

[30] In that case R_{sp} might have been the same among the two outer electrodes if the area of those is the same and the saline electrolyte is uniform, especially close to the surface of the electrodes.

[31] R_{sp} can also be revealed from the high frequency asymptote of the real part of the electrode impedance, as it provides the same information as is available from the modulus plot. Conversely, the low frequency asymptote reveals the value of R_{sp} in series with R_{ct}.

CPE needs to have, respectively, can be both obtained from the imaginary part of the electrode impedance (c.f. fig. 5.36b). Knowing the resistance values at the low and high frequency intercepts then $R_{ct}=R_0-R_\infty$. In our case, since we are dealing with blocking electrodes (i.e. absence of a low frequency limit might suggest blocking behaviour, e.g., see inset of fig. 5.36b), the magnitude of the electrode impedance tends to ∞ as frequency tends toward zero and therefore $R_{ct}\rightarrow\infty$. In addition, knowing the value of α, instead of working out R_{sp} from the graph of the high frequency asymptote, we can make use of eqn. 4.8a with $X_{CPE}=Z_j$ and $R_{CPE}=Z_r-R_{sp}$ (i.e. since now we are interested in the whole electrode impedance and not just on the CPE) to obtain its value, or even plot it as a function of frequency, using eqn. 5.13 below.

$$R_{sp} = \lim_{f\to\infty} Z_r\left(f\right) - \frac{\lim_{f\to\infty} Z_j\left(f\right)}{\tan\left(-\alpha\frac{\pi}{2}\right)} \qquad (5.13)$$

Concluding, the scaling factor of the NIC should be calculated in conjunction with the targeted value of K and in accordance to the selected scaling factor S that the chosen CPE PCB arranged for trimming has. From previous discussion (c.f. §5.3.4.3 and fig. 5.18) we know that the CPE coefficient K is equal to the scaling factor S used for the construction of a CPE PCB and therefore the scaling ratio of the NIC can be calculated as:

$$Factor_{NIC} = \frac{S_{PCB}}{K_{electrode}} \qquad (5.14)$$

In the case of the 90% Pt-10% Ir sphere electrode that was used in the in-vitro experiment of this chapter we have: $NIC_{factor}=(10^7\ \Omega/s^{+\alpha})/(683\ k\Omega/s^{+\alpha})\approx14.6$ which is close to the 15.5 we used to perform the impedance data fit of fig. 5.38[32]. Also notice that the value of K for the 90% Pt-10% Ir sphere electrode is smaller in comparison to the 100% Pt (i.e. $K=1.083\ M\Omega/s^{+\alpha}$) since the magnitude of the double-layer capacitance C_{dl} increases with electrode surface area.

5.8.3 IC implementation

The main hurdle in implementing the proposed interference neutralisation technique in an IC form is the size of the multiple pF capacitors of a 20 stages Schrama RC ladder network. Integrating 3 CPE PCBs with a frequency exponent α in the 0.777 to 0.888 range (i.e. $\varphi_{CPE}\approx-70°$ to $-80°$) would require laying out 57 capacitors, if we assume that the 3 capacitors of the first stage (i.e. 5.91, 11.95 and 24 nF, respectively – c.f. Appendix B for exact values) will be external to the chip due to their large size in comparison to the rest. Conversely, performing an IC layout of the $k\Omega$ resistors (0.047 min, 7.65 max) is not a problem in terms of area, especially if the appropriate polysilicon layer is used (e.g.

---

[32] The value for the CPE coefficient K of the sphere electrode (i.e. $K_{electrode}$) was obtained from the imaginary part of the impedance following the exact same procedure as previously described in §5.7.3.2 for the 100% Pt sphere electrode.

high resistive poly). As a figure of merit, the die layout area occupied by the 57 capacitors having a summed capacitance of $C_{tot}=C_{\alpha=0.777}+C_{\alpha=0.833}+C_{\alpha=0.888}\approx16.9$ nF+21 nF+23.5 nF$\approx$61.4 nF, measures approximately 71.4 mm^2 (i.e. 1 nF occupies about 1.21 mm^2) of layout area in the AMS C35 (i.e. 0.35 μm CMOS) process. In addition, the layout area of a 10 kΩ resistor using the high resistive poly module with a minimum allowable by the process width measures W=0.8 μm by L=5 μm.

A monolithic 3D-IC process could be used to significantly reduce the layout area. With this process a chip with two or more layers of active electronic components, integrated both vertically and horizontally into a single circuit can be manufactured. A 3D-IC should not be confused to 3D packaging which saves space by stacking separate chips in a single package. This packaging does not integrate the chips into a single circuit and the chips in the package communicate with off-chip signalling, much as if they were mounted in separate packages on a normal circuit board. In contrast, a 3D-IC is a single chip and as such all components on the layers communicate with on-chip signalling. Therefore, apart from achieving a significant amount of reduction in chip size, reduced power consumption and increased speed (i.e. due to shorter wiring) are some more of the advantages of 3D-IC. Nevertheless, at the time of writing this semiconductor technology is certainly not mature enough and consequently there might also be some challenges involved like the increased cost and high rate of defects (e.g. thermal build-up), which someone should carefully look into before considering using this process.

Finally, implementing the proposed neutralisation technique in silicon also involves some practical considerations. For instance, we cannot integrate a trimmer pot as a passive device. The pot used both for setting the scaling factor of the NIC and the value of R_{sp} will have to be replaced by an appropriate number of resistors in a bank supplemented with an n-to-n decoder for selecting the appropriate value of resistance via opening and closing switches. If we assume the use of a decoder for individually controlling 8 switches using an 8-bit binary word then there will be 2^8=256 possible combinations of resistance. Transmission gates (i.e. CMOS switch) can be used for implementing an analogue switch, biased by an appropriate voltage signal level (i.e. either VDD or 0 V) supplied from the output of the decoder. The top-level design of the approach is illustrated in fig. 5.41 with the corresponding truth table shown in table 5.7. In this example, only the value of R_{sp} can be tuned, while we expect using a similar approach for selecting the scaling factor of the NIC for tuning K. Setting bits D_n ($0 \leq n \leq 7$) will open the switch and select the corresponding resistance value. Additionally, we assume that the switches have a resistance R_{on} and R_{off} of zero and infinity, respectively.

From the relevant literature we know that R_{sp} can range from few ohms to hundreds of ohms, subject to working electrode cross-sectional area and conductivity of the electrolyte. As an indication [Ragheb et al., 1992] reports an R_{sp} of 23.6 Ω and 10 Ω for their 0.473 cm and 1.11 cm in diameter spherical electrodes, respectively, in 0.9% saline. Also, we should not neglect the effect that the electrolyte conductivity has on the value of R_{sp}; using eqn. 4.3, for our two spherical electrodes (i.e. 100% Pt and 90 Pt-10% Ir) R_{sp} computes to: 1348 Ω to 139 Ω and 1160 Ω to 120 Ω for 1.595 mS/cm and 15.45 mS/cm electrolyte conductivities, respectively (i.e. the particular conductivities represent the two

boundary cases of tissue growth at the interface, c.f. §3.4.1)[33]. Although those are values that might not directly relate to the R_{sp} of the balancing network, we notice that there are cases where the value of R_{sp} exceeds the maximum value that the bank of resistors of fig. 5.41 can achieve (i.e. 637 Ω when all switches are open). Nevertheless, as our implanted cuff electrodes have a much bigger area, we expect that figure to be significantly less even when substantial amount of regenerative tissue has grown around the electrodes.
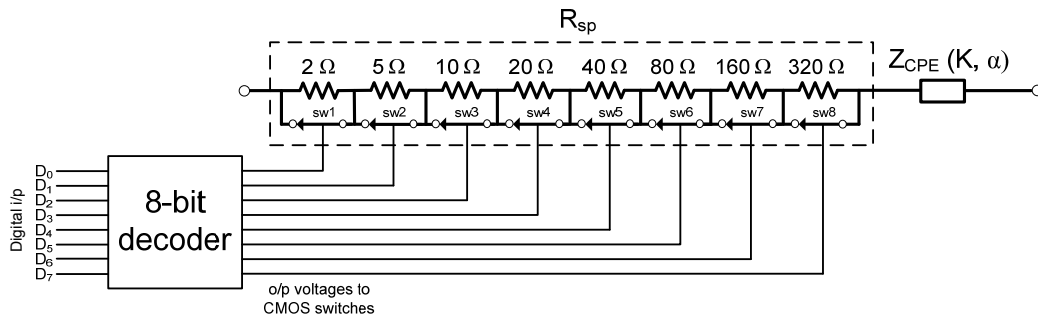
Figure 5.41: Schematic representation of how selectivity of R_{sp} can be achieved in a trimming impedance Z_{trim} network. A bank of 8 resistors with switches controlled by an application specific 8-bit decoder is used for the purpose.

R_{sp} (Ω)	D_0 (sw1)	D_1 (sw2)	D_2 (sw3)	D_3 (sw4)	D_4 (sw5)	D_5 (sw6)	D_6 (sw7)	D_7 (sw8)
2	1	0	0	0	0	0	0	0
5	0	1	0	0	0	0	0	0
7	1	1	0	0	0	0	0	0
10	0	0	1	0	0	0	0	0
12	1	0	1	0	0	0	0	0
15	0	1	1	0	0	0	0	0
17	1	1	1	0	0	0	0	0
20	0	0	0	1	0	0	0	0
22	1	0	0	1	0	0	0	0
25	0	1	0	1	0	0	0	0
27	1	1	0	1	0	0	0	0
30	0	0	1	1	0	0	0	0
32	1	0	1	1	0	0	0	0
35	0	1	1	1	0	0	0	0
37	1	1	1	1	0	0	0	0
40	0	0	0	0	1	0	0	0
.	.	.	.	.	.	.	.	.
637	1	1	1	1	1	1	1	1

Table 5.7: Truth table mapping the 8-bit binary word input of the decoder to an appropriate value of resistance R_{sp}. A binary sequence for only the first 4 MSB is fully developed. The maximum value of R_{sp} that can be achieved with this configuration is 637 Ω.

---

[33] Any major discrepancy between the values of R_{sp} calculated using eqn. 4.3 and those obtained earlier from the high frequency asymptotes (c.f. fig. 5.36b and fig. 5.38) are subject to errors in the actual diameter of the electrode and the precise conductivity of the electrolyte.

5.8.4 Noise from NIC

It is rather important to have an idea of the noise contributed by the trimming network. We expect the NIC circuit to generate the most noise, essentially dictating the minimum ENG signal that can be picked up from the recording electrodes. The spot noise voltage density of the two stage floating NIC circuit (c.f. §5.7.1.2 and fig. 5.29) utilised towards the impedance magnitude scaling of a 20 stages Schrama RC ladder network with α=0.666 (i.e. φ_{CPE}≈−60°), is shown in fig. 5.42 (blue curve). In addition, the simulated, using Cadence™, input referred RMS noise in the 500 Hz to 10 kHz ENG bandwidth is about 7.87 µV. Plotted on the same graph as a figure of merit also are: a) the noise density of a 10 kΩ resistor which was used to bias the NIC circuit and set its reduction ratio (red curve); b) the CPE with α=0.666 (green curve, i.e., the same as that of fig. 5.23); c) the noise of a single XFAB™ aopac07 op-amp connected as a unity gain buffer[34] (magenta curve). Calculating the total equivalent noise by taking into account all the components that make up the NIC circuit[35], we have:

$$Vn_{eq} = \sqrt{(4*Vn_{op-amp})^2 + \left(6*Vn_{R=1k}\right)^2 + \left(2*Vn_{R=10k}\right)^2 + \left(Vn_{CPE}\right)^2}$$

Plotting the total equivalent noise (black curve) and comparing it against the noise of the full (c.f. fig. 5.33) two stage floating NIC circuit (blue curve) we see that although those are comparable at high frequencies (i.e. >6 kHz), at 100 Hz they have about one order of magnitude difference. Nonetheless, this is something to be expected since the noise for each of the four aopac07 op-amps was not calculated while being configured in a NIC arrangement. In addition, the mismatch in the two noise curves means that there must be a scale factor involved in the noise density of the NIC circuit due to its impedance conversion function. Indeed, doing a simulation analysis with respect to the noise density contribution of each of the components in the NIC circuit, one of the 10 kΩ resistors was reported to contribute 38.4 nV of noise at 1 kHz, whereas it is clear from fig. 5.42 that the same value of resistance produces a flat 12.9 nV noise, i.e., about 3 times less.

The amplitude of a naturally occurring ENG signal depends on several factors (c.f. §2.3.4.1). In our case we want to use intra-thecal electrodes to record from sacral anterior (efferent motor) roots in a hope that the ENG signal can be used to show when the bladder contracts so that a stimulator can neuromodulate via stimulus pulses the sacral posterior (afferent sensory) roots to suppress the contraction. Despite we do not know the exact ENG signal amplitude we are going to record from those efferent nerve fibres in the pudendal pathway while the bladder contracts – as no one has tried it before – an ENG

---

[34] In order for the equivalent input and output noise density to be the same. Moreover, the simulated equivalent input and output noise of the NIC circuit was also found to be the same, meaning that the gain of the NIC is unity.

[35] More specifically, four aopac07 op-amps, six 1 kΩ biasing resistors (i.e. four for the phase recovery stage and two for the impedance scaling stage as: Z_1=Z_5=R_1=R_5=1 kΩ), two 10 kΩ biasing resistors (i.e. Z_2=Z_4=R_2=R_4=10 kΩ), and the 20 stages Schrama RC ladder network.

signal in the order of sub-µV is perhaps a sensible guesstimate[36]. Apart from the noise of the trimming network, the ENG will also be degraded by noise from the recording amplifier, its resistor bias network, and the source impedance (e.g. cabling, electrodes, tissue). Therefore, we should be aiming for as low noise contribution as possible from the former. Undoubtedly it is possible for someone to design an amplifier with a much lower noise density than the one that was reported for the XFAB™ aopac07 cell (c.f. fig. 5.42). For example, the LT1028 op-amp (Linear Technology) has a reported worst case input noise voltage density of 1.1 nV/√Hz at 1 kHz, i.e., about 27 times less than the aopac07. Finally, another way of indirectly compensating for the effect of noise is to carefully design cuffs which fit snugly to the nerve root or pair of roots that they intend to hold so to allow for better confinement of the action potential currents and therefore maximise the ENG amplitude, thus moving it further away from the noise floor.
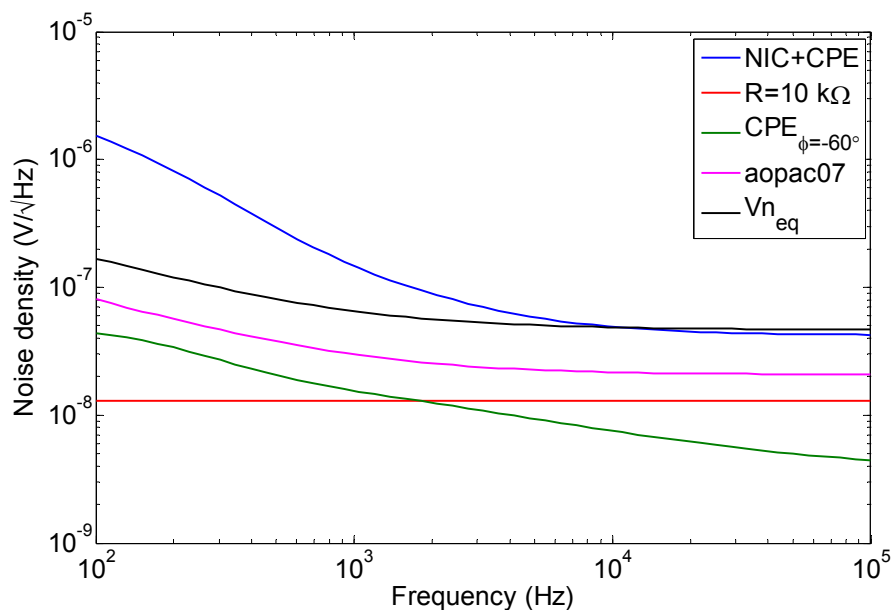
Figure 5.42: Graph showing the equivalent input noise of: the full two stage floating NIC circuit made with four XFAB™ aopac07 op-amps having an impedance scaling ratio of 1/10 (blue curve), the 20 stages Schrama RC ladder network alone with $\varphi_{CPE} \approx -60°$ (green curve), the aopac07 op-amp connected as a unity gain buffer (magenta curve), and finally the 10 kΩ resistor used in the NIC circuit for biasing purposes (red curve). The total equivalent noise Vn_{eq} calculated from all the components taking part in the NIC circuit is also shown for comparison (black curve).

In terms of the noise contribution of the CPE, plotting (in fig. 5.43) the input equivalent RMS noise in the 500 Hz to 10 kHz ENG bandwidth of interest, as a function of the number of stages in a Schrama RC ladder network, reveals that the noise decreases with increasing number of stages and reaches a plateau after a certain limit (i.e. in this case 20 stages). This is something we anticipated, since, as the stage number in the ladder

---

[36] [Kurstjens et al., 2005] made intraoperative recordings using cuff electrodes temporarily placed on the extradural S3 sacral root in 6 spinal cord injured patients and found very small amplitude changes (i.e. about 0.1 µV).

network increases, more parallel capacitors of smaller size are added to the already existing ones (i.e. extending the pore's length of fig. 5.6 to the right) and therefore the capacitive reactance for a particular frequency increases as we move down the ladder. Although adding more stages increases the noise density at low frequencies (i.e. since the stage to stage resistance also increases), now the frequency where the capacitive reactance is non-significant[37] tends to zero, as illustrated via the inset of fig. 5.43. As such, any more stages added at the end of the ladder do not contribute to the input impedance at those frequencies and therefore to the RMS noise. Finally, although increasing the frequency exponent α, reduces the RMS noise in a particular bandwidth (i.e. since the stage to stage resistance then decreases), the frequency above (i.e. 500 Hz) where the noise density remains the same is not affected much[38]. Therefore, the stage limit where the RMS noise remains constant does not strictly depend on the chosen frequency exponent α (i.e. for ladder networks with the same scaling factor S).
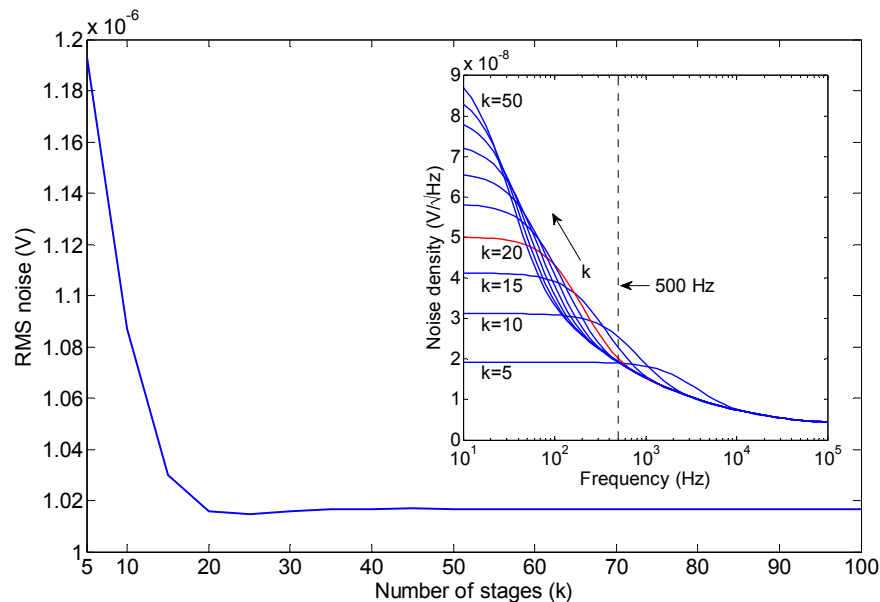
Figure 5.43: RMS voltage noise calculated in Matlab™ as a function of the number of stages in a Schrama RC ladder network with α=0.666. Inset: noise density as a function of stage number and frequency. Increasing the number of stages beyond k=20 (marked in red) does not have an effect on the (RMS) noise in the 500 Hz to 10 kHz bandwidth of interest.

Reducing R and increasing C by 10 times, the RMS noise of the ladder network is reduced threefold but at the same time the layout area is increased by tenfold to approximately 71.4 cm², which is something we might have to accept (i.e. layout area increase) in the end in wanting to have a technique which is plausible in terms of noise performance. Furthermore, the amount of noise contributed from the NIC circuit will also

---

[37] In a sense that the added capacitors are acting as a short to ground, thus reducing the contributed noise density from the real part of the impedance of subsequent stages.

[38] The frequency above where the noise density remains the same, and consequently the number of stages we have to add to the ladder network in order for the RMS noise to remain constant, are affected more as the frequency exponent α decreases since then the stage to stage capacitive reactance to ground is increased.

depend on the amount of imbalance in the cuff. As the scaling ratio applied by the NIC depends on the size of its biasing resistors, the total RMS noise will also be affected. As we do not know whether the 17% imbalance in the model of fig. 5.30 is a realistic one for our case[39] it would have been redundant to determine the noise performance of that arrangement.

5.9 Summary of part 2

In part 2 we went from theory to practice: the Schrama CPE was realised in a hardware PCB with measured results found to be in very good agreement with actual simulated data. The CPE PCB after a NIC circuit was then used towards balancing a Wheatstone bridge arrangement comprising a custom made electrochemical cell, similarly as would have been done with balancing the QT. The utilised trimming impedance network resembled the structure of the electrode impedance and was able to adapt to its frequency response. Therefore, someone would expect the bridge to be fully balanced throughout the ENG band and interference due to EMG to be constantly small. Although, for the various reasons explained, the impedance data fit was not perfect, an average reduction of about 100 times less EMG breakthrough at the differential output of the bridge was achieved. Based on Cadence™ and Matlab™ simulation results which were strengthened by the in-vitro verification performed later on the chapter, the idea of balancing the neural recording tripole by appropriately modelling the neutralisation impedance, albeit cannot be considered passive anymore, nevertheless seems promising. With the use of a NIC circuit to choose the appropriate magnitude, and a selection of RC ladder networks to obtain the right CPE phase angle required for balancing a recording tripole, the trimming impedance "adapts" to the frequency response of electrodes and balance of the bridge can be achieved with no continuous adjustment. The technique seems to be plausible in terms of silicon area and IC implementation perspective, while most of the exhibited noise is contributed by the NIC circuit due to its impedance conversion function and therefore efforts to minimise it should focus on that specific part of the design.

---

[39] The purpose of the model was only to illustrate that balance using the floating NIC circuit is possible and to assess the neutralisation performance in terms of the impedance conversion non-idealities of the NIC op-amps.

CHAPTER
SIX

General Conclusion and Future Work

6.1 Summary of work

In this work a novel neural recording amplifier configuration based on the conventional QT was presented. Chapter 1 introduced the motivation and project aims, together with an idea for a possible application, i.e., that of conditional neuromodulation by detecting the small changes in neural signal when the bladder contracts, in individuals with SPI having lost their continence, and suppressing those via stimulation. Chapter 2 addressed many of the fundamental theoretical aspects linked to this work, like the underlying neurophysiology of the PNS and the different amplifier configurations used for recording neural activity from peripheral nerves via implanted cuff electrodes without the presence of unwanted interference. Chapter 3 analysed the factors that are causing myoelectric and CM interference to be picked up by the cuff electrodes thus appearing at the output of the QT amplifier, while at the same time proposed a new approach for effectively neutralising them. In addition, it was demonstrated through a number of in-vitro experiments that both sources of interference can be successfully neutralised with EMG removed completely at a spot frequency and reduced about 10 times at the rest of the ENG spectrum. One of the key advantages of this approach is that interference can be neutralised passively and with only one instrumentation amplifier, therefore, being more power efficient in comparison to the TT and AT configurations. Having highlighted the advantages and disadvantage of the new configuration, ways of improving it were investigated. The main idea was based on the fact that as there are models that can mimic the frequency response of metal electrodes, interference could be uniformly removed in the entire ENG band with no continuous adjustment. This made it necessary to devote a chapter (i.e. Chapter 4) on modelling of the impedance of implanted electrodes. As such, the reasons why metallic electrodes behave the way they do were looked into and the small-signal 3-component electrode impedance model of fig. 4.1 together with the very important, for describing the frequency dispersion of real electrodes in contact with solid or aqueous electrolytes CPE, were introduced. Simulation results in Matlab™ demonstrated that real electrode impedance data can be adequately represented by the 3-component model when the effect of the double-layer capacitance is replaced by the pseudo-capacitive CPE impedance (i.e. Cole model). The pinnacle of this work was reached in Chapter 5 which was divided in two parts: part 1 dealt with the theoretical aspects of the work, while part 2 was devoted to the practical side of things, set out to evaluate the performance of the upgraded interference neutralisation approach of Chapter 3. More specifically, in part 1 the reasons behind the observed frequency dispersion and CPE behaviour of electrodes were critically analysed by reviewing the majority of the

literature on the topic, investigating what others have done to understand this behaviour and how to appropriately model it. This led to the introduction of the single-pore model and a comparison of 3 different approaches of CPE emulation with the most suitable one for the purpose – i.e. a zero-order non-uniform Schrama RC ladder network – eventually chosen due to its ease of use in respect to the other two. In part 2, the new trimming network was put to the test in a different in-vitro experiment than that of Chapter 3 with results indicating that appropriately modelling the trimming impedance required to balance the recording tripole (c.f. fig. 5.31) and the impedance of a sphere monopole (c.f. fig. 5.39) using an electrical circuit model that takes into account the porosity and roughness of the electrode-electrolyte interface (c.f. fig. 5.4) can offer an improvement in the way interference is neutralised.

Coming up with an entirely novel amplifier configuration for the purpose of recording neural information from peripheral nerves is certainly not an easy task. At the beginning of this project an idea of improving the performance of an existing configuration – that of QT – first proposed by [Struijk and Thomsen, 1995], was adopted. This was based on seeing the QT as a Wheatstone bridge that could be balanced by placing a potentiometer across the two outer electrodes to allow adjustment. In our case, an impedance term in the form of a series or parallel RC model was first tried out, offering significant improvement in the way interference is neutralised in QT. The outcome of this was a recording configuration which we called the mQT, due to essentially being a modified version of the conventional QT (i.e. it connects the same way to electrodes). Nevertheless, despite the similar connectivity to the recording electrodes, it is important to emphasise that the mQT is different in the way interference is neutralised, offering better signal-to-interference ratio with still only one instrumentation amplifier and therefore low power consumption. With the revised (frequency adaptive) version of the mQT, the advantage of less power consumption might have been lost due to eventually having to use some active circuitry (i.e. a NIC) as a way of having independent control over the magnitude and phase that is required to be added to reach balance. In-vitro results have shown that with this revised trimming network EMG breakthrough at the output of the recording amplifier is on average at least 100 times less in the ENG band, and most importantly the initial requirement of continuous adjustment to reach balance at each frequency is now redundant. However, whether the signal-to-interference ratio performance of the frequency adaptive mQT is better than that of TT still requires investigation.

Due to the high input impedance that each electrode is presented with from an input of the recording amplifier, the TT is superior in reducing a broadband EMG interference signal than the mQT, owing to the frequency-dependence of the electrode impedance (c.f. fig 3.12). This was demonstrated by [Cirmirakis et al., 2010] in an in-vitro comparison using the first (i.e. passive) version of the mQT, presented in Chapter 3. In fact it is expected the mQT once adjusted to neutralise interference completely at a spot frequency and better than the TT. This is true, since the mQT also compensates for the capacitive reactance of the electrode impedance, whereas the TT depends solely on minimising its effect, nonetheless, this effect cannot be completely neglected (c.f. fig. 3.10). Most importantly, when the electric field is altered after adjustment, the interference is greater for the TT than the mQT and as quite rightfully commented by [Cirmirakis et al., 2010],

in an implant the interference is likely to come from nearby active muscles and the fields will be continuously changing, as action potentials propagate along the muscle fibres with a range of propagation velocities, rather being stationary like in the tank experiment. When a cuff is close to an active muscle the electric field produced will not be confined in a symmetrical space like in the case of the T-shaped tank and therefore will not be solinoidal. As the muscle field in reality is time-varying, the TT is not able to track such a changing field very well and therefore cannot appropriately neutralise it. Therefore, it is likely that mQT will be better than the TT in that aspect. Experiments under true biological conditions (i.e. in-vivo experiments in small animal models) should give a definite answer to this postulation.

From work in Chapter 3 (c.f. §3.5.1) we have shown that electrical imbalance varies more slowly than geometric asymmetry. Although the reason why this is the case was not investigated at the time, the problem exists in the significance of the frequency-dependent electrode impedance. Therefore, any mismatch in the two outer electrodes of the mQT can have a significant effect on imbalance. This problem is worsened when electrodes have mismatches, even down to microscopic level since it is a well-known experimental fact that the frequency response of metallic electrodes is sensitive to surface properties. If we assume that it is possible to manufacture electrodes of exact same area, it is difficult to say how feasible it will be to manufacture electrodes with identical surface texture, resulting to ambiguous interfacial micrometer scale texture which is different from one electrode to the other and difficult to reproduce. In particular, interference field lines will not converge evenly onto an uneven surface, since an electrode surface that appears smooth might have irregularities of various shapes like cliffing, cratering, and channelling. Regardless of the details of the structure, it follows that the distributed double-layer interface capacitance will be charged unevenly, and that the admittance will be time and frequency-dependent. Because of the roughness, the effective solution resistance will also vary along the surface, causing an inhomogeneous current density distribution and hence a broad distribution of the time constant. Hence, surface roughness results to different frequency dispersion (and therefore different CPE) for each of the two outer electrodes, leading to imbalance.

Even today, very little is known in detail about the porous interface from first principles, aside from a general knowledge of how the porous electrode behaviour deviates from flat electrode behaviour. Tissue and electrodes in electrolyte solutions have the important property of a more or less constant phase angle. Although in part 1 of Chapter 5 an attempt was made to investigate the reasons behind this mystifying property by going through the relevant literature, the view that seemed to prevail was that the surface texture is the main cause of frequency dependence and non-ideal capacitive behaviour of electrodes, nonetheless, the bottom line was that this might not be the sole cause, or even that surface roughness is indirectly related to the observed frequency dispersion of the electrode impedance but it is not the main cause behind it. In other words, apart from chemical inhomogeneities of interfacial origin (i.e. electrolyte ion adsorption effects) and geometrically inhomogeneities of the surface (i.e. porosity and roughness) there might also be other processes responsible for the CPE behaviour of electrodes. Specifically, it would be useful to know more on how the complicated

topology of the porous metal electrode contributes to the electrical properties of the interface. As an indication of the complexities involved in trying to understand this behaviour, [Jorcin et al., 2006] studied both the global and local impedance of an AZ91 Mg alloy and pure aluminium (i.e. non-ideally polarisable) disk electrodes in Na_2SO_4 electrolyte. The impedance of the whole electrode (i.e. global impedance) was measured in the traditional "three-electrode cell" way and the frequency exponent of the CPE of the AZ91 Mg alloy electrode was obtained, having a value of $\alpha=0.91$. The local impedance was also measured by placing a sub-mm current probe a short distance over the working electrode. The local impedance was measured as a function of the distance along the radius of the electrode. In particular, the spectrum above 1 Hz was fitted to a 3-component circuit (c.f. fig. 4.1) and the values of the charge transfer resistance R_{ct} and double-layer capacitance C_{dl} were obtained by regression of the local impedance diagrams. Near the centre, the frequency exponent α of the CPE was 1.0, indicating a true capacitance with α being independent of the radial distance of the electrode (i.e. α was found to be the same both at the centre and at the edge of the disk electrode). Conversely, C_{dl} was independent of the radial position, whereas R_{ct} increased significantly near the periphery of the electrode (i.e. 5000 μm radial distance from the centre). Therefore, the CPE behaviour that appeared on the global impedance measurements is thus explained by the 2D distribution of the R_{ct} resistance (i.e. the microstructure of the AZ91 Mg alloy – in other words a change in α – did not cause the CPE behaviour). In contrast to the results obtained for the AZ91 Mg alloy, for the pure aluminium electrode both R_{ct} and K (i.e. a CPE was used this time to perform a fit) were found to be functions of radial position. This indicates that the variation of R_{ct} and CPE coefficient K cannot be attributed to local microstructural features (e.g. surface roughness) and is more likely associated with the current and potential distribution seen on disk electrodes. Thus, the CPE behaviour that appeared on the global impedance of pure aluminium is explained by a 3D rather a 2D distribution of time constants.

6.2 Proposals for future work

At the time of writing, a tripolar amplifier configuration employing a novel interference neutralisation technique has been developed in simulation and designed using discrete circuit components, with its performance being initially evaluated in-vitro with promising results. Nevertheless, there are certain differences between an in-vitro and in-vivo arrangement. For example, it is apparent that under physiological conditions the variability of the electrode impedance, as well as the proximity and orientation of an interference source, and therefore imbalance in the tripole, will probably be different than the one observed under laboratory conditions. Therefore, in-vivo tests with animal models should be performed for a better evaluation of the new configuration. In addition, a proper assessment of the floating version of the NIC circuit which will be in practice required for balancing a recording tripole needs to be performed initially in-vitro. It would also be interesting to know how the effect of altering the interference field affects the neutralisation performance of the frequency adaptive mQT. Testing the technique in-vivo using a stimulus-induced ENG would offer results which could help us answering this question. Finally, a detailed noise analysis of the floating NIC circuit with

calculations showing how the NIC amplifier noise compares to the rest of the components of the trimming network also needs to be performed.

The idea of using an audio transformer for downconverting the magnitude of the Z_{CPE} (i.e. by the square of the turns ratio n), instead of using a NIC circuit, was briefly discussed in the last paragraph of §5.3.5. This was tested with an audio output transformer (RS components) having 15:1 to 128:1 ratios, available in our laboratory. At first instance, we wanted to see whether the transformer could perform the conversion (i.e. based on a selected n) having a particular CPE PCB as the load. Therefore, the secondary of the transformer (i.e. about 4 Ω resistance) was connected to the impedance analyser (Wayne Kerr Electronics, model 6520BD1, 20 Hz-20 MHz), while the primary was connected to a 20 stages Schrama RC ladder network with α=0.666 (i.e. $|Z_{CPE}|\approx134$ kΩ at 100 Hz). From measurements we found the impedance magnitude of the load to be higher than the transformer could handle (i.e. the measurement of the impedance analyser was the actual magnitude and phase of the transformer itself; the reflected impedance to the secondary winding (i.e. Z_{CPE}/n^2) was an open circuit). Hence, the inductance of the particular transformer at ENG frequencies was simply too low for the task. In order to increase the load driving capability of the transformer we need to increase its L (i.e. inductance of coil windings), meaning having a bigger core size with more turns and therefore a bigger overall size transformer. Nonetheless, by doing so the passband of the transformer will be reduced and this is a disadvantage for our application. The fact that $|Z_{CPE}|$ drops as the phase angle of the CPE increases is encouraging knowing that the frequency exponent of real electrodes has been reported to lie in the 0.75 to 0.95 range. This is in agreement with the values of α we found in our electrode impedance measurements (c.f. table 5.3, fig. 5.36 and fig. 5.38). Undoubtedly, the use of an audio transformer requires further investigation.

Overall, the technique has demonstrated good potential and to the author's belief it is the way to go, as improved neutralisation performance in applications like ours, where low power consumption is crucial, make it important. The system has been designed and built in discrete, wanting first to evaluate the operating principle and form the specifications for an IC implementation. A custom-made amplifier design used in place of the XFAB™ aopac07 cell could reduce the exhibited noise (i.e. in favour of increased bias current), while from a preliminary study on the overall size of the RC components that the technique employs it seems plausible to incorporate everything into a single IC. Finally, the use of transformers is not efficient from an implementation point of view due to their large physical size as well as trimming resolution (i.e. fixed ratios). To summarise, the following is a list of suggestions of what needs to be done next:

- Analysis of the noise for the floating NIC circuit.
- A floating NIC circuit made from low-noise instrumentation amplifiers that can be demonstrated to work in practice.
- Measurements of the noise from this NIC version.
- Experimental results preferably from a real book or cuff in a saline bath.
- A realistic discussion about miniaturisation/integration of the device.
- Acute in-vivo evaluation of the technique using the floating NIC arrangement.

Appendix A

Ideal Tripolar Cuff Model

In fig. A.1 is a model of the tripolar cuff showing the tissue resistances outside the cuff R_{o1} and R_{o2}, the tissue resistances inside and along the cuff (i.e. axial resistances) R_{t1} and R_{t2}, being separated between the middle electrode and the two end electrodes, while Z_{e1} to Z_{e3} are the electrode impedances which have capacitive reactance. Also shown are the three sources contributing to the differential input voltage V_d of the recording amplifier, i.e., V_{ENG} due to action potentials propagating along the nerve trapped inside the cuff (i.e. often represented as a floating voltage source in series with the middle electrode), I_{INT} which represents the interference current flowing outside and inside the cuff due to external to the cuff electric fields, and finally V_{CM} which is a common-mode interference due to potential differences that may occur between the cuff electrodes and the reference electrode. Since the model is ideal we assume that $R_{t1}=R_{t2}=0.5R_t$ (i.e. the cuff is perfectly symmetrical and the tissue inside is evenly spread), as well as $Z_e=Z_{e1}=Z_{e2}=Z_{e3}$. In reality, however, the cuff is affected by factors that cause its properties to drift away from the ideal model. Nonetheless, this model allows an analysis of the voltages appearing between the electrodes in terms of the currents of the nerve (i.e. action potentials) and muscle sources (i.e. myoelectric interference) with the tissue resistances and electrode impedances.
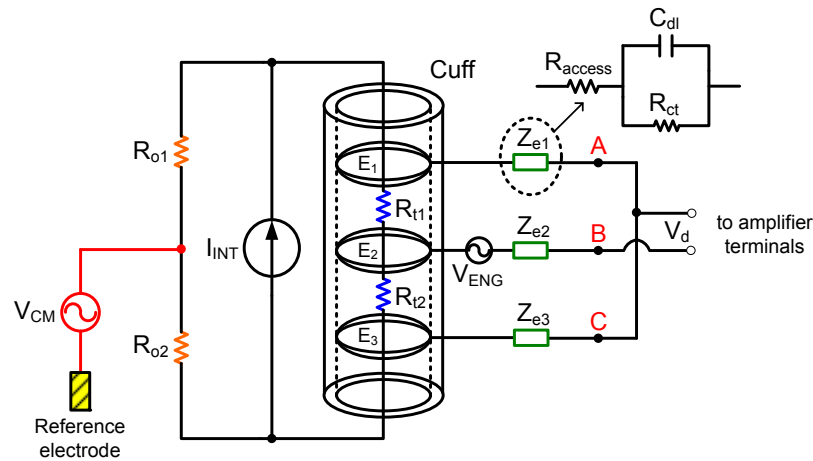
Figure A.1: Lumped QT cuff model showing the electrode impedances (Z_{e1}, Z_{e2}, Z_{e3}), the tissue resistances (R_t, R_o), and the three sources (V_{ENG}, I_{INT}, V_{CM}) contributing to the differential input voltage V_d of the amplifier. Nodes E_1, E_2, and E_3 are within the tissue, while A, B, and C are circuit nodes. Model is also valid for tripolar book. Recording is carried out between the middle and the two shorted outer electrodes. Typical values of components, subject to the actual geometry of the electrode-electrolyte interface, are [Donaldson et al., 2003]: C_{dl}=2.5 µF, R_{ct}=16 kΩ, R_{access}=327 Ω, $R_{t1}=R_{t2}$=842 Ω, and $R_o=R_{o1}+R_{o2}$=230 Ω. Cuff electrode impedances Z_e are reported to have a magnitude of about 3 kΩ (measured at 1 kHz) [Haugland and Hoffer, 1994].

Appendix B

RC Values for Schrama Ladder Network

Tables of pre-calculated RC values for a total of nine 20 stages Schrama ladder networks, where: alpha (α) is the frequency exponent of the exhibited CPE, φ is the respective phase angle in degrees, and finally S is the scaling factor (c.f. §5.3.4.3) for the particular set of RC values.

	alpha=0.5, φ=−45°, S=10^6		alpha=0.555, φ=−50°, S=10^6		alpha=0.611, φ=−55°, S=10^7	
Stage	R (kΩ)	C (pF)	R (kΩ)	C (pF)	R (kΩ)	C (pF)
1	1.0	2000	0.468	3852	2.16	758.5
2	2.0	2000	1.17	3307	6.78	549.5
3	2.0	2000	1.255	3117	7.86	487
4	2.0	2000	1.31	3002	8.59	451
5	2.0	2000	1.35	2919	9.155	426
6	2.0	2000	1.39	2854	9.62	408
7	2.0	2000	1.415	2802	10.01	393
8	2.0	2000	1.44	2758	10.36	380
9	2.0	2000	1.46	2720	10.67	370
10	2.0	2000	1.48	2687	10.96	361
11	2.0	2000	1.50	2658	11.215	353
12	2.0	2000	1.51	2631	11.455	346
13	2.0	2000	1.53	2607	11.68	339.5
14	2.0	2000	1.54	2585	11.89	334
15	2.0	2000	1.55	2565	12.08	328.5
16	2.0	2000	1.565	2546	12.27	324
17	2.0	2000	1.58	2529	12.45	319
18	2.0	2000	1.59	2512	12.62	315
19	2.0	2000	1.60	2497	12.78	311
20	2.0	2000	1.61	2483	12.93	308

	alpha=0.666, φ=−60°, S=10^7		alpha=0.722, φ=−65°, S=10^7		alpha=0.777, φ=−70°, S=10^7	
Stage	R (kΩ)	C (pF)	R (kΩ)	C (pF)	R (kΩ)	C (pF)
1	1.01	1488	0.466	2975	0.218	5910
2	4.025	895	2.42	1441	1.52	2225
3	5.03	746	3.26	1127	2.205	1633
4	5.74	665	3.89	966	2.75	1346
5	6.31	611	4.42	862	3.23	1167
6	6.8	571	4.88	788	3.65	1043

7	7.22	540	5.29	731	4.04	950
8	7.6	515	5.665	686	4.40	877
9	7.94	494	6.01	649	4.74	818
10	8.26	476	6.33	617	5.055	769
11	8.55	460	6.64	590	5.36	727
12	8.83	447	6.92	567	5.65	691.5
13	9.09	434.5	7.195	546	5.93	660
14	9.33	423.5	7.455	528	6.20	633
15	9.56	413.5	7.70	511	6.46	608
16	9.78	404.5	7.94	496	6.71	586
17	10	396	8.175	483	6.95	566
18	10.2	388.5	8.40	470	7.19	548
19	10.4	381	8.61	459	7.42	531
20	10.58	375	8.82	448	7.65	516

	alpha=0.833, $\varphi=-75°$, S=10^7		alpha=0.888, $\varphi=-80°$, S=10^7		alpha=0.944, $\varphi=-85°$, S=10^7	
Stage	R (kΩ)	C (pF)	R (kΩ)	C (pF)	R (kΩ)	C (pF)
1	0.1005	11950	0.047	24000	0.0217	48870
2	1.0	3266	0.745	4265	0.731	4220
3	1.57	2242	1.265	2737	1.345	2520
4	2.06	1775	1.73	2081.5	1.93	1840
5	2.49	1495	2.16	1704	2.49	1460
6	2.89	1306	2.57	1454	3.03	1220
7	3.26	1167	2.96	1276	3.56	1050
8	3.61	1060	3.335	1140.5	4.085	920
9	3.95	975	3.70	1034	4.60	830
10	4.27	905	4.05	948	5.11	750
11	4.58	846	4.40	877	5.61	680
12	4.88	796	4.735	817	6.10	630
13	5.17	753	5.07	766	6.59	590
14	5.46	715.5	5.39	721	7.08	550
15	5.73	682	5.71	682	7.56	510
16	6.0	652.5	6.02	648	8.04	480
17	6.265	626	6.33	617	8.51	460
18	6.52	602	6.64	590	8.98	430
19	6.78	580	6.94	565	9.45	410
20	7.02	560	7.24	542	9.91	390

Appendix C

Floating NIC Input Impedance Derivation

The following is the analytical derivation of the input impedance Z_{eq} of the floating NIC circuit arrangement. The derivation is made with the assumption that the two amplifiers have infinite input impedance and an open-loop gain G.
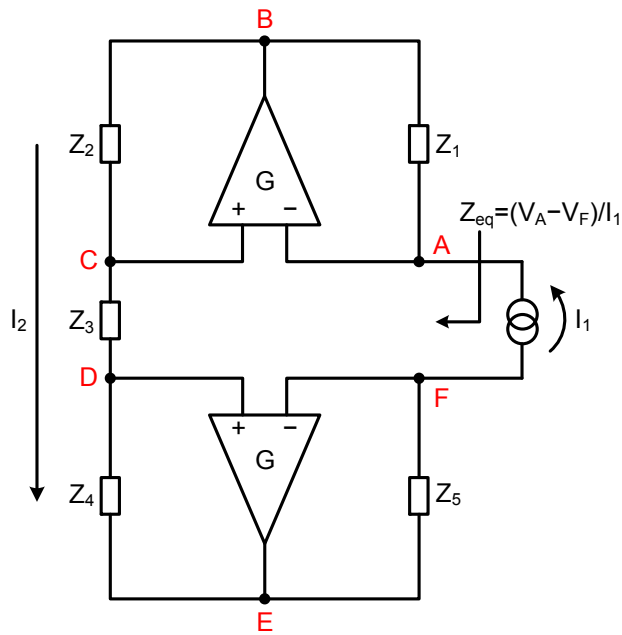
Figure C.1: Schematic of a single stage floating NIC circuit used for the analysis. Notice that the input (I_{Z1}) and output (I_{Z5}) currents are equal since there is no path to ground.

For the two amplifiers:

$$V_B = G(V_C - V_A) \quad (1)$$
$$V_E = G(V_D - V_F) \quad (2)$$

For the five biasing impedances:

$$V_A - V_B = I_1 Z_1 \quad (3)$$
$$V_B - V_C = I_2 Z_2 \quad (4)$$
$$V_C - V_D = I_2 Z_3 \quad (5)$$
$$V_D - V_E = I_2 Z_4 \quad (6)$$
$$V_E - V_F = I_1 Z_5 \quad (7)$$

From (1) $\rightarrow V_B = GV_C - GV_A \Leftrightarrow V_C = \dfrac{V_B + GV_A}{G} = V_A + \dfrac{V_B}{G}$ (1a)

From (2) $\rightarrow V_E = GV_D - GV_F \Leftrightarrow V_D = \dfrac{V_E + GV_F}{G} = V_F + \dfrac{V_E}{G}$ (2a)

From (4) & (1a) $\rightarrow V_B - V_C = I_2 Z_2 \Leftrightarrow V_B - \left(V_A + \dfrac{V_B}{G} \right) = I_2 Z_2 \Leftrightarrow V_B \left(1 - \dfrac{1}{G} \right) - V_A = I_2 Z_2$ (4a)

From (5) & (1a) & (2a) $\rightarrow V_C - V_D = I_2 Z_3 \Leftrightarrow \left(V_A + \dfrac{V_B}{G} \right) - \left(V_F + \dfrac{V_E}{G} \right) = I_2 Z_3 \Leftrightarrow$

$V_A - V_F + \dfrac{1}{G} \left(V_B - V_E \right) = I_2 Z_3$ (5a)

From (6) & (2a) $\rightarrow V_D - V_E = I_2 Z_4 \Leftrightarrow \left(V_F + \dfrac{V_E}{G} \right) - V_E = I_2 Z_4 \Leftrightarrow V_F - V_E \left(1 - \dfrac{1}{G} \right) = I_2 Z_4$ (6a)

From (3) − (7) $\rightarrow V_A - V_F = I_1 Z_1 + I_1 Z_5 + V_B - V_E \Leftrightarrow V_A - V_F = I_1 \left(Z_1 + Z_5 \right) + V_B - V_E$ (8)

From (5a) $\rightarrow I_2 = \dfrac{V_A - V_F}{Z_3} + \dfrac{1}{GZ_3} \left(V_B - V_E \right)$ (5b)

From (5b) & (4a) $\rightarrow V_B \left(1 - \dfrac{1}{G} \right) - V_A = Z_2 \left(\dfrac{V_A - V_F}{Z_3} + \dfrac{V_B - V_E}{GZ_3} \right) = \dfrac{Z_2}{Z_3} V_A - \dfrac{Z_2}{Z_3} V_F +$

$+ \dfrac{Z_2}{GZ_3} V_B - \dfrac{Z_2}{GZ_3} V_E \Leftrightarrow V_A \left(1 + \dfrac{Z_2}{Z_3} \right) + V_B \left(\dfrac{Z_2}{GZ_3} + \dfrac{1}{G} - 1 \right) - \dfrac{Z_2}{GZ_3} V_E - \dfrac{Z_2}{Z_3} V_F = 0$ (4b)

From (5b) & (6a) $\rightarrow V_F - V_E \left(1 - \dfrac{1}{G} \right) = Z_4 \left(\dfrac{V_A - V_F}{Z_3} + \dfrac{V_B - V_E}{GZ_3} \right) = \dfrac{Z_4}{Z_3} V_A - \dfrac{Z_4}{Z_3} V_F +$

$+ \dfrac{Z_4}{GZ_3} V_B - \dfrac{Z_4}{GZ_3} V_E \Leftrightarrow V_A \dfrac{Z_4}{Z_3} + V_B \dfrac{Z_4}{GZ_3} + V_E \left(1 - \dfrac{1}{G} - \dfrac{Z_4}{GZ_3} \right) - V_F \left(1 + \dfrac{Z_4}{Z_3} \right) = 0$ (6b)

From (4b) $\rightarrow \left(V_B - V_E \right) \left(\dfrac{Z_2}{GZ_3} \right) + V_B \left(\dfrac{1}{G} - 1 \right) = V_F \left(\dfrac{Z_2}{Z_3} \right) - V_A \left(1 + \dfrac{Z_2}{Z_3} \right)$ (4c)

From (6b) $\rightarrow \left(V_B - V_E \right) \left(\dfrac{Z_4}{GZ_3} \right) - V_E \left(\dfrac{1}{G} - 1 \right) = V_F \left(1 + \dfrac{Z_4}{Z_3} \right) - V_A \left(\dfrac{Z_4}{Z_3} \right)$ (6c)

From (4c) + (6c) $\rightarrow \left(V_B - V_E \right) \left(\dfrac{Z_2}{GZ_3} + \dfrac{Z_4}{GZ_3} \right) + \left(V_B - V_E \right) \left(\dfrac{1}{G} - 1 \right) = V_F \left(1 + \dfrac{Z_2}{Z_3} + \dfrac{Z_4}{Z_3} \right) -$

$- V_A \left(1 + \dfrac{Z_2}{Z_3} + \dfrac{Z_4}{Z_3} \right) \Leftrightarrow \left(V_B - V_E \right) \left(\dfrac{Z_2 + Z_4}{GZ_3} + \dfrac{1}{G} - 1 \right) = \left(V_F - V_A \right) \left(1 + \dfrac{Z_2}{Z_3} + \dfrac{Z_4}{Z_3} \right) \Leftrightarrow$

$\dfrac{\left(V_B - V_E \right)}{G} \left(\dfrac{Z_2 + Z_4}{Z_3} + 1 - G \right) = \left(V_F - V_A \right) \left(1 + \dfrac{Z_2 + Z_4}{Z_3} \right) \Leftrightarrow$

$$V_B - V_E = \frac{G\left(V_F - V_A\right)\left(1 + \dfrac{Z_2 + Z_4}{Z_3}\right)}{\left(1 + \dfrac{Z_2 + Z_4}{Z_3} - G\right)} \quad (9)$$

Assuming that $G \gg 1$ and $G \gg (Z_2 + Z_4)/Z_3$, eqn. 9 becomes:

$$V_B - V_E = -\left(V_F - V_A\right)\left(1 + \frac{Z_2 + Z_4}{Z_3}\right) = \left(V_A - V_F\right)\left(1 + \frac{Z_2 + Z_4}{Z_3}\right) \quad (10)$$

From (8) & (10) $\rightarrow V_A - V_F = I_1\left(Z_1 + Z_5\right) + \left(V_A - V_F\right)\left(1 + \frac{Z_2 + Z_4}{Z_3}\right)$

$$\left(V_A - V_F\right)\left(1 - 1 - \frac{Z_2 + Z_4}{Z_3}\right) = I_1\left(Z_1 + Z_5\right) \Leftrightarrow \left(V_A - V_F\right)\left(-\frac{Z_2 + Z_4}{Z_3}\right) = I_1\left(Z_1 + Z_5\right)$$

$$\frac{\left(V_A - V_F\right)}{I_1} = Z_{eq} = -Z_3\left(\frac{Z_1 + Z_5}{Z_2 + Z_4}\right)$$

Appendix D

XFAB™ Op-Amp Cell Schematic and Data Sheet

The circuit schematic of the 0.6 µm CMOS op-amp used for the implementation of the NIC in Cadence™ circuit simulator is shown in fig. D.1 below. The output impedance of the particular op-amp measured in simulation was found to be about 343 Ω.

Figure D.1: Circuit schematic of a two stage operational transconductance amplifier with PMOS input stage (i.e. M1-M4 form the differential pair stage having a current mirror active load) and common-source output stage (i.e. M11-M12) employing miller compensation. The cell that is used to provide the bias voltage input VBN is not shown.
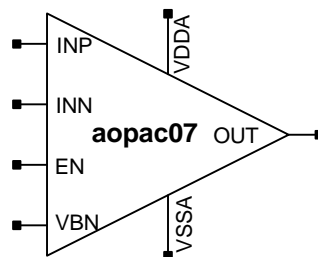
Description:

Aopac07 is a general purpose internally compensated CMOS OpAmp with P-MOS input stage and rail-to-rail output stage.

- The recommended bias cells are abiac02 +abgpc01/abgpc02 and abiac05.
  With abiac05, a bit higher dependancy of some parameters (esp. speed and current consumption) on supply voltage variations is observed.
- Physical size (h x w): 150.0 µm x 116.7 µm (standard core cell)
- XC06, CMOS cap/res module

Symbol:

Pin description:

VDDA	positive power supply
VSSA	ground
INP	non-inverting input
INN	inverting input
VBN	bias voltage input
EN	enable input (active high)
OUT	output

Parameters (bias provided by abiac02 + abgpc02) :

Parameter	Description	min	typ	max	Unit	Conditions
V_{IO}	Input offset voltage		5	10	mV	V_{DD}=5V;V_{CM}=V_{DD}/2;T=25°C (absolute values)
V_{IL}	Low input voltage		0.12	0.4	V	V_{DD}=5V; T=25°C
V_{IH}	High input voltage	3.4	3.51		V	V_{DD}=5V; T=25°C
V_{OL}	Low output voltage		0.05	0.1	V	V_{DD}=5V; T=25°C; R_L=1MΩ
V_{OH}	High output voltage	V_{DD}-0.1	V_{DD}-0.05		V	V_{DD}=5V; T=25°C; R_L=1MΩ
A_{VO}	Open loop voltage gain	90	99		dB	V_{DD}=5V;V_{CM}=V_{DD}/2;T=25°C R_L=100kΩ
GBW	Gain bandwidth	1.89	2.68		MHz	V_{DD}=5V;V_{CM}=V_{DD}/2;T=25°C R_L=100kΩ; C_L=50pF, Fig. 2
SR	Slew Rate Rise Fall	1.86 1.97	2.70 2.82		V/µs	V_{DD}=5V;V_{CM}=V_{DD}/2;T=25°C R_L=100kΩ; C_L=50pF, Fig. 3
FPBW	Full power bandwidth		89		kHz	V_{DD}=5V;V_{CM}=V_{DD}/2;T=25°C R_L=100kΩ; C_L=50pF

Parameters (continued):

| Parameter	Description	min	typ	max	Unit	Conditions
C_L	Load capacitance		30	50	pF	V_{DD}=5V; T=25°C
R_L	Load resistance	100	500		kΩ	V_{DD}=5V; T=25°C
PM	Phase margin	70	85		deg	V_{DD}=5V; V_{CM}=V_{DD}/2; T=25°C R_L=100kΩ; C_L=50pF
GM	Gain margin	-12	-17		dB	V_{DD}=5V; V_{CM}=V_{DD}/2; T=25°C R_L=100kΩ; C_L=50pF
E_N	Equivalent Input Noise Voltage		60		nV/√Hz	f= 1KHz, See Fig. 5
			40		nV/√Hz	f=10KHz, See Fig. 5
PSRR	Power supply rejection ratio		86		dB	V_{DD}=5V; V_{CM}=V_{DD}/2; T=25°C (evaluated at DC)
V_{DD}	Supply voltage	4.5	5	5.5	V	T=-40 to 85 ^{o}C
I_{DD}	Supply current		215	300	µA	V_{DD}=5V; T=25°C

Typical performance characteristics: measured values
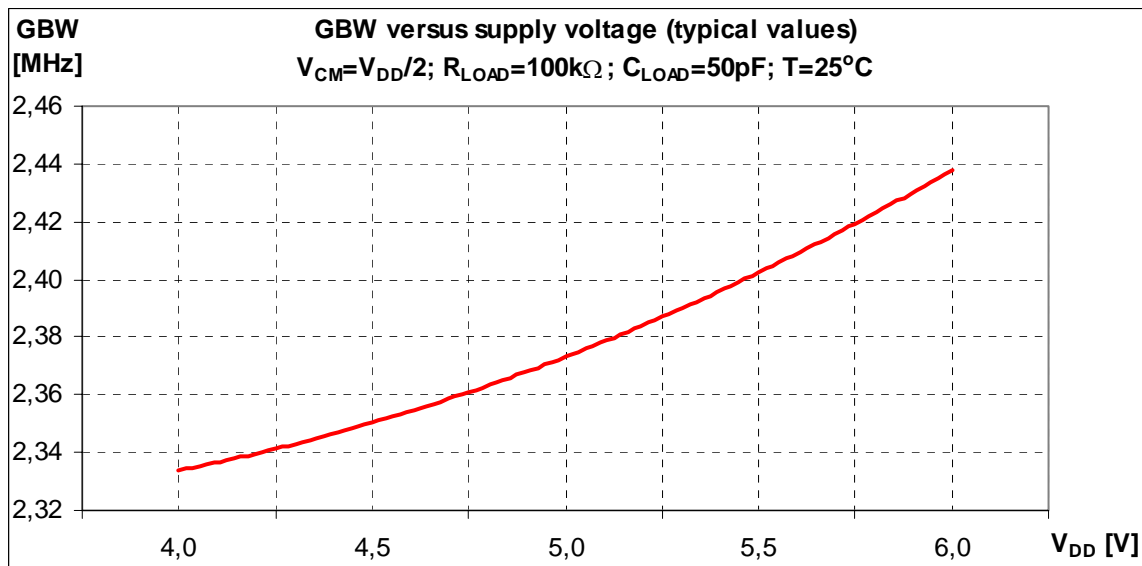
Fig.1 GBW versus supply voltage
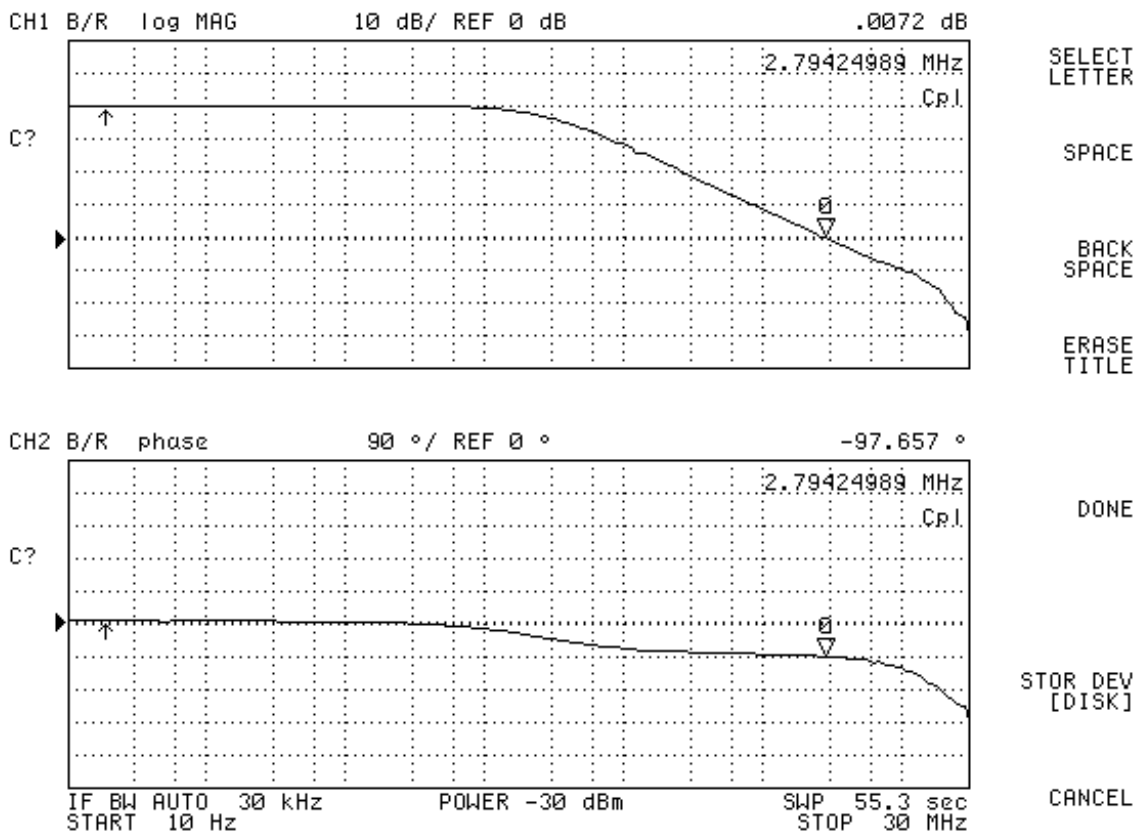
Typical performance characteristics: measured values

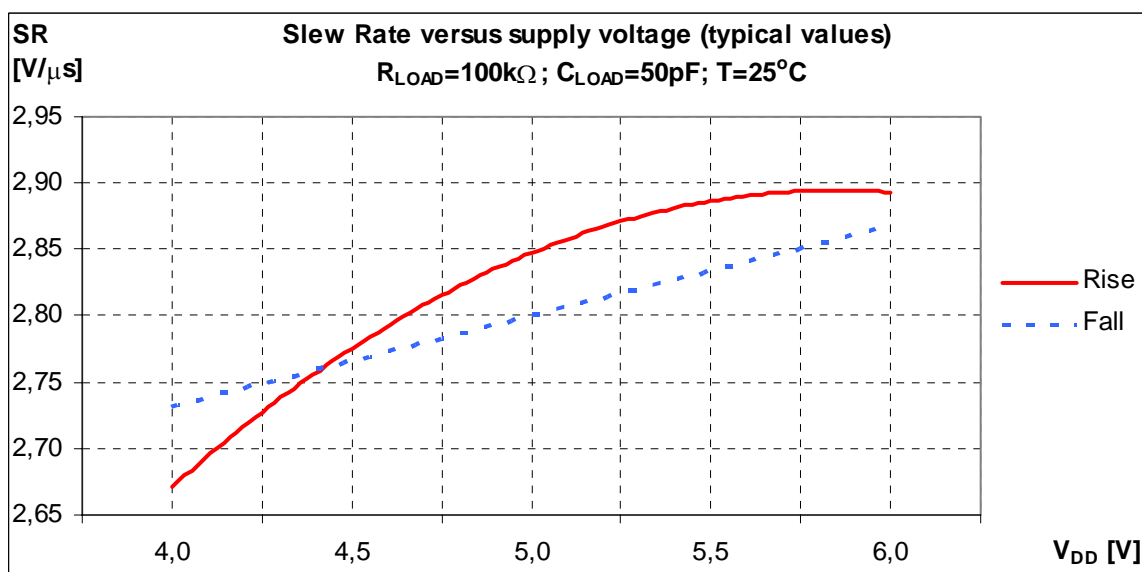Fig. 2 Gain and Phase vs. Frequency, C_L= 50pF, R_L=100kΩ

Fig. 3 Slew Rate versus supply voltage
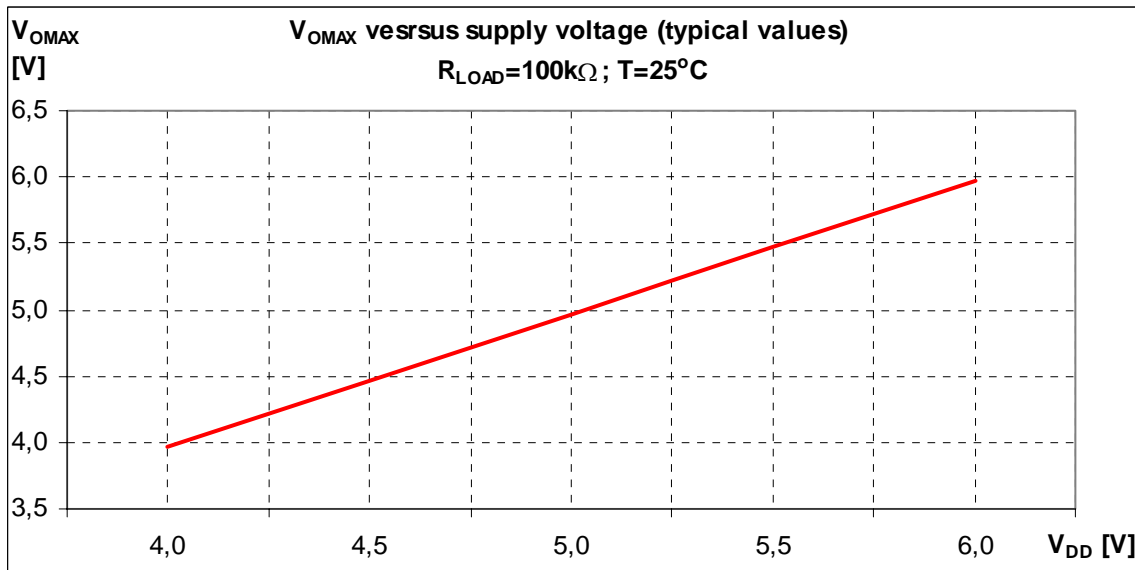
Typical performance characteristics: measured values
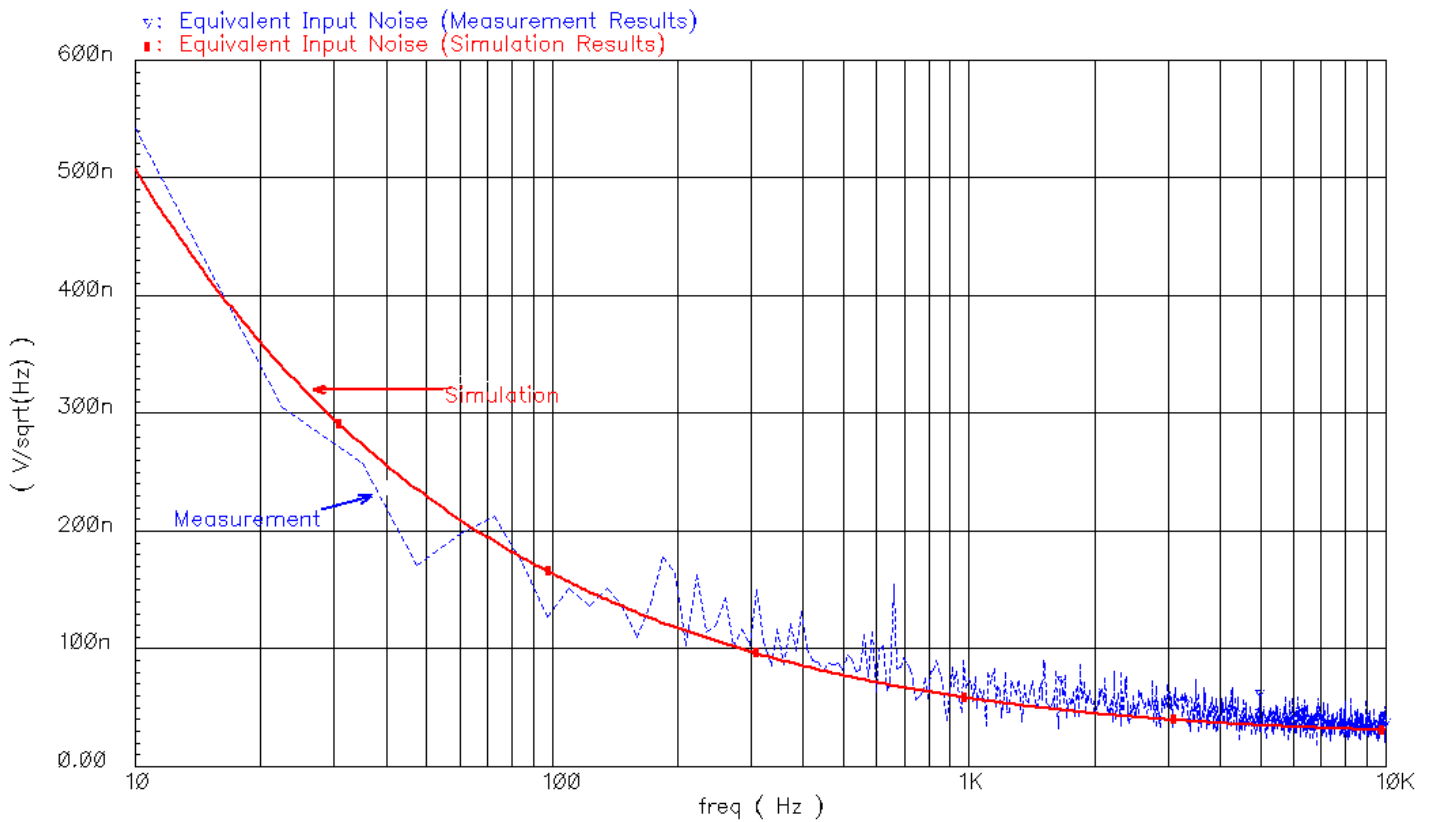

Fig. 4 Output swing versus supply voltage

Fig. 5 Equivalent Input Noise Voltage versus Frequency

References

Agnew W. F., and McCreery D. B., Neural Prostheses: Fundamental Studies, London, U.K.: Prentice-Hall, 1990, pp. 1-23.

Andreasen L. N. S., Struijk J. J., and Haugland M., "An artificial nerve fiber for evaluation of nerve cuff electrodes," Proc. IEEE Eng. Med. and Biol., vol. 5, pp. 1997-1999, 1997.

Andreasen L. N. S., Struijk J. J., and Lawrence S., "Measurement of the performance of nerve cuff electrodes for recording," Med. and Biol. Eng. and Comput., vol. 38, pp. 447-453, 2000.

Andreasen L. N. S., and Struijk J. J., "Signal strength versus cuff length in nerve cuff electrode recordings," IEEE Trans. Biomed. Eng., vol. 49, no. 9, pp. 1045-1050, September 2002.

Andreasen L. N. S., and Struijk J. J., "Artefact reduction with alternative cuff configurations," IEEE Trans. Biomed. Eng., vol. 50, no. 10, pp. 1160-1166, October 2003.

Antoniou A., "Floating negative-impedance converters," IEEE Trans. Circ. Theory, vol. 19, no. 2, pp. 209-212, March 1972.

Apparelyzed: SCI peer support, "SCI: quadriplegic and paraplegic injuries," available at: http://www.apparelyzed.com, last accessed: September 2010.

Armstrong R. D, and Burnham R. A., "The effect of roughness on the impedance of the interface between a solid electrolyte and a blocking electrode," J. Electroanal. Chem., vol. 72, pp. 257-266, 1976.

Bard A. J., and Faulkner L. R., Electrochemical Methods: Fundamentals and Applications, 2nd ed. London, U.K.: John Wiley & Sons, 2001.

Barsoukov E., and Macdonald J. R., Impedance Spectroscopy: Theory, Experiment, and Applications, 2nd ed. London, U.K.: John Wiley & Sons, 2005.

Bates J. B., Wang J. C., and Chu Y. T., "Impedance of metal-solid electrolyte interfaces," Solid State Ionics, vol. 18 & 19, pp. 1045-1049, 1986.

Bates J. B., Chu Y. T., and Stribling W. T., "Surface topography and impedance of metal-electrolyte interfaces," Phys. Rev. Lett., vol. 60, no. 7, pp. 627-630, February 1988.

Biswas K., Sen S., and Dutta P. K., "Realization of a constant phase element and its performance study in a differentiator circuit," IEEE Trans. Circ. Syst. II, vol. 53, no. 9, pp. 802-806, September 2006.

Blunt M., "The impedance of a self-affine surface," J. Phys. A: Math. Gen., vol. 22, pp. 1179-1192, 1989.

Bottelberghs P. H., and Broers G. H. J., "Interfacial impedance behaviour of polished and paint platinum electrodes at Na_2WO_4–Na_2MoO_4 solid electrolytes," J. Electroanal. Chem., vol. 67, pp. 155-167, 1976.

Boyer S., Sawan M., Abdel-Gawad M., Robin S., and Elhilali M. M., "Implantable selective stimulator to improve bladder voiding: design and chronic experiments in dogs," IEEE Trans. Rehab. Eng., vol. 8, no. 4, pp. 464-470, December 2000.

Brindley G. S., "Electrode-arrays for making long-lasting electrical connexion to spinal roots," J. Physiol., vol. 222, no. 2, pp. 135-136, April 1972.

Brindley G. S., Polkey C. E., and Rushton D. N., "Sacral anterior root stimulators for bladder control in paraplegia," Paraplegia, vol. 20, pp. 365-381, 1982.

Brindley G. S., Polkey C. E., Rushton D. N., and Cardozo L., "Sacral anterior root stimulators for bladder control in paraplegia: the first 50 cases," J. Neurol. Neurosurg. Psychiatry, vol. 49, no. 10, pp. 1104-1114, October 1986.

Brindley G. S., "The first 500 patients with sacral anterior root stimulator implants: general description," Paraplegia, vol. 32, no. 12, pp. 795-805, December 1994.

Bugbee M. B., "An implantable stimulator for selective stimulation of nerves," Ph.D. dissertation, Dept. of Medical Physics and Bioeng., University College London, London, U.K.: 2000.

Casas O., and Pallas-Areny R., "Optimal bias circuit for instrumentation amplifiers," Proc. XIV IMEKO World Congress, vol. IVB, pp. 143-148, 1997.

Cirmirakis D., Demosthenous A., and Donaldson N., "Comparison of methods for interference neutralisation in tripolar nerve recording cuffs," IEEE Proc. ISCAS, pp. 3465-3468, August 2010.

Cole K. S., and Cole R. H., "Dispersion and absorption in dielectrics: I. alternating current characteristics," J. Chem. Phys., vol. 9, no. 4, pp. 341-351, April 1941.

Craggs M., and McFarlane J., "Physiological society symposium: the physiology and pathophysiology of the lower urinary tract," Exper. Physiol., vol. 84, pp. 149-160, 1999.

de Boer R. W., and van Oosterom A., "Electrical properties of platinum electrodes: impedance measurements and time-domain analysis," Med. and Biol. Eng. & Comp., vol. 16, pp. 1-10, January 1978.

de Levie R., "On porous electrodes in electrolyte solutions," Electrochimica Acta, vol. 8, pp. 751-780, 1963.

de Levie R., "The influence of surface roughness of solid electrodes on electrochemical measurements," Electrochimica Acta, vol. 10, pp. 113-130, 1965.

de Levie R., "Fractals and rough electrodes," J. Electroanal. Chem., vol. 281, pp. 1-21, 1990.

De Marcellis A., Ferri G., and Stornelli V., "NIC-based capacitance multipliers for low-frequency integrated active filter applications," IEEE Proc. PRIME, pp. 225-228, July 2007.

DeCarlo R. A., and Lin P.-M., Ch. 10, Linear Circuit Analysis: Time Domain, Phasor, and Laplace Transform Approaches, 2nd ed. Oxford, U.K.: Oxford University Press, 2001.

Demosthenous A., Taylor J., Triantis I. F., Rieger R., and Donaldson N., "Design of an adaptive interference reduction system for nerve-cuff electrode recording," IEEE Trans. Circuits Syst. I: Fundamental Theory and Applications, vol. 51, no. 4, pp. 629-639, April 2004.

Demosthenous A., and Triantis I. F., "An adaptive ENG amplifier for tripolar cuff electrodes," IEEE JSSC, vol. 40, no. 2, pp. 412-421, February 2005.

Demosthenous A., Pachnis I., Rahal M., Jiang D., and Donaldson N., "An ENG amplifier with passive EMG neutralization," IEEE Proc. ICECS, pp. 66-69, December 2007.

Demosthenous A., Jiang D., Pachnis I., Liu X., Rahal M., and Donaldson N., "A programmable ENG amplifier with passive EMG neutralization for FES applications," IEEE Proc. ISCAS, pp. 1552-1555, May 2008.

Donaldson N. de N., Zhou L., Perkins T. A., Munih M., Haugland M., and Sinkjaer T., "Implantable telemeter for long-term electroneurographic recordings in animals and humans," Med. Biol. Eng. Comput., vol. 41, no. 6, pp. 654-664, 2003.

Donaldson N., Perkins T., Pachnis I., Vanhoest A., and Demosthenous A., "Design of an implant for preventing incontinence after spinal cord injury," Artif. Organs, vol. 32, no. 8, pp. 586-591, August 2008.

Duck F. A., Physical Properties of Tissue – A Comprehensive Reference Book, London, U.K.: Academic Press, 1990.

Fisher A. C., Electrode Dynamics, Oxford, U.K.: Oxford University Press, 2006.

Franks W., Schenker I., Schmutz P., and Hierlemann A., "Impedance characterization and modeling of electrodes for biomedical applications," IEEE Trans. Biomed. Eng., vol. 52, no. 7, pp. 1295-1302, July 2005.

Geddes L. A., da Costa C. P., and Wise G., "The impedance of stainless-steel electrodes," Med. and Biol. Eng., vol. 9, pp. 511-521, 1971.

Geddes L. A., "Historical evolution of circuit models for the electrode-electrolyte interface," Ann. Biomed. Eng., vol. 25, pp. 1-14, 1997.

Geddes L. A., and Roeder R., "Measurement of the direct-current (faradic) resistance of the electrode-electrolyte interface for commonly used electrode materials," Ann. Biomed. Eng., vol. 29, pp. 181-186, 2001.

Grill W. M., and Mortimer J. T., "Electrical properties of implant encapsulation tissue," Ann. Biomed. Eng., vol. 22, pp. 23-33, 1994.

Grimnes S., and Martinsen Ø. G., Bioimpedance and Bioelectricity Basics, London, U.K.: Academic Press, 2000.

Hansen M., Haugland M., Sinkjaer T., and Donaldson N., "Real time foot drop correction using machine learning and natural sensors," Neuromodulation, vol. 5, no. 1, pp. 41-53, 2002.

Haugland M. K., and Hoffer J. A., "Artifact-free sensory nerve signals obtained from cuff electrodes during functional electrical stimulation of nearby muscles," IEEE Trans. Rehab. Eng., vol. 2, no. 1, pp. 37-40, March 1994.

Haugland M. K., and Sinkjaer T., "Cutaneous whole nerve recordings used for correction of footdrop in hemiplegic man," IEEE Trans. Rehab. Eng., vol. 3, no. 4, pp. 307-317, December 1995.

Haugland M., "A flexible method for fabrication of nerve cuff electrodes," Proc. IEEE Eng. Med. and Biol. Soc., vol. 1, pp. 359-360, November 1996.

Haugland M., Lickel A., Riso R., Adamczyk M. M., Keith M., Jensen I. L., Haase J., and Sinkjaer T., "Restoration of lateral hand grasp using natural sensors," Artif. Organs., vol. 21, no. 3, pp. 250-253, March 1997.

Haugland M., Lickel A., Haase J., and Sinkjaer T., "Control of FES thumb force using slip information obtained from the cutaneous electroneurogram in quadriplegic man," Trans. Rehab. Eng., vol. 7, no. 2, pp. 215-227, June 1999a.

Haugland M., and Sinkjaer T., "Interfacing the body's own sensing receptors into neural prosthesis devices," Technol. Health Care, vol. 7, no. 6, pp. 393-399, January 1999b.

Hoffer J. A., Marks W. B., and Rymer W. Z., "Nerve fibre activity during normal movements," Proc. Annu. Society for Neuroscience Meeting, vol. 4, p. 300, 1974.

Hsu C. H., and Mansfeld F., "Concerning the conversion of the constant phase element parameter Y_0 into a capacitance," Corrosion, vol. 57, no. 9, pp. 747-748, 2001.

Jezernik S., Wen J. G., Rijkhoff N. J. M., Djurhuus J. C., and Sinkjaer T., "Analysis of bladder related nerve cuff electrode recordings from preganglionic pelvic nerve and sacral roots in pigs," J. Urol., vol. 163, no. 4, pp. 1309-1314, April 2000.

Jorcin J.-B., Orazem M. E., Pebere N., and Tribollet B., "CPE analysis by local electrochemical impedance spectroscopy," Electrochimica Acta, vol. 51, pp. 1473-1479, 2006.

Kallesoe K., Hoffer J. A., Strange K., and Valenzuela I., "Implantable cuff having improved closure," U.S. Patent No. 5.487.756, 1996.

Kaplan T., and Gray L. J., "Effect of disorder on a fractal model for the ac response of a rough interface," Phys. Rev. B, vol. 32, no. 11, pp. 7360-7366, December 1985.

Kaplan T., Liu S. H., and Gray L. J., "Inverse-Cantor-bar model for the ac response of a rough interface," Phys. Rev. B, vol. 34, no. 7, pp. 4870-4873, October 1986.

Kaplan T., Gray L. J., and Liu S. H., "Self-affine fractal model for a metal-electrolyte interface," Phys. Rev. B, vol. 35, no. 10, pp. 5379-5381, April 1987.

Keddam M., and Takenouti H., "Impedance of fractal interfaces: new data on the Von Koch model," Electrochimica Acta, vol. 33, no. 3, pp. 445-448, 1988.

Keiser H., Beccu K. D., and Gutjahr M. A., "Abschätzung der porenstruktur poröser elektroden aus impedanzmessungen," Electrochimica Acta, vol. 21, pp. 539-543, 1976.

Keynes R. D., and Aidley D. J., Nerve and Muscle, 3rd ed., London, U.K.: Cambridge University Press, 2001.

Kirkham A. P. S., Knight S. L., Craggs M. D., Casey A. T. M., and Shah P. J. R., "Neuromodulation through sacral nerve roots 2 to 4 with a Finetech-Brindley sacral posterior and anterior root stimulator," Spinal Cord, vol. 40, no. 6, pp. 272-281, June 2002.

Kramer M., and Tomkiewicz M., "Porous Electrodes I: Numerical simulation using random network and single-pore models," J. Electrochem. Soc., vol. 131, no. 6, pp. 1283-1288, June 1984.

Kurstjens G. A. M, Borau A., Rodriguez A., Rijkhoff N. J. M., and Sinkjaer T., "Intraoperative recording of electroneurographic signals from cuff electrodes on extradural sacral roots in spinal cord injured patients," J. Urol., vol. 174, no. 4 Pt-1, pp. 1482-1487, October 2005.

Kurtyka B., and de Levie R., "Frequency dispersion associated with a non-homogeneous interfacial capacitance," J. Electroanal. Chem., vol. 322, pp. 63-77, 1992.

Le Mehaute A., and Crepy G., "Introduction to transfer and motion in fractal media: the geometry of kinetics," Solid State Ionics, vol. 9 & 10, pp. 17-30, 1983.

Liu S. H., "Fractal model for the ac response of a rough interface," Phys. Rev. Lett., vol. 55, no. 5, pp. 529-532, July 1985.

Liu S. H., Kaplan T., and Gray L. J., "AC response of fractal interfaces," Solid State Ionics, vol. 18 & 19, pp. 65-71, 1986.

Liu X., Demosthenous A., and Donaldson N., "Platinum electrode noise in the ENG spectrum," Med. and Biol. Eng. & Comp., vol. 46, pp. 997-1003, 2008.

Mandelbrot B. B., The Fractal Geometry of Nature, Rev. ed. New York, U.S.: W. H. Freeman & Co., 1982.

Maritan A., and Toigo F., "On skewed arc plots of impedance of electrodes with an irreversible electrode process," Electrochimica Acta, vol. 35, no. 1, pp. 141-145, 1990.

Mathers L. H., The Peripheral Nervous System: Structure, Function, and Clinical Correlations, Wokingham, U.K.: Addison-Wesley, 1985.

Mayer S., Geddes L. A., Bourland J. D., and Ogborn L., "Faradic resistance of the electrode/electrolyte interface," Med. and Biol. Eng. & Comp., vol. 30, pp. 538-542, September 1992.

McAdams E. T., and Jossinet J., "The detection of the onset of electrode-electrolyte interface impedance nonlinearity: a theoretical study," IEEE Trans. Biomed. Eng., vol. 41, no. 5, pp. 498-500, May 1994.

McAdams E. T., and Jossinet J., "Tissue impedance: a historical overview," Physiol. Meas., vol. 16, pp. A1-A13, 1995a.

McAdams E. T., Lackermeier A., McLaughlin J. A., and Macken D., "The linear and non-linear electrical properties of the electrode-electrolyte interface," Biosens. And Bioelectro., vol. 10, pp. 67-74, 1995b.

McAdams E. T., Bioelectrodes Ch., Encyclopedia of Medical Devices and Instrumentation, 2nd ed., edited by Webster J. G., London, U.K.: John Wiley & Sons, 2006.

Naples G. G., Mortimer J. T., Scheiner A., and Sweeney J. D., "A spiral nerve cuff electrode for peripheral nerve stimulation," IEEE Trans. Biomed. Eng., vol. 35, no. 11, pp. 905-916, November 1988.

National spinal cord injury statistical center (NSCISC), "Spinal cord injury facts and figures at a glance," available at: https://www.nscisc.uab.edu, last accessed: September 2010.

Nikolic Z. M., Popovic D. B., Stein R. B., and Kenwell Z., "Instrumentation for ENG and EMG recordings in FES systems," IEEE. Trans. Biomed. Eng., vol. 41, no. 7, pp. 703-706, July 1994.

Nyikos L., and Pajkossy T., "Fractal dimension and fractional power frequency-dependent impedance of blocking electrodes," Electrochimica Acta, vol. 30, no. 11, pp. 1533-1540, 1985.

Nyikos L., and Pajkossy T., "Electrochemistry at fractal interfaces: the coupling of ac and dc behaviour at irregular electrodes," Electrochimica Acta, vol. 35, no. 10, pp. 1567-1572, 1990.

Onaral B., and Schwan H. P., "Linear and nonlinear properties of platinum electrode polarisation. Part 1: frequency dependence at very low frequencies," Med. and Biol. Eng. & Comp., vol. 20, pp. 299-306, May 1982.

Orazem M. E., Pebere N., and Tribollet B., "Enhanced graphical representation of electrochemical impedance data," J. Electrochem. Soc., vol. 153, no. 4, pp. B129-B136, 2006.

Pachnis I., Demosthenous A., and Donaldson N., "Passive neutralization of myoelectric interference from neural recording tripoles," IEEE Trans. Biomed. Eng., vol. 54, no. 6, pp. 1067-1074, June 2007.

Pachnis I., Demosthenous A., and Rahal M., "Adaptive EMG neutralization using the modified QT," IEEE Proc. ISCAS, pp. 2941-2944, May 2008.

Pachnis I., Demosthenous A., and Donaldson N., "Interference reduction techniques in neural recording tripoles: an overview," IEEE Proc. PRIME, pp. 332-335, July 2009a.

Pachnis I., Demosthenous A., and Donaldson N., "Realization of constant phase element in metallic electrodes for interference reduction in neural recording tripoles," IFMBE Proceedings 25/IX WC, pp. 353-357, September 2009b.

Pachnis I., Demosthenous A., and Donaldson N., "Towards an adaptive modified quasi-tripole amplifier configuration for EMG neutralization in neural recording tripoles," IEEE Proc. ISCAS, pp. 3144-3147, May 2010.

Pajkossy T., and Nyikos L., "Impedance of fractal blocking electrodes," J. Electrochem. Soc., vol. 133, no. 10, pp. 2061-2064, October 1986.

Pajkossy T., and Nyikos L., "Comments on J. C. Wang's paper on the impedance of a fractal electrolyte-electrode interface," Electrochimica Acta, vol. 33, no. 5, pp. 713-715, 1988.

Pajkossy T., and Nyikos L., "Scaling-law analysis to describe the impedance behavior of fractal electrodes," Phys. Rev. B, vol. 42, no. 1, pp. 709-719, July 1990.

Pajkossy T., "Electrochemistry at fractal surfaces," J. Electroanal. Chem., vol. 300, pp. 1-11, 1991.

Pajkossy T., and Nyikos L., "Impedance of planar electrodes with scale-invariant capacitance distribution," J. Electroanal. Chem., vol. 332, pp. 55-61, 1992.

Pajkossy T., "Impedance of rough capacitive electrodes," J. Electroanal. Chem., vol. 364, pp. 111-125, 1994.

Pajkossy T., "Impedance spectroscopy at interfaces of metals and aqueous solutions – Surface roughness, CPE and related issues," Solid State Ionics, vol. 176, pp. 1997-2003, 2005.

Peckham P. H., and Knutson J. S., "Functional electrical stimulation for neuromuscular applications," Annu. Rev. Biomed. Eng., vol. 7, pp. 327-360, 2005.

Pflaum C., Riso R. R., and Wiesspeiner G., "An improved nerve cuff recording configuration for FES feedback control system that utilise natural sensors," Proc. IFESS, pp. 407–410, 1995.

Pflaum C., Riso R. R., and Wiesspeiner G., "Performance of alternative amplifier configurations for tripolar nerve cuff recorded ENG," Proc. IEEE Eng. Med. and Biol., vol. 1, pp. 375-376, 1996.

Pollak V., "An equivalent diagram for the interface impedance of metal needle electrodes," Med. and Biol. Eng., vol. 12, no. 4, pp. 454-459, July 1974a.

Pollak V., "Computation of the impedance characteristic of metal electrodes for biological investigations," Med. and Biol. Eng., vol. 12, no. 4, pp. 460-464, July 1974b.

Pollak V., "Impedance measurements on metal needle electrodes," Med. and Biol. Eng., vol. 12, no. 5, pp. 606-612, September 1974c.

Popovic D. B., Stein R. B., Jovanovic K. Lj., Dai R., Kostov A., and Armstrong W. W., "Sensory nerve recording for closed-loop control to restore motor functions," IEEE Trans. Biomed. Eng., vol. 40, no. 10, pp. 1024-1031, October 1993.

Ragheb T., and Geddes L. A., "Electrical properties of metallic electrodes," Med. and Biol. Eng. & Comp., vol. 28, pp. 182-186, March 1990.

Ragheb T., Riegle S., Geddes L. A., and Amin V., "The impedance of a spherical monopolar electrode," Ann. Biomed. Eng., vol. 20, pp. 617-627, 1992.

Rahal M., Winter J., Taylor J., and Donaldson N., "Application of closed-loop control in the reduction of interference in nerve cuff recordings," IEEE Proc. ICECS, vol. 2, pp. 1039-1042, September 1999.

Rahal M., Taylor J., and Donaldson N., "The effect of nerve cuff geometry on interference reduction: a study by computer modelling," IEEE Trans. Biomed. Eng., vol. 47, no. 1, pp. 136-138, January 2000a.

Rahal M., Winter J., Taylor J., and Donaldson N., "An improved configuration for the reduction of EMG in electrode cuff recordings: a theoretical approach," IEEE Trans. Biomed. Eng., vol. 47, no. 9, pp. 1281-1284, September 2000b.

Rahal M., "Optimisation of nerve cuff electrode recordings for functional electrical stimulation applications," Ph.D. dissertation, Dept. of Electronic and Electrical Eng., University College London, London, U.K.: 2000c.

Rajagopalan V., Cruz A.-V., and Popovic D. B., "Control of functional electrical stimulation for walking and standing of hemiplegics," IEEE EUROCON, vol. 1, pp. 48-51, November 2005.

Rammelt U., and Reinhard G., "On the applicability of a constant phase element (CPE) to the estimation of roughness of solid metal electrodes," Electrochimica Acta, vol. 35, no. 6, pp. 1045-1049, 1990.

Raspopovic S., Carpaneto J., Udina E., Navarro X., and Micera S., "On the identification of sensory information from mixed nerves by using single-channel cuff electrodes," J. Neuroeng. Rehabil., vol. 7, no. 17, April 2010.

Reeve-Irvine research center, "Module: anatomy 101," available at: http://www.reeve.uci.edu, last accessed: September 2010.

Research Solutions & Resources LLC., "Explaining a constant phase element (CPE): what causes a CPE?," available at: http://www.consultrsr.com/resources/eis/cpe2.htm, last accessed: March 2010.

Roy S. C. D., and Shenoi B. A., "Distributed and lumped RC realization of a constant argument impedance," J. Franklin Inst., vol. 282, no. 5, pp. 318-329, November 1966.

Sahin M., Durand D. M., and Haxhiu M. A., "Whole nerve recordings with the spiral nerve cuff electrode," Proc. IEEE Eng. Med. and Biol. Soc., vol. 1, pp. 372-373, November 1994.

Sapoval B., "Fractal electrodes and constant phase angle response: exact examples and counter examples," Solid State Ionics, vol. 23, pp. 253-259, 1987.

Scheider W., "Theory of the frequency dispersion of electrode polarization. Topology of networks with fractional power frequency dependence," J. Phys. Chem., vol. 79, no. 2, pp 127-136, 1975.

Schrama J., On the phenomenological theory of linear relaxation processes, Ph.D. dissertation, University of Leiden, Netherlands, 1957.

Sedra A. S., and Smith K. C., Microelectronic Circuits, 3rd ed., London, U.K.: Saunders College Publishing, 1991.

Sevcencu C., Rijkhoff N. J. M., and Sinkjaer T., "Colon emptying induced by sequential electrical stimulation in rats," IEEE Trans. Neural Sys. and Rehab. Eng., vol. 13, no. 4, pp. 516-523, December 2005.

Simpson R. W., Berberian J. G., and Schwan H. P., "Nonlinear AC and DC polarization of platinum electrodes," IEEE Trans. Biomed. Eng., vol. BME-27, no. 3, pp. 166-171, March 1980.

Sinkjaer T., Haugland M. K., and Haase J., "Natural neural sensing and artificial muscle control in man," Exp. Brain Res., vol. 98, pp. 542-545, 1994.

Stein R. B., Charles D., Davis L., Jhamandas J., Mannard A., and Nichols T. R., "Principles underlying new methods for chronic neural recording," Le J. Can. des Sciences Neurologiques, vol. 2, pp. 235-244, 1975.

Stein R. B., Peckham P. H., and Popovic D. P., Neural Prostheses: Replacing Motor Function After Disease or Disability, New York, U.S.: Oxford University Press, 1992.

Struijk J. J., and Thomsen M., "Tripolar nerve cuff recording: stimulus artifact, EMG, and the recorded nerve signal," IEEE Eng. Med. and Biol., vol. 2, pp. 1105-1106, September 1995.

Struijk J. J., Thomsen M., Larsen J. O., and Sinkjaer T., "Cuff electrodes for long-term recording of natural sensory information," IEEE Eng. Med. and Biol., vol. 18, no. 3, pp. 91-98, May/June 1999.

Tesfayesus W., Yoo P., and Durand D. M., "Blind source separation of nerve cuff recordings," IEEE Proc. EMBS, pp. 2507-2510, September 2003.

Triantis I. F., Demosthenous A., Donaldson N., and Struijk J. J., "Experimental assessment of imbalance conditions in a tripolar cuff for ENG recordings," Proc. IEEE Eng. Med. and Biol., pp. 380-383, March 2003.

Triantis I. F., "An adaptive amplifier for cuff imbalance correction and interference reduction in nerve signal recording," Ph.D. dissertation, Dept. of Electronic and Electrical Eng., University College London, London, U.K.: 2005a.

Triantis I. F., Demosthenous A., and Donaldson N., "On cuff imbalance and tripolar ENG amplifier configurations," IEEE Trans. Biomed. Eng., vol. 52, no. 2, pp. 314-320, February 2005b.

Triantis I. F., and Demosthenous A., "The effect of interference source proximity on cuff imbalance," IEEE Trans. Biomed. Eng., vol. 53, no. 2, pp. 354-357, February 2006.

Upshaw B., and Sinkjaer T., "Digital signal processing algorithms for the detection of afferent nerve activity recorded from cuff electrodes," IEEE Trans. Rehab. Eng., vol. 6, no. 2, pp. 172-181, June 1998.

Vanhoestenberghe A., "Implanted devices: improved methods for nerve root stimulation," Ph.D. dissertation, Dept. of Medical Physics and Bioeng., University College London, London, U.K.: 2007.

Wang J. C., and Bates J. B., "Model for the interfacial impedance between a solid electrolyte and a blocking metal electrode," Solid State Ionics, vol. 18 & 19, pp. 224-228, 1986.

Wang J. C., "Realizations of generalized Warburg impedance with RC ladder networks and transmission lines," J. Electrochem. Soc., vol. 134, no. 8, pp. 1915-1920, August 1987.

Wang J. C., "Comparison of fractal and pore models for electrolyte/electrode interfaces," Solid State Ionics, vol. 28-30, pp. 1436-1440, 1988a.

Wang J. C., "Impedance of a fractal electrolyte-electrode interface," Electrochimica Acta, vol. 33, no. 5, pp. 707-711, 1988b.

Wang J. C., "Comments on a fractal model for blocking interfaces," Electrochimica Acta, vol. 34, no. 7, pp. 987-990, 1989.

Webster J. G., Medical Instrumentation: Application and Design, 4th ed. London, U.K.: John Wiley & Sons, 2010.

Weinman J., and Mahler J., "An analysis of electrical properties of metal electrodes," Med. Electron. Biol. Eng., vol. 2, pp. 299-310, 1964.

Wikipedia: the free encyclopedia, "Neuron," available at: http://en.wikipedia.org/wiki/Neuron, last accessed: September 2010; "Nervous system," available at: http://en.wikipedia.org/wiki/Nervous_system, last accessed: September 2010; "Action potential," available at: http://en.wikipedia.org/wiki/Action_potential, last accessed: September 2010.

Wolff I., "A study of polarization capacity over a wide frequency band," Phys. Rev., vol. 27, pp. 755-763, June 1926.